



UNIVERSITY OF
BIRMINGHAM

A DIGITAL TWIN OF THE HUMAN COLON FOR THE
DESIGN AND OPTIMISATION OF COLON-TARGETED
DRUG DELIVERY SYSTEMS

by

MICHAEL SCHÜTT

A thesis submitted to the University of Birmingham for the degree of
DOCTOR OF PHILOSOPHY

School of Chemical Engineering
College of Engineering and Physical Sciences
University of Birmingham
September 2022

UNIVERSITY OF
BIRMINGHAM

University of Birmingham Research Archive

e-theses repository

This unpublished thesis/dissertation is copyright of the author and/or third parties. The intellectual property rights of the author or third parties in respect of this work are as defined by The Copyright Designs and Patents Act 1988 or as modified by any successor legislation.

Any use made of information contained in this thesis/dissertation must be in accordance with that legislation and must be properly acknowledged. Further distribution or reproduction in any format is prohibited without the permission of the copyright holder.

ABSTRACT

The performance of a solid dosage form targeting the colon is commonly assessed using standardised pharmacopeial dissolution apparatuses like the USP II or the miniaturised replica, the mini-USP II. However, these dissolution apparatuses fail to replicate the hydrodynamics and shear stresses in the colonic environment. These parameters are crucial for the tablet's drug release process and the distribution of the dissolved active pharmaceutical ingredient along the colon. The ascending part of the colon is the most favourable side for colonic drug delivery as it offers the most suitable environmental conditions for drug dissolution. In this thesis, a mesh-less particle method called Discrete Multiphysics is used where particles represent both the fluid and solid phases. This framework combines particle methods such as Smoothed Particle Hydrodynamics for fluid mechanics and Lattice Spring Model for solid mechanics. The modelling technique is used to build three different types of models: (i) a model of the proximal colon, which can replicate in vivo motility patterns, (ii) a model of a tablet that dissolves/disintegrates in the colonic environment; and (iii) a model of the mini-USP II dissolution apparatus to compare the performance of a solid dosage form in a standardised dissolution apparatus and a biorelevant colon model. These Discrete Multiphysics models have made it possible to analyse the hydrodynamics in the colon, the shear rates acting on a tablet, and the performance of different motility patterns in the colon concerning drug distribution and therefore offers the first step to a spatiotemporal dissolution profile of the colon.

Keywords: Discrete Multiphysics; Mathematical modelling, Smoothed Particle Hydrodynamics; Lattice Spring Model; Fluid Dynamics; Peristalsis; Large intestine;

Colon; Proximal colon; Fluid-Structure interaction; Colonic drug delivery; Tablet disintegration; Drug release profile; Dissolution profile; Spatiotemporal concentration profile; Shear rate; Tablet disintegration; Dissolution apparatus; Digital twin; mini-USP II

To my family.

ACKNOWLEDGEMENTS

First and foremost, I would like to thank my primary supervisor Dr. Alessio Alexiadis for giving me the opportunity to write this PhD thesis and for supporting and guiding me throughout the research. I thank him for his confidence in my potential and for helping me to grow as a researcher as well after I had already gained experience in the industry.

I would also like to thank my co-supervisors, Prof. Dr. Mark Simmons and Dr. Konstantinos Stamatopoulos, for their support during my PhD. In particular, I would like to thank Dr Konstantinos Stamatopoulos for his fruitful discussions and support and for providing his expertise in the field. Many thanks also to Prof. Dr. Hanna Batchelor for her support, rich discussions and good suggestions, and for providing her expertise in the area of research. I also would like to acknowledge Engineering and Physical Sciences Research Council (EPSRC) for funding this PhD project.

Special thanks go to my former professor Prof. Dr.-Ing. Uwe Großmann and my industry colleague Dr. André Lalla who also made significant contributions. Thank you for encouraging me and supporting my carrier development. Many thanks to Dr. Stefan Effkemann, who unknowingly gave me the inspiration/motivation for this journey.

I also want to thank my family for the total support, especially my wife, for supporting me physically and emotionally. I would also like to thank her for the shared experiences in a foreign country that made us overcome obstacles together and even stronger as a team. Many thanks to my daughter Maja Elea and my son Milo Kian

for their patience and sacrifices. Hopefully, living abroad in a multicultural environment will benefit their personal and professional future.

A huge thank you to my parents for the unconditional support that they accepted our separation and showed patience over these years.

CONTENT LISTING

- LIST OF PEER-REVIEWED PUBLICATIONS
- LIST OF FIGURES
- LIST OF TABLES

PEER-REVIEWED PUBLICATIONS

From the work of this thesis, the following papers have been published or submitted:

- **Schütt, M.;** Stamatopoulos, K.; Simmons, M.J.H.; Batchelor, H.K.; Alexiadis, A. Modelling and simulation of the hydrodynamics and mixing profiles in the human proximal colon using Discrete Multiphysics. *Comput Biol Med* 2020, 121, 103819. DOI: 10.1016/j.compbimed.2020.103819
(Chapter 4)
- **Schütt, M.;** Stamatopoulos, K.; Batchelor, H.K.; Simmons, M.J.H.; Alexiadis, A. Modelling and Simulation of the Drug Release from a Solid Dosage Form in the Human Ascending Colon: The Influence of Different Motility Patterns and Fluid Viscosities. *Pharmaceutics* 2021, 13, 859. DOI: 10.3390/pharmaceutics13060859
(Chapter 5)
- **Schütt, M.;** O'Farrell, C.; Stamatopoulos, K.; Hoad, C.L.; Marciani, L.; Sulaiman, S.; Simmons, M.J.H.; Batchelor, H.K.; Alexiadis, A. Simulating the Hydrodynamic Conditions of the Human Ascending Colon: A Digital Twin of the Dynamic Colon Model. *Pharmaceutics* 2022, 14, 184. DOI: 10.3390/pharmaceutics14010184
(Chapter 6)

- **Schütt, M.;** Stamatopoulos, K.; Batchelor, H.K.; Simmons, M.J.H.; Alexiadis, A. Development of a digital twin of a tablet that mimics a real solid dosage form: differences in the drug release profile in conventional mini-USP II and a biorelevant colon model. *European Journal of Pharmaceutical Sciences* 2022, 179, 106301. DOI: 10.1016/j.ejps.2022.106310
(Chapter 7)

TABLE OF CONTENTS

CHAPTER 1	GENERAL INTRODUCTION	1
1.1	OVERVIEW	2
1.2	AIM AND OBJECTIVES OF THE THESIS	7
1.3	THESIS BREAKDOWN	8
CHAPTER 2	THE COLONIC ENVIRONMENT: FUNCTION, STRUCTURE, DATA ASSESSMENT, DRUG DELIVERY AND MODELS TO DATE	12
2.1	PHYSIOLOGY OF THE HUMAN COLON.....	13
2.1.1	<i>Accessibility to Human Colon Transit.....</i>	<i>21</i>
2.1.2	<i>Human Colon Motility.....</i>	<i>24</i>
2.1.2.1	Recording Techniques and Colonic Motor Functions.....	24
2.1.3	<i>Colon Targeting Drug Delivery.....</i>	<i>31</i>
2.1.3.1	Types of Drug Release Mechanisms	31
2.1.3.2	Layered Tablets for Immediate and Delayed Drug Release.....	34
2.1.3.3	Modified Release Tablets and their Extended-Release Mechanisms.....	35
2.1.4	<i>Dissolution Testing of Oral Administrated Dosage Forms</i>	<i>42</i>
2.1.5	<i>Physiologically Based Pharmacokinetic Modelling.....</i>	<i>47</i>
2.1.6	<i>In Silico Models Existing to Date</i>	<i>49</i>
2.1.6.1	Colon (Large intestine).....	50
2.1.6.2	Small intestine	51
2.1.6.3	USP Dissolution Apparatuses.....	53
CHAPTER 3	METHODOLOGY.....	56
3.1	THE DISCRETE MULTIPHYSICS (DMP)	57

3.1.1	<i>Introduction</i>	57
3.1.2	<i>Particle-Based Methods in DMP</i>	60
3.1.3	<i>Smoothed Particle Hydrodynamics</i>	62
3.1.3.1	<i>Introduction</i>	62
3.1.3.2	<i>Fundamental Equations of SPH</i>	62
3.1.3.3	<i>Smoothing Kernel Functions and Smoothing Length h</i>	65
3.1.3.4	<i>Governing Fluid Dynamic Equations</i>	67
3.1.3.5	<i>Viscous Term</i>	69
3.1.4	<i>Lattice Spring Model</i>	70
3.1.5	<i>Coupling SPH-LSM: The Discrete Multiphysics</i>	73
3.1.5.1	<i>Solid Boundary Conditions</i>	74
3.1.5.2	<i>Repulsive Interactions</i>	75
3.1.5.3	<i>Stationary Particles</i>	77
3.1.6	<i>Mass Transfer</i>	77
3.1.7	<i>Model Design</i>	78
3.1.7.1	<i>Geometry Design and Particle Distribution</i>	78
3.1.7.2	<i>Design of Different Contraction Patterns</i>	78
3.1.7.3	<i>Design of Solid Dosage Form (Tablet)</i>	79

CHAPTER 4	MODELLING AND SIMULATION OF THE HYDRODYNAMICS AND MIXING PROFILES IN THE HUMAN PROXIMAL COLON USING DISCRETE MULTIPHYSICS	82
4.1	ABSTRACT	83
4.2	INTRODUCTION	83
4.3	METHODOLOGY	85
4.3.1	<i>Modelling Approach</i>	85

4.3.2	<i>Model Geometry</i>	86
4.3.3	<i>Model and Simulation Parameters</i>	89
4.3.4	<i>Colon Contraction</i>	91
4.4	SOFTWARE	92
4.5	RESULTS AND DISCUSSION.....	93
4.5.1	<i>Comparison with manometric data and other studies</i>	93
4.5.2	<i>Comparison of completely-filled model with partially-filled model</i>	95
4.5.3	<i>Influence of a Gaseous Phase Present</i>	102
4.5.4	<i>Comparison of the Velocity Profiles of all Three Models</i>	105
4.6	CONCLUSION.....	107

CHAPTER 5 MODELLING AND SIMULATION OF THE DRUG RELEASE

FROM A SOLID DOSAGE FORM IN THE HUMAN ASCENDING COLON: THE INFLUENCE OF DIFFERENT MOTILITY PATTERNS AND FLUID VISCOSITIES.....109

5.1	ABSTRACT.....	110
5.2	INTRODUCTION	111
5.3	METHODOLOGY.....	115
5.3.1	<i>Modelling Approach</i>	115
5.3.2	<i>Colon-Model Geometry</i>	115
5.3.2.1	Membrane	117
5.3.2.2	Fluid.....	119
5.3.2.3	Fluid-Structure and Global Boundary Conditions	119
5.3.2.4	Tablet and Tablet Disintegration.....	123
5.3.3	<i>Model Motility Patterns</i>	128
5.3.4	<i>Method of Analysis</i>	134

5.3.5	<i>Software</i>	137
5.4	RESULTS AND DISCUSSION.....	137
5.4.1	<i>Comparison of Different Motility Patterns on the Drug Release/ Disintegration on the Tablet at Different Fluid Viscosities</i>	137
5.4.2	<i>Comparison of the API Distribution along the Colon</i>	144
5.4.3	<i>Influence of the Diffusion Coefficient on the Drug Release from Tablet</i>	149
5.4.4	<i>Strength and Limitations of the Model</i>	152
5.5	CONCLUSIONS	153
5.6	SUPPLEMENTARY MATERIALS.....	155
5.7	APPENDIX A: DIMENSIONAL ANALYSIS OF THE SYSTEM	155
CHAPTER 6 SIMULATING THE HYDRODYNAMIC CONDITIONS OF THE HUMAN ASCENDING COLON: A DIGITAL TWIN OF THE DYNAMIC COLON MODEL.....		
158		
6.1	ABSTRACT.....	159
6.2	INTRODUCTION	159
6.3	METHODOLOGY.....	165
6.3.1	<i>Experimental work</i>	165
6.3.1.1	MRI Protocol.....	165
6.3.2	<i>Modelling Approach</i>	167
6.3.2.1	DCMDT Geometric Design	169
6.3.2.2	DCMDT and Computational Simulation Parameters	171
6.3.3	<i>Software</i>	178
6.3.4	<i>Methods of Analysis</i>	179
6.3.4.1	MRI Data Analysis.....	179
6.3.4.2	DCMDT Data Analysis	181

6.3.4.3	<i>In Vitro</i> and <i>In Silico</i> Comparison Data Analysis.....	183
6.4	RESULTS AND DISCUSSION.....	184
6.4.1	<i>Wall Motion</i>	184
6.4.2	<i>Velocity Profile of the Contents</i>	184
6.4.2.1	Shear rates.....	192
6.5	CONCLUSION.....	197
6.6	ACKNOWLEDGEMENTS	199

CHAPTER 7 DEVELOPMENT OF A DIGITAL TWIN OF A TABLET THAT MIMICS A REAL SOLID DOSAGE FORM: DIFFERENCES IN THE DISSOLUTION PROFILE IN CONVENTIONAL MINI-USP II AND A

BIORELEVANT COLON MODEL200

7.1	ABSTRACT.....	201
7.1.1	<i>Graphical abstract</i>	202
7.2	INTRODUCTION	202
7.3	METHODOLOGY.....	204
7.3.1	<i>Modelling approach</i>	204
7.3.2	<i>Mini-USP II</i>	205
7.3.2.1	Geometry container and impeller	205
7.3.2.2	Dimensionless analysis	207
7.3.3	<i>Colon model</i>	209
7.3.3.1	Geometry, Membrane, Fluid, and Colonic motility	209
7.3.4	<i>Fluid</i>	212
7.3.4.1	Fluid structure interactions	213
7.3.5	<i>Tablet</i>	217
7.3.5.1	Tablet disintegration	218

7.3.5.2	Development of the tablet and data analysis	221
7.3.6	<i>Software</i>	224
7.4	RESULTS AND DISCUSSION	224
7.4.1	<i>Model validation – hydrodynamics</i>	224
7.4.2	<i>Evaluation of the tablet disintegration/dissolution</i>	225
7.4.3	<i>Comparison of the drug release profile from the experimental tablet in the mini-USP II with the drug release profile of the modelled tablet in the colon model.....</i>	234
7.5	CONCLUSION	238
7.6	ACKNOWLEDGEMENTS	239
CHAPTER 8	CONCLUSIONS AND FUTURE WORK SUGGESTIONS	240
8.1	CONCLUSIONS	241
8.2	FUTURE WORK SUGGESTIONS	244
BIBLIOGRAPHY	246

LIST OF FIGURES

Figure 1.1 Schematic representation of the project ‘road map’. The shown <i>in vitro</i> model is called Dynamic Colon Model (DCM), a biorelevant model representing the human ascending colon. The image of the DCM (<i>in vitro</i> model) is adopted from (O’Farrell et al., 2021)	6
Figure 2.1 The human gastrointestinal tract (GI) (Vertzoni et al., 2019).....	13
Figure 2.2 Anatomy of the human colon. Adopted from (Moby’s Medical Dictionary, 9 th Edition, 2013).....	15
Figure 2.3. (a) Structure of the human colon (Johns Creek (GA): Ebix, c1997-2021) and (b) Detailed structure of the colon wall. Adapted from (https://www.britannica.com/science/human-digestive-system/Secretions , accessed 04/12/2021).....	16
Figure 2.4 Anatomy of the colon: Properties of the faeces along the colon. The intestinal contents are more fluid when they enter the colon (bottom left: ileocecal valve) and solidify along the colon to the rectum (bottom right) (modified from Taber’s Cyclopedic Medical Dictionary, 23 th Edition, 2017).....	18
Figure 2.5 Example of a section of colonic manometry recorded with different sensor spacings: 10 cm (top), 5 cm (middle), and 1 cm (bottom). Antegrade propagating sequences (PSs) are visualised by red arrows and retrograde PSs by blue arrows. (adapted from (Dinning et al., 2013b))	26
Figure 2.6 Schematic representation of a tablet’s immediate drug release profile (modified from (Alderborn and Frenning, 2018)).....	32
Figure 2.7 Schematic representation of a tablet’s extended drug release profile (modified from (Alderborn and Frenning, 2018)).....	33

Figure 2.8 Schematic representation of a tablet's delayed drug release profile (modified from (Alderborn and Frenning, 2018)).	34
Figure 2.9 Schematic representation of the difference between a multi-layered and a press-coated tablet (modified from (Awad et al., 2021)).	35
Figure 2.10 Schematic representation of the dissolution-controlled drug release systems where (a) is the matrix system and (b) the reservoir system (modified from (Awad et al., 2021)).	36
Figure 2.11 Schematic representation of the diffusion-controlled drug release systems where (a) is the reservoir system and (b) the matrix system (or monolithic system) (modified from (Awad et al., 2021)).	37
Figure 2.12 Schematic representation of the osmotically-controlled drug release systems where (a) is the elementary osmotic pump and (b) the osmotic push-pull system (modified from (Awad et al., 2021)).	40
Figure 2.13 Schematic representation of the ion exchange-controlled drug release systems (modified from (Awad et al., 2021)).	41
Figure 2.14 Schematic representation of the mini-USP II used in this thesis with dimensions according to (Stamatopoulos et al., 2015)	46
Figure 2.15. Schematic representation of the GI tract as it is compartmentalised in the PBPK model (modified from (Stamatopoulos, 2022))	47
Figure 3. 1 Schematic representation of the difference between the Eulerian and the Lagrangian mesh or grid-based method.	58
Figure 3.2 Schematic representation of the difference between a mesh or grid-based and meshless simulation methods (modified from https://powersys-solutions.com/product/?software=ParticleWorks , accessed 03/11/2021).	59

Figure 3.3 Structure of a typical particle-based algorithm (modified from (Alexiadis, 2015a)).....61

Figure 3.4 Schematic representation of the kernel function W and the support domain of the smoothing kernel function for the particle of interest i64

Figure 3.5 Schematic representation of the support domain with its kernel radius (smoothing length) κh of the smoothing kernel function and the particle of interest i66

Figure 3.6 Schematic representation of the lattice spring model from its molecular origin (adapted from (Brely et al., 2015))72

Figure 3.7 Types of particle interactions in the DMP framework (adapted from (Alexiadis, 2015a))74

Figure 3.8 Modelling of the tablet using LSM: (a) linear and diagonal bonds with a harmonic potential, (b) bond breaks if the distance between two particles is larger than the threshold distance d_{max} (modified from (Alexiadis, 2015a))..... 80

Figure 4.1 (a) and (b): 3D sketch of the flexible membrane, showing the contraction and expansion of the wall. The particles representing the membrane are connected by a network of springs. The probe (catheter) for pressure measurements is represented as black, stationary particles. (c) 2D Illustration of the elastic membrane with tethered springs at equilibrium state as well as after the application of three different radial forces (see Table 4.2 for details).87

Figure 4.2 Comparison between manometric measurements from Ref. (Bassotti and Gaburri, 1988), and simulation data from our completely-filled model.94

Figure 4.3 Representation of a peristaltic wave. In the enlarged section, the formation of a vortex is shown in a vector representation, where the direction of the vectors indicates the flow direction respectively.....95

Figure 4.4 Representation of a peristaltic wave in the partially-filled model. The enlarged section shows the formation of a vortex in the DI region96

Figure 4.5 Comparison of a peristaltic wave with content coloured by the velocity magnitude and shear stress, where (a) and (c) show the completely-filled model and (b) and (d) the partially-filled model.97

Figure 4.6 Mixing profile of (a) completely-filled model and (b) partially-filled model with tracking particles (red coloured) at different time-steps.98

Figure 4.7 Visualisation of the time dependent trajectory of a tablet in the different models.100

Figure 4.8 Visualisation of shear stresses occurring in the fluid and the location of a naturally buoyant tablet (black) in the completely-filled model (a) and the partially-filled model (b).101

Figure 4.9 (a) and (b) Comparison of a peristaltic wave with content coloured by the velocity magnitude in the gas-liquid model. In (a) the velocities of the liquid phase and in (b) the gaseous phase are analysed. (c) Representation of the shear stresses in the liquid phase.103

Figure 4.10 Vector representation of the (a) gaseous phase and (b) liquid phase in the gas-liquid model, where the length of the vector indicates the velocity.....104

Figure 4.11 Mixing profile of gas-liquid model using tracking particles (red coloured) at different time-steps.105

Figure 4.12 Graphical representation of the axial velocity along the colon models at different time-steps, where (a) represents the completely-filled model and (b) the partially-filled model and (c) the gas-liquid model.....106

Figure 5.1 (a) Section of the flexible membrane, showing the colon's *haustra* and the intestinal fluid inside the colon. The membrane is built of particles which are

connected by a network of springs to achieve a flexible behaviour. (b) 3D sketch of the tablet. The particles representing the tablet are connected by linear and diagonal springs to obtain a solid behaviour.....116

Figure 5.2 (a) 2D representation of the membrane particle anchored by a spring in equilibrium position and after the application of a radial force. (b) Illustration the particles representing the colon’s membrane including its characteristic *haustra*, before and after applying an individual radial force to each ring (‘circular muscle’).....117

Figure 5.3 The model is represented in two different forms: ‘Particle representation’ and a more realistic ‘Continuum representation’. This is an example of the dissolution process of a tablet in the colonic environment at three different time steps. Colonic contractions lead to the motion of the fluid and accordingly to the movement of the tablet which dissolves in the intestinal fluid. In the particle representation the shear stress acting on the tablet, and the API concentration in the surrounding of the tablet, i.e., in the fluid is shown.....127

Figure 5.4 Illustration of the different motility pattern, where (a) is the Baseline, (b) the Stimulant PEG, (c) the Stimulant Maltose, (d) the Comparison pattern and (e) the CPPW motility pattern. Here, the *x*-axis represents the time and duration of the actions taking place and the *y*-axis the colon section (*haustrum*) addressed. The different actions are indicated by different hatches.....131

Figure 5.5 Representation of how the occlusion degree is defined.133

Figure 5.6 Representation of the initial position of the tablet, which is in all models identical.....133

Figure 5.7 Comparison of the drug release profile of the different models at medium fluid viscosity conditions as well as the comparison of the shear stress/shear rate acting on the tablet.138

Figure 5.8 Comparison of the drug release profile of the different models at high fluid viscosity conditions as well as the comparison of the shear stress/shear rate acting on the tablet.....140

Figure 5.9 Comparison of the drug release profile of the different models at high fluid viscosity conditions as well as the comparison of the shear stress/shear rate acting on the tablet.....142

Figure 5.10 Comparison of the different models in respect to the distribution of the API along the colon at four different times at low fluid viscosity conditions.....145

Figure 5.11 Comparison of the different models in respect to the distribution of the API along the colon at four different times at medium fluid viscosity conditions.....146

Figure 5.12 Comparison of the different models in respect to the distribution of the API along the colon at four different times at high fluid viscosity conditions.147

Figure 5.13 Comparison of the influence of different diffusion coefficients on the drug release profiles, where ‘high D’ represents the drug release profile of the high diffusion coefficient and ‘low D’ the drug release profile of the low diffusion coefficient simulation.150

Figure 5.14 System parameter for the Dimensional Analysis.....156

Figure 6.1 Schematic of the Dynamic Colon Model (DCM), Adapted from (O’Farrell et al., 2021). The DCM has a segmented appearance reflecting that of the human proximal colon: segment 1 is adjacent to the *caecum*, through to segment 10 adjacent to the *hepatic flexure*.161

Figure 6.2 Schematic view (top) and a cross-sectional view (bottom) of the computational model (DCMDT). The DCMDT comprises 10 sections reflecting the DCM. Segment 1 is adjacent to the *caecum* and segment 10 is adjacent to the *hepatic*

flexure. The *hepatic flexure* is modelled as a reduction to create a backpressure, guided by the *in vivo* situation.163

Figure 6.3 Particle representation of the model showing the colon *haustra*, the flexible membrane, and the fluid inside the colon.168

Figure 6.4 Cross section of the digital twin of the DCM and the ‘drain tank’. The antegrade direction in this image is from the right to the left.169

Figure 6.5 Shape of the segment during relaxing, where (a) is the computational model and (b) is a segment of the DCM.170

Figure 6.6 Rheological behaviour of LOVIS and HIVIS fluids in the DCM and the simulated counterparts *in silico*. Rheological measurements were made at 25 °C. ...174

Figure 6.7 Comparison of the fluid velocities and wall displacement profiles of the DCM and the DCMDT with 60% fluid volume and slower propagating PPW. Parts (a) and (b) compare the mean fluid velocities with LOVIS and HIVIS respectively.....186

Figure 6.8 Comparison of the maximum fluid velocities and wall displacement profiles of the DCM and the DCMDT at low fluid volume, low fluid viscosity, and slow propagating PPW conditions are compared.....187

Figure 6.9 Comparison of the fluid velocities and wall displacement profiles of the DCM and the computational model at high fluid volume and slow propagating PPW. In (a) the mean fluid velocities at low fluid viscosity and in (b) the mean fluid velocities at high fluid viscosity are compared.....188

Figure 6.10 Comparison of the fluid velocities and wall displacement profiles of the DCM and the DCMDT at low fluid volume and fast propagating PPW. In (a) the mean fluid velocities at low fluid viscosity and in (b) the mean fluid velocities at high fluid viscosity are compared.189

Figure 6.11 Comparison of the fluid velocities and wall displacement profiles of the DCM and the DCMDT at high fluid volume and fast propagating PPW. In (a) the mean fluid velocities at low fluid viscosity and in (b) the mean fluid velocities at high fluid viscosity are compared.191

Figure 6.12 Comparison of the fluid velocities at different fluid volumes and different fluid viscosities of segment 6. (a) represents data for the slower propagating PPW and (b) for the faster propagating PPW (b). In the table for the Total Sum of Squares, the following abbreviations are used: LV-low viscosity, HV-high viscosity.192

Figure 6.13 Average shear rates versus maximum shear rates for each parameter combination, where (A) represents DCM 'segment 2', (B) DCM 'segment 6', (C) DCMDT 'segment 2', and (D) DCMDT 'segment 6'. USP II shear rate data was reproduced from (Hopgood et al., 2018). Here they use the CFD package Fluent version 17.2.0 (Fluent Incorporated, Canterra Resource Park, NH).193

Figure 6.14 Main effects of wave speed, media viscosity and volume on mean shear rate at the bottom wall during local wall contraction at segment 6 in the DCM and the COM. N = 4 mean data points at each level (low and high). The shaded areas represent the confidence interval.....195

Figure 7.1 Graphical abstract202

Figure 7.2 Schematic representation of the mini-USP II with the dimensions used in (Stamatopoulos et al., 2015) (a) and the computational model (b) including the variables for the dimensional analysis (Chapter 7.3.2.2).206

Figure 7.3 Representation of the colon model showing the construction of the membrane, the constrictions of the membrane building the haustrum, and the SPH particles representing the fluid inside the colon.210

Figure 7.4 3D-representation of the tablet. Linear and diagonal springs connect the particles representing the tablet to obtain a solid structure.218

Figure 7.5 Validation of the computational mini-USP II model by comparison of the velocity profile from the simulation with experimental and simulated data from Wang et al. (Wang and Armenante, 2016). a) shows the dimensions of the mini-USP II used in both, the experimental and computational part, b) Experimental and computational data reproduced with permission from Wang et al., and c) the velocity profile obtained from the simulation.225

Figure 7.6 Mass flow rate ϕ of the API from the tablet obtained from the simulations in the mini-USP II for different X and for different diffusion coefficients D226

Figure 7.7 a) Representation of the results obtained from the simulations and a characteristic data point from the experimental tablet. b) Enlarged section from a) of the region of the experimental tablet.227

Figure 7.8 Comparison of the tablet disintegration/ dissolution process of a real tablet (top) and the computational tablet (middle and bottom) at different phases of the tablet disintegration/ dissolution process. The particles of the modelled tablet (middle) are coloured according to their API concentration, where red indicates 100% API and dark blue 0% API. At the bottom the particles of the modelled tablet are coloured according to the shear rate exposed, where purple indicates low, and yellow a high shear rate.229

Figure 7.9 Drug release and tablet disintegration of the modelled tablet in the mini-USP II with $X = 0.35$ and $D = 8.0 \times 10^{-6} \text{ m}^2 \text{ s}^{-1}$. The blue line represents the drug release and the orange line the number of tablet particles not yet dissolved in the fluid.230

Figure 7.10 Drug release and tablet disintegration of the modelled tablet in the mini-USP II with $X = 0.35$ and $D = 8.0 \times 10^{-6} \text{ m}^2 \text{ s}^{-1}$. The blue line represents the drug release and the orange line the average shear stress acting on the tablet particles.	232
Figure 7.11 Drug release and tablet disintegration of the modelled tablet in the mini-USP II with $X = 0.35$ and $D = 8.0 \times 10^{-6} \text{ m}^2 \text{ s}^{-1}$ and the experimental data for a simple buffer reproduced from Stamatopoulos et al. (Stamatopoulos et al., 2015).....	233
Figure 7.12 Drug release of the modelled tablet with $X = 0.35$ and $D = 8.0 \times 10^{-6} \text{ m}^2 \text{ s}^{-1}$ in the colon model using two different in vivo motility pattern from (Schütt et al., 2021).....	234
Figure 7.13 Shear rate acting on the modelled tablet during the drug release process represented in Figure 7.12 (colon model).....	235
Figure 7.14 Drug release profile in the mini-USP II at different paddle speeds.	236
Figure 7.15 Shear rate acting on the modelled tablet during the drug release process in the mini-USP II shown in Figure 7.14.....	237

LIST OF TABLES

Table 2.1. US pharmacopoeia dissolution apparatuses with the main stirred vessel method in bold ((Awad et al., 2021), images modified from http://www.pharmacy180.com/article/considerations-in-in-vivo-bioavailability-study-design-2532/ , accessed 09/01/2022).....	44
Table 4.1. Fundamental model parameters used in all simulations: for more details of the physical and mathematical meaning of the simulation parameters h , c_0 , k_b and k_v , the reader is referred to Ref (Kot et al., 2015, Liu and Liu, 2003, Lloyd et al., 2007, Pazdniakou and Adler, 2012).....	88
Table 4.2. Specific model parameter for the different models.	89
Table 5.1. Model parameter of the Membrane.	118
Table 5.2. Model parameter of the Fluid.	122
Table 5.3. Fundamental model parameter.	125
Table 5.4. Model parameter of the Tablet.....	126
Table 5.5. Model parameter motility patterns.	132
Table 5.6. Disintegration degree or disintegration time of the solid dosage form (tablet) for all models/motility patterns at different fluid viscosities: % = degree of tablet disintegration φ at $t = 60$ min in %; min = time in minutes until complete tablet disintegration.	144
Table 5.7. Variables for the Dimensional Analysis.	157
Table 5.8. Dimensionless variables for the Dimensional Analysis.....	157
Table 6.1. MRI scanner parameters.	166
Table 6.2. Model parameters of the membrane.....	172
Table 6.3. Fluid rheological model parameter.....	173

Table 6.4. Model parameter of the fluid.	177
Table 6.5. Fundamental model parameter.	178
Table 7.1. mini-USP II parameters.....	207
Table 7.2. Variables for the dimensional analysis.....	208
Table 7.3. Dimensionless variables for the dimensional analysis.....	209
Table 7.4. Colon membrane parameters.....	212
Table 7.5. Fluid parameters	213
Table 7.6. Fundamental model parameters.....	217
Table 7.7. Tablet parameters	221
Table 7.8. Values for the constant ϵ	226

Chapter 1

General Introduction

1.1 Overview

Many people worldwide are affected by colonic diseases. One of the most common diseases of the colon is inflammatory bowel disease (IBD), which also includes Crohn's disease (CD) and ulcerative colitis (UC). The number of people suffering from IBD has risen continuously in recent years: From 3.75 million in 1990 to 6.8 million in 2017 (Alatab et al., 2020). European data show that in Europe alone, 2.5 – 3 million people are affected by IBD, which is estimated to cost the healthcare system about 4.6 - 5.6 billion Euro/year (i.e., approx. £3.8 – £4.2 /year) (Burisch et al., 2013). In the United Kingdom alone, approximately 620,000 people are affected (Molodecky et al., 2012).

UC is a chronic IBD that causes ulceration of the colonic mucosa and affects most commonly the rectum and sigmoid colon. CD is similar to UC, but it occurs anywhere along the gastrointestinal tract (GI), i.e., all regions from the mouth to the anus can be affected. Most commonly, CD affects the small intestine (i.e., terminal ileum) and the proximal colon (i.e., ascending and transverse colon). Phases of remission and exacerbation characterise both diseases. The typical symptoms of UC and CD are cramping pain, abdominal tenderness, tiredness, feeling unwell or feverish, bleeding, frequent diarrhoea, dehydration and weight loss (McCance and Huether, 2019). IBD is not limited to the inflammation of the mucosa and muscular components of the GI tract, and it may also involve the enteric nervous system (ENS) (Bassotti et al., 2014). The increasing number of people affected and suffering from IBD (Kaplan, 2015) has led to a significant amount of research being carried out on the effective delivery of drugs to the locally inflamed regions of the colon (Goffredo et al., 2016, Teruel et al., 2020). Colon-targeted drug delivery offers opportunities for an improved systematic treatment of local diseases while simultaneously minimising side effects (e.g., a

smaller dose is required) (Amidon et al., 2015). In addition to the improved treatment of colon-specific diseases, the targeted delivery of drugs into the colon received much more interest, especially for peptide and protein-containing drugs. This is because the enzymatic activity that could render these drugs is lower in the colonic environment than in the small intestine (Patel and Mirsa, 2011, Watts and Illum, 1997).

The most common route for the administration of drugs and medicines, due to its convenience, is the oral route. This also includes drugs that target the colon. The proximal colon is the targeted site for colonic drug delivery. The environmental conditions in this region are more suitable for a controlled and predictable drug disintegration/dissolution process compared to other regions of the colon. Crucial factors for a controlled and more predictable drug release include water availability for drug dissolution, viscosity of the intestinal content and less variable transit times (Christensen, 1994, Kumar et al., 2012, Murray et al., 2017, Watts and Illum, 1997). Therefore, it is essential to analyse the hydrodynamics in the proximal colon and understand their impact on the performance of a solid drug formulation.

Before reaching the colon, orally administered solid dosage forms (tablets) must pass through the complex upper GI tract. For this purpose and to improve the local and systematic drug delivery, several modified-release (MR) drug delivery systems targeting the colon have been developed in recent years. MR formulations are usually manufactured to be coated with a protective layer that dissolves on its course (e.g., pH-dependent) to the colon (Long and Chen, 2009). Consequently, the actual active pharmaceutical ingredient (API) release occurs in the highly dynamic colonic environment. To evaluate the performance of a drug formulation, pharmacopoeia disintegration and dissolution tests are usually performed. These tests are used to mimic the complex *in vivo* dissolution/disintegration process of the drug *in vitro*

(Tenjarla, 2015). *In vivo* studies (i.e., on humans and animals) are usually required to develop, optimise, and evaluate formulations. These predictive dissolution methods can contribute to reducing the number of costly *in vivo* studies.

The dissolution tests in pharmaceutical development are commonly performed using the United States Pharmacopeia Apparatus 2 (USP II) to replicate the *in vivo* environment (Zuleger et al., 2002). However, this conventional oversimplified dissolution method does not mimic the hydrodynamics, and the *in vivo* wall-motion-induced shear stresses that act on the solid dosage form and decisively influence the disintegration/dissolution process. Consequently, results obtained using, e.g., the USP II, do not provide reliable data on a solid dosage form's disintegration and dissolution behaviour in the colonic environment.

In recent years, much research has been done to develop a more realistic and thus biorelevant *in vitro* model that provides an environment with significant potential for optimising colon targeted dosage forms (Minekus, 2015, Stamatopoulos et al., 2016b, Venema, 2015). Some of these *in vitro* models have been developed to the point where they are physiologically realistic and can replicate the motility patterns occurring in the colon to a certain extent (O'Farrell et al., 2021, Stamatopoulos et al., 2020). However, the technical possibilities to perform a complete analysis of the entire system are limited.

Computer simulation and mathematical modelling have become valuable tools, especially in biological and medical applications. *In silico* models can be used in a supportive way to extend traditional *in vivo* and *in vitro* models to understand biomechanical and physiological phenomena better. In many cases, *in vivo* models and experiments are time-consuming and can be very expensive (Hur et al., 2011). Thus, a significant advantage of *in silico* models is that, in some cases, they can replace *in vivo*

experiments or even *in vitro* models. Already 22 years ago, Kohl et al. claimed that *in silico* models may be one of the key tools for biomedical research and development in the future (Kohl et al., 2000). Considering the numerous publications in this field, this case has obviously occurred (see e.g., Chapter 2.1.6).

To date, there is limited to no data in the literature that gives detailed insights into the hydrodynamics and mixing profiles occurring in the colonic environment evoked by the motility patterns (i.e., wall motion) (Dinning et al., 2008, Stamatopoulos et al., 2020). Currently, it is only possible to visualise the release from an MR formulation *in vivo* using Magnetic Resonance Imaging (MRI) or scintigraphy. However, both techniques are costly, time-consuming, and thus not practical for product development and optimisation (Stamatopoulos et al., 2020). Therefore, an *in silico* model replicating both the *in vivo* colonic environments and a pharmaceutical formulation's disintegration/dissolution process would benefit drug development. Consequently, new data showing the distribution of the released drug in the colon could provide the opportunity for more systematic and effective treatment of colonic diseases.

In vivo experiments and the generation of *in vivo* data are the basis for developing *in vitro* and *in silico* models. They are therefore inevitable, even though, as mentioned before, they are cost, time, and labour intensive. Besides the large number of recourses needed in *in vivo* experiments, they also have the major disadvantage that individual parameters can only be influenced to a certain extent, or it is even impossible to adjust the parameter to obtain specific data. The access to data that cannot be captured in *in vivo* experiments biorelevant *in vitro* models offer the possibility of more profound insight into the *in vivo* conditions and, therefore, to better understand the 'colonic laws'. For the development and validation of *in vitro* models, *in vivo* data are required

In silico models are also very flexible in terms of adaptability and provide additional data or data at a higher resolution, as is currently the case with *in vitro* models. However, a computational model highly depends on knowledge gained *in vitro* to inform the computational counterpart. Therefore, the quality and quantity of the data describing the interrelationships in the colonic environment will always depend on the interaction between *in vitro* and *in silico* models. In combination, these models provide crucial data for pharmaceutical research and industry.

There are several modelling techniques for developing *in silico* models. In this thesis, when newly developed *in silico* models are mentioned, these models are created by using the so-called Discrete Multiphysics (DMP) simulation technique.

1.2 Aim and Objectives of the Thesis

This thesis aims to build a 3D computational model using Discrete Multiphysics (i) to gain a detailed insight into the hydrodynamics of the human proximal colon evoked by the movement of the colon wall (i.e., membrane), (ii) how this affects the mixing process of a dissolved drug and (iii) in particular how the dissolution/ disintegration process of a solid dosage form is affected by different motility patterns found in the colonic environment and to what extent are these motility patterns able to distribute the active pharmaceutical ingredient along the colon under different fluid viscosities. To achieve these goals, this thesis pursues the following objectives:

- To develop a biorelevant *in silico* model of the human proximal colon using Discrete Multiphysics that reproduces the key features of the organ (i.e., anatomy and motility patterns).
- To study fluid dynamics and mixing profiles in the colon under different predetermined conditions such as filling levels (i.e., fluid volume), motility pattern and the influence of multi-phase conditions (i.e., liquid and gaseous phase).
- To implement a solid dosage form (tablet) into the model and study the disintegration/dissolution process under different *in vivo* motility patterns.
- To study the performance of different *in vivo* motility patterns in terms of the distribution of a released drug from the tablet along the colon at different fluid viscosities to provide data for a spatiotemporal concentration profile.
- To validate the computational model with *in vitro* data from the Dynamic Colon Model by modelling a digital counterpart (i.e., digital twin).
- To investigate the advantage of the computational model in terms of bio-relevance compared to conventional dissolution apparatuses.

1.3 Thesis Breakdown

This thesis is structured into one literature review chapter, one methodology chapter and four paper-format chapters:

Chapter 2 introduces the physiology of the colon and explains how to access characteristic data (e.g., transit time and motility) in the colonic environment. The

various tablet dissolution systems that are important for colonic drug delivery are discussed, and the commonly used US Pharmacopoeia dissolution apparatuses are introduced. This chapter also includes a summary of other *in silico* models of the US Pharmacopoeia apparatuses I & II, small intestine, and colon that have been developed to date.

Chapter 3 introduces the methodology used in this work, called Discrete Multiphysics. Discrete Multiphysics is based on the coupling of different particle-based simulation techniques. In this study, Smoothed Particle Hydrodynamics and Lattice Spring Model are combined. This chapter also represents the treatment of specific phenomena such as mass transfer.

Chapter 4 presents a 3D model of the proximal colon to investigate the fluid flow, mixing profiles, shear stresses, and the behaviour of an undissolved solid dosage form under different conditions. Therefore, three different models are developed: a colon model completely filled with fluid, partially filled and partially filled with gas and fluid.

Chapter 5 develops a Discrete Multiphysics model of a disintegrating/dissolving solid dosage form in the intestinal environment under different, biorelevant motility patterns and fluid viscosities. This chapter focuses on the influence of varying motility patterns and fluid viscosities on the tablet's drug release profile, as this is one of the crucial measurements in drug development and optimisation. As hydrodynamic parameters such as shear rate are decisive in the drug release process of a solid dosage form, the shear rates acting on the surface of the solid dosage form are analysed.

Chapter 6 represents the development of a computational counterpart (i.e., digital twin) of the Dynamic Colon Model (DCM), a biorelevant and validated *in vitro* model of the proximal colon. The digital twin mimics the design and motility of the DCM. Both models were used to investigate the effects of wave propagation velocity, media viscosity, and media volume on the flow and, consequently, the shear rates inside the lumen. The analyses were also used to assess the ability of the digital twin to reproduce the DCM results and, accordingly, to validate the computational model at the same time.

The work presented in this chapter has been compared and verified with novel experimental data published in the same article, rather than taking data from other references. Therefore, the generation of the experimental data is not part of this thesis and is only presented in this chapter as it is part of the published manuscript.

Chapter 7 represents the development of a computational model of the mini-USP II dissolution apparatus and a method to create a computational tablet (i.e., digital twin) that behaves like a real solid dosage form. The hydrodynamic conditions inside the mini-USP II model are validated with experimental and computational data, the behaviour of the computational tablet with experimental data. This chapter compares the dissolution profile in a conventional mini-USP II dissolution apparatus and a biorelevant colon model.

Chapter 8 provides a summary of the findings and identifies possible perspectives for future research.

Chapters 4, 5, 6 and 7 are presented according to the *alternative format thesis guidelines* of the University of Birmingham regulation scheme. Therefore, certain sentences and descriptions of the models and theory may be unclearly formulated or repetitive. Although the published articles are a result of collaborative work, it is important to clarify that Michael Schütt was responsible for the conceptualisation, developing of the models and performing all simulations, data analyses, interpreting the data, writing, and editing the manuscripts in full. Alessio Alexiadis helped with the conceptualisation, interpreting the data, revising the manuscript, and assisting with the modelling part. Konstantinos Stamatopoulos helped conceptualise, interpret the data, and revise the manuscripts. Hannah K. Batchelor and Mark J. H. Simmons helped with interpreting the data and revising the manuscripts (Chapters 4, 5, 6, 7). Connor O'Farrell was responsible for the experiments, the data analyses and interpretation of the experimental data, writing and editing the manuscript. Caroline L. Hoad, Luca Marciani and Sarah Sulaiman helped with revising the manuscript (Chapter 6).

The author of this thesis would also like to acknowledge Dr. Alessio Alexiadis, Dr. Konstantinos Stamatopoulos, Prof. Dr. Mark Simmons, Prof. Dr. Hannah Batchelor, Mr. Connor O'Farrell, Dr. Caroline L. Hoad, Prof. Dr. Luca Marciani, and Ms. Sarah Sulaiman for their contributions to the submitted/published articles.

Chapter 2

The Colonic Environment: Function, Structure, Data Assessment, Drug Delivery and Models to Date

2.1 Physiology of the Human Colon

The gastrointestinal (GI) tract characterises all digestive system organs from the mouth to the anus, which are more precisely the oesophagus, stomach, small intestine, and colon (Figure 2.1). There are different physiological terms to describe the same organ in the literature: colon, large intestine, and large bowel. Hence, the terms used in the text are interchangeable.

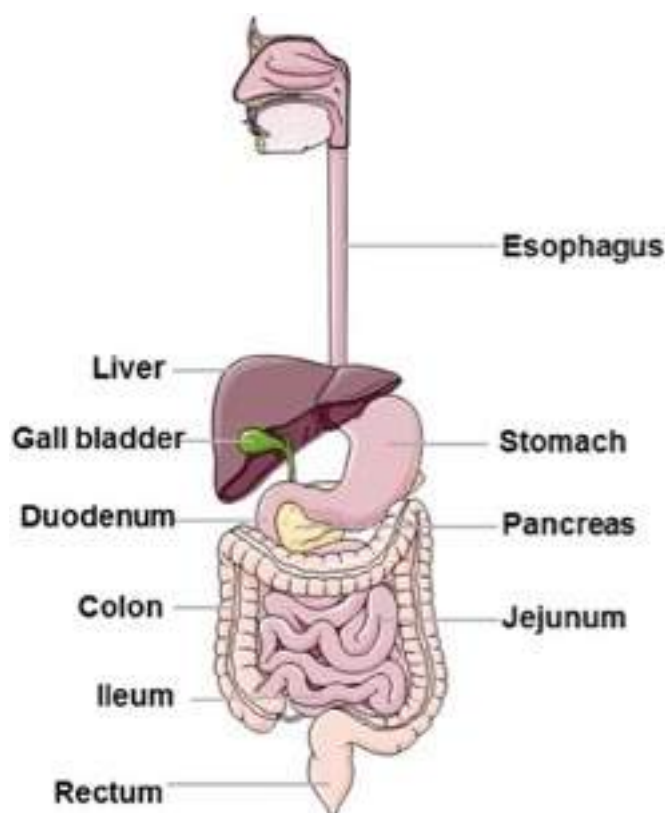


Figure 2.1 The human gastrointestinal tract (GI) (Vertzoni et al., 2019)

In the GI tract, food and drinks are converted into a more absorbable form. The food that has not yet been digested when it reaches the lower end of the small intestine is exposed to bacteria in the colon for fermentation. The undigested food (chyme) flow from the small intestine to the *caecum* of the colon is regulated by the *ileocecal valve*.

Residues that were not fermented or dead bacterial cells are excreted in the faeces. Low-molecular-weight carboxylic acids and gases such as carbon dioxide are the end products of bacterial fermentation (Cummings et al., 1987, Wilson, 2010). While the primary function of the GI tract is the processing of food and drinks into a more absorbable form (Söderlind and Dressman, 2010), the specific functions of the colon are as follows: absorption of electrolytes and water, fermenting of unused energy substrates, training the immune system, production and absorption of vitamins and hormones, transport of the faeces to the rectum, and storage of faeces until for elimination (Ramakrishna, 2013, Bharucha and Camilleri, 2019, Siri et al., 2020). The colon has a shape of an imperfect cylinder with a total length of about 1.5 m and a diameter of up to 6 – 8 cm and is mainly fixed in position (Christensen, 1994, Siri et al., 2020). These values are only averages, as there are also gender- and age-dependent differences in the diameter and length of the colon (Sadahiro et al., 1992).

Furthermore, the diameter of the colon also actively changes depending on the diet (Sulaiman and Marciani, 2019). Anatomically, the colon is divided into four major parts (Figure 2.2) which are namely the ascending colon (20 – 25 cm), the transverse colon (40 – 45 cm), the descending colon (10 – 15 cm) and the sigmoid colon (35 – 40 cm) (Christensen, 1994, Prasanth et al., 2012). The ascending colon reach from the ileocecal valve to the *hepatic flexure*, the transverse colon from the *hepatic flexure* to the *splenic flexure* and the descending colon from the *splenic flexure* to the sigmoid colon. The *caecum*, ascending colon, and transverse colon are also called proximal colon (Figure 2.2).

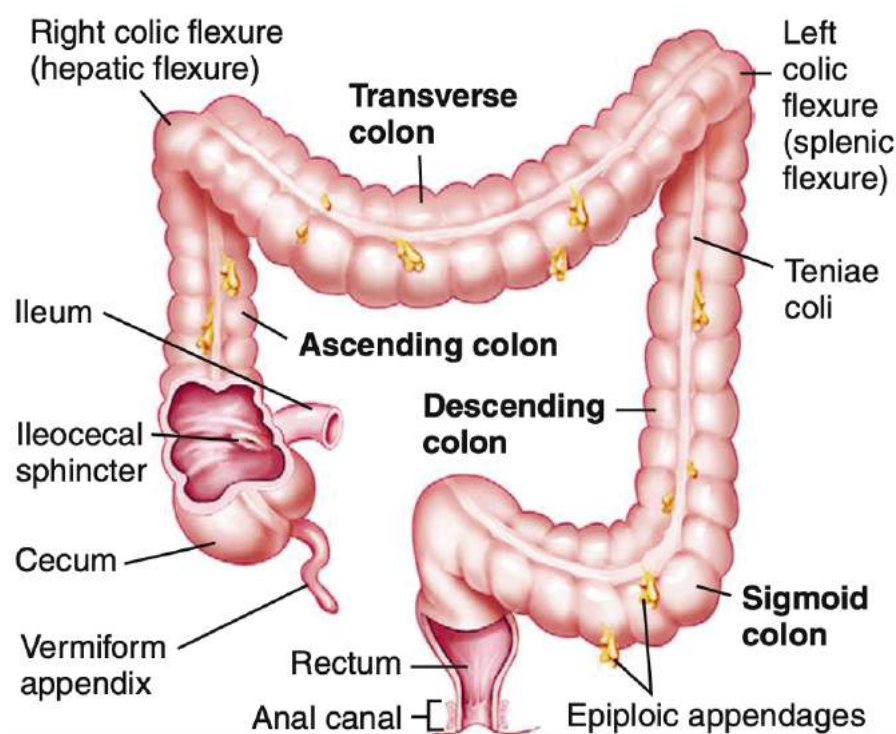


Figure 2.2 Anatomy of the human colon. Adopted from (Moby's Medical Dictionary, 9th Edition, 2013)

As shown in Figure 2.2, three separate longitudinal bands of smooth muscle are outside on the ascending, transverse, descending and sigmoid colon, but not on the appendix and rectum. These about 1.5 cm wide bands are called teniae coli (also taeniae coli) and represent the longitudinal layer of the muscle wall of the colon. Because the teniae coli is shorter than the colon to which it is attached, the typical sac-like called *haustra* are formed (Ellis and Mahadevan, 2014). The colon comprises four main layers: mucosa, submucosa, the longitudinal and circumferential muscle layers (muscularis propria), and the serosa. A representation of the different layers is depicted in Figure 2.3 (a), where Figure 2.3 (b) shows an even more detailed inside into the structure of the colon membrane.

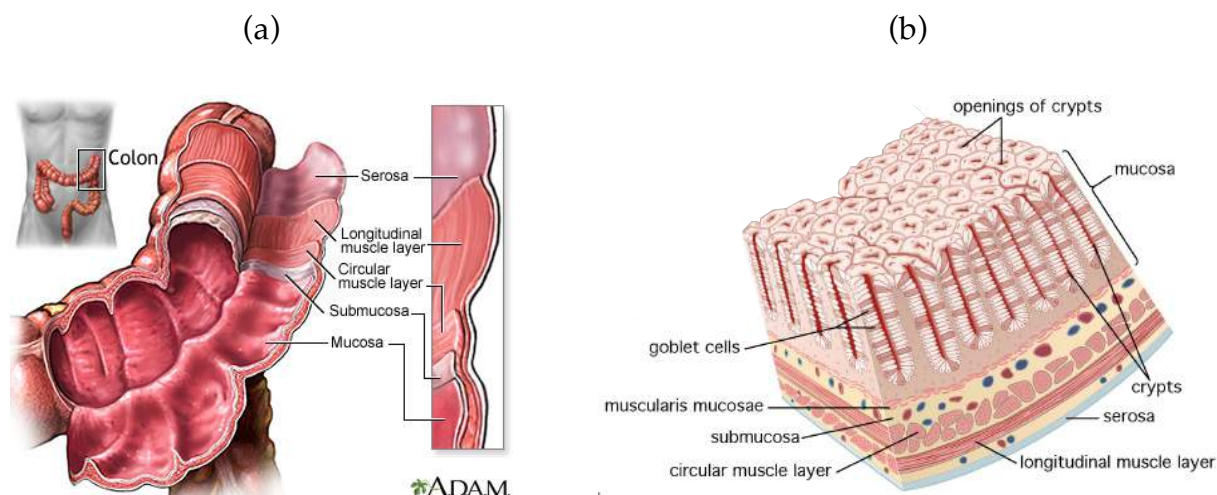


Figure 2.3. (a) Structure of the human colon (Johns Creek (GA): Ebix, c1997-2021) and (b) Detailed structure of the colon wall. Adapted from (<https://www.britannica.com/science/human-digestive-system/Secretions>, accessed 04/12/2021)

The mucosa or mucous membrane is the inner moist lining or tissue that covers most of the organs and the cavities of the human body, such as the mouth, nose, lungs, and intestines. The mucosa consists of goblet cells, which are special epithelial cells that produce mucus and secrete it directly onto the surface of the glandular tissue (Edsman and Hägerström, 2005). The epithelium in the colon is built into large cylindrical structures called crypts, where the secretory and absorptive processes (mostly water) occur (Siri et al., 2020). The mucus is a water-insoluble gel that forms a protective layer over the surface and acts as a protective barrier. This semipermeable barrier selectively filters the passage of pathogens, nutrients, gases, and pollutants and is also an obstruction for drug products (Pacheco et al., 2019, Taherali et al., 2018). In the region of the GI tract, the mucus's main function is to lubricate the surface and minimise the frictional forces between the content (i.e., food) and the surface to protect the surfaces from mechanical damages during the peristaltic transport. It also protects the

epithelial cells from fluids and substances (e.g., gastric acid and bacterial toxins) that are harmful to them (Strugala et al., 2003).

Further, the mucus comprises enterocytes, responsible for absorption processes and enteroendocrine cells, which produce hormones (Snoeck et al., 2005). The so-called submucosa is a fibrous connective tissue between the mucosa and the circular muscle layer, supporting the mucosa (Edsman and Hägerström, 2005). The submucosa contains important blood and lymph vessel branches to supply the colon (Siri et al., 2020). From the submucosa to the outside, the colon wall has two outer muscle layers: The circular smooth muscle cells are the muscle cells in the colon that narrow the lumen to varying degrees and can also occlude the lumen completely. Therefore, these muscle cells effectively mix, turn over, and propel as they propagate along the colon. Longitudinal muscle contraction leads to a shortening of the length of the colon and thus minimal mixing and propulsion functions (Sarna, 2010). The temporal sequence of different occlusion degrees and propagating directions (i.e., antegrade – in direction to the anus or retrograde – in direction to the *caecum*) result in different motility patterns in the colon. Details of motility patterns are discussed in Chapter 2.1.1. The outer layer of the colon is called serosa. It consists of a single layer of squamous epithelia cells that form the mesothelium (i.e., the membrane) (Siri et al., 2020).

Undigested food (chyme) passes from the small intestine through the ileocecal valve into the *caecum*/ascending colon. At this stage, the faeces are still very liquid. It gradually solidifies as it travels through the colon due to a progressive absorption of water and electrolytes. Once the faeces reach the end of the colon (i.e., the rectum), the faeces are stored in the colon until excretion. The material is fluid or semi-solid in the *caecum* and ascending colon; solidification starts in the transverse colon, and solid faeces have formed in the descending colon (Figure 2.4).

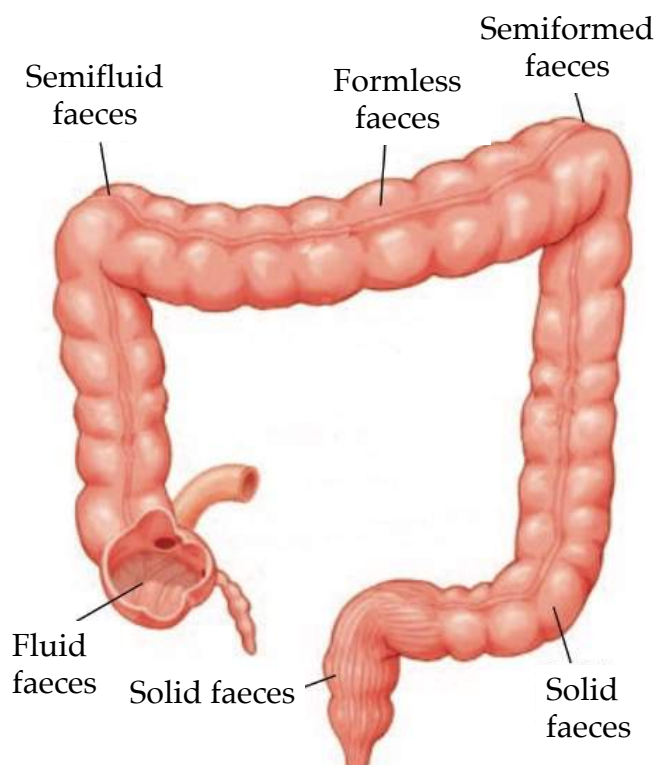


Figure 2.4 Anatomy of the colon: Properties of the faeces along the colon. The intestinal contents are more fluid when they enter the colon (bottom left: ileocecal valve) and solidify along the colon to the rectum (bottom right) (modified from Taber's Cyclopedic Medical Dictionary, 23th Edition, 2017)

The absorptive capacity of the colon is as high as 1800 mL a day (Watts and Illum, 1997), with an absorbing surface area of about 0.05 m² (Sulaiman and Marciani, 2019). In challenging situations and as long as the continuous infusion rate of the fluids entering the *caecum* is as low as approx. 1 to 2 mL/minute, the colon can absorb up to 5.000 to 6.000 mL a day (Hammer and Phillips, 1993). The amount of dry material in the human colon is estimated to be just 35 g, corresponding to about 220 g of wet material (Watts and Illum, 1997).

Although much research concerning the GI tract has already been carried out, the colon is the least researched region regarding drug absorption phenomena (Prasanth et al., 2012). However, colon targeting has obtained much more attention due to a low

enzymic and proteolytic activity in the colon. Colon-targeted formulations aim not only to treat local diseases but also to offer an alternative way to deliver active substances. The colon provides an environment that allows, e.g. the intact absorption of peptide and protein drugs (Sulaiman and Marciani, 2019). The permeability of peptide and protein drugs across the colon is relatively weak. With the combination of a high local residence time and absorption enhancers, which in studies showed a more successful performance in the colon than in the upper GI tract (Yang et al., 2002), the colon has become a favourable site for drug absorption. Accordingly, colon targeting drug delivery systems have been investigated (Friend, 1991, Friend, 2005, Kumar et al., 2012, Patel and Mirsa, 2011, Prasanth et al., 2012), and new therapeutic agents for the treatment of colonic diseases have been developed (Watts and Illum, 1997).

One crucial parameter for drug dissolution and drug absorption is the availability of free water in the colon. The proximal colon is the most exciting part of dosage form design due to the higher volume of fluids available. The total amount of free liquid available for drug dissolution is between 0 to 49 mL in the entire colon, with most of the free liquid found in the ascending colon (Murray et al., 2017, Schiller et al., 2005). Another study used a scintigraphic method to determine the average total fluid volume in the ascending colon. It was estimated as 162 mL with single values ranging from 82 to 303 mL (Badley et al., 1993). This total fluid volume corresponds to a fill level of about 40% in the ascending colon. Besides the free liquid, the proximal colon also has a less variable residence time than the other parts of the colon (Söderlind and Dressman, 2010, Van den Mooter, 2006), which is also a crucial parameter in formulation development. The transit time through the transverse and descending colon varies from a few minutes to many hours (Söderlind and Dressman, 2010). Food

intake and stimulation of the gastrocolic reflex can result in a transit time of the bolus from the transverse colon in the direction of the rectum of a few minutes, whereby a bowel movement frequency of just three to four times a week is still regular (Söderlind and Dressman, 2010). The colonic transit time is influenced, for example, by diet, stress, mobility, drugs, disease, and gender and tends, therefore, to be very variable (Van den Mooter, 2006, Stamatopoulos et al., 2021). Commonly used techniques to access the colonic transit are described in Chapter 2.1.1.

One study determined the colonic transit time using the radiopaque marker technique. Here, the average colonic transit time was 35.0 ± 2.1 h, with segmental transit times of 11.3 ± 1.1 h for the ascending and part of the transverse colon, 11.4 ± 1.4 h for a part of the transverse and descending colon and 12.4 ± 1.1 h for the rectosigmoid colon (Metcalf et al., 1987). In contrast, Wilson et al. reported colonic transit times for the ascending colon 3 – 5 h, the transverse colon 0.2 – 4.0 h, and the descending and sigmoid colon 5 – 72 h (Wilson, 2010), which elucidated the variability of the colonic transit.

For Modified released (MR) colon targeted dosage forms coated with a layer that erodes depending on the pH value (Long and Chen, 2009), the pH value in the colon is also a crucial factor for drug delivery. Different colon sections (i.e., ileum, *caecum*, ascending colon, transverse colon, and descending colon) have slightly varying pH values. In healthy patients, the pH value in the ileum is between 7.4 and 9.0; in the *caecum*, it drops between 6.2 and 7.4 in the ascending colon, the pH value is between 5.0 and 8.0, the transverse colon between 6.0 and 8.0, and in the descending colon between 7.0 and 8.0 (Stamatopoulos et al., 2021, Wilson, 2010). In patients where the colon is infected with a disease such as CD, the pH value in the ileum will drop to a

value between 6.0 and 8.0 and in the *caecum* to a value between 5.0 and 7.2 (Wilson, 2010).

2.1.1 Accessibility to Human Colon Transit

Many diseases can occur in the GI tract, e.g., indigestion, caused by delayed gastric emptying, abnormal small intestine motility or visceral hypersensitivity (Bonapace et al., 2000). It is often unclear whether the abnormalities involve the region of the stomach, the small intestine, or the colon. To identify and diagnose the cause, different techniques have been developed to assess the transit time of the GI tract, i.e., of the stomach, small intestine and colon simultaneously. For example, transit times can be used to identify common disorders such as delayed gastric emptying or accelerated colonic transit (Bharucha and Camilleri, 2019). The most common methods used to date are the '*Radiopaque Marker Technique*', the '*Scintigraphic Technique*', and the '*pH-Pressure Capsule*'.

Since the invention by Hinton et al., the method of using the *radiopaque marker* to quantify gastrointestinal transit, or more specifically colonic transit, has been modified by several researchers (Bharucha and Camilleri, 2019). Initially, a predefined number of radiopaque markers were administered orally at one time. By analysing the excretion in the faeces, the 'mouth to anus' transit is determined, which is also widely accepted as the colonic transit, even if the undetermined 'mouth to small intestine' part is included. The time for the radiopaque markers to reach the small intestine is assumed to be negligible compared to the total time in the small and large intestine. To calculate the colonic transit, a plain abdominal radiograph must be taken on

consecutive days or hours to determine the position of the radiopaque markers (Hinton et al., 1969, von der Ohe and Camilleri, 1992). This technique is more applicable to measuring colonic transit sufficiently than diagnosing disturbed motor functions, such as accelerated colonic transit. The latter would require many X-ray images to obtain a dynamic picture of colonic activity, which consequently leads to increased radiation exposure (von der Ohe and Camilleri, 1992).

Further, the radiopaque marker technique is widely used, but the radiopaque particles may not behave like a typical meal. They may also accumulate at different GI tract locations over a different period. Consequently, this behaviour of the markers means that the radiopaque particles do not represent the actual meal behaviour in the region of interest (ROI) (Notghi et al., 1993, Maqbool et al., 2009).

Scintigraphy is a technique that was initially developed to measure gastric emptying. Nowadays, scintigraphy is also used to measure the transit time of the GI tract, which includes gastric emptying, small intestine transit, and the transit through the colon. This technique uses different methods to administrate radioactivity into the GI tract that can be visualised with a gamma camera. Radioactive substances such as technetium 99m (^{99m}Tc) or indium 111 (^{111}In) are commonly used for radiolabeling the administrated meal, or a delayed-release capsule containing the radioactive substance is administrated. The capsule is usually covered with a pH-sensitive coating which dissolves accordingly to release the radioactive substance in the ROI. A third possibility is that the isotope is delivered, for example, into the colon, by orocecal (i.e., from the mouth to the *caecum*) intubation (Bharucha and Camilleri, 2019, Bonapace et al., 2000). To access the local transit times, imaging begins immediately after administration of the isotope carrier, if necessary, and ends when all required data/images are available. Depending on the objective of the examination and the

ROI, the time interval between image acquisitions can vary and extend over several days (Notghi et al., 1993). Compared to the radiopaque marker technique scintigraphy has the advantage that only minimal radiation is required to access the various transit times, regardless of the number of images or the duration of the examination (Maqbool et al., 2009, Notghi et al., 1993).

Smart pills are small electromechanical, transmitting devices used for a wide range of applications, such as measuring environmental conditions in the GI tract or for local drug delivery (Goffredo et al., 2016, Maqbool et al., 2009). An example of determining transit time through the human GI tract is the ambulatory wireless motility capsule called 'SmartPill®'. This pH-pressure capsule is administered orally and records the luminal pH, temperature, and pressure data at regular intervals as it travels through the GI tract. The patient must wear a portable receiver during the examination. The battery life of the SmartPill® is approximately five days, which allows for recording the entire GI tract. Based on characteristic conditions in the different sections, such as changes in pH value, the specific transit times, i.e., gastric emptying, small intestine transit, and colonic transit, can be quantified. The sum of all sectional transit times determines the total transit time through the GI tract. (Diaz Tartera et al., 2017, Maqbool et al., 2009, Bharucha and Camilleri, 2019). This relatively new technology showed good overall agreement with the radiopaque marker technique and scintigraphy. It is also less laborious than the other two techniques and provides fast results in graphical and report representation (Bharucha and Camilleri, 2019, Maqbool et al., 2009).

All the methods represented have the advantage that the markers used to measure the transit time can be swallowed like tablets and do not require intubation, which may also be problematic in ill patients. In addition, the measurements represent entire

gastrointestinal motor activity in the form of the overall propagation of the chyme over time, which is, for example, not accessible with manometric methods (von der Ohe and Camilleri, 1992).

2.1.2 Human Colon Motility

In patients with specific colonic disorders, such as constipation, it has been found that motility proceeds differently than in healthy patients. Single propagating sequences, for example, are reduced in length or no longer connected. This anomaly thus results in the intestinal contents not being propelled, as usual, leading to constipation (Dinning and Di Lorenzo, 2011). It was also found that the motility patterns in the colon depend on ingredients in the diet. Here, MRI was used to investigate the response of the motility patterns in the colon by oral ingestion of different stimulant solutions (i.e., maltose or a polyethylene glycol (PEG) electrolyte) (Hoad et al., 2016, Marciani et al., 2014, Stamatopoulos et al., 2020).

These examples show the complex conditions within the colon, which are influenced by several parameters.

2.1.2.1 Recording Techniques and Colonic Motor Functions

The colonic motor patterns in the colonic environment are mainly examined and discovered using manometric studies. In the colon, rhythmic contractions of smooth muscles propel the intestinal contents. These contractions are called peristalsis. Some

colonic diseases can be diagnosed by analysing the manometric data, possibly showing abnormal colonic contractility. The ability to detect abnormalities in the colonic motor pattern mainly depends on the spatial resolution of the recording sites on the manometric catheter being used (Arkwright et al., 2009a). The spacing of the pressure sensors on a colonic catheter is mostly >7.5 cm so that contractions propagating over a short distance are missed. Therefore, wide-spaced pressure sensors are inadequate for accurately identifying the complex nature of motor activity in the human colon. Accordingly, it is hard to find biomarkers for health and diseased states. It obstructs the possibility of examining normality accurately and correspondingly abnormalities (Arkwright et al., 2009a, Arkwright et al., 2009b). The only propagating activity that could be detected, independent of the sensor spacing, was the high amplitude propagating contraction, which is characterised by a mean amplitude of 110.0 ± 6.3 mmHg, mean duration of 14.15 ± 0.80 s, and a mean propagation velocity of 1.11 ± 0.10 cm s⁻¹ (Bampton and Dinning, 2013, Bassotti and Gaburri, 1988). To overcome the problem of missing short propagating waves, high-resolution manometry (HRM) has been developed. HRM uses a spacing of 1 cm between the recording sites, which also detects short-range motor patterns (Arkwright et al., 2009a, Arkwright et al., 2009b, Bampton and Dinning, 2013, Chen et al., 2017, Dinning et al., 2013a). Most propagating events propagate less than 10 cm (i.e., approx. 3 – 10 cm) along the colon and are therefore not detectable with sensor spacing larger or equal to 10 cm (Dinning et al., 2013a, Dinning et al., 2008). To detect propagating pressure waves with sensors spaced 10 cm, the pressure wave must propagate at least 20 cm (Bampton and Dinning, 2013, Dinning et al., 2013a). Consequently, an increase of sensor spacing (e.g., 2, 3, 5, 7, 10 cm) results in a decreased frequency of identified antegrade and retrograde pressure waves, an increase in the ratio between antegrade

to retrograde propagating pressure waves identified, and an increase of the incorrectly labelled propagating pressure waves (Dinning et al., 2013a). With a sensor spacing of 10 cm spacing, less than 20% of the propagating activity can be detected compared to a 1 cm sensor spacing (Bampton and Dinning, 2013). An example of an increased sensor spacing and hence loss of details in the results is shown in Figure 2.5.

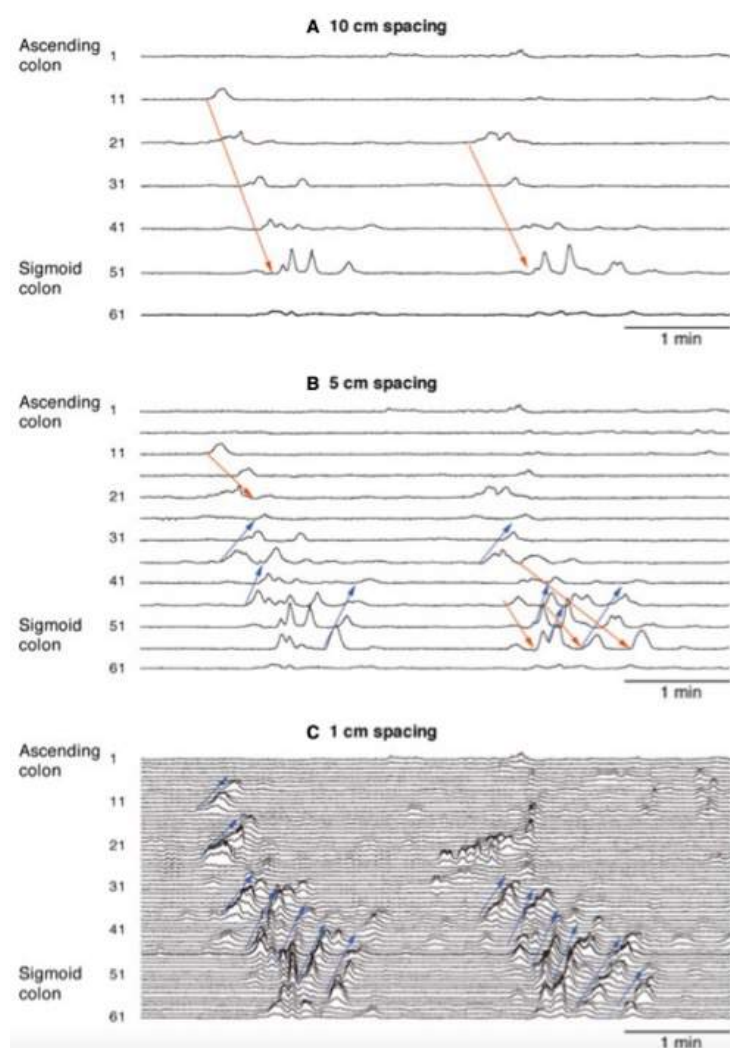


Figure 2.5 Example of a section of colonic manometry recorded with different sensor spacings: 10 cm (top), 5 cm (middle), and 1 cm (bottom). Antegrade propagating sequences (PSs) are visualised by red arrows and retrograde PSs by blue arrows. (adapted from (Dinning et al., 2013b))

Dinning et al. determined that doubling the sensor spacing from 1 to 2 cm almost reduced the number of pressure waves detected by 50%, and tripling the sensor space (i.e., from 1 to 3 cm) even resulted in a 30% chance of incorrectly labelling of the detected pressure wave (Dinning et al., 2013a).

To improve the reliability of results from manometric measurements due to low resolution, different HRM technologies have been employed: solid-state pressure and water-perfusion sensors. The water-perfuse catheters' main advantages are that they are robust, inexpensive, relatively flexible, and can be sterilised in an autoclave. The drawbacks of this type of catheter are that it requires external bulky water perfusion pumps, distributors, and bulky external transducers and suffers from a lower frequency response (i.e., lower pressure rise rate) than solid-state sensors. The main advantage of solid-state catheters is that they have a high-frequency response. The drawbacks of this technique are that solid-state sensors become less flexible with an increase in pressure sensors; they are not autoclavable, costly and fragile. However, both techniques have the main disadvantage: the catheter diameter increases by complexity and, therefore by, increasing the number of pressure sensors on the device. Therefore, to date, a practical limitation in terms of pressure sensors on the device is ~36 for the solid-state technology and ~20 for the water-perfused technology. Unfortunately, both techniques have limitations when they are to be used in the intestinal environment. The solid-state catheter is limited by its limited flexibility, while the water discharge into the intestinal region under investigation may interfere with the phenomena under investigation (Arkwright et al., 2009a).

To address these limitations of these techniques, high-resolution optical fibre manometry catheters have been developed. These catheters offer similar functionality to the solid-state and water-perfused sensors but have a smaller diameter and

significantly more flexibility than solid-state catheters (Arkwright et al., 2009a). Fibre optic sensing technology offers up to 120 sensors spaced 1 cm (Dinning and Di Lorenzo, 2011). To examine the colon, Arkwright et al. developed a sectional high-resolution optical fibre manometry device with 72 sensors that can analyse the whole colon concurrently. Here, sensor 1 - 10 was placed in the ascending colon, sensor 12 - 32 in the transverse colon, sensor 35 - 65 in the descending colon, and sensor 63 - 72 in the sigmoid colon (Arkwright et al., 2009b). Motility patterns determined with manometry are commonly characterised by pressure amplitude and duration. When comparing different parts of the colon (e.g., comparing the ascending colon with the transverse colon), care should be taken as manometry is less sensitive when the diameter of the colon exceeds 5.6 cm and will therefore lead to incorrect results (von der Ohe et al., 1994). Using HRM, two types of motility patterns have been found in the colonic environment. They can be classified as non-propagating motor activity and propagating sequences (or propagating contractions) (Dinning and Di Lorenzo, 2011). The non-propagating motor activity is the most common activity recorded in the colon (Dinning and Di Lorenzo, 2011). They consist of cyclic or single pressure waves recorded at one or more pressure sensors. The functional significance of these motor patterns is still unknown, although they are probably related to the mixing and propulsion of colonic contents. Patients with constipation have been found to have increased activity in the rectum and sigmoid colon (Dinning and Di Lorenzo, 2011). Propagating sequences (PS) have been found as antegrade and retrograde propagating pressure waves. PSs are defined as a sequence of three or more pressure waves recorded from adjacent recording sides. The conduction velocity within that sequence lay between 1 and 12 cm/sec (Arkwright et al., 2009b, Bampton et al., 2000, Dinning et al., 2004). Antegrade propagating pressure waves often occur in the same period as

luminal transit and defecation. Therefore, they are of great physiological importance in the colon (Dinning and Di Lorenzo, 2011). As most single PS do not span the length of the colon, a series of linked PSs can do so. Retrograde propagating sequences have been primarily found in the ascending colon (Dinning and Di Lorenzo, 2011). The two more general motor activities can be further subdivided and described in more detail by their characteristics (i.e., pressure amplitude and propagating distance): During simultaneous pressure waves (SPW), the pressure increases simultaneously of at least 2.5 s duration with an amplitude of at least 5 mmHg appearing at most or all pressure sensors. Propagating pressure waves (PPW) show 5 mmHg in amplitude but less than 100 mmHg and propagate in an antegrade or retrograde direction. High amplitude pressure waves (HAPW) show a pressure amplitude of >100 mmHg, detected by three or more sensors. Isolated pressure transients (IPT) are short-lasting pressure increases with an amplitude of 5 mmHg to >100 mmHg. This pressure increase is only present in one sensor and is not connected to other pressure changes in adjacent sensors (Chen et al., 2017). Colonic manometry and high-resolution scintigraphy can be performed simultaneously to access the relationship between colonic motility and luminal propulsion. At the same time, the overall resolution is limited by the frame rate of the scintiscanning equipment (Dinning et al., 2008).

In addition to manometry, *magnetic resonance imaging* (MRI) is another method of examining colonic motility. To access the colonic motility, commonly cine MRI is used, which is a type of MRI where cine images are obtained by repeatedly imaging the region of interest (ROI) for a predefined period and within a single slice (Kido and Togashi, 2016, O'Farrell et al., 2021, Stamatopoulos et al., 2020). From these images, for example, wall motion, the flow of luminal content and shear rates at the colonic walls can be determined (Marciani et al., 2014, O'Farrell et al., 2021, Stamatopoulos et al.,

2020, Sulaiman and Marciani, 2019). One of the milestones in using MRI images to examine the colonic environment was implementing a manual quantification method with that the volume of the different parts of the colon, in fasted and fed state, could be determined. However, in the fed state, it was possible to distinguish between a liquid and gas phase and therefore, the measured volumes included both phases (Pritchard et al., 2014). Murray et al. developed the MRI technique further. Nowadays, it is also possible to access the liquid volume (i.e., free water content, which is crucial for tablet dissolution) in the different parts of the colon (Murray et al., 2017). Compared to conventional manometry, this relatively new analysis technique offers several advantages as it is a non-invasive approach that provides fast and accurate results (Hoad et al., 2016, Vriesman et al., 2021). Because it is a non-invasive method, the natural environment of the colon is not disturbed during the examination (Hoad et al., 2016). By visually assessing each contraction (i.e., even slight contraction), cine MRI provides the same ability to create maps of pressure change as are produced by HRM. These motility plots are created from extracted data like the colon wall deformation and wall contraction/relaxation velocity (Hoad et al., 2016).

Additionally, MRI images show phenomena that conventional manometry cannot detect, like increases in the luminal diameter (Kirchhoff et al., 2011). Manometric examinations are usually performed with patients in horizontal positions, replicating just some hours a day (i.e., commonly at night) of the real-life situation. In the future, a vertical MRI scanner might offer the possibility to examine patients in an upright position (i.e., standing) and thus gain new insights into the 'colonic laws', which is another significant advantage of this imaging technique.

2.1.3 Colon Targeting Drug Delivery

The administration of drug products in the form of solid dosage forms (i.e., tablets or capsules) are widely accepted by patients as they are usually easy to swallow, are non-invasive and can be self-administered and easy to handle (Awad et al., 2021). Tablets and capsules can have different ways of administration. Some are intended to be swallowed, some should be chewed or kept in the mouth, and others must be dissolved before being ingested (Awad et al., 2021, Alderborn and Frenning, 2018). Tablets can be used for local (e.g., in the treatment of Crohn's disease (CD), ulcerative colitis (UC), or colon cancer) and systematic drug delivery, whereas in general systematic drug delivery is more common (Awad et al., 2021, Alderborn and Frenning, 2018). This chapter describes the different types of tablets and their drug release mechanisms that may be suitable for use in the colon. It is therefore not an exhaustive list of the types of tablets available.

2.1.3.1 Types of Drug Release Mechanisms

The drug release mechanisms from solid dosage forms taken orally can be classified into three main release types: immediate, extended, and delayed drug release.

Immediate drug release tablets release the drug immediately after oral administration.

The typical drug release profile of an immediate-release tablet is shown in Figure 2.6:

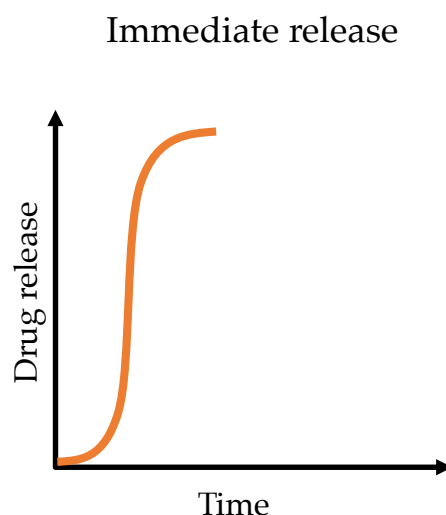


Figure 2.6 Schematic representation of a tablet's immediate drug release profile (modified from (Alderborn and Frenning, 2018)).

After ingestion or erosion/dissolution of a protective cover, the tablet starts to absorb water and thus softens the solid structure, leading to a relatively slow drug release at the beginning. After the solid structure is broken up, the rate of drug release increases. Over time, the decrease in size leads to a decreased drug release rate before the tablet (i.e., Active Pharmaceutical Ingredient (API)) is completely dissolved.

Modified drug release tablets (also called controlled release), on the other hand, have the feature of a manipulated or modified drug release, which leads to an extending drug release or the delaying of the drug release (Alderborn and Frenning, 2018, Awad et al., 2021).

Extended drug release tablets (or sustained-release or prolonged-release) release the API over a prolonged period, slowly, at an almost constant rate, and therefore reduces the frequency of dosing (Awad et al., 2021, Alderborn and Frenning, 2018). The typical drug release profile of an extended drug release tablet is shown in Figure 2.7:

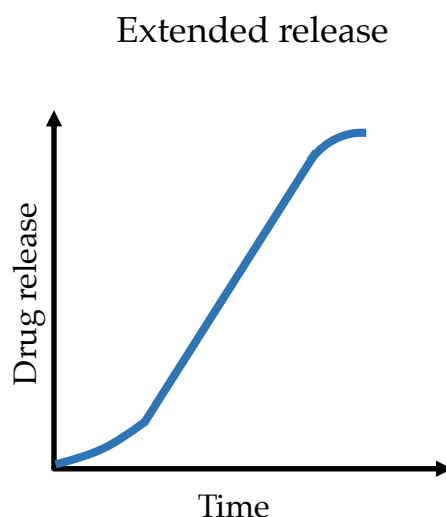


Figure 2.7 Schematic representation of a tablet's extended drug release profile (modified from (Alderborn and Frenning, 2018)).

The release mechanisms of extended-release tablets lead to a relatively constant drug release which may decrease slightly before the API is completely dissolved.

Delayed drug release tablets are designed to release the drug, for example, at a predefined time or in a specific region of the GI tract (e.g., the colon). The drug delivery to a specific region is also known as site-specific targeting (e.g., colon targeted drug delivery). The delayed drug release can be achieved using pH-dependent or physiologically activated coatings acting like a protective layer. pH-dependent coatings, for example, resist the low pH value in the upper part of the GI tract (i.e., the stomach) and dissolve/erodes in the lower part of the GI tract (e.g., colon) where the tablet should disintegrate, and the drug dissolve (Awad et al., 2021, Habashy et al., 2022). As soon as the coating disappears, the disintegration profile of these tablets is comparable with the disintegration profile from *immediate-release* tablets (Alderborn and Frenning, 2018). Accordingly, these tablets that resist low pH values are known as gastro-resistant, or enteric dosage forms (Awad et al., 2021). The typical drug release profile of a delayed drug release tablet is shown in Figure 2.8:

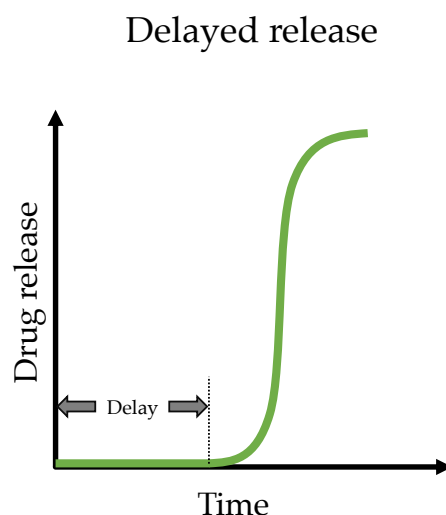


Figure 2.8 Schematic representation of a tablet's delayed drug release profile (modified from (Alderborn and Frenning, 2018)).

For the purpose, for example, of local treatment of the lower small intestine or colon, delayed drug release tablets can also be combined with extended drug release tablets to achieve a prolonged treatment (Alderborn and Frenning, 2018).

2.1.3.2 Layered Tablets for Immediate and Delayed Drug Release

Another type of tablet is called a *layered tablet*. Layered tablets (also called multiple compressed tablets) contain more than one layer, one on top of the other. They are therefore also called multi-layered tablets (or multiple-layered tablets) (Figure 2.9 (a)). When the core is enclosed in a tablet shell, this type of layered tablet is called press-coated (Figure 2.9 (b)). It is used, for example, for the simultaneous administration of different drugs or / and the combination of several release profiles like immediate and delayed drug release of the active substance from the core tablet. Press-coated tablets can also be used for taste masking (Awad et al., 2021).

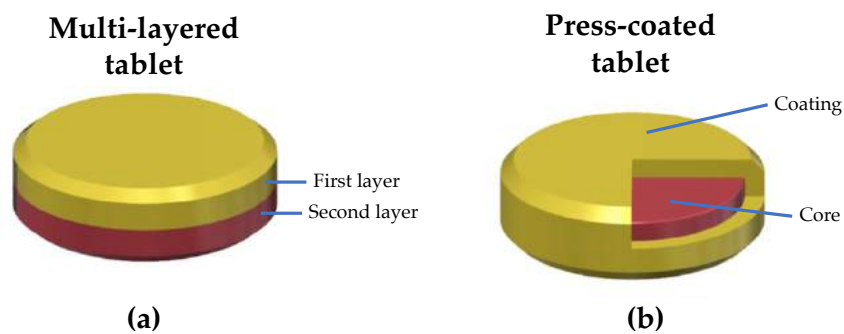


Figure 2.9 Schematic representation of the difference between a multi-layered and a press-coated tablet (modified from (Awad et al., 2021)).

2.1.3.3 Modified Release Tablets and their Extended-Release Mechanisms

Extended-release tablets are commonly characterised by their drug release mechanism. To control the drug release to be slow and constant, four different drug release mechanisms are used to date (Adepu and Ramakrishna, 2021, Awad et al., 2021): dissolution-controlled, diffusion-controlled, osmotically-controlled, and ion exchange-controlled.

Dissolution-controlled tablets: The drug release rate for this drug release mechanism is controlled by the rate of dissolution of the drug or another ingredient in the gastrointestinal fluids. In general, dissolution-controlled release systems can be subdivided into two different types: matrix and reservoir systems. These systems are presented in Figure 2.10.

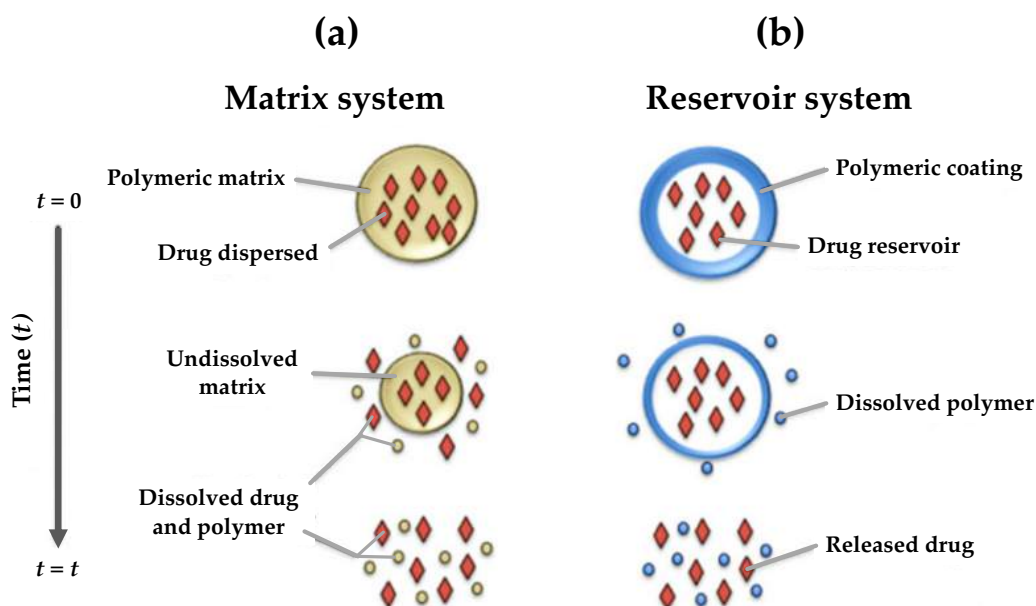


Figure 2.10 Schematic representation of the dissolution-controlled drug release systems where (a) is the matrix system and (b) the reservoir system (modified from (Awad et al., 2021)).

The matrix system (Figure 2.10 (a)) (also known as erosion-controlled release system) is the most commonly used system for controlled drug release (Alderborn and Frenning, 2018). Here, the Active Pharmaceutical Ingredient (API) is homogeneously distributed in a polymer matrix. The API is released as soon as the polymer matrix dissolves in the surrounding fluid. The dissolution of the polymer matrix leads to a decrease in tablet size over time, resulting in a nonlinear drug release profile (Awad et al., 2021). The dissolution rate of the carrier (i.e., polymer matrix) defines the drug release rate. (Alderborn and Frenning, 2018).

The reservoir system (Figure 2.10 (b)) is a drug release system that can be used to design tablets with a specific release profile or for targeted drug delivery. In this system, the API is in the tablet's core, surrounded by a polymeric coating. Over time the polymeric coating dissolves in the fluid. Once the polymeric coating is completely dissolved, the drug is released immediately. Therefore, the drug release is like an

immediate-release tablet. The thickness of the polymer coating and/or specific polymers that only dissolve at specified pH defines the delayed drug release (Awad et al., 2021, Alderborn and Frenning, 2018).

Diffusion-controlled tablets: The API diffuses through a polymer membrane or a matrix in the diffusion-controlled drug release systems. Depending on where the drug diffusion process occurs, this system can be divided into the reservoir system and matrix system (also known as the monolithic system) (Alderborn and Frenning, 2018, Awad et al., 2021). Both diffusion-controlled drug release systems are shown in Figure 2.11.

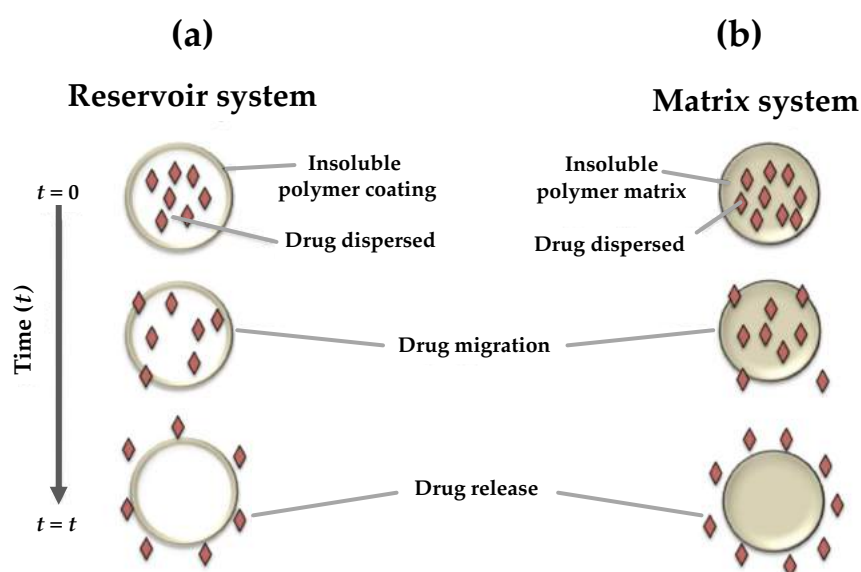


Figure 2.11 Schematic representation of the diffusion-controlled drug release systems where (a) is the reservoir system and (b) the matrix system (or monolithic system) (modified from (Awad et al., 2021)).

The diffusion process in the reservoir system (Figure 2.11 (a)) occurs in a thin insoluble polymer coating surrounding the API. The insoluble polymer coating leads to a constant diffusion distance and, consequently, as long as the concentration gradient is

maintained, to a constant drug release rate (Alderborn and Frenning, 2018). Reservoir systems can further be subdivided into two systems called non-porous and microporous (Awad et al., 2021). In non-porous systems, the API diffuses through the thin insoluble polymer coating into the surrounding fluid. In contrast, in microporous systems, the polymer coating of the tablet forms micropore channels in contact with water (in combination with pore-forming agents). Once the micropores have formed, the API molecules diffuse through the micropore channels and are released (Awad et al., 2021).

Also, diffusion-controlled matrix systems (Figure 2.11 (b)) can be further subdivided into hydrophilic and insoluble matrix systems (Awad et al., 2021). In both systems, the API is dispersed as solid particles in the matrix (Alderborn and Frenning, 2018). In hydrophilic matrix systems (also known as swelling soluble matrices), the API is dispersed in a hydrophilic polymer that swells when in contact with water creating a gel matrix. The drug release into the surrounding fluid occurs by dissolution or erosion of the matrix. The diffusion of water controls the drug release rate into the tablet and the hydrated gel layer (Awad et al., 2021).

In insoluble matrix systems, the solid API is dispersed in an insoluble and, therefore, inert matrix. The matrix consists of microchannels through which water can penetrate the tablet and dissolve the API, which is then released. The drug particles on the tablet's surface are dissolved immediately, while the API inside the tablet dissolves later, resulting in a prolonged drug release of the API. Three factors mainly control the drug release from an insoluble matrix system: (1) amount of drug in the matrix, (2) porosity, (3) tortuosity of the microchannels and length, (4) pore size, (5) solubility of the drug (i.e., concentration gradient) (Alderborn and Frenning, 2018, Awad et al., 2021). To modify the microchannels (i.e., pores) in an insoluble matrix system and

therefore the drug release characteristics of the tablet, soluble excipients can be added to the matrix or/and the compaction pressure while tableting can be adjusted (Alderborn and Frenning, 2018).

Osmosis-based tablets: Osmosis is based on concentration gradients (i.e., osmotic pressure), where water passes through a semipermeable membrane from the compartment with lower solute concentration into a solution with higher solute concentration. The semipermeable membrane only allows the solvent to pass through, but not the solute (Alderborn and Frenning, 2018, Awad et al., 2021, Verma et al., 2002). A particular characteristic of this drug release mechanism is that the drug release is mainly independent of gastric pH and other physiological parameters (e.g., hydrodynamics) (Awad et al., 2021, Verma et al., 2002). The osmotic drug release systems can be classified into two different systems: elementary osmotic pump and osmotic push-pull system. The area of application of the two systems depends on the water-solubility of the drug. The elementary osmotic pump can only be used if the drug is water-soluble. If the drug is poorly water-soluble, only the osmotic push-pull system can be used. Both systems are shown in Figure 2.12 (a) and (b), respectively.

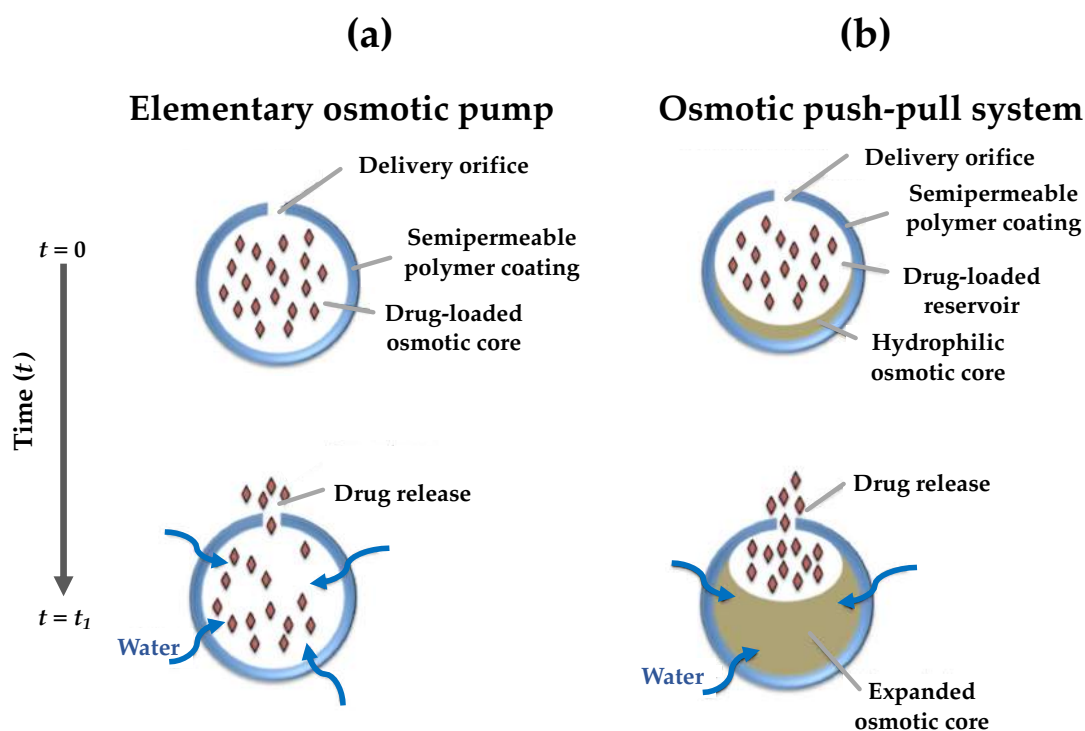


Figure 2.12 Schematic representation of the osmotically-controlled drug release systems where (a) is the elementary osmotic pump and (b) the osmotic push-pull system (modified from (Awad et al., 2021)).

In the elementary osmotic pump system (Figure 2.12 (a)), the drug core is surrounded by a semipermeable membrane in which a small orifice is drilled (e.g., with a laser). Water penetrates the tablet through a semipermeable membrane when ingested and gradually dissolves the drug in the core. The drug is then released through the orifice in the membrane. The drug release rate in this system is proportional to the water that enters the tablet (Awad et al., 2021). The push-pull drug delivery system (Figure 2.12 (b)) consists of a bilayer core, one part being the drug reservoir and the other part being a hydrophilic expanding compartment. As in the elementary osmotic pump, the tablet is surrounded by a semipermeable membrane containing a delivery orifice on the side of the drug reservoir. After administration, water penetrates the tablet resulting in the formation of a drug suspension/solution in the drug reservoir on the

one hand and swelling/expansion of the hydrophilic compartment on the other. The swelling/expansion of the latter compartment exerts an additional force on the system, which ensures that the drug is released through the orifice (Awad et al., 2021, Verma et al., 2002).

Ion exchange-controlled tablets: The drug release mechanism of this type of tablet is based on differently charged ions. The tablets consist of a water-insoluble polymer that is functionalised with ionic groups. The drug molecules are bonded to the ionic units in polymer by electrostatic interactions due to opposite charges. A schematic representation of the drug release process of ion exchange-controlled tablets is shown in Figure 2.13.

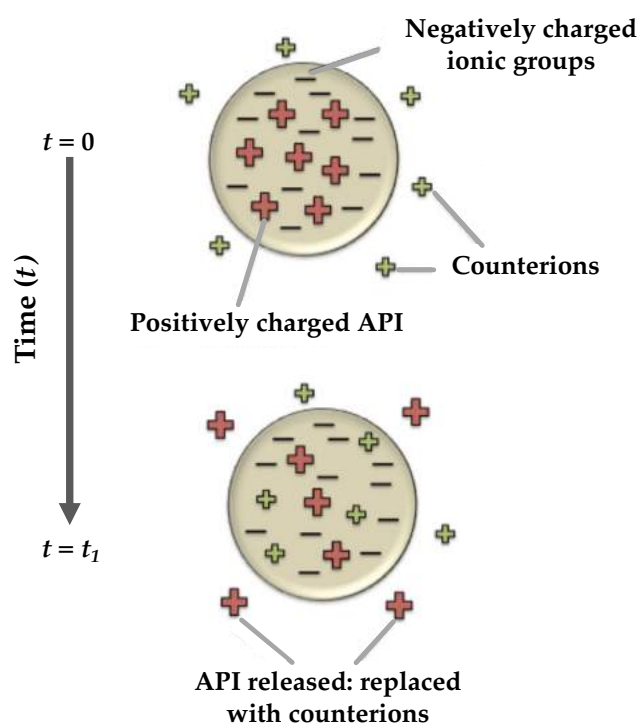


Figure 2.13 Schematic representation of the ion exchange-controlled drug release systems (modified from (Awad et al., 2021)).

After ingestion and the associated contact with an aqueous environment, the process of API release begins. In this process, the API molecules in the polymer are replaced by ions (i.e., with counterions) with the same charge, leading to the API's release from the ion exchange resin system. To control the drug release rate of this drug release system, the ion exchange resins can, for example, be coated with water-insoluble polymers to achieve diffusion-controlled drug release (Awad et al., 2021, Puttewar et al., 2010). In addition to the actual purpose, the controlled release of the API, the ion exchange mechanism is also used to mask the taste of orally administered solid dosage forms, e.g., to avoid a bitter taste and thus increase acceptance of certain medicinal products patients (Puttewar et al., 2010).

2.1.4 Dissolution Testing of Oral Administrated Dosage Forms

In the development, optimisation and production of solid dosage forms, dissolution testing under reproducible conditions is one of the essential aspects (Baxter et al., 2005). Dissolution testing provides the opportunity to access factors that influence the bioavailability of the drug from a solid dosage form and also to monitor the quality during production. The bioavailability of a drug, i.e., for its absorption in the intestinal environment, requires that the drug is in solution. This is because only dissolved drugs can permeate through the intestinal mucosa (Alderborn and Frenning, 2018, Awad et al., 2021). During a tablet dissolution test, the cumulative amount of drug dissolved in the dissolution medium over time is measured. In the best case, the resulting dissolution profile provides information for Physiologically Based Pharmacokinetic Modelling (PBPK) (see Chapter 2.1.5) to predict how the tablet will behave *in vivo*, or



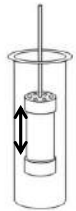

it serves as quality control in the manufacturing process (Bai et al., 2007a). Although there are several different dissolution apparatuses, the most commonly used are those specified and standardised in the European or US pharmacopoeias monographs. Standard dissolution tests are usually performed at a dissolution medium temperature equivalent to that of the human body (i.e., $37^{\circ}\text{C} \pm 5^{\circ}\text{C}$) unless otherwise specified (Alderborn and Frenning, 2018, Awad et al., 2021). The dissolution medium's composition can vary between test situations, depending on which part of the GI tract is replicated. For example, the pH can be changed during the dissolution test by adding acid or base to the dissolution medium at specific intervals. To mimic the physiological conditions, e.g., in the intestine, substances can be added to the dissolution medium, increasing fluid viscosity to exhibit biorelevant properties (Alderborn and Frenning, 2018).

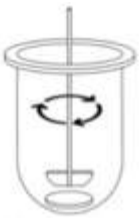

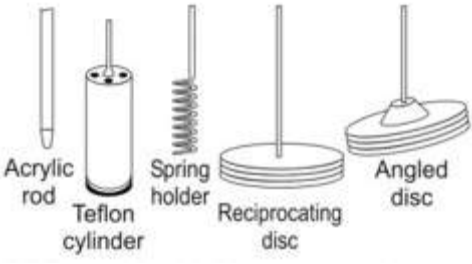
In the US pharmacopoeia, seven types of dissolution apparatuses are designated for testing different dosage forms. In literature, the various US Pharmacopoeia dissolution apparatuses are abbreviated USP, with a subsequent number indicating the type (e.g., USP I for US Pharmacopoeia dissolution apparatus type one). The most important stirred vessel methods are the rotating-basket method (USP I) and the paddle method (USP II). The pharmaceutical industry commonly uses the USP II dissolution apparatus to perform dissolution testing (Bai et al., 2007b, D'Arcy et al., 2010). This thesis considers only a miniaturised version of the USP II (i.e., 1000 mL dissolution medium) the mini-USP II (i.e., 100 mL dissolution medium). This smaller apparatus replicates, for example, the low amount of liquid available in the colon to dissolve a solid dosage form better than the USP II. Another advantage of this apparatus is the reduced mass of material required while retaining the analytical method and set-up of the conventional device (Stamatopoulos et al., 2016a). Additionally, a large volume of

expensive biorelevant dissolution medium may lead to high testing costs (Wang and Armenante, 2016).

For the sake of completeness, a summary of all US pharmacopoeia dissolution apparatuses available is given in Table 2.1.

Table 2.1. US pharmacopoeia dissolution apparatuses with the main stirred vessel method in bold ((Awad et al., 2021), images modified from <http://www.pharmacy180.com/article/considerations-in-in-vivo-bioavailability-study-design-2532/>, accessed 09/01/2022)

Dissolution apparatus type	Name		Tested dosage forms
I	Basket apparatus		Tablets, capsules
II	Paddle apparatus		Orally disintegrating and chewable tablets, capsules, and suspensions
III	Reciprocating cylinder		Tablets, capsules, suspensions, granules
IV	Flow-through cell		All dosage forms

V	Paddle over disk		Transdermal patches
VI	Rotating cylinder		Transdermal patches
VII	<p>Reciprocating holder</p>  <p>Acrylic rod Teflon cylinder Spring holder Reciprocating disc Angled disc</p>	Non-disintegrating tablets and transdermal patches	

The mini-USP II (Figure 2.14) consist of a cylindrical vessel with a hemispherical bottom. The agitator is called a paddle and has a shape of a trapezoid.

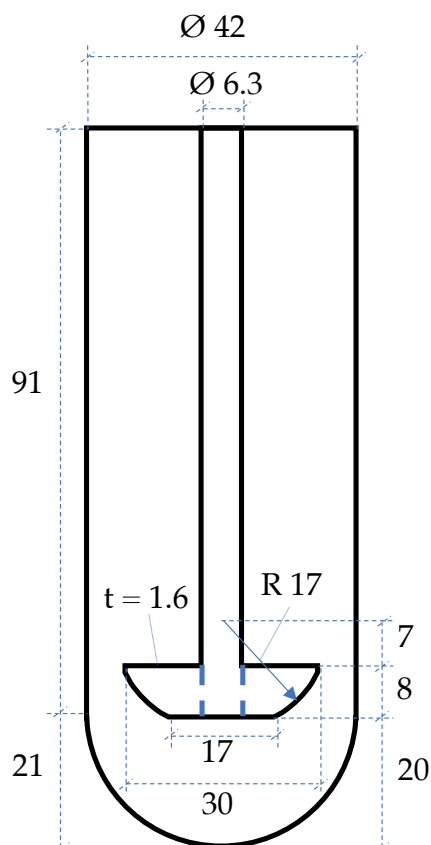


Figure 2.14 Schematic representation of the mini-USP II used in this thesis with dimensions according to (Stamatopoulos et al., 2015)

The length of the upper part of the paddle is approximately 30 mm, the lower part is 17 mm, and the thickness of the paddle is about 1.6 mm. The edges of the paddle are rounded with a radius of 17 mm. The solid dosage form is placed in the centre of the hemispherical bottom for dissolution testing. Depending on the shear rates that act on the solid dosage form and, in the best case, represent a value that is as biorelevant as possible, the paddle speed is adjusted accordingly. Typically, paddle speeds between 25 and 200 rpm are used (Stamatopoulos et al., 2016a, Stamatopoulos et al., 2015, Wang and Armenante, 2016, Wang et al., 2018).

Although the pharmaceutical dissolution apparatuses mentioned above allow control of the dissolution media properties, the vessels hardly correspond to the geometry of

the colon and use simplified mixing methods that, for example, do not replicate the hydrodynamic conditions of the human colon *in vivo* (Schütt et al., 2021, Stamatopoulos et al., 2016a, Stamatopoulos et al., 2015, Wang et al., 2018, Schütt et al., 2022).

2.1.5 Physiologically Based Pharmacokinetic Modelling

Physiologically Based Pharmacokinetic (PBPK) models use a mathematical framework in which the human body is divided into a series of compartments. These compartments present different organs or tissues in the body. In the present commercial PBPK software, the GI tract is subdivided into nine compartments. One compartment is used for the stomach, one for the duodenum, two for the jejunum, four for the ileum and one for the colon (see Figure 2.15).

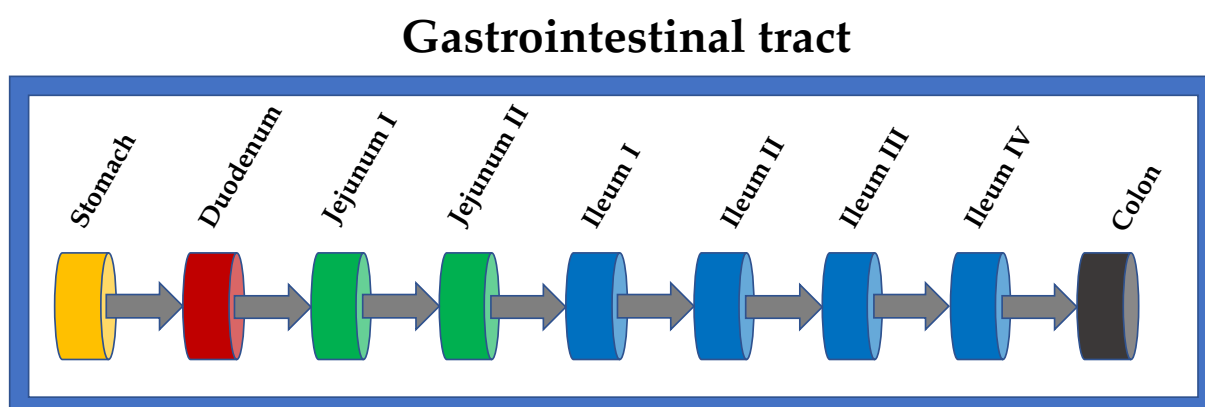


Figure 2.15. Schematic representation of the GI tract as it is compartmentalised in the PBPK model (modified from (Stamatopoulos, 2022))

The PBPK models use physiological input parameters to mimic the conditions (e.g., hydrodynamics and drug permeability into the bloodstream) in the GI tract and to

predict drug absorption based on the properties of the drug (e.g., solubility and dissolution) (Stamatopoulos, 2022). The commercial PBPK platforms such as GastroPlus™ and SimCYP® use a simple first-order forward transit rate model and therefore consider, for example, the colon as a single well-mixed and homogenised compartment.

Further, transit times for different dosage forms (e.g., tablets, pellets, and fine particles) are also considered constant, although they are affected by motility, volumes, and viscosity changes *in vivo*. In the colonic compartment, the PBPK platforms process the disintegration and dissolution of the solid dosage form as an immediate event (i.e., without considering shear stresses acting on the dosage form, which is crucial for the drug release process), and the distribution of the released API is uniform along the colon. Commonly, the dissolution process is modelled with velocities of the dissolution medium derived from Computational Fluid Dynamics (CFD) and USP II analyses. Thus, analyses from non-biorelevant simulations or apparatuses are used to describe *in vivo* conditions (i.e., hydrodynamics). Although PBPK models use simplified assumptions in their mathematical descriptions, they are an essential tool for developing and optimising solid dosage forms. PBPK models have already been used to support the approval process for new drugs and reduce the number of animal experiments and clinical trials during the drug development process (Stamatopoulos, 2022).

2.1.6 *In Silico* Models Existing to Date

In recent years, computer simulations have proven to be a successful tool for saving costs while reducing clinical and animal testing. Furthermore, computer simulations allow a deeper insight into, for example, the hydrodynamic conditions and shear stress distributions that are crucial for the dissolution process of the tablet and the distribution of API in the corresponding region of interest.

As described in Chapter 2.1.4, dissolution tests are commonly performed in one of the USP dissolution apparatuses, which do not replicate the anatomical and, consequently, hydrodynamic conditions of the different parts of the GI tract. In addition, small changes in the dissolution testing procedure that are still within the limits specified by US Pharmacopoeia may lead to different results (Bai and Armenante, 2008). The non-biorelevant conditions in the USP dissolution apparatuses and the burden of errors during the test procedure (Kukura et al., 2004) led to the development of CFD simulations that mimic the USP dissolution apparatuses. These simulations helped to investigate the hydrodynamics in the vessel itself and the correlation between hydrodynamics and tablet disintegration/dissolution, which is not or very difficult to access with experiments. In addition, CFD simulations of the gastrointestinal tract (i.e., the stomach, small intestine, and colon) with biorelevant geometries and conditions (e.g., motility patterns) have been developed.

2.1.6.1 Colon (Large intestine)

The colon has experienced less attention in computer simulations than the USP dissolution apparatuses and the small intestine. Sinnott et al. used the particle-based simulation technique SPH to develop a 3D model of the colon to investigate the relationships between peristaltic contraction and fluid transport. Their study modelled the colon as a cylindrical body with a visco-elastic membrane that can contract, relax, and replicate a peristaltic wave accordingly. The colon model is completely filled with a fluid whose viscosity is varied. The results showed decreased volumetric flow rate of digested content when the fluid viscosity increases. In addition, the volumetric flow rate is dependent on the occlusion degree. A higher occlusion degree results in a higher volumetric flow rate. This is true for low and high viscous fluid (Sinnott et al., 2012).

Alexiadis et al. (Alexiadis et al., 2017) used a similar simulation approach to Sinnott et al. (Sinnott et al., 2012) to investigate the hydrodynamics in a biorelevant *in vitro* model developed at the University of Birmingham called Dynamic Colon Model (DCM) (Stamatopoulos et al., 2016b). This 2D model is just partially filled with fluid and comprises the natural convolution of the human colon called *haustra* (see Figure 2.2), as the DCM also replicates it. The authors found three major mass propagation modes: pouring, surfing, and ineffective surfing mode. The different modes are results of the momentum that a fluid element experiences from the movement of the colon's membrane (i.e., contraction).

Alexiadis et al. (Alexiadis et al., 2021) developed a technique on how to couple multiphysics (i.e., SPH coupled with LSM) and artificial neural networks (ANN). Their study showed the strength of their approach on a colon model, which adjusts its contraction pattern according to the physical properties of the luminal contents. The

ANN replicates the enteric nervous system (ENS) activity, a complex network of nerve cells (neurons), and it runs through almost the entire GI tract and controls its function. The colon is an example of a possible *in silico* model of human organs that adapt their response to external stimuli independently. The results from the colon model corresponded with *in vivo* measurements and, in addition, responded to atypical variations (i.e., making the model artificially ill) of its functioning with actions as they occur in real diseases like Inflammatory Bowel Disease (IBD).

2.1.6.2 Small intestine

The CFD studies focusing on the small intestine describe the duodenum, the first part of the small intestine after the stomach (Figure 2.1). The duodenum is a C-shaped tube where mixing the chyme from the stomach with the digestive juices from the pancreas and liver takes place (Hari et al., 2012).

The CFD models that have been developed to date range from simplified 2D models with a rectangular shape (Hari et al., 2012, Love et al., 2013), a 2D model with a simple rectangular shape but with circular folds (Zha et al., 2021), a 3D model simplified as a cylindrical body (Sinnott et al., 2017), a 3D model with C-shape (Trusov et al., 2016) to an anatomically correct 3D model with realistic contraction patterns (Palmada et al., 2020, Palmada et al., 2022). All the studies use mesh-based simulation techniques except Sinnott et al., who developed a particle-based (i.e., meshless) Smoothed Particle Hydrodynamics (SPH) model coupled with the Discrete Element Method (DEM).

The studies investigated the fluid flow inside the duodenum and the mixing efficiency dependent on different fluid conditions (i.e., fluid viscosity, solid content, and type of

fluid: Newtonian or non-Newtonian), contraction amplitude, the roughness of the membrane (i.e., circular folds). The primary conclusions are that the level of mixing depends on the fluid viscosity and the amplitude of the contractions (i.e., higher fluid viscosity resulted in an increased level of mixing as well as greater amplitude) (Palmada et al., 2020). The findings referring to the fluid viscosity are surprising as the authors found more long-lasting vortices and no stagnation points in the low viscous fluid (i.e., water), which should reinforce the mixing. The findings also contradict results in the colon, where the authors found a decreasing mixing efficiency with increased fluid viscosity. This is explained by an increased momentum needed to move a high viscous fluid and sounds more plausible (Schütt et al., 2021).

Love et al. modelled the flow of digested contents through the small intestine to explore the effects of varying the rheological properties. Their study found that a diet with a high portion of fibre will lead to a higher viscous digesta and consequently reduce the formation of vortices at the wall, which simultaneously impairs the absorption efficiency in the small intestine (Love et al., 2013).

In a particle-based simulation approach with a flexible membrane, Sinnott et al. investigated the fluid flow inside the small intestine with different solid concentrations. The results showed that, due to the laminar flow conditions, the concentration of solid particles in the fluid does not significantly influence the flow pattern (i.e., velocity profile) (Sinnott et al., 2017).

All the models, except Zha et al., simplified the small intestine wall as a smooth wall without any irregularities, which is not the case. Therefore Zha et al. developed a computational model of the small intestine with circular folds and investigated the influence of these folds on mixing intensification. They found that circular folds effectively intensify the radial and axial mixing in a laminar flow regime under

segmentation contraction. In addition, compared to a smooth surface, long-lasting vortices could be identified, and higher shear rates were observed (Zha et al., 2021).

2.1.6.3 USP Dissolution Apparatuses

For the pharmaceutical industry's most important USP dissolution apparatuses (i.e., USP I, USP II and mini-USP II), several CFD simulations were performed to investigate the conditions in these apparatuses. All the studies mentioned in this chapter used mesh-based simulation techniques performed with commercial simulation software such as ANSYS® FLUENT®, Altair AcuSolve™, and SOLIDWORKS®. The studies include hydrodynamic and shear stress inside the USP II at constant agitator speed (Bai et al., 2007b), different agitator speeds (Bai et al., 2011, Kukura et al., 2004, Wang and Armenante, 2016) and small changes of impeller locations (Bai and Armenante, 2008). In the literature, there are various models to describe the fluid dynamics, e.g., in dissolution apparatuses. In Bai et al. (Bai et al., 2007b), different turbulent models were tested (i.e., the $k-\omega$ Model with low Reynolds number correction, the RNG $k-\varepsilon$ Model, the Realizable $k-\varepsilon$ Model, or with no turbulence model at all, assuming laminar flow). Finally, the $k-\omega$ Model with low Reynolds number correction was selected and in accordance with the results also used in their subsequent work Bai et al. (Bai et al., 2007a), Bai et al. (Bai and Armenante, 2008), and Bai et al. (Bai et al., 2011). Likewise, based on the results of Bai et al. (Bai et al., 2007b), Wang et al. (Wang and Armenante, 2016) also used the $k-\omega$ Model with low Reynolds number correction. In contrast, Kingden et al. (Kindgen et al., 2015) used the Standard $k-\varepsilon$ Model. The Standard $k-\omega$

Model and the Standard k - ϵ Model are empirical models based on transport equations for the turbulence kinetic energy (k) and the specific dissipation rate (ω) or (ϵ), respectively (Bai et al., 2007b). In D'Arcy et al. (D'Arcy et al., 2006, D'Arcy et al., 2010), the fluid flow was modelled using a rotating reference frame and a multiple reference frame, which depends on the region to be modelled. In Kukura et al. (Kukura et al., 2004), the Spalart-Allmaras Model is used to model the hydrodynamics.

One of the main essential observations, in the case of hydrodynamics and shear stress, is that even small changes in the agitator location, which were still within the limits specified by US Pharmacopoeia, changed the velocity and shear stress profiles in the USP II significantly. This is especially true for an agitator location that led to non-symmetry conditions (Bai and Armenante, 2008). Another crucial finding is that an increased paddle speed does not increase shear homogeneity within the apparatus. Therefore, the existing uneven distribution of hydrodynamic forces in the USP II explains the variability in dissolution rate (Kukura et al., 2004).

To record the drug release over time during dissolution testing, the sample must be taken from the dissolution medium, which should accordingly be well mixed. Therefore, Bai et al. (Bai et al., 2007a) determined in their study the blend time. The blend time is defined as the time to achieve a predefined level of homogeneity of a tracer in a mixing vessel. It is also an important parameter to evaluate the mixing efficiency of mixing devices. The authors concluded that fluid in the USP II dissolution apparatus could be considered relatively well mixed and correspondingly fulfil the requirements for a typical dissolution test.

Other studies focused on the dissolution process of a solid dosage form itself. Different solid dosage forms were used to investigate the dissolution rate of a tablet with a

curved and planar surface. The tablet was placed centrally and non-centrally at the bottom of the USP II. CFD was also used to simulate the fluid flow around the dosage form at the different positions to determine the relationship between local hydrodynamics and dissolution rate for these regions. The authors found that the dissolution rate increased from the centre to the off-centre positions for each surface examined (D'Arcy et al., 2010).

Despite the investigation on the USP II dissolution apparatus, one study has focused on the USP I and compared the velocity profiles of both devices (D'Arcy et al., 2006). They found a similar fluid velocity at the same rotation speeds, supporting equivalent dissolution rates from these locations. Kindgen et al. investigated the hydrodynamics and, consequently, the forces acting on the surface during disintegrating testing of a solid dosage form in the USP I. They performed the simulations for different fluids (i.e., various fluid viscosities) and compared the results to experimental and *in vivo* data. The authors concluded that the operational conditions of the commonly used USP disintegration test device do not correctly replicate the *in vivo* situation because the forces acting on the dosage form are too small compared to *in vivo* situations (Kindgen et al., 2015).

Chapter 3

Methodology

3.1 The Discrete Multiphysics (DMP)

3.1.1 Introduction

Computer simulations are becoming increasingly popular for solving complicated problems in various fields of engineering and science. Numerical simulations offer alternatives to experiments, which are sometimes very expensive, take much time, or are dangerous. Computer simulations also provide insight into difficult or impossible areas to cover with experiments. Computational fluid dynamics (CFD) and computer simulations, in general, are also widely used in engineering to support the planning of new industrial plants or improve production and maintenance efficiency. The gastrointestinal tract (GI) can be thought of as a complex system of pipes, pumps, valves, and mixers and therefore represents a classical engineering system. The complexity of these bioengineering systems results from the individual 'components' and their modes of operation. Because there are anatomical differences from person to person, CFD enables many parameters to be investigated under more bio-relevant conditions than is usually the case. CFD simulations can be divided into two methods: the mesh (or grid) and the meshless (or mesh-free) method. In the mesh or grid method, the computational domain is divided into discrete cells or elements, where each node has a fixed number of predefined neighbours (Khohtali et al., 2021). The discretisation of the physical domain into sub-domains is called meshing or grid generation. The connectivity and the information of two neighbour nodes can be used to define mathematical operators to solve the desired equations of the domain. The accuracy of the result, rate of convergence, and computational time required depend highly on the quality of the generated grid, which must be created 'manually' using,

for example, appropriate software. The limitations of the grid-based simulation method arise when complex geometries are involved, or/and the material simulated can move around or is engaged in large deformations. Mesh or grid-based methods can be either a Eulerian or a Lagrangian approach. In the Eulerian formulation, the space is discretised in which the material flows. Thus, the grid is fixed in space, and no movement of nodes and elements is required. On the other hand, in the Lagrangian formulation, the material is discretised, and the simulation elements move with the material. The nodes are not fixed in space and change every time step according to their spatial geometry position (Figure 3. 1).

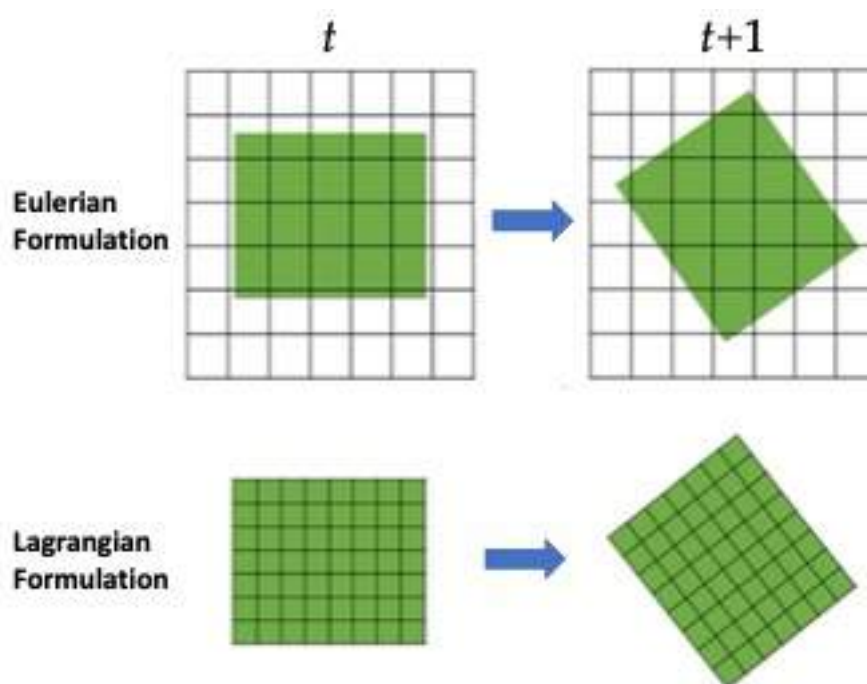


Figure 3. 1 Schematic representation of the difference between the Eulerian and the Lagrangian mesh or grid-based method.

The Lagrangian approach allows a better simulation/treatment of high deformations and the simulation of free-surface flow (Amicarelli et al., 2017). In meshless simulation methods (Lagrangian formulation), for example, like Smoothed Particle

Hydrodynamics (SPH), the computational domain is discretised into a finite number of particles that are treated as physical particles with mass and density. These particles can move around over time. The stationary nodes in the grid methods are, in simple terms, replaced by free-moving particles. The mathematical equations are numerically solved only for neighbouring particles in a certain, predefined distance. A schematic representation between a Eulerian grid-based method and a Lagrangian meshless method is given in Figure 3.2.

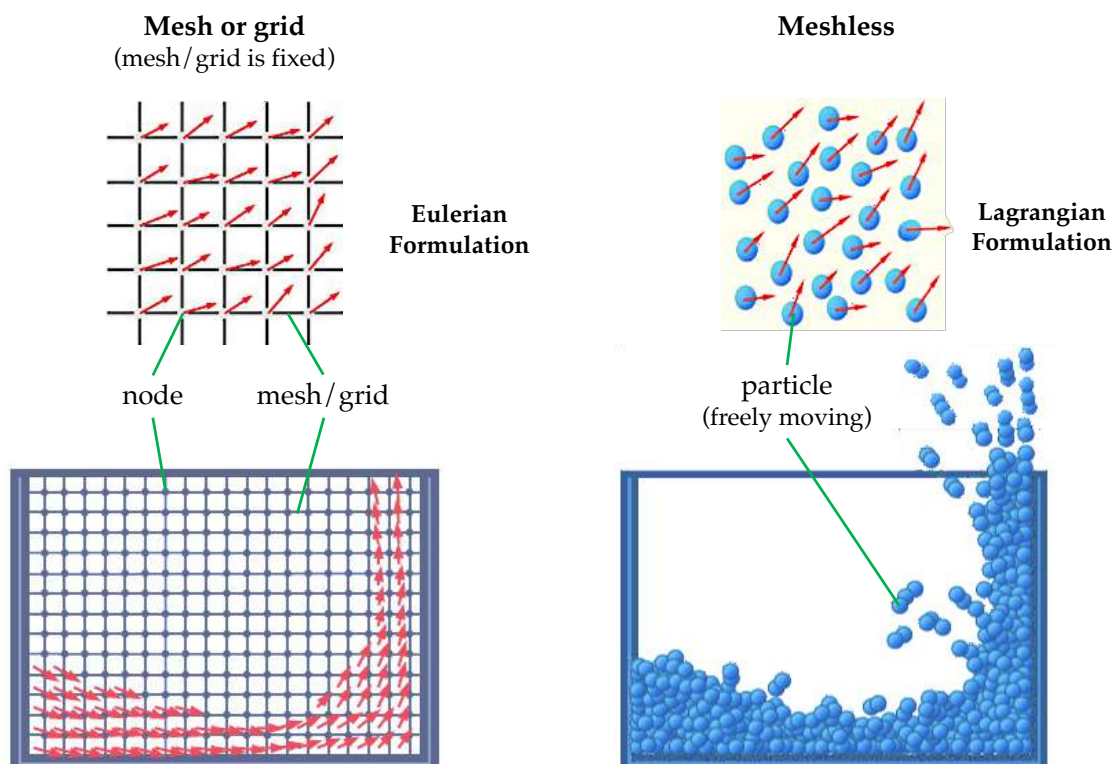


Figure 3.2 Schematic representation of the difference between a mesh or grid-based and meshless simulation methods (modified from <https://powersys-solutions.com/product/?software=ParticleWorks>, accessed 03/11/2021)

3.1.2 Particle-Based Methods in DMP

Particle-based modelling is based on the principle that the system is represented by particles that move according to the Newtonian equation of motion (vectors are represented in bold in this thesis),

$$m_i \frac{d\mathbf{v}_i}{dt} = m_i \frac{d^2\mathbf{r}_i}{dt^2} = \sum_{i \neq j} \mathbf{F}_{i,j} + \sum \mathbf{F}_E \quad (3.1)$$

where m_i is the mass, \mathbf{v}_i the velocity and \mathbf{r}_i the position of particle i . \mathbf{F}_E are the external forces and $\mathbf{F}_{i,j}$ are the internal or inter-particle forces of particles i and j .

The Discrete Multiphysics (DMP) simulation technique is used to study multi-physics problems. In DMP, different particle-based modelling techniques such as Smoothed Particle Hydrodynamics (SPH), Lattice Spring Model (LSM), also known as Mass Spring Model (MSM) in the literature and Discrete Element Method (DEM), are coupled, following the same framework and algorithm structure.

All these particle-based methods use the same sequence in their algorithm: definition of the boundary conditions and calculation of the internal and external forces (Figure 3.3).

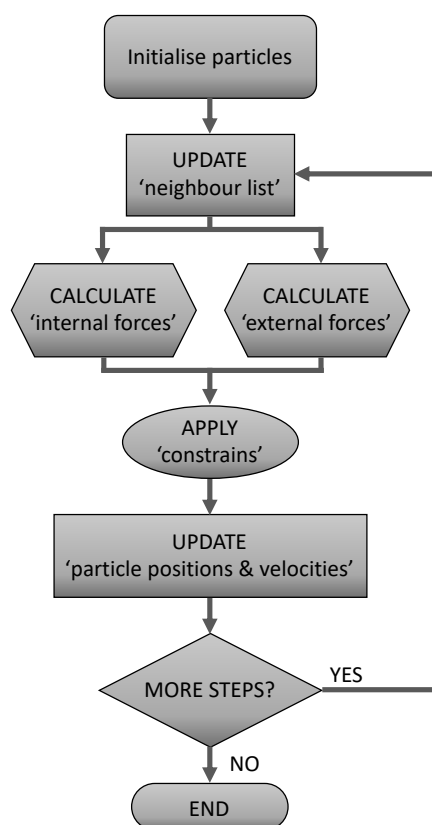


Figure 3.3 Structure of a typical particle-based algorithm (modified from (Alexiadis, 2015a))

In the various particle-based modelling techniques, the internal forces differ according to the area of application of the particular technique: In SPH, the internal forces represent the hydrodynamic forces (i.e., viscous and pressure forces); in LSM, the deformation forces (i.e., interaction forces between two particles) and in DEM the collision forces (i.e., contact forces between two colloid particles).

The models developed in this thesis only account for SPH and LSM, where treatment of the fluid is implemented with the SPH (Liu and Liu, 2003, Gingold and Monaghan, 1977), and the solid structures with LSM (Kot et al., 2015, Lloyd et al., 2007, Pazdniakou and Adler, 2012, Kot, 2021) and the interaction solid-liquid with the DMP (Alexiadis, 2015a).

3.1.3 Smoothed Particle Hydrodynamics

3.1.3.1 Introduction

This chapter aims to introduce the basics of SPH. The SPH method is a Lagrangian particle method first developed and introduced by Lucy and Gingold and Monaghan independently in 1977 (Lucy, 1977, Gingold and Monaghan, 1977). Initially, SPH was used to capture astrophysical problems. However, the SPH method was further developed and successfully applied to a broad range of applications, including multifluid flows, free-surface flows, solid mechanical applications, and elastic bodies (Monaghan, 2012, Alexiadis, 2015a).

3.1.3.2 Fundamental Equations of SPH

The SPH equations of motion result from the discrete approximations of the Navier-Stokes equation at a set of points. This set of points results from the discretisation of the continuum domain and can be thought of as particles. The particles are characterised by their mass, velocity, pressure, and density. SPH is based on the mathematical identity, which can be represented in the *integral representation* or also called *kernel approximation*:

$$f(\mathbf{r}) = \iiint f(\mathbf{r}')\delta(\mathbf{r} - \mathbf{r}')d\mathbf{r}', \quad (3.2)$$

where $f(\mathbf{r})$ is any scalar function defined over the volume V . The vector \mathbf{r} is a three-dimensional point in V . $d(\mathbf{r})$ is the three-dimensional Dirac delta function which is approximated in the SPH formulations by a smoothing function $W(\mathbf{r} - \mathbf{r}', h)$, where W is the so-called *smoothing kernel function* with a characteristic width or smoothing length h describing the influenced area of the smoothing function, which is also called the support domain or neighbouring domain. The smoothing function W can be assumed to be similar to a Gaussian function (Monaghan, 1992) and should satisfy the following conditions:

$$\iiint W(\mathbf{r} - \mathbf{r}', h) d\mathbf{r}' = 1 \quad (\text{normalisation or unity condition}), \quad (3.3)$$

$$\lim_{h \rightarrow 0} W(\mathbf{r} - \mathbf{r}', h) = \delta(\mathbf{r} - \mathbf{r}') \quad (\text{limit condition}), \quad (3.4)$$

$$W(\mathbf{r} - \mathbf{r}', h) = 0 \quad \text{when} \quad |\mathbf{r} - \mathbf{r}'| > h \quad (\text{compact condition}). \quad (3.5)$$

A schematic representation of the supporting domain of the smoothing kernel function W is shown in Figure 3.4.

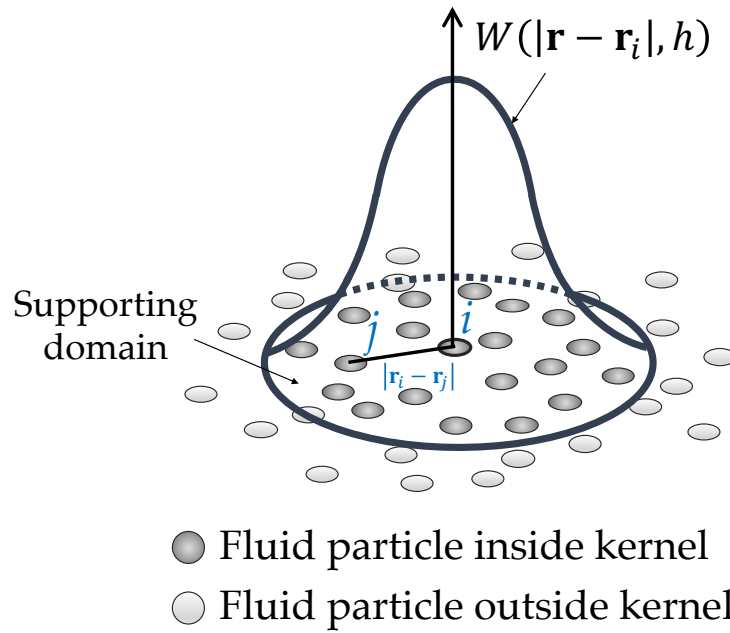


Figure 3.4 Schematic representation of the kernel function W and the support domain of the smoothing kernel function for the particle of interest i .

By replacing the delta function by a kernel or smoothing function W , the approximation to the function $f(\mathbf{r})$ (Equation 3.2) results in

$$f(\mathbf{r}) \approx \iiint f(\mathbf{r}')W(\mathbf{r} - \mathbf{r}', h)d\mathbf{r}'. \quad (3.6)$$

By discretising over a series of particles of mass $m = \rho(\mathbf{r}')d\mathbf{r}'$, and summing up the nearest neighbour particles, the identity equation (Equation 3.6) results in the *particle approximation* (Monaghan, 1992):

$$f(\mathbf{r}) \approx \sum_i \frac{m_i}{\rho_i} f(\mathbf{r}_i)W(\mathbf{r} - \mathbf{r}_i, h), \quad (3.7)$$

where m_i and r_i are the mass and density of the i^{th} particle, respectively, and i ranges over all particles within the smoothing kernel W (i. e. $|\mathbf{r} - \mathbf{r}_i| < h$).

3.1.3.3 Smoothing Kernel Functions and Smoothing Length h

The simulations in this thesis are performed using the original Lucy kernel function (Lucy, 1977):

$$W(\mathbf{r} - \mathbf{r}_i, h) = \alpha_d \left[1 + 3 \frac{|\mathbf{r} - \mathbf{r}_i|}{h} \right] \cdot \left[1 - \frac{|\mathbf{r} - \mathbf{r}_i|}{h} \right]^3 \quad \text{for } |\mathbf{r} - \mathbf{r}_i| \leq h, \quad (3.8)$$

$$W(\mathbf{r} - \mathbf{r}_i, h) = 0 \quad \text{for } |\mathbf{r} - \mathbf{r}_i| > h,$$

where $\alpha_d = 5/4h$, $5/\pi h^2$ and $105/16\pi h^3$ in one, two and three dimensions, respectively.

The Lucy kernel function has been successfully used in previous studies simulating water (Lucy, 1977), cardiovascular flows (Ariane et al., 2017a, Ariane et al., 2018a, Ariane et al., 2017b) and intestinal contents with the same conditions used in this thesis (Alexiadis et al., 2017).

In literature, there are several kernel functions available. An overview and more details on other smoothing kernel functions can be found in (Liu and Liu, 2003).

The smoothing length h is an essential parameter in SPH simulations and directly influences the efficiency of the computation and the accuracy of the results. The smoothing length h multiplied by a factor κ determines the support domain in which the smoothing kernel function applies (Figure 3.5).

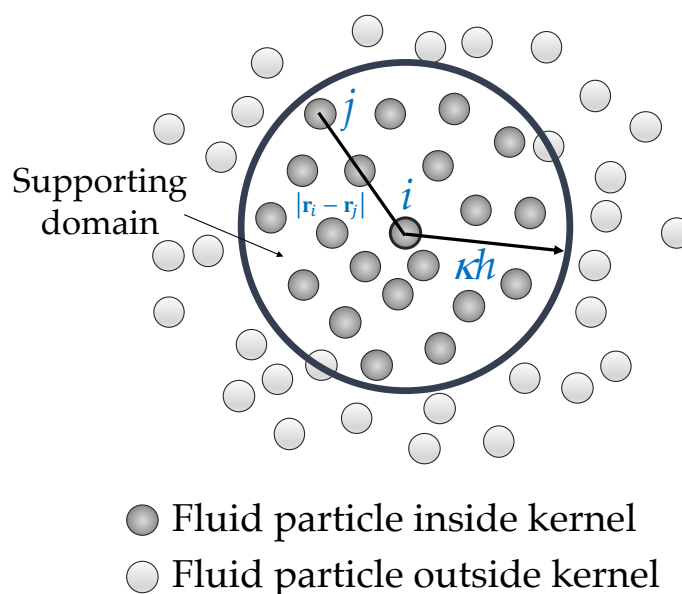


Figure 3.5 Schematic representation of the support domain with its kernel radius (smoothing length) κh of the smoothing kernel function and the particle of interest i .

Depending on the application, the smoothing length can either be constant, vary both temporarily or spatially, or even vary in dimensions. Here, the smoothing length is a scalar in 1D, a vector in 2D or a tensor in 3D (Liu and Liu, 2003). A too small h may result in a too small number of particles in the support domain κh to apply forces on a particular particle, resulting in low accuracy. This can also happen if the smoothing length h is too large and details of the particle or local properties are smoothed out. A good compromise can usually be achieved by setting the smoothing length to a value resulting in a number of neighbouring particles of about 5, 21 and 57 in one, two and three dimensions, respectively (Liu and Liu, 2003). In the simulations performed in this study, a constant smoothing length is used, and different values of h are tested for each study. The best value of h , which represents the best compromise between accuracy and computational times, has been selected.

3.1.3.4 Governing Fluid Dynamic Equations

The discrete approximation of a generic continuous field is represented by Equation 3.1 can be used to approximate the Navier-Stokes equation of motion

$$m_i \frac{dv_i}{dt} = \sum_j m_i m_j \left(\frac{P_i}{\rho_i^2} + \frac{P_j}{\rho_j^2} \right) \nabla_j W_{i,j} + \sum \mathbf{F}_E \quad , \quad (3.9)$$

where m is the mass, v the velocity, P the pressure, ρ the density, $W_{i,j}$ the concise form of $W(\mathbf{r}_j - \mathbf{r}_i, h)$, the term ∇_j the gradient of the kernel with respect to the coordinate r_j and \mathbf{F}_E the external forces. The density approximation is a decisive factor in the SPH method, as the density determines the particle distribution. In SPH, for the density approximation, two approaches are available (Monaghan, 1994). The first approach is the so-called *continuity density*

$$\frac{d\rho_i}{dt} = \sum_j m_j v_{i,j} \nabla_j W_{i,j} \quad . \quad (3.10)$$

where v_i is the velocity of particle i ($v_{i,j} = v_i - v_j$). The second approach for the density approximation is the so-called *summation density*, where the density of particle i is calculated from Equation (3.6). Here, the function $f(\mathbf{r})$ is substituted with the density ρ

$$\rho_i = \sum_j \frac{m_j}{\rho_j} W(\mathbf{r}_{i,j}, h) \quad . \quad (3.11)$$

The fluid in the SPH concept is often considered as weakly compressible (i.e., +/- 1% of the reference density) or incompressible.

To calculate the pressure forces between the particles representing the liquid, Tait's equation-of-state (EOS) of the form

$$P = \frac{c_0^2 \rho_0}{7} \left[\left(\frac{\rho}{\rho_0} \right)^7 - 1 \right] , \quad (3.12)$$

is used to link the density ρ and the pressure P , where c_0 is the reference speed of sound and ρ_0 is the reference density at zero applied stress. Tait's equation was also successfully used to simulate free-surface flows with SPH (Monaghan, 1994). The reference speed of sound is usually taken to be one order of magnitude larger than the maximal flow velocity to keep the density variations below 1% (Monaghan, 1994, Monaghan, 2005, Violeau and Issa, 2007):

$$c_0 \approx 10 v_{max} . \quad (3.13)$$

For the calculation of the pressure forces in a gaseous phase, the ideal-gas EOS is used to link the density ρ and the pressure P :

$$P(\rho, e) = (\gamma - 1)\rho e . \quad (3.14)$$

Here, e is the thermal energy and γ is the polytropic index, which depends on the material. This study uses a value for γ of 1.4 (corresponding to dry air).

3.1.3.5 Viscous Term

For the simulation of shock waves, the original SPH formulations led to excessive unphysical oscillations of the numerical results of the shock front, which had to be treated differently or with a different method (Monaghan and Gingold, 1983). This was achieved by simulating the conversion of kinetic energy into heat energy. This energy transversion is physically similar to viscous dissipation (Liu and Liu, 2003). In the mathematical framework, the momentum equation (Equation (3.9)) is extended by a viscous term $\Pi_{i,j}$, which is the so-called artificial viscosity

$$m_i \frac{dv_i}{dt} = \sum_j m_i m_j \left(\frac{P_i}{\rho_i^2} + \frac{P_j}{\rho_j^2} + \Pi_{i,j} \right) \nabla_j W_{i,j} + \sum \mathbf{F}_E \quad . \quad (3.15)$$

There are various expressions for the tensor $\Pi_{i,j}$ available in the literature. In this thesis, two different expressions are used, as one of them is more suitable depending on the flow conditions (Ganzenmüller et al., 2011, Morris et al., 1997): for laminar flows, the form from (Morris et al., 1997) is used:

$$\Pi_{i,j} = \frac{(\mu_i + \mu_j) v_{i,j}}{\rho_i \rho_j \mathbf{r}_{i,j}} \quad , \quad (3.16)$$

where μ is the dynamic viscosity. In the case of turbulent flow conditions, the following form from (Monaghan and Gingold, 1983) is used:

$$\Pi_{i,j} = -\alpha h \frac{c_0}{\rho_{i,j}} \frac{v_{ij} \mathbf{r}_{i,j}}{\mathbf{r}_{i,j}^2 + b h^2} , \quad (3.17)$$

where ρ_{ij} is the density and v_{ij} the relative velocity of particle i and j , respectively. α is a dimensionless factor controlling the dissipation strength to obtain a stable simulation, and h is the smoothing length. The constant b is introduced and used with $b \approx 0.01$ to avoid unstable simulations. This is particularly the case with compact particles whose distance between each other is very small.

The artificial viscosity can be recognized as an effective kinematic viscosity ν . Depending on the desired effective kinematic viscosity in the simulation, the value of α can be calculated according to the following relation for the three-dimensional case (Monaghan, 2005), where c is the artificial speed of sound in the fluid:

$$\nu = \frac{\alpha h c}{10} . \quad (3.18)$$

3.1.4 Lattice Spring Model

The lattice spring model (LSM) is a simplified representation of complicated systems using discrete mass points (e.g., particles) connected by springs and arranged in a lattice. These systems are coarser than real atomic systems (Zhao et al., 2011). LSM models are used to model, e.g., solid bodies and soft bodies like deformable cells, vesicles, and capsules to replicate their physical behaviour and to access fracture and fracture propagation in different materials (Alexiadis, 2015a, Alexiadis, 2015b, Alexiadis et al., 2017, Ariane et al., 2017a, Ariane et al., 2018a, Ariane et al., 2017b,

Schütt et al., 2020, Ruiz-Riancho et al., 2021). LSM modelling is also used in the field of computer graphics and virtual reality (Kot et al., 2015). In literature, different names can be found for the LSM modelling technique, which is mathematically seen all identical and therefore interchangeable. The scale described in the respective literature gives the name of the model. Literature dealing with microscopic scale usually uses the term Coarse-Grained Molecular Dynamics (CGMD), whereas literature dealing with macroscopic scale usually uses the term LSM or Mass spring model (MSM) (Alexiadis et al., 2017).

Molecular Dynamics (MD) is a particle-based method (Frenkel and Smit, 2002) to simulate the movement of atoms and molecules and their interactions. The Newtonian equation of motion describes the motion of atoms and molecules in the classical MD:

$$m_i \frac{d^2 \mathbf{r}_i}{dt^2} = - \frac{\partial}{\partial \mathbf{r}} U_{tot}(\mathbf{r}_1, \mathbf{r}_2, \dots, \mathbf{r}_N,) + \sum F_E \quad , \quad (3.19)$$

where U_{tot} is the overall inter-atomic potential. The negative gradient presents the inter-atomic force $\mathbf{F}_{i,j}$ as shown in Equation (3.1). The inter-atomic potential can be divided into two subgroups which are: non-bonded and intramolecular. The non-bonded potentials can be represented by attractive or repulsive forces (e.g., Lennard-Jones potential, soft potential). Non-bonded potentials used in this thesis are discussed in Chapter 3.1.5.2. The intra-molecular potential can be divided further into three subgroups: bond potential, angle potential and dihedral potential. In this thesis, only the bond potential is used. The potential used in this thesis is the linear and so-called harmonic potential of the form:

$$U_{bond} = k_b(r - r_0)^2 \quad , \quad (3.20)$$

where k_b is the Hookean coefficient, and r_0 is the equilibrium distance of two particles in a lattice. The intramolecular potential shown in Equation (3.20) allow modelling of various mechanical material properties and physical phenomena like phase change. The bond potential (Equation (3.20) and Figure 3.6) is usually used to connect two atoms with a cohesion force and an equilibrium distance r_0 to mimic stretching and can therefore be used, for example, to model elastic materials (elastic modulus) like a membrane or biological cells.

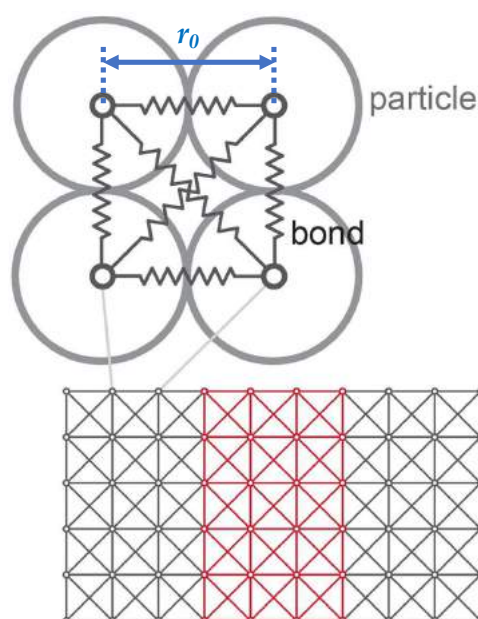


Figure 3.6 Schematic representation of the lattice spring model from its molecular origin (adapted from (Brely et al., 2015))

Originating from the representation of the molecular form as represented in Figure 3.6, where the atoms are arranged in a regular cubic lattice structure, LSM provides the opportunity to implement various material properties such as bulk modulus and Young modulus (Kot et al., 2015).

The breakage of a material or the melting can be achieved by implementing different threshold parameters (i.e., particle distance or temperature), which leads to the breakage of a bound if the threshold is exceeded. The same approach can be used for solidification but vice versa. If the specified condition is achieved, inter-particle bonds are created (Alexiadis, 2015a).

In some cases, the implementation of frictional interaction between two particles is necessary (i.e., to model Kelvin-Voigt materials, which are viscoelastic materials). This can be achieved by applying a viscous damping force to the interacting particles

$$F_{friction} = -k_v v_i , \quad (3.21)$$

where k_v is the viscous damping coefficient, and v_i is the velocity of particle i .

3.1.5 Coupling SPH-LSM: The Discrete Multiphysics

This thesis deals with fluid dynamics, fluid-structure interactions, and solid mechanics, representing a multi-physics problem. Discrete Multiphysics (DMP) is a modelling technique that couples different particle-based modelling techniques such as SPH and LSM. These modelling techniques are discussed in Chapters 3.1.3 and 3.1.4. Figure 3.7 represents an overview of the different particle interactions that need to be modelled with sub-set models in the DMP framework.

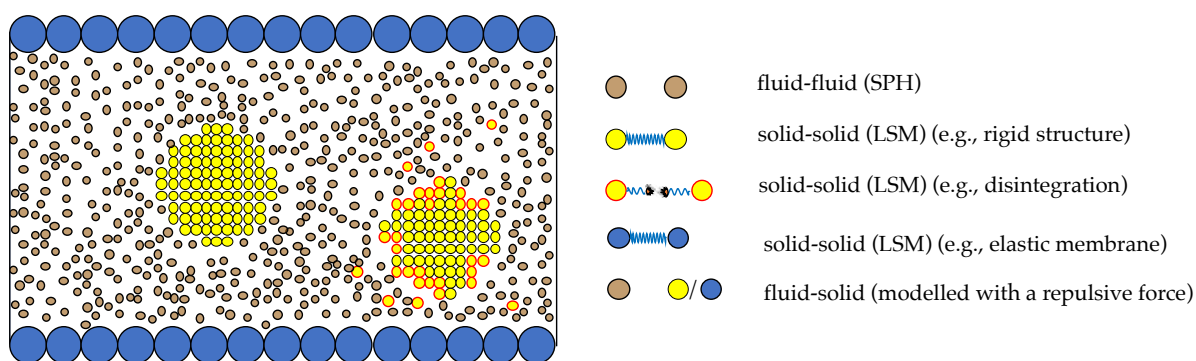


Figure 3.7 Types of particle interactions in the DMP framework (adapted from (Alexiadis, 2015a))

In this thesis, three different types of interactions can be defined in the DMP framework used: (type 1) fluid-fluid interactions modelled with SPH particles and relate to viscous and pressure forces (Equation (3.9) and (3.10)); (type 2) solid-solid interactions modelled with LSM particles, where bonds connect particles (Equation (3.20)); (type 3) fluid-solid interactions are modelled with repulsive forces (Equation (3.25) and (3.26)) to fulfil the following boundary conditions: no-penetration, no-slip, and continuity of stresses between the solid-fluid interface (see Chapter 3.1.5.1) (Alexiadis, 2015a).

3.1.5.1 Solid Boundary Conditions

Boundary conditions in particle methods are commonly modelled by the implementation of interaction forces between the solid and fluid particles to satisfy the following conditions, which are: no-penetration, no-slip, and continuity of stresses between the solid-fluid interface

$$\left(\frac{\partial}{\partial t} \mathbf{u} - \mathbf{v}\right) \cdot \mathbf{n} = 0 \quad (\text{no - penetration}) , \quad (3.22)$$

$$\left(\frac{\partial}{\partial t} \mathbf{u} - \mathbf{v}\right) \times \mathbf{n} = 0 \quad (\text{no - slip}) , \quad (3.23)$$

$$\sigma_s \mathbf{n} = \sigma_f (-|\mathbf{n}|) \quad (\text{continuity of stresses}) , \quad (3.24)$$

where \mathbf{u} is the displacement of the solid, \mathbf{v} is the velocity of the fluid and \mathbf{n} is the normal to the boundary. The stresses in the solid and fluid are represented by σ_s and σ_f , respectively (Alexiadis, 2015a, Müller et al., 2004).

If a solid is considered impermeable, the no-penetration condition ensures that no fluid particle is allowed to cross the solid/fluid boundary. Therefore, this condition ensures no mixing of different phases. This condition can be satisfied by implementing a repulsive interaction between the solid and fluid particles (see Chapter 3.1.5.2). With the no-slip condition, friction between the solid and fluid is modelled and can be achieved by overlaying the solid particles at the interface with a fluid ghost particle. Since particle methods satisfy the Newtonian equation of motion (Equation (3.1)), the continuity of stress is automatically satisfied.

3.1.5.2 Repulsive Interactions

The repulsive interactions in particle methods are often implemented using a repulsive Lennard-Jones potential. There are different forms of the Lennard-Jones potential

available in the literature. A purely repulsive form that is also often used is the following:

$$f(r) = D \left[\left(\frac{r_0}{r} \right)^{n_1} - \left(\frac{r_0}{r} \right)^{n_2} \right] \frac{r}{r^2}, \quad (3.25)$$

where r_0 is the initial distance between two particles, r is the actual particle distance, D is a constant chosen by the present physical configuration. The force goes to zero if $r > r_0$. The exponents n_1 and n_2 must fulfil the condition $n_1 > n_2$ and are often set to 4 and 2, respectively (Monaghan, 1994).

Another purely repulsive potential, which is often and also used in this thesis (here, e.g., to keep the fluid particles out of a tablet), is the so-called soft potential of the following form:

$$f(r) = A \left[1 + \cos \left(\frac{\pi r}{r_c} \right) \right] \quad \text{with } r < r_c, \quad (3.26)$$

where A is an energy constant. These potentials can be used between two fluid particles, between a fluid and solid particle or in some cases, between two solid particles. The latter case is sometimes used to model an ‘artificial pressure’ between stationary particles (e.g., wall particles) to avoid compenetration of solid and fluid particles (Albano et al., 2021, Violeau and Issa, 2007). When using several potentials between two particles, the interaction between these particles is calculated by additive superposition of the potentials used.

3.1.5.3 Stationary Particles

Fixed and, therefore stationary particles are commonly used to model, e.g., rigid solid walls, which should not move during the simulation. Thus, at every time step, time integration for the internal energy and the local density, but not for the position and velocity of the particles, is performed. In this thesis, the fixed particle approach is used, for example, to model the pressure probe in the colon and the modelling of the standardised dissolution apparatus mini-USP II (i.e., modelling of the vessel).

3.1.6 Mass Transfer

The SPH framework can be used to include mass transfer into DMP. Mass transfer can be used to model the variation of a specific concentration (e.g., the concentration of the Active Pharmaceutical Ingredient (API)). Therefore, a specific concentration is added to each individual particle. For a multi-component system, the diffusive mass balance can be written in the SPH framework in the following form (Alexiadis, 2015a):

$$\frac{dw_i}{dt} = - \sum_j \frac{m_i m_j (D_i + D_j)(C_i - C_j)}{\rho_i \rho_j r_{i,j}^2} r_{i,j} \cdot \nabla_j W_{i,j} , \quad (3.27)$$

where, w_i is the mass of the fluid in the particle, D_i is the diffusion coefficient of particle i and C_i is the concentration of the particle i . To close equation (3.27), m_i , C_i and r_i can be linked according to the following relation (Alexiadis, 2015a):

$$w_i = C_i \frac{m_i}{\rho_i} , \quad (3.28)$$

Now, each particle is characterised by its position, its velocity, its density, its pressure, and its concentration.

3.1.7 Model Design

3.1.7.1 Geometry Design and Particle Distribution

To generate the particle distribution for models with relatively simple geometries, the coordinates of the single particles can be created with the simulation software itself (e.g., LAMMPS (Albano et al., 2021, Ganzenmüller et al., 2011, Plimpton, 1995, Thompson et al., 2022)) using the integrated algorithm. Another alternative is to use standard programming codes such as MATLAB and Python. For complex geometries, pre-processing is required, for example, with Computer-Aided Design (CAD) software, where the structure of the model is constructed and meshed. The mesh is then replaced by particles whose coordinates are known.

3.1.7.2 Design of Different Contraction Patterns

The colon model consists of a cylindrical body, and the membrane is modelled by individual rings consisting of a defined number of particles. Each of these rings represents a circular muscle fibre of the colon that can be activated independently or

in groups. The contraction or descending inhibition (DI) is modelled by applying a radial force to the membrane particles. DI is a feature of a HAPW in which the area in front of the bolus actively relaxes, increasing the diameter of the colon (Sarna, 2010). Depending on how the rings are activated, waves can be modelled in antegrade direction, retrograde direction, and individual single contractions.

Furthermore, the antegrade and retrograde waves can be modelled in two ways: a smooth wave achieved by ring-wise contraction, or segment-wise, which requires that the colon is divided into segments. The advantages resulting from the particle-like structure of the model make it possible to mimic any motility pattern found in the colon, including contraction velocity, relaxation velocity, degree of occlusion, and wave speed. Material properties such as the viscoelastic behaviour of the membrane can also be implemented.

3.1.7.3 Design of Solid Dosage Form (Tablet)

As discussed in Chapter 2.1.3, different types of solid dosage forms and consequently different disintegration/dissolution mechanisms are available. This thesis focused on the disintegration mechanism of a tablet comparable with an extended-release (ER) tablet whose coating disintegrated in the upper gastrointestinal and small intestinal environment. Once it reaches the colon, the ER tablet behaves like an immediate-release (IR) tablet, which dissolves/disintegrates immediately in the colonic fluid.

The shape and size of the tablet (e.g., cylindrical, round, rectangle, capsule oval) and the number of particles representing the Active Pharmaceutical Ingredients (API) or excipients are adaptable to the desired conditions. Pharmaceutical excipients are

substances that, for example, in solid dosage forms, support the manufacturing process and support/enhance the stability of the tablet. They can also support bioavailability but are not responsible for the direct therapeutic effect (Haywood and Glass, 2011).

The solid dosage forms used in this thesis are modelled as follows: The solid dosage form is discretised in a defined number of particles with adjacent particles connected with linear and diagonal, breakable bonds to achieve a rigid structure. Figure 3.8 (a) shows a schematic representation of the linear bonds between two neighbouring particles d_l and the diagonal bonds d_d . If two particles move too far apart and exceed a predefined distance d_{max} , the bond breaks, and the tablet disintegrates. This mechanism is shown in Figure 3.8 (b).

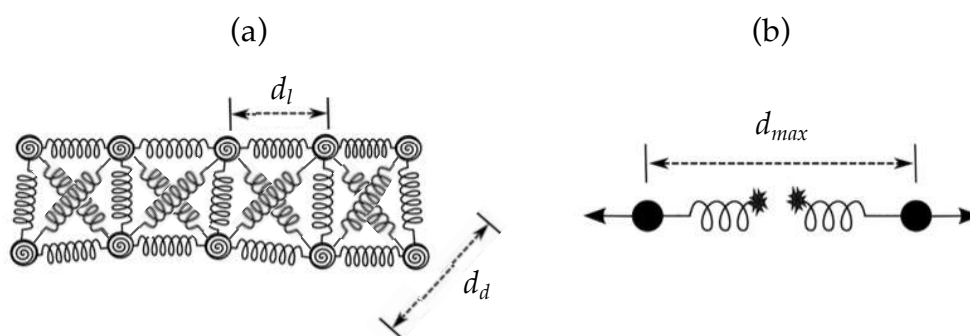


Figure 3.8 Modelling of the tablet using LSM: (a) linear and diagonal bonds with a harmonic potential, (b) bond breaks if the distance between two particles is larger than the threshold distance d_{max} (modified from (Alexiadis, 2015a))

For the case that the tablet contains 100% drug (i.e., API), a specific concentration is set to each of the tablet particles. The bonds between the bonded particles break according to predefined conditions/thresholds (e.g., API concentration of proximal particles or/and particle distance caused by shear stress) and thus replicate the disintegration process of a solid dosage form. The dissolution of the Active Pharmaceutical

Ingredient is modelled with a second predefined threshold. When the concentration of a drug particle falls below this threshold, the type of the particle changes (i.e., from a solid tablet particle to a fluid particle) and behaves like a fluid particle from then on. When excipients are added to the tablet, a concentration is only set to the particles representing the drug. The particles representing the excipients are inert, meaning they are not involved in any mass transfer processes (i.e., dissolution) during tablet disintegration/dissolution. The excipients help the tablet to retain its shape. As soon as the active ingredient has dissolved or the tablet loses stability due to the dissolution process, the excipients are automatically released and float in the fluid. Also, with this type of tablet, the disintegration/dissolution process is modelled in the same way as with a pure drug tablet.

Chapter 4

Modelling and Simulation of the Hydrodynamics and Mixing Profiles in the Human Proximal Colon using Discrete Multiphysics

Published article:

Computers in Biology and Medicine 121 (2020)

4.1 Abstract

The proximal part of the colon offers opportunities to prolong the absorption window following oral administration of a drug. In this work, we use computer simulations to understand how the hydrodynamics in the proximal colon might affect the release from dosage forms designed to target the colon. For this purpose, we develop three different models and compared: a completely-filled colon, a partially-filled colon and a partially-filled colon with a gaseous phase present (gas-liquid model).

The highest velocities of the liquid were found in the completely-filled model, which also shows the best mixing profile, defined by the distribution of tracking particles over time. No significant differences with regard to the mixing and velocity profiles were found between the partially-filled model and the gas-liquid model. The fastest transit time of an undissolved tablet was found in the completely-filled model. The velocities of the liquid in the gas-liquid model are slightly higher along the colon than in the partially-filled model. The filling level has an impact on the existing shear forces and shear rates, which are decisive factors in the development of new drugs and formulations.

4.2 Introduction

Whilst a significant amount of research has already been carried out on drug delivery in the gastrointestinal (GI) tract (e.g., Ref. (Goffredo et al., 2016)), the colon has received less attention (Prasanth et al., 2012). For colonic delivery, dosage forms generally target the ascending colon due to its less variable transit times (measured with radiotelemetry capsule), and higher volumes of less viscous fluids available compared

to the transverse and descending parts of the colon (Christensen, 1994, Kumar et al., 2012, Watts and Illum, 1997).

Peristaltic muscle contractions in the colon causes motion of the intestinal content resulting in tangential and perpendicular forces that act as shear and normal stresses on the surface of a dosage form (e.g., tablet) (Abrahamsson et al., 2005). Modified release dosage forms are formulated to be slowly eroding or swelling matrix systems where the rate of drug release is controlled by fluid ingress/erosion of the tablet thus the hydrodynamic environment will influence their rate of drug release (Alvarez-Fuentes et al., 2004, Markl and Zeitler, 2017, Nokhodchi et al., 2012).

The study of the fluid dynamics and fluid mechanics of the proximal colon, therefore, is paramount to understand the disintegration/erosion of dosage forms as well as the dissolution and diffusion of the released drug. In this regard, computational fluid dynamics has been proven as a valuable investigation tool (e.g., Ref. (Alexiadis et al., 2017, Sinnott et al., 2012, Sinnott et al., 2015)) since it can achieve a level of detail that it is not possible by direct visualisation of the actual human colon. However, with one exception (Alexiadis et al., 2017), all computational studies performed so far (e.g., Ref. (Sinnott et al., 2012, Sinnott et al., 2015)) refer to a colon completely filled with liquid, whereas most of the time, the colon is only partially filled with liquid/solid material (Schiller et al., 2005). Some studies found a freely mobile liquid volume from 0 to 49 mL in the entire colon, whereby most of the free liquid was found in the ascending colon (Murray et al., 2017, Schiller et al., 2005). Gases are also present in the colon due to swallowed air, blood gases diffusion through the intestinal membrane, and bacterial fermentation (Askevold, 1956, Cummings et al., 1987, Kurbel et al., 2006). The volume of gases in the proximal colon can be significant: one study (Diakidou et al., 2009), for instance, measured about 90% gas and 10% liquid/solid material. However, to the

best of our knowledge, so far, no modelling work, has account for the presence of gasses in the colon.

In this paper, we use an approach similar to Alexiadis et al. (Alexiadis et al., 2017) applied to three models describing and comparing the hydrodynamics in a completely-filled colon (liquid), a partially-filled colon (liquid) and a multiphase (gas + liquid) partially-filled colon. The intestinal content is propelled by a peristaltic wave. The hydrodynamic results are used to evaluate the affects they have on different dosage forms and to visualise how an undissolved dosage form (tablet) will behave in the different models.

4.3 Methodology

4.3.1 Modelling Approach

The simulations in this study are based on Discrete Multiphysics (DMP), a modelling technique also used in Alexiadis et al. (Alexiadis, 2015a, Alexiadis, 2015b, Alexiadis et al., 2017) and Ariane et al. (Ariane et al., April 2016, Ariane et al., 2017a, Ariane et al., 2018a, Ariane et al., 2017b). DMP is based on coupling various particle-based modelling techniques such as Smoothed Particle Hydrodynamics (SPH), Lattice Spring Model (LSM), and the Discrete Element Method (DEM). Theoretical insights on DMP are discussed in Alexiadis et al. (Alexiadis, 2015a, Alexiadis et al., 2017). In this study, the model accounts only for SPH and LSM. The theory for SPH can be found just in Ref. (Liu and Liu, 2003) and for the LSM in Ref. (Kot et al., 2015, Lloyd et al., 2007, Pazdniakou and Adler, 2012).

4.3.2 Model Geometry

In our 3D model, we investigated the proximal colon of an adult human. The geometry used is a cylindrical body with a total length of 60 cm, a diameter of 5 cm and open ends. Periodic boundary conditions were used at each end, which means that the fluid exiting the tube on one side re-enters from the other one; this is to mimic the real-world situation of continuous transit through the colon.

The modelling of the peristaltic wave and the colonic motility is described in 4.3.4.

Discrete Multiphysics is based on coupling various particle-based modelling techniques. In this study, SPH is used for the fluids (both liquid and gas) and LSM for the elastic membrane of the colon. For the recording of the manometric data, we used in the model stationary SPH particles that mimic the presence of a real physical probe, to accurately replicate data obtained *in vivo*. In fact, in *in vivo* studies, manometric data are recorded using fibre-optic catheter with sensors spaced at 1 cm (Bampton and Dinning, 2013) or water-perfused catheters with pressure sensors spaced every 10 cm (Liem et al., 2012).

In Figure 4.1 (a) and (b), a schematic sketch of the model, including the probe, is shown. More details are given in Table 4.1 and Table 4.2.

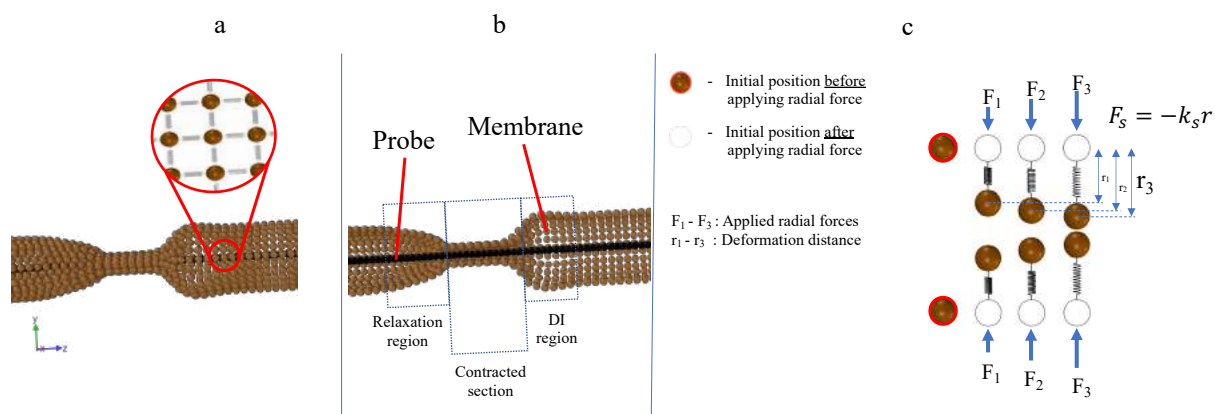


Figure 4.1 (a) and (b): 3D sketch of the flexible membrane, showing the contraction and expansion of the wall. The particles representing the membrane are connected by a network of springs. The probe (catheter) for pressure measurements is represented as black, stationary particles. (c) 2D Illustration of the elastic membrane with tethered springs at equilibrium state as well as after the application of three different radial forces (see Table 4.2 for details).

Table 4.1. Fundamental model parameters used in all simulations: for more details o the physical and mathematical meaning of the simulation parameters h , c_0 , k_b and k_v , the reader is referred to Ref (Kot et al., 2015, Liu and Liu, 2003, Lloyd et al., 2007, Pazdniakou and Adler, 2012).

Parameter	Value
SPH	
Number of SPH membrane particles (1 layer)	2,500
Number of SPH probe particles	134
Initial distance among particles Δr	6.28×10^{-3} m
Smoothing length h	9.42×10^{-3} m
Artificial sound of speed c_0	0.1 m s^{-1}
Time-step Δt	5×10^{-4} s
Density (liquid) $\rho_{L,0}$	1030 kg m^{-3}
Density (gas) $\rho_{G,0}$	1.2 kg m^{-3}
Dynamic viscosity (liquid) $\eta_{L,0}$	0.525 mPa s
Dynamic viscosity (gas) $\eta_{G,0}$	$1.84 \times 10^{-5} \text{ Pa s}$
LSM	
Hookian coefficient k_b (membrane)	0.2 J m^{-2}
Viscous damping coefficient k_v (membrane)	$1 \times 10^{-2} \text{ kg s}^{-1}$
Equilibrium distance r_0	6.28×10^{-3} m

Table 4.2. Specific model parameter for the different models.

SPH Parameter	Value
<i>Completely-Filled model (100% liquid volume)</i>	
Number of SPH liquid particles	29,728
Mass of each particle (solid)	3.9×10^{-4} kg
Mass of each particle (liquid)	3.2×10^{-5} kg
Radial contraction force F	1.280×10^{-3} N
<i>Partially-Filled model (40% liquid volume)</i>	
Number of SPH liquid particles	8142
Mass of each particle (solid)	3.9×10^{-4} kg
Mass of each particle (liquid)	2.42×10^{-5} kg
Radial contraction force F	0.942×10^{-3} N
<i>Partially-Filled with a gaseous phase present (40% liquid and 60% gas volume)</i>	
Number of SPH liquid particles	8,188
Number of SPH gas particles	627
Mass of each particle (solid)	3.9×10^{-4} kg
Mass of each particle (liquid)	3.9×10^{-5} kg
Mass of each particle (gas)	4.55×10^{-7} kg
Radial contraction force F	0.9677×10^{-3} N

4.3.3 Model and Simulation Parameters

In our model, the membrane is built of 2,500 LSM particles spaced of 6.28×10^{-3} m and its particles are anchored to their initial position with a Hookean force (Figure 4.1 (c)). The structure and hence the number of membrane particles is a compromise between complexity and performance (i.e., computational resources and run time) of the model. The number of SPH particles representing the fluid varies due to the different filling levels from model to model as shown in Table 4.2. According to Diakidou et al. (Diakidou et al., 2009), the volume of liquid/solid material in the ascending colon is

about 10%. Standardised dissolution tests are performed with a liquid volume of about 900 mL (Long and Chen, 2009). This corresponds to a filling of the proximal colon of about 80%. As a compromise between the results of the study and dissolution tests currently performed, we have chosen a filling level of 40% fluid for the partially-filled model (Table 4.2).

The number of fluid particles used in the particular models is the result of several simulations performed with different resolutions. Between these simulations we compared the velocity fields obtained for the completely-filled colon and selected the simulation with approximately 30,000 fluid particle as the best compromise between accuracy and shorter computational times.

The probe records the pressure along the tube every 2.5 cm. This distance was chosen to get a reasonable pressure profile for the comparison of our model with experimental data.

In our model, we used a liquid inside the colon with a similar viscosity to the fluids used for *in vitro* studies in the literature, see Table 4.1 (Stamatopoulos et al., 2016b). Although in the real case the fluid is likely to be non-Newtonian, in this work, for simplicity, it is assumed Newtonian.

For the evaluation of the influence of a gaseous phase we used the partially-filled model and added SPH particles, representing the gas. The pressure of the gaseous phase in the colon is not well known. According to Kurbel et al. (Kurbel et al., 2006), the total gas pressure due to bubble formation in the colon is at atmospheric pressure or slightly above. In the model, we assume a gauge pressure of 60 Pa. Chemically, the model assumes that the gas phase is comparable to dry air and follows the ideal gas equation of state: technically speaking this is not true, but given the small gauge

pressure, we assume that this is an acceptable simplification. Gravitational acceleration in the y -direction is also added to all particles.

For the simulations in this study, we used three different models: a completely-filled colon, a partially-filled colon and a gas-liquid model. The numerical values we used for the different models and simulations are listed in Table 4.1 and Table 4.2.

4.3.4 Colon Contraction

The effect of the contraction of the colonic muscles upon the motion of the fluid inside the colon was investigated through the simulations. In humans, there are different patterns (waves), caused by the contraction the circular and the longitudinal muscle layers which form the membrane of the colon. Here, we focus on the High Amplitude Propagating Pressure Wave (HAPW) (Christensen, 1989, Sarna, 2010), which transports the digested materials along the colon. The contraction of the circular muscle cells leads to a partial or complete occlusion of the lumen, and therefore creating effective mixing as they propagate. The contraction of the longitudinal muscle leads to a shortening of the length of the colon and has thus minimal mixing and propulsive functions (Sarna, 2010). The actual shape of a peristaltic wave is still unknown and therefore is estimated according to the data available. For simplicity, and the limited influence of the longitudinal muscle, in respect to mixing and propulsion of the intestinal content (Sarna, 2010), the contraction itself is modelled as a local contraction/activation of the circular muscle which propagates along the colon. The contraction wave (peristalsis) is modelled according to manometric measurements of HAPWs, which show a contraction time of about five seconds (Chen et al., 2017)

and a propagation velocity of about one metre per second (Bassotti and Gaburri, 1988, Liem et al., 2012, Sarna, 2010). The HAPW is the only wave type that always occludes the lumen completely and additionally produces a feature called Descending Inhibition (DI), where the region in front of the bolus actively relaxes (Sarna, 2010). These characteristics were also implemented in the model; the contraction is modelled by applying a radial force to the membrane particles that, in our simulation, is represented by a ring of 25 particles. Each ring represents one circular muscle fibre, which can be activated independently. The numerical value of the radial force is chosen to allow full closure of the intestinal lumen avoiding interpenetration of the membrane and probe computational particles, which would result in sudden and unrealistic pressure peaks. The same HAPW is used in all three models.

4.4 Software

The open-source code LAMMPS (Ganzenmüller et al., 2011, Plimpton, 1995) is used for the numerical calculations. The open-source code of OVITO (Stukowski, 2010) is used for the visualisation and postprocessing of the simulation data.

4.5 Results and Discussion

4.5.1 Comparison with manometric data and other studies

To assess the model, we compared our recorded pressures with the pressure profiles from experimental manometric measurements (Bassotti and Gaburri, 1988). The absolute pressure is different because our model refers to a shorter section of the colon with periodic boundary conditions.

Therefore, in Figure 4.2 we compare the experimental data with the simulations based on relative pressure:

$$p^* = \frac{p}{p_0} \tag{4.1}$$

where p is the experimental or simulation pressure (Pa) and p_0 the reference pressure, which is the maximum pressure in the experiment (16,430 Pa) and in the simulation (1,260 Pa).

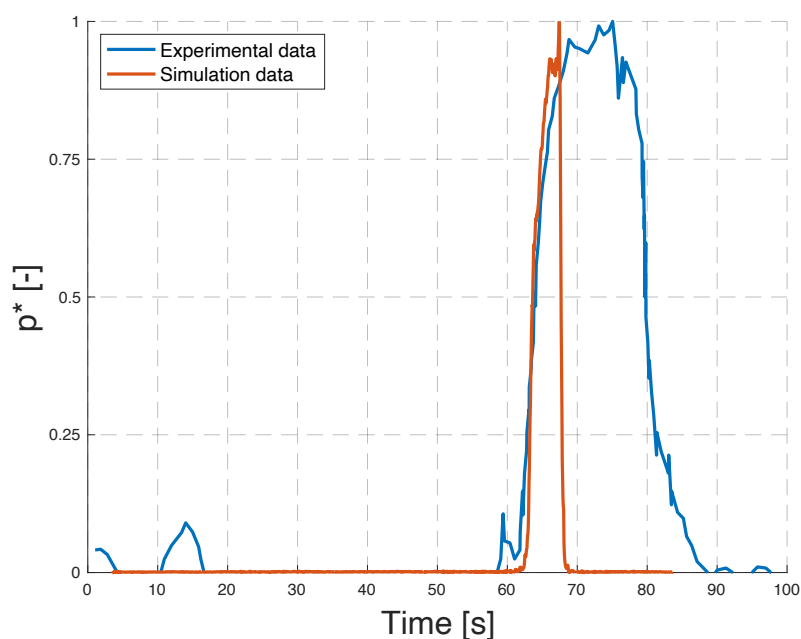


Figure 4.2 Comparison between manometric measurements from Ref. (Bassotti and Gaburri, 1988), and simulation data from our completely-filled model.

The pressure peak in the manometric data and in the simulations is similar (Figure 4.2). However, it looks like the contraction in the simulation is cut short with respect to the manometric data. In our model, the contracting section (Figure 4.1 (b)) is around three times shorter than the real one (Bassotti and Gaburri, 1988). This is due to the periodic boundary conditions; in fact, if the contracting section is too large, there would be not enough room for the displaced liquid. However, this difference is only expected to affect the length of the contracting section and not the hydrodynamics in the relaxing region, the DI region (Figure 4.3) and along the colon.

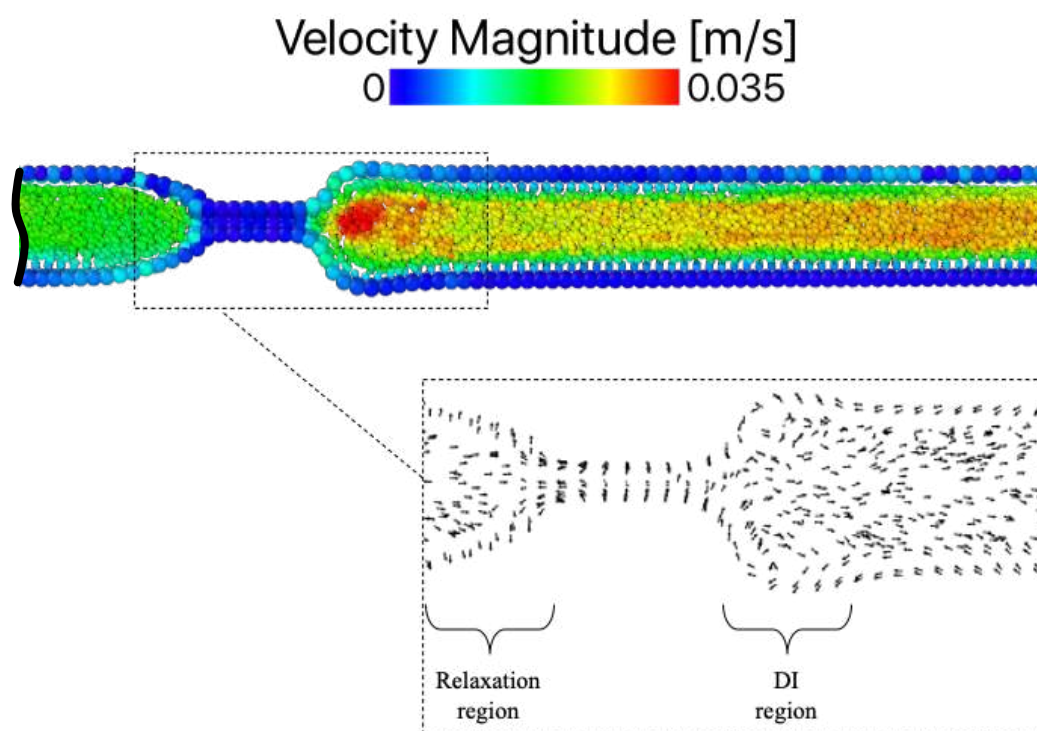


Figure 4.3 Representation of a peristaltic wave. In the enlarged section, the formation of a vortex is shown in a vector representation, where the direction of the vectors indicates the flow direction respectively

Figure 4.3 shows an example of a peristaltic contraction travelling in antegrade direction (in our model, from left to right). The higher velocities are in the DI region, directly in front of the peristaltic wave. In this region, we can observe the formation of a vortex under peristaltic flow conditions as also reported by other studies (Connington et al., 2009, Sinnott et al., 2012).

4.5.2 Comparison of completely-filled model with partially-filled model

The magnitude of the applied contraction force is in the partially- filled model smaller than in the completely-filled model to achieve the same pressure measurements. This is due to the fact that fully- contracting a partially-filled colon, in fact, is easier than

contracting a completely full colon. The partially-filled model also shows the formation of vortices as presented in Figure 4.4.

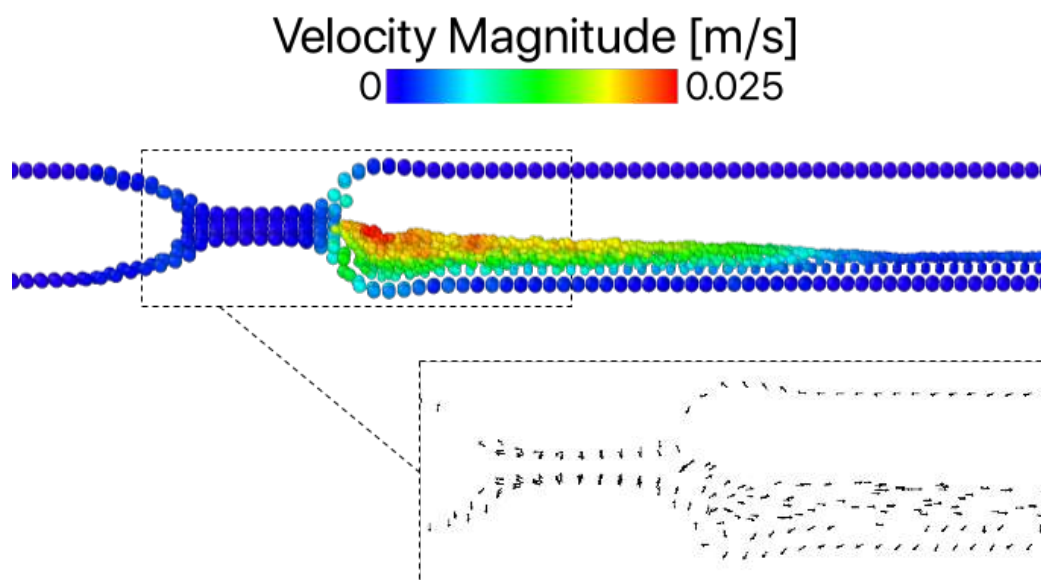


Figure 4.4 Representation of a peristaltic wave in the partially-filled model. The enlarged section shows the formation of a vortex in the DI region

Compared to the completely-filled model the velocities are smaller. As shown in Figure 4.5, the velocities of the liquid particles are in both models different. They differ in magnitude as well as in the distribution over time.

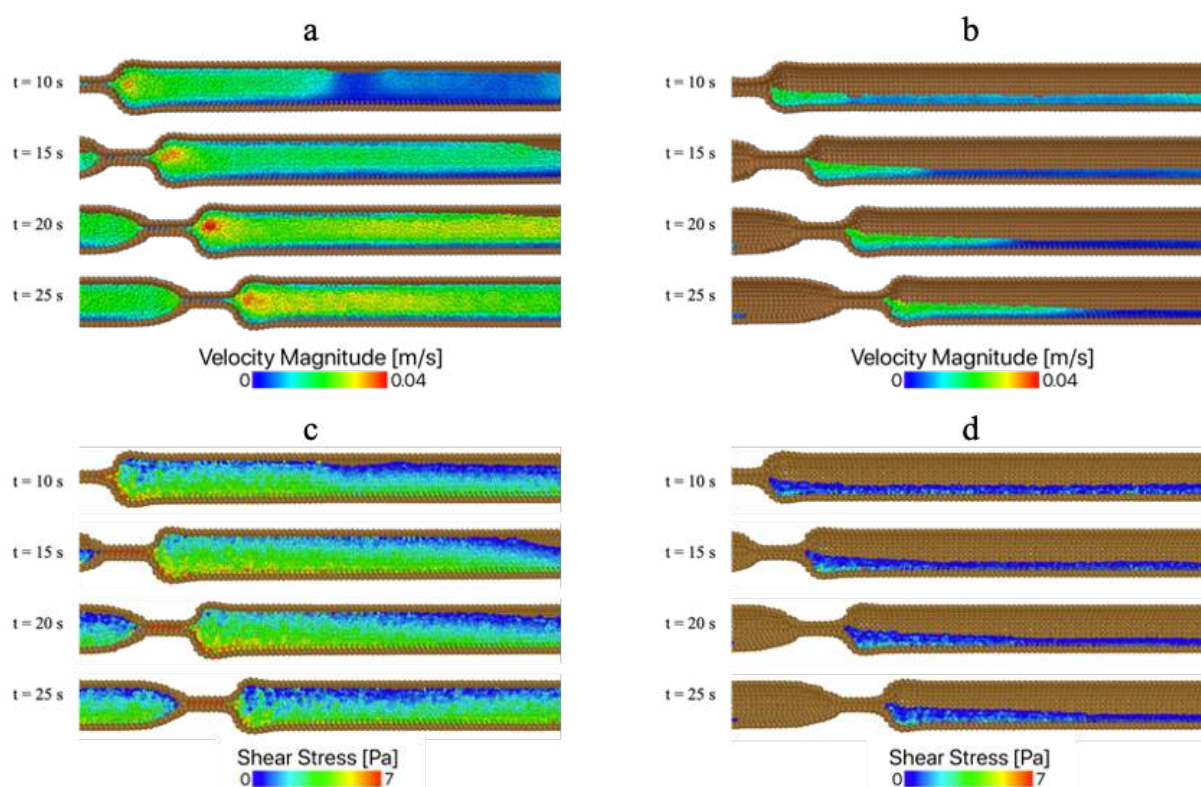


Figure 4.5 Comparison of a peristaltic wave with content coloured by the velocity magnitude and shear stress, where (a) and (c) show the completely-filled model and (b) and (d) the partially-filled model.

The highest velocities in the completely-filled model arise in the centre of the tube, while in the partially-filled model the highest velocities occur on liquids free surface. Moreover, the vortex in the completely-filled model Figure 4.5 (a)) is more pronounced than in the partially-filled model (Figure 4.5 (b)), which we can be trace to the higher velocities found in the DI region.

Also, the shear stresses in the completely-filled model (Figure 4.5 (c)) are higher than in the partially-filled model (Figure 4.5 (d)). In both models, the highest shear stresses are found in the lower part of the DI region where the contraction leads to an active movement of the membrane and pushes the fluid. The shear rates that occur are not presented here because we assumed that the fluid is Newtonian and therefore shear rate and shear stress are proportional.

These results provide insight into the disintegration of a solid dosage form, e.g., tablets and thus the release of drug particles containing the Active Pharmaceutical Ingredient (API). The shear stress is a critical parameter (Lee, 2003) and a higher shear stress acting on the tablet leads to a faster breakage and a corresponding faster release of the API. Once the API has been released the mixing profile is important for the distribution of the API and thus has a direct influence on the successful treatment.

We analyse the mixing in the system by looking at the dispersion of tracking particles with the same properties of the fluid: a passive scalar like the concentration of a dissolving drug will follow the same streamlines of the tracking particles. For this reason, Figure 4.6 gives an idea on how a dissolving drug will mix in the luminal content. To give a visually representation of the difference in the mixing performance of both models, we track the evolution of a group of fluid particles (red particles in Figure 4.6).

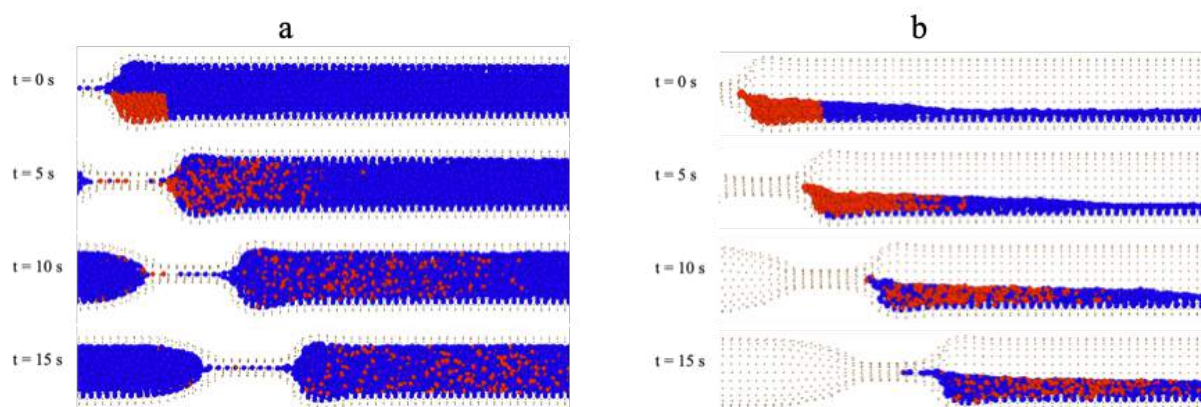


Figure 4.6 Mixing profile of (a) completely-filled model and (b) partially-filled model with tracking particles (red coloured) at different time-steps.

The results may be summarised thus:

- After 5 seconds, the distance travelled by the tracking particles is almost identical in both models.

- After 10 seconds, the tracking particles in the completely-filled model cover a distance of about 20% more than in the partially-filled model and the particles in the completely-filled model are more spread out.
- After 15 seconds, in the completely-filled model, the particles are uniformly distributed, while the partially-filled model still shows some patches of higher concentration.

Drugs and medicines are administered in a wide variety of forms as tablets, as capsules, as granulates, as a liquid or as a foam (Friend, 2005, Pithadia and Jain, 2011). Some of these forms (e.g., emulsions and suspensions of micro- and nano particles in which the API is finely dispersed) are dispersed in the luminal content and, therefore, behave like the tracking particles discussed above.

Studies with a time dependent API release showed an increase in IBD treatment success (Lamprecht et al., 2001). A time depending release results in a low but constant API concentration along the colon which is comparable with the mixing profile of our completely-filled model. The tracking particle are distributed faster along the colon which results in an increased exposure time of API. In Figure 4.6, we discussed dosage forms that are finely dispersed in the luminal content.

The opposite scenario occurs when the drug is released slowly like the case of a tablet that is not very soluble in the luminal content. In Figure 4.7, we consider the extreme scenario of an insoluble tableted. The tablet is cylindrical with a diameter of 10 mm, a height of 5 mm and neutrally buoyant. Here we look at tablet with a regular shape that, in reality, will not have such a regular shape because it already passed through the stomach and the small intestine before reaching the colon. Figure 4.7 compares the

trajectory of the tablet among the completely-filled model, the partially-filled model and the gas-liquid model.

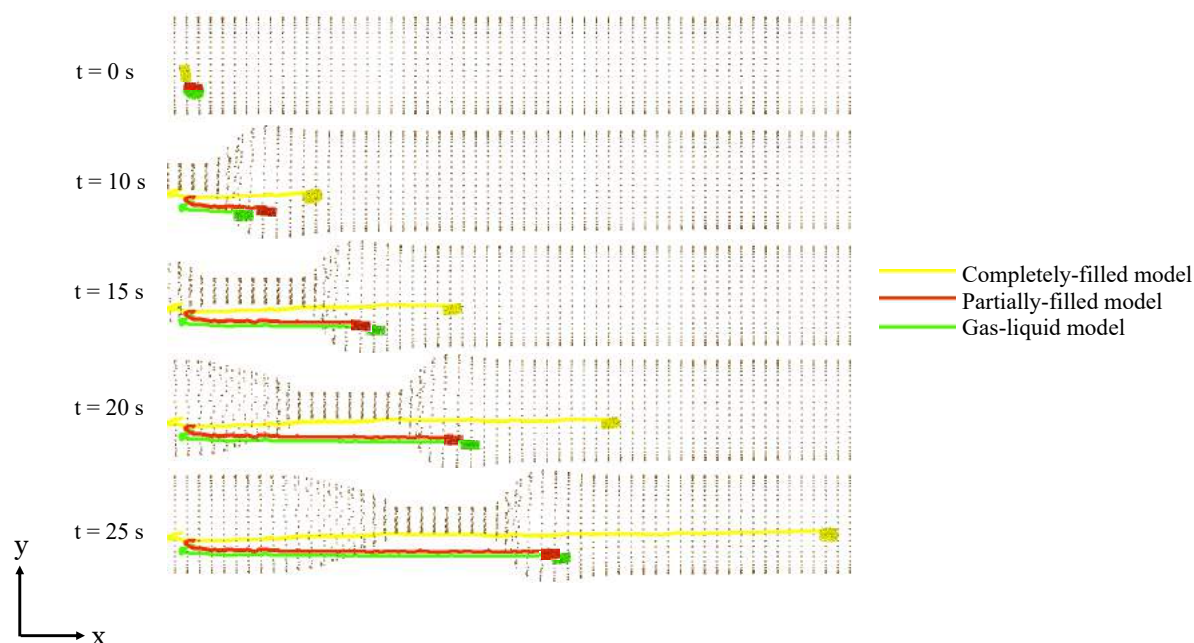


Figure 4.7 Visualisation of the time dependent trajectory of a tablet in the different models.

The trajectory of the tablet is recorded from the moment the peristaltic wave begins. In all models, the tablet initially moves slightly to the left before being pushed by the peristaltic wave in the direction of propagation.

In the completely-filled model, the tablet remains its initial y-position, whereas in the partially-filled model and the gas-liquid model the tablet is pushed by the peristaltic wave (swirl) to the bottom of the colon. The velocity of the tablet in the partially-filled model and the gas-liquid model are approximately equal. At the beginning (10 seconds) the velocity of the tablet in the partially-filled model is slightly higher than in the gas-liquid model, but this changes between 10 seconds and 15 seconds, so that the distance travelled by the tablet in the gas-liquid model is greater than in the partially-filled model. From 15 seconds on, the velocity of the tablet in the partially-

filled model and the gas-liquid model are about the same. The highest tablet velocity was found at all times in the completely-filled model.

As shown in Figure 4.5 (c) and (d) the highest existing shear stresses in the completely-filled and the partially-filled model are found in the lower part of the DI region (see Figure 4.1 (b)). From Figure 4.8 we can obtain that in the completely-filled model the neutrally buoyant tablet does not remain in the region of the highest shear stresses present (Figure 4.8 (a)), but rather in the centre of the colon where lower shear stress and fewer turbulence occur.

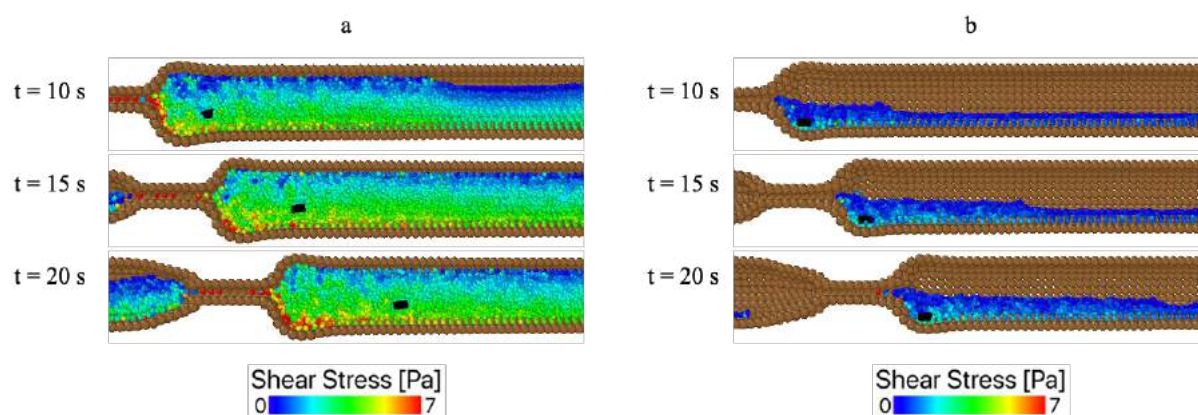


Figure 4.8 Visualisation of shear stresses occurring in the fluid and the location of a naturally buoyant tablet (black) in the completely-filled model (a) and the partially-filled model (b).

In the partially-filled model, the tablet is located in the DI region, where the highest velocities (Figure 4.5 (b)) and shear stresses (Figure 4.8 (b)) are present. For the maximum local shear stress acting on the tablet surface we found 0.24 Pa in the completely-filled model and 5.6 Pa in the partially-filled model. The magnitude of the shear stresses determined corresponds to the values found in other studies, which however focus on the stomach (Abrahamsson et al., 2005, Kindgen et al., 2015).

From the results, we can observe that the forces acting on the tablet and thus responsible for its disintegration depend to a large extent on the location of the tablet

in the colon. Although the highest shear stresses occur in the completely-filled model, higher shear stresses act on the surface of a tablet in the partially-filled model.

4.5.3 Influence of a Gaseous Phase Present

Figure 4.9 a) and (b) shows the particles representing the liquid and gaseous phase, respectively, coloured by the velocity magnitude, caused by a peristaltic wave at different timesteps. Figure 4.9 (c) represents the shear stress occurring in the liquid phase.

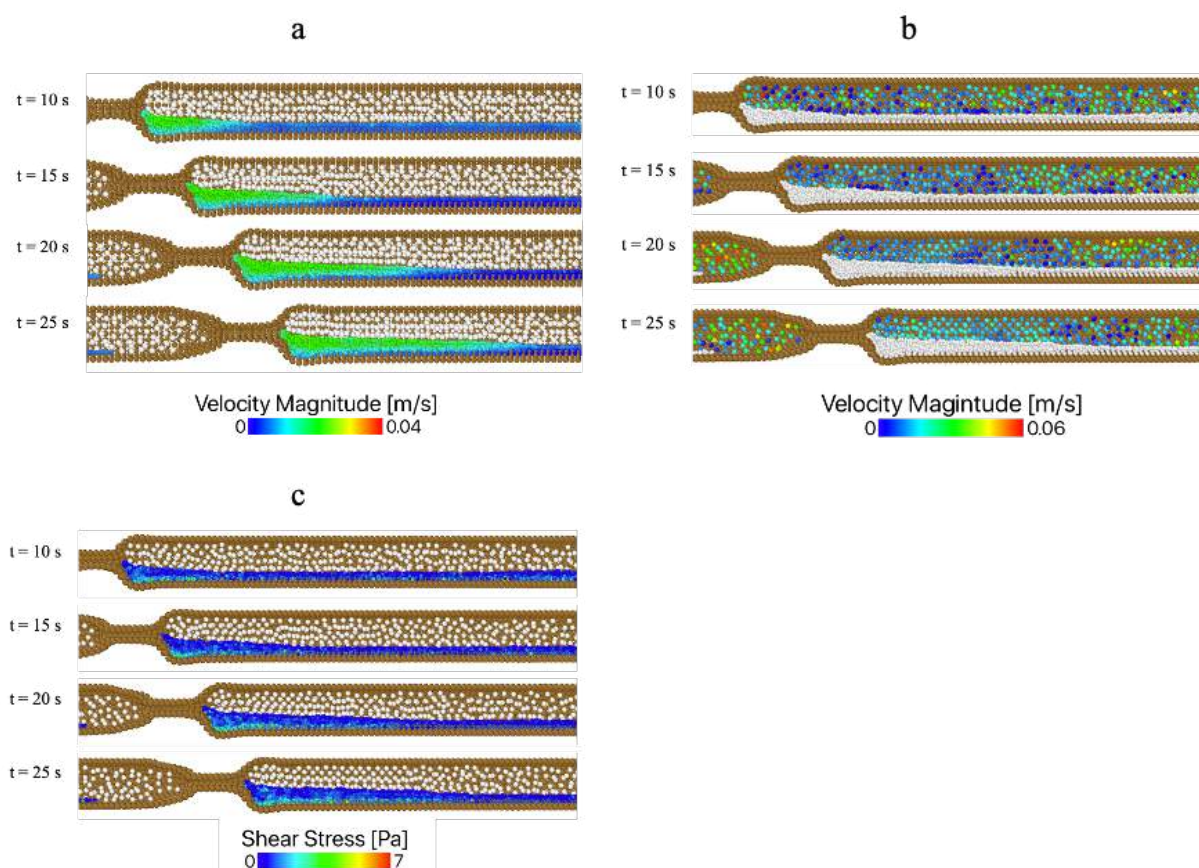


Figure 4.9 (a) and (b) Comparison of a peristaltic wave with content coloured by the velocity magnitude in the gas-liquid model. In (a) the velocities of the liquid phase and in (b) the gaseous phase are analysed. (c) Representation of the shear stresses in the liquid phase.

The liquid phase (Figure 4.9 (a)) shows almost the same velocities as seen in the partially-filled model (Figure 4.5 (b)). After 25 seconds the velocity in the gas-liquid model is slightly higher along the colon compared to the model without a gas phase. The velocity magnitude of the gaseous phase (Figure 4.9 (b)) in front of the peristaltic wave stays in the range of the propagation velocity of the peristaltic wave. Except the gas particles entering on the left side again (e.g., at 20 seconds and 25 seconds) show a slightly increased velocity magnitude.

Also the shear stress in the liquid phase (Figure 4.9 (c)) shows almost the same distribution and magnitude as seen in the partially-filled model (Figure 4.5 (d)). As

there are no significant differences, it can be assumed that the gas phase has less or no influence in the shear stresses that occur.

From Figure 4.10 (a) it can be seen that the velocity magnitude of the gaseous phase in front of the peristaltic wave is relatively constant and the arrows show a quite linear flow pattern. The gas particles entering on the left-hand side whereas showing higher velocities and swirl.

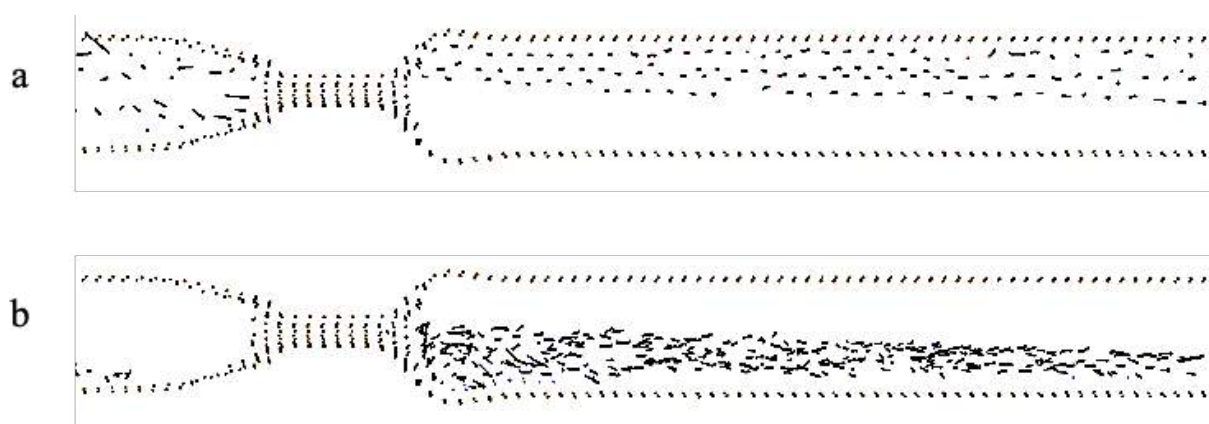


Figure 4.10 Vector representation of the (a) gaseous phase and (b) liquid phase in the gas-liquid model, where the length of the vector indicates the velocity.

The liquid phase as shown in Figure 4.10 (b) indicates the same flow pattern as in the partially-filled model (Figure 4.4) where a vortex is formed in front of the peristaltic wave. With respect to the velocity profile, in our model, the gaseous phase does not influence the liquid flow properties. Also, the mixing profile of the gas-liquid model (Figure 4.11), is practically identical to the partially-filled model (Figure 4.6 (b)).

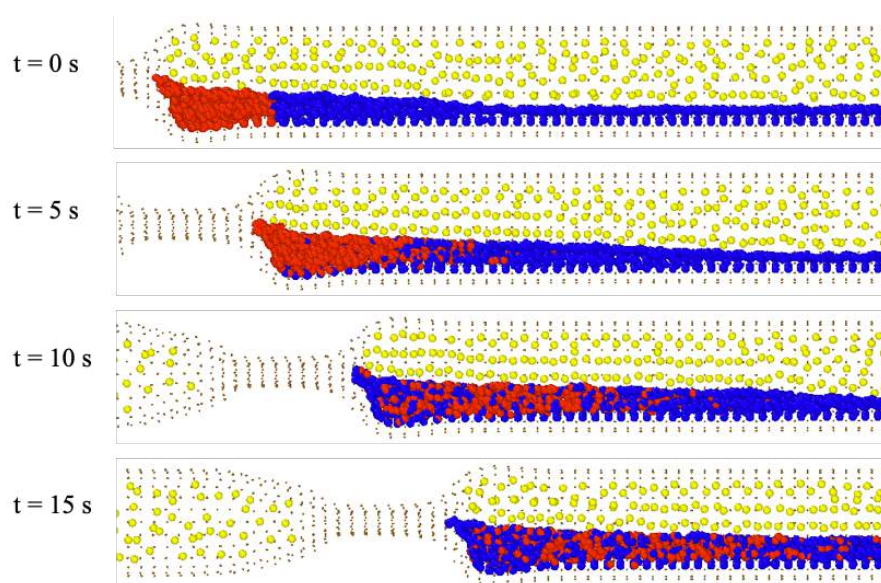


Figure 4.11 Mixing profile of gas-liquid model using tracking particles (red coloured) at different time-steps.

4.5.4 Comparison of the Velocity Profiles of all Three Models

The diagrams in Figure 4.12 show the axial velocity distribution of the liquid particles along the axial direction at three different time-steps: (a) represents the completely-filled model, (b) the partially-filled model and (c) the gas-liquid model.

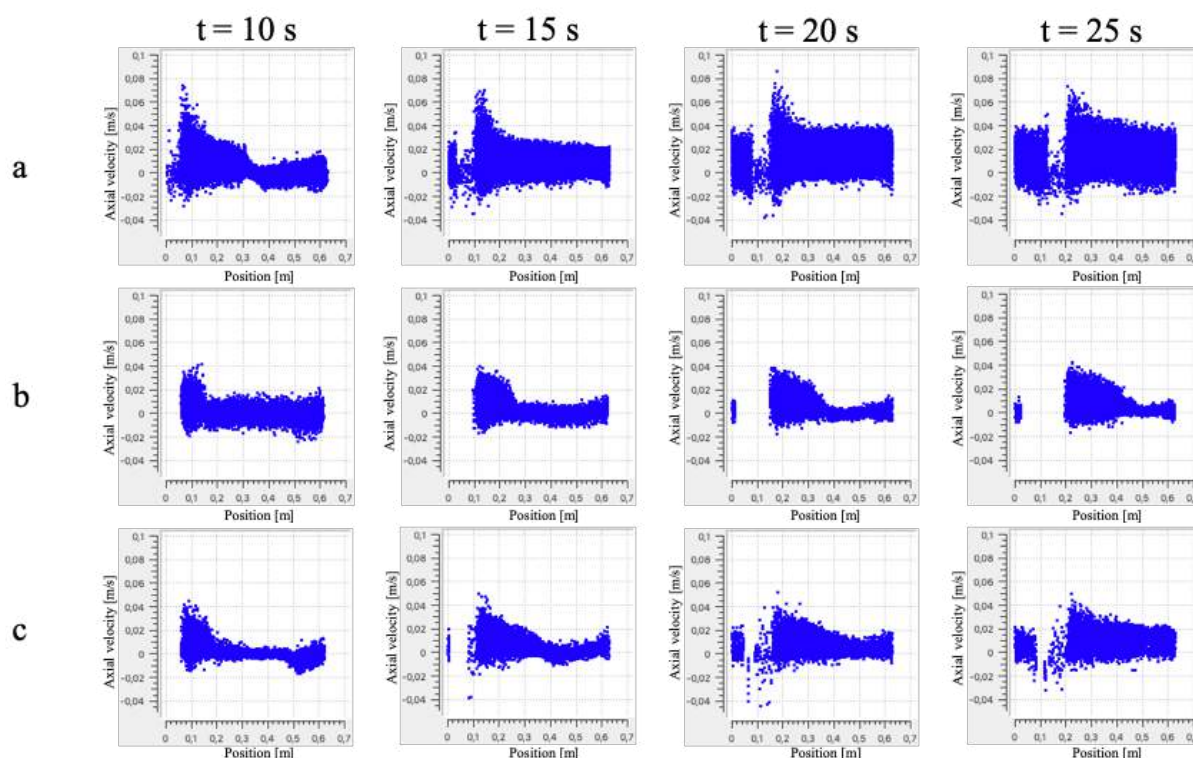


Figure 4.12 Graphical representation of the axial velocity along the colon models at different time-steps, where (a) represents the completely-filled model and (b) the partially-filled model and (c) the gas-liquid model

In all models, the highest velocity magnitude (Figure 4.5 and Figure 4.9) as well as the highest axial velocities are found in the region right in front of the peristaltic contraction in the DI region. If we compare compare the three models, w can establish that the maximum axial velocity of the particles representing the liquid is in the completely-filled model, which is approximately twice as high as in the other two models. The axial velocity distribution shows in all models a different pattern, whereas the partially-filled model and the gas-liquid model only show a slight difference.

In the completely-filled model the mean axial velocity distribution increases between 10 and 20 seconds by about 40% and stays constant, whereas the axial velocity distribution in partially-filled model remain almost constant. After 25 seconds the gas-liquid model shows a slight increase in the mean axial velocity.

As the reduction of fluid in the colon model by approximately 60% resulted in a 50% reduced liquid axial velocity. The addition of another fluid – in this case gas particles – suggests that in the gas-liquid model the axial velocity of the liquid is slightly higher than in the partially-filled model without gas.

In terms of dosage forms, the velocities in Figure 4.12 explain the result of Figure 4.6, Figure 4.7, and Figure 4.11. The completely-filled model, in fact, shows both higher axial velocities and a larger distribution of axial velocities. This is reflected in a faster propagation along the colon of both finely dispersed tracking particles (Figure 4.6) and large tablets (Figure 4.7), and in the more uniform distribution of particles in Figure 4.6 (a) compared to Figure 4.6 (b).

4.6 Conclusion

In our study, we develop three different computational models to describe the peristaltic motion in the colon. These models consider different filling levels as well as the presence of the gaseous phase. We also simulated the mixing of fully dispersed tracking particles and the motion of intact tablets are simulated.

Our study investigates how the hydrodynamics are influenced by different filling levels and the presence of the gas phase. The filling level in the colon has an influence on the shear stresses, mixing, concentration, and the hydrodynamic profiles, which can be highly relevant for medical research as well as pharmaceutical applications including the design of a modified release dosage form. For the disintegration/erosion of the dosage form and, thus, the release of drug particles, the existing shear forces and shear rates are one of the critical parameters. Conventional *in vitro* dissolution tests for

targeted drug delivery predictions are performed under standardised conditions with limited consideration of the environmental motility conditions (Long and Chen, 2009). Our results show that, the liquid fill volume of the colon plays a crucial role in future models of drug dissolution and drug disintegration. This is true for both the case of solid dosage form (tablet) and fully dispersed form.

The model, therefore, provides a more realistic environment for drug dissolution testing compared to the standardised dissolution tests and apparatuses currently in use (Long and Chen, 2009). In this study, we focus on the two extreme cases of completely dispersed drugs and insoluble tablets, but the model can be further improved by introducing tablets that gradually disintegrate in the colon lumen (Rahmat et al., 2019). This also affects the reliability of the prediction of *in vivo* performance, which is one of the main focuses in biopharmaceutical research (Long and Chen, 2009). In fact, computer simulations may in the near future refine and reduce the number of *in vitro* tests performed or even replace the standardised tools used.

Chapter 5

Modelling and Simulation of the Drug Release from a Solid Dosage Form in the Human Ascending Colon: The Influence of Different Motility Patterns and Fluid Viscosities

Published article:

Pharmaceutics 13 (2021)

5.1 Abstract

For colonic drug delivery, the ascending part of the colon is the most favourable site as it offers the most suitable environmental conditions for drug dissolution. Commonly, the performance of a drug formulation is assessed using standardised dissolution apparatus, which does not replicate the hydrodynamics and shear stress evoked by wall motion in the colon. In this work, computer simulations are used to analyse and understand the influence of different biorelevant motility patterns on the disintegration/drug release of a solid dosage form (tablet) under different fluid conditions (viscosities) to mimic the ascending colonic environment. Furthermore, the ability of the motility pattern to distribute the drug in the ascending colon luminal environment is analysed to provide data for a spatiotemporal concentration profile. The motility patterns used are derived from *in vivo* data representing different motility patterns in the human ascending colon. The applied motility patterns show considerable differences in the drug release rate from the tablet, as well as in the ability to distribute the drug along the colon. The drug dissolution/disintegration process from a solid dosage form is primarily influenced by the hydrodynamic and shear stress it experiences, i.e., a combination of motility pattern and fluid viscosity. Reduced fluid motion leads to a more pronounced influence of diffusion in the tablet dissolution process. The motility pattern that provoked frequent single shear stress peaks seemed to be more effective in achieving a higher drug release rate. The ability to simulate drug release profiles under biorelevant colonic environmental conditions provides valuable feedback to better understand the drug formulation and how this can be optimised to ensure that the drug is present in the desired concentration within the ascending colon.

5.2 Introduction

The number of people worldwide affected by colonic diseases such as inflammatory bowel disease (IBD) (i.e., Crohn's disease (CD) and ulcerative colitis (UC)) has steadily increased from 3.7 million in 1990 to 6.8 million in 2017 (Alatab et al., 2020). Colon-specific drug delivery has been the focus of numerous studies in recent years (e.g., (Goffredo et al., 2016, Teruel et al., 2020)), as it offers opportunities to improve the treatment of local diseases such as CD and UC while minimising side effects at the same time (Amidon et al., 2015).

The oral route, due to its convenience, is the primary method of administration for most medicines, including those that target the colon. Generally, the proximal colon is the targeted site for colonic drug delivery due to its more suitable environmental conditions (i.e., water availability for drug dissolution, fluid viscosities, less variable transit times), compared to the distal part of the colon (Christensen, 1994, Kumar et al., 2012, Murray et al., 2017, Watts and Illum, 1997). Modified release (MR) dosage formulations are usually coated with a protective layer that dissolves on its way (e.g., pH dependent) to the colon so that the actual drug release takes place in the colonic environment (Long and Chen, 2009). To assess the performance of a drug formulation, disintegration/dissolution tests are commonly performed using United States Pharmacopeia (USP) apparatus to mimic *in vitro* the complex *in vivo* process (Tenjarla, 2015). However, this simplified model does not replicate the hydrodynamics and the *in vivo* shear stresses, evoked by wall motion, which act on the MR formulation and influence the disintegration/dissolution process. Stamatopoulos et al. (Stamatopoulos et al., 2016b) developed an anatomically accurate *in vitro* model, the Dynamic Colon Model (DCM), where the hydrodynamics can be controlled using a hydraulic system and fluids with different compositions can be used to better replicate the human adult

colon. To enable a more realistic environment compared with the USP and to support the data from *in vitro* tests performed with the DCM or even replace experimental work, (Schütt et al., 2020) developed an *in silico* model which gives detailed insight into the hydrodynamics and mixing profiles occurring in the colonic environment at different conditions. Currently, the release from an MR formulation *in vivo* can only be visualised using Magnetic Resonance Imaging (MRI) or scintigraphy which is costly, time-consuming and not practical for product development and optimisation (Stamatopoulos et al., 2020). Moreover, the *in silico* models, including Physiologically Based Pharmacokinetic (PBPK) platforms such as GastroPlus™ and Simcyp®, use simple first order forward transit rate model. Thus, the colonic environment is considered as a single well-mixed and homogenized compartment. Although, different transit times are used for different entities (e.g., tablet, pellets, and fine particles), however, they are not related to the motility, volumes and viscosity. Thus, a tablet will have a fixed transit time regardless of the motility, volumes and viscosity changes *in vivo*. Any variation (i.e., coefficient of variance, % CV) applied on the transit times is done just to reflect observed inter-subject variability.

However, this modelling strategy does not allow for intra-occasional and intra-subject variability. This is because motility patterns are not constant in each subject and there are limited *in vivo* studies that monitor motility and transit times of different entities at the same time. Moreover, the released and/or dissolved drug particles in GastroPlus™ and Simcyp® will be instantly and uniformly distributed throughout the colonic compartment which is in contradiction to findings from *in vivo* bioimaging studies. Further compartmentalization of the colon (i.e., splitting a single *in silico* compartment to many sub-compartments), will not provide a solution. In addition, shear stresses applied on the dosage form and on released drug particles are not used

by GastroPlus™ and Simcyp®. Instead, average velocities derived from Computational Fluid Dynamics (CFD) analysis of USP II are used. Thus, a non-biorelevant apparatus is used to describe *in vivo* hydrodynamics. Furthermore, these average velocities are not linked to transit times or to motility patterns. Thus, changes in transit times in these PBPK platforms does not mean changes in the fluid velocities.

Finally, although PBPK models may contain complex algorithms to account for the interconnection of the different organs/compartments, are simply first order models and they cannot reproduce multiphysical phenomena such as the complex interplay between, e.g., wall motion, fluid motion, fluid viscosity, particle-particle and particle-fluid interactions. This is the reason why PBPK platforms cannot utilize either *in vivo* studies providing motility patterns (i.e., wall motion) or pressure amplitudes and link all the components affecting hydrodynamics, e.g., fluid volumes, fluid viscosity, transit times, direction of fluid, and spatiotemporal distribution of, e.g., fluid velocities and shear forces according to the intestinal wall motion. Thus, advanced modelling techniques are required to provide an increase understanding of the behaviour of a dosage form in a complex and dynamically changing *in vivo* environment. Therefore, in this work an *in silico* model that replicates, both the *in vivo* colonic environment and the disintegration/dissolution process of a pharmaceutical formulation to provide the distribution of the released drug along the colon would be beneficial for pharmaceutical development.

In this study, five motility patterns were chosen to replicate *in vivo* motility: three different motility patterns identified in Stamatopoulos et al. (Stamatopoulos et al., 2020) and Marciani et al. (Marciani et al., 2014) plus two additional motility patterns with data from (Dinning et al., 2014, Sarna, 2010). The influence of these five motility patterns on the disintegration/dissolution process of a solid dosage form (tablet) at

different fluid viscosities are analysed and compared. The motility patterns in Stamatopoulos et al. (Stamatopoulos et al., 2020) were derived from cine-MRI data of the *caecum*-ascending colon in healthy adult humans (Marciani et al., 2014). Additionally, we analyse the performance of the motility patterns in terms of the distribution of the dissolved drug along the colon at different fluid viscosities, providing data for a spatiotemporal concentration profile.

Effective drug therapy relies on the active pharmaceutical agent (API) being released from the solid oral dosage form and subsequently dissolving into the luminal fluid such that it can act locally on the receptor or traverse the membrane for systemic uptake. This rate of dissolution is a function of the formulation, the API and the conditions for dissolution. Simulation of the tablet dissolution within the colonic model provides further insights as a model that provides understanding of the *in vivo* performance of a drug formulation enables feedback early in development such that the drug product and manufacturing process can be optimised.

These new data also provide further information that can be used for the development of future drug formulations, as the different motility patterns in the colonic environment may have a crucial role in the disintegration/dissolution process of a solid dosage form. For the simulations, we use an approach similar to Schütt et al. (Schütt et al., 2020), further optimised to replicate the *haustra* and with closed ends, so that the model is closer to real environmental conditions. We also implement, a solid dosage form that can disintegrate/dissolve in the colonic fluid. The drug release/disintegration process of the tablet can be adapted to real tablet data (drug release/disintegration behaviour) and thus a large variety of different solid dosage forms can be replicated.

5.3 Methodology

5.3.1 Modelling Approach

The simulation technique used in this study is based on Discrete Multiphysics (DMP), a modelling technique already successfully used in Alexiadis et al. (Alexiadis, 2015a, Alexiadis, 2015b, Alexiadis et al., 2017), Ariane et al. (Ariane et al., 2017a, Ariane et al., 2018a, Ariane et al., 2017b), Mohammed et al. (Mohammed et al., 2020) and Schütt et al. (Schütt et al., 2020) to model human organs. DMP couples different particle-based modelling techniques such as Smoothed Particle Hydrodynamics (SPH), Lattice Spring Model (LSM), and the Discrete Element Method (DEM). The model in this study only accounts for SPH and LSM and it is related to Schütt et al. (Schütt et al., 2020). Theoretical background for DMP can be found in Alexiadis et al. (Alexiadis, 2015a, Alexiadis et al., 2017), while for SPH and LSM it may be found in Ref. (Liu and Liu, 2003) and Refs. (Kot et al., 2015, Lloyd et al., 2007, Pazdniakou and Adler, 2012) respectively. The dissolution of the tablet is modelled according to the methodology in Rahmat et al. (Rahmat et al., 2020a).

5.3.2 Colon-Model Geometry

Our 3D model represents an enlarged model of the human ascending colon (length scale 3:1, diameter 1:1). We developed five models that differ only in their operating conditions relating to the motility pattern and the number of sections (*haustra*) used. In all cases, the geometry of the model is the same: a cylindrical body with a total

length of 6.0×10^{-1} m and an inner diameter of 4.0×10^{-2} m. All models are built with closed ends, which means that the fluid cannot exit the tube and back pressure is created when the fluid flow reaches the end. This mimics the presence of the *hepatic flexure* which is a sharp bend between the ascending and the transverse colon. *In vivo* studies observed that in the proximal colon, the majority of the waves only propagate over a short distance and commonly stop before the *hepatic flexure*, resulting in backflow/back pressure (Bampton et al., 2000, Dinning et al., 2008). The model is divided into sections of equal size representing the colon's *haustra* (Figure 5.1). To simulate the conditions reported in (Stamatopoulos et al., 2020) the number of sections differs from model to model.

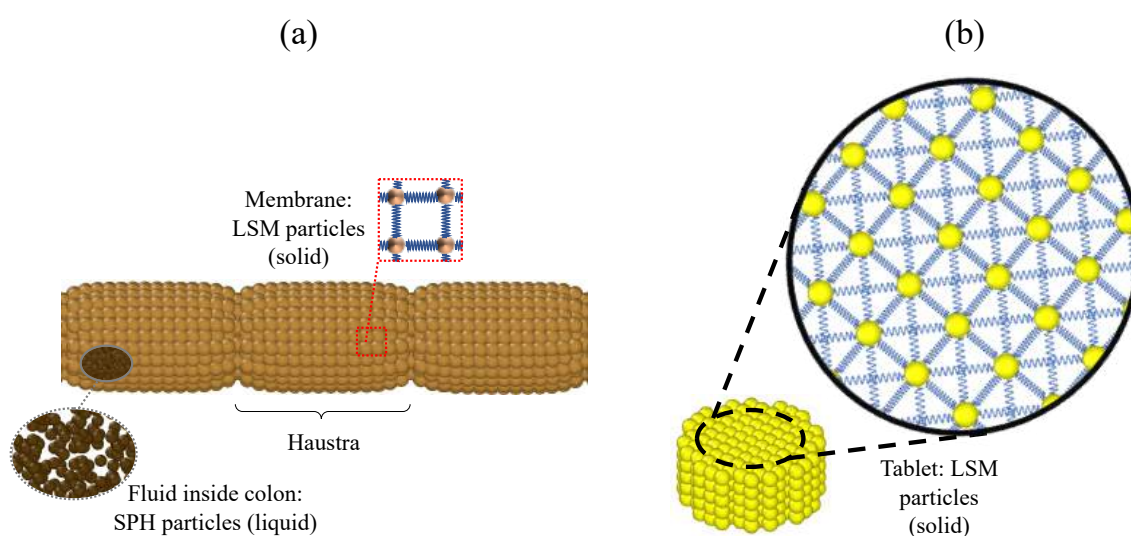


Figure 5.1 (a) Section of the flexible membrane, showing the colon's *haustra* and the intestinal fluid inside the colon. The membrane is built of particles which are connected by a network of springs to achieve a flexible behaviour. (b) 3D sketch of the tablet. The particles representing the tablet are connected by linear and diagonal springs to obtain a solid behaviour.

There are a wide range of tablets of different sizes and shapes on the market, for the sake of simplicity, in this study, the geometry of the tablet is set as a cylinder with a

diameter of 1.0×10^{-2} m and a height of 5.0×10^{-3} m (Figure 5.1 (b)). For more details on the modelling of the tablet, see Chapter 5.3.2.4.

In the model, SPH is used for the fluid and LSM for the elastic membrane and the solid tablet. During the tablet dissolution process, fluid diffuses into the tablet. If the concentration of the computational particles representing the tablet is below a certain threshold, the particle detaches from the tablet. In this case (as discussed in more detail in Chapter 5.3.2.4), the status of the particle switches from solid to liquid, i.e., from LSM to SPH.

In Figure 5.1 (a), a schematic sketch of the model, including the membrane, the colon *haustra* and the fluid inside the colon, is shown.

5.3.2.1 Membrane

The membrane is modelled similarly to (Schütt et al., 2020) by 2,500 LSM particles tethered to their initial position with a Hookean spring (Figure 5.2 (a)).

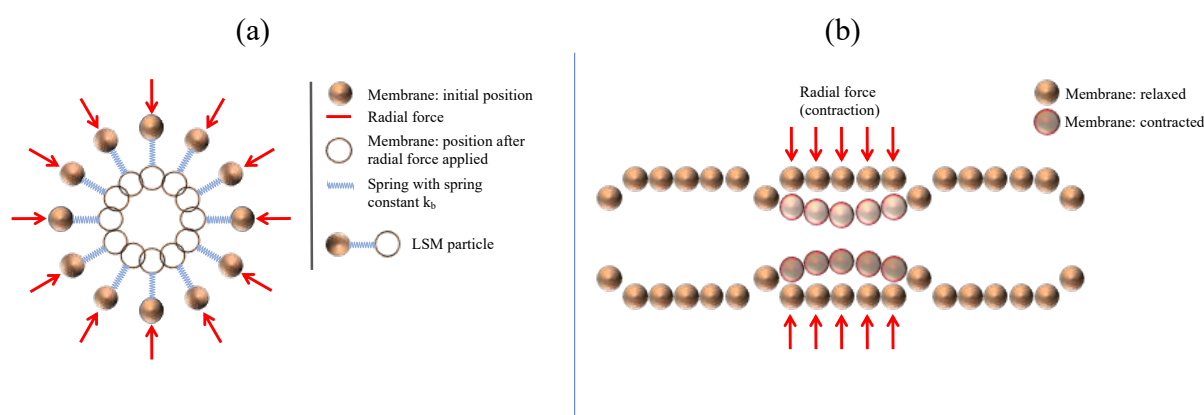


Figure 5.2 (a) 2D representation of the membrane particle anchored by a spring in equilibrium position and after the application of a radial force. (b) Illustration the particles representing the colon's membrane including its characteristic *haustra*, before and after applying an individual radial force to each ring ('circular muscle').

An additional Hookean force is applied between the adjacent particles as shown in Figure 5.1 (a). The corresponding forces are calculated using Hooke's law:

$$F_{ij} = k(r_{ij} - r_0) \quad , \quad (5.1)$$

where F_{ij} is the existing spring force between particle i and j , k is the Hookean constant, r_0 is the equilibrium distance between particle i and j and r_{ij} is the current distance. The membrane is composed of 100 rings of 25 particles each. One ring represents one circular muscle fibre of the colon, which can be activated independently to mimic a colonic motor pattern (Figure 5.2 (b)).

For activation, we use a radial force applied to the particles of a specific *haustra* to cause contraction or relaxation. Further details of the membrane are shown in Table 5.1.

Table 5.1. Model parameter of the Membrane.

Parameter Membrane	Value
SPH	
Number of SPH particles (1 layer)	2,500
Mass of each particle $m_{M,0}$	3.89×10^{-4} kg
LSM	
Hookean coefficient (bonds) $k_{M,b}$	0.2 J m^{-2}
Hookean coefficient (position anchor) $k_{M,p}$	0.012 J m^{-2}
Viscous damping coefficient $k_{M,v}$	$1.0 \times 10^{-2} \text{ kg s}^{-1}$
Equilibrium distance $r_{M,0}$	$6.28 \times 10^{-3} \text{ m}$

5.3.2.2 Fluid

All models account for the same level of luminal content modelled with 25,758 SPH particles. The amount of fluid is taken from the study of Badley et al. (Badley et al., 1993) that used scintigraphy to measure the fluid volume in the ascending colon. The average value is 162 mL, with single values ranging from 82 to 303 mL. This corresponds to a filling level of about 40% in the ascending colon (Prasanth et al., 2012), which is used in the simulations. In reality, different motility patterns are triggered by different filling levels (Marciani et al., 2014). However, the value of 40% is fixed for all models to assess the drug release rate of the tablet under different motility patterns for the same level conditions. Resolution analysis (i.e., number of computational particles used to discretize the system) can be found in (Schütt et al., 2020).

5.3.2.3 Fluid-Structure and Global Boundary Conditions

The SPH equations of motion result from the discrete approximations of the Navier–Stokes equation at a set of points. This set of points results from the discretization of the continuum domain and can be thought of as particles. The particles are characterised by their mass, velocity, pressure, and density. SPH is based on the mathematical identity:

$$f(\mathbf{r}) = \iiint f(\mathbf{r}')\delta(\mathbf{r} - \mathbf{r}')d\mathbf{r}' \quad , \quad (5.2)$$

where $f(\mathbf{r})$ is any scalar function defined over the volume V and the vector \mathbf{r} is a three-dimensional point in V . $\delta(\mathbf{r})$ is the three-dimensional delta function which is approximated in the SPH formulations by a smoothing kernel W with a characteristic width or smoothing length h :

$$\lim_{h \rightarrow 0} W(\mathbf{r}, h) = \delta(\mathbf{r}) \quad (5.3)$$

In the literature, there are several kernel functions available. In this study, we use the Lucy kernel function (Lucy, 1977). By replacing the delta function by a kernel or smoothing function W , the approximation to the function $f(\mathbf{r})$ results in

$$f(\mathbf{r}) \approx \iiint f(\mathbf{r}') W(\mathbf{r} - \mathbf{r}', h) d\mathbf{r}' \quad (5.4)$$

By discretising over a series of particles of mass $m = \rho(\mathbf{r}') d\mathbf{r}'$, the identity equation results in

$$f(\mathbf{r}) \approx \sum_i \frac{m_i}{\rho_i} f(\mathbf{r}_i) W(\mathbf{r} - \mathbf{r}_i, h) \quad (5.5)$$

where m_i and ρ_i are the mass and density of the i th particle, respectively, and i ranges over all particles within the smoothing kernel W (i.e., $|\mathbf{r} - \mathbf{r}_i| < h$). The discrete approximation of a generic continuous field is represented by Equation (5.5) and can be used to approximate the Navier–Stokes equation

$$m_i \frac{dv_i}{dt} = \sum_j m_i m_j \left(\frac{P_i}{\rho_i^2} + \frac{P_j}{\rho_j^2} + \Pi_{i,j} \right) \nabla_j W_{i,j} + \mathbf{f}_i , \quad (5.6)$$

where v_i is the velocity of particle i , P is the pressure, W_{ij} is the concise form of $W(\mathbf{r}_j - \mathbf{r}_i, h)$, the term ∇_j is the gradient of the kernel with respect to the coordinate r_j , \mathbf{f}_i a volumetric body force, and $\Pi_{i,j}$ denotes the viscous forces. There are various expressions for the tensor $\Pi_{i,j}$ available in the literature; here we use (Monaghan and Gingold, 1983):

$$\Pi_{ij} = -\alpha h \frac{c_0}{\rho_{ij}} \frac{v_{ij} r_{ij}}{\rho_{ij}^2 + b h^2} , \quad (5.7)$$

where ρ_{ij} is the density and v_{ij} the relative velocity of particle i and j , respectively. α is a dimensionless factor to control the dissipation strength to obtain a stable simulation and h is the smoothing length. The constant b is introduced and used with $b \approx 0.01$ to avoid unstable simulations. This is particularly the case with compact particles whose distance between each other is very small. The artificial viscosity can be recognised as an effective kinematic viscosity ν . Depending on the desired effective kinematic viscosity in the simulation, the value of α is chosen accordingly (Monaghan, 2005):

$$\nu = \frac{\alpha h c}{10} . \quad (5.8)$$

The viscosities chosen in this study are consistent to those already used elsewhere (Stamatopoulos et al., 2016b).

To calculate the pressure forces between the fluid particles and fulfil Equation (5.6), the Tait equation is used to link the density ρ and the pressure P

$$P = \frac{c_0^2 \rho_0}{7} \left[\left(\frac{\rho}{\rho_0} \right)^7 - 1 \right], \quad (5.9)$$

where c_0 is the reference speed of sound and ρ_0 the reference density at zero applied stress. Further details of the fluid properties are shown in Table 5.2.

Table 5.2. Model parameter of the Fluid.

SPH Parameter Fluid	Value
Number of SPH fluid particles	25,758
Mass of each particle $m_{F,low\ viscosity}$	1.19×10^{-5} kg
Mass of each particle $m_{F,medium\ viscosity}$	1.21×10^{-5} kg
Mass of each particle $m_{F,high\ viscosity}$	1.22×10^{-5} kg
Density (fluid) $\rho_{F,low\ viscosity}$	1000 kg m ⁻³
Density (fluid) $\rho_{F,medium\ viscosity}$	1017 kg m ⁻³
Density (fluid) $\rho_{F,high\ viscosity}$	1020 kg m ⁻³
Dynamic viscosity (fluid) $\eta_{L,low\ viscosity}$	1 mPa s
Dynamic viscosity (fluid) $\eta_{L,medium\ viscosity}$	13 mPa s
Dynamic viscosity (fluid) $\eta_{L,high\ viscosity}$	98 mPa s

The solid-fluid interaction is modelled with a soft repulsive potential for the following purposes: to avoid compenetration among the computational solid-fluid particles (i.e., membrane and tablet), to keep the fluid inside the colon and to keep fluid particles out of the solid tablet. The type of soft potential has the following form:

$$E_{ij} = A \left[1 + \cos \left(\frac{\pi r_{ij}}{r_c} \right) \right] \quad \text{with} \quad r_{ij} < r_c \quad (5.10)$$

Here, r_{ij} represents the distance between particle i and j , r_c is the cut-off distance and A is an energy constant. The no-slip boundary conditions between the solid and fluid particles are approximated by viscous forces as shown in Equation (5.7).

5.3.2.4 Tablet and Tablet Disintegration

In the model, the tablet is composed of 445 particles and is modelled as naturally buoyant. To model the dissolution and disintegration of the tablet, a specific concentration is set for each particle of the tablet, which represents the concentration of the Active Pharmaceutical Ingredient (API) in the tablet. Tablet dissolution is achieved by mass diffusion between the fluid and the tablet particles and between the tablet particles themselves. The diffusive mass balance for multicomponent systems can be written in the SPH framework in the following form (Alexiadis, 2015a):

$$\frac{dw_i}{dt} = - \sum_j \frac{m_i m_j}{\rho_i \rho_j} \frac{(D_i + D_j)(C_i - C_j)}{r_{i,j}^2} r_{i,j} \cdot \nabla_j W_{i,j} \quad , \quad (5.11)$$

where, w_i is the mass of the fluid in the particle, D_i is the diffusion coefficient and C_i is the concentration which is associated with each particle i . To close Equation (5.11), m_i , C_i and ρ_i can be linked according to the following relation (Alexiadis, 2015a):

$$w_i = C_i \frac{m_i}{\rho_i} . \quad (5.12)$$

A typical ingredient used in colonic formulations is mesalazine (Iacucci et al., 2010, Ye and van Langenberg, 2015). Its diffusion coefficient is estimated to be $7.46 \times 10^{-10} \text{ m}^2\text{s}^{-1}$, determined in an aqueous solution containing triprotic buffer (French and Mauger, 1993), which is very small and requires very long computational times (10 h of real-time, i.e., approx. 10 days of computational time) for observing the complete disintegration of the tablet in the simulation. To reduce the computational time, we initially use a value 10 times higher which only take one hour of real-time (2 days of computational time) for disintegrating the tablet. For more details on the computer architecture used, see Chapter 5.3.5.

The solubility of commercially available mesalazine formulations, depending on the pH value, were determined to be 1.2 – 5.5 mg/mL (Tenjarla, 2015). This corresponds to a solubility of 50 – 100% under simulation conditions. Accordingly, the dissolution and disintegration of the tablet are modelled as follows: if the concentration, of at least one of two neighbouring tablet particles falls below $C_B = 30\%$ (i.e., 70% dissolved), the bond between these particles is removed, weakening locally the structure of the tablet. When a computational particle has no bonds with any other particle of the tablet, the particle detaches completely simulating the disintegration of the tablet. Finally, when the concentration of the active ingredient in the tablet is below its solubility concentration C_S (defined as 25%, i.e., 75% dissolved), we change the type of the particle from LSM to SPH. For the parameter C_B and C_S , we use generic values as a reference to show the potential of the model. The actual numbers will depend on the physicochemical and mechanical properties of the tablet (i.e., the material used, but also how the tablet is compacted). The values for C_B and C_S should be derived from

real data/observations. From the theoretical point of view, the values used for C_B and C_S (i.e., $C_B > C_S$), provide to the tablet the option to disintegrate (i.e., break into pieces) before it dissolves into the fluid.

In the model, the fluid and the tablet were discretised differently (i.e., different resolution), so that the initial particle distance between the fluid particles and the tablet particles is different. Therefore, a different ‘momentum’ smoothing length is used between the fluid particles and the tablet particles. The ‘diffusion’ smoothing length between the fluid and tablet particles is obtained from a weighted smoothing length based on the smoothing length of the fluid particles and the tablet particles. Further details of the general model parameter and specific model properties are given in Table 5.1, Table 5.2, Table 5.3, and Table 5.4.

Table 5.3. Fundamental model parameter.

Parameter	Value
SPH	
Artificial speed of sound c_0	0.1 m s^{-1}
Time-step Δt	$5.0 \times 10^{-4} \text{ s}$
Smoothing length membrane h	$9.42 \times 10^{-3} \text{ m}$
Momentum–Smoothing length (fluid) $h_{M,F}$	$4.71 \times 10^{-3} \text{ m}$
Momentum–Smoothing length (tablet) $h_{M,T}$	$1.41 \times 10^{-3} \text{ m}$
Momentum–Smoothing length (fluid / tablet) $h_{M,F/T}$	$4.71 \times 10^{-3} \text{ m}$
Diffusion–Smoothing length (fluid / tablet) $h_{D,F/T}$	$3.35 \times 10^{-3} \text{ m}$
Diffusion–Smoothing length (fluid) $h_{D,F}$	$4.71 \times 10^{-3} \text{ m}$
Diffusion–Smoothing length (tablet) $h_{D,T}$	$1.41 \times 10^{-3} \text{ m}$
Diffusion coefficient (tablet) D_T	$1.0 \times 10^{-30} \text{ m}^2\text{s}^{-1}$
Diffusion coefficient (fluid / tablet) $D_{F/T}$	$7.46 \times 10^{-9} \text{ m}^2\text{s}^{-1}$

Table 5.4. Model parameter of the Tablet.

Parameter Tablet	Value
SPH	
Number of SPH tablet particles	445
Mass of each particle $m_{T,low\ viscosity}$	8.82×10^{-7} kg
Mass of each particle $m_{T,medium\ viscosity}$	8.97×10^{-7} kg
Mass of each particle $m_{T,high\ viscosity}$	9.00×10^{-7} kg
Density (Tablet) $\rho_{T,low\ viscosity}$	1000 kg m ⁻³
Density (Tablet) $\rho_{T,medium\ viscosity}$	1017 kg m ⁻³
Density (Tablet) $\rho_{T,high\ viscosity}$	1020 kg m ⁻³
LSM	
Hookean coefficient $k_{T,b}$	0.2 J m ⁻²
Equilibrium distance (linear bonds) $r_{TL,0}$	0.012 J m ⁻²
Equilibrium distance (diagonal bonds) $r_{TD,0}$	6.28×10^{-3} m

Figure 5.3 illustrates an example of the filled colon model, in which a tablet disintegrates and dissolves in the fluid at three different consecutive times t .

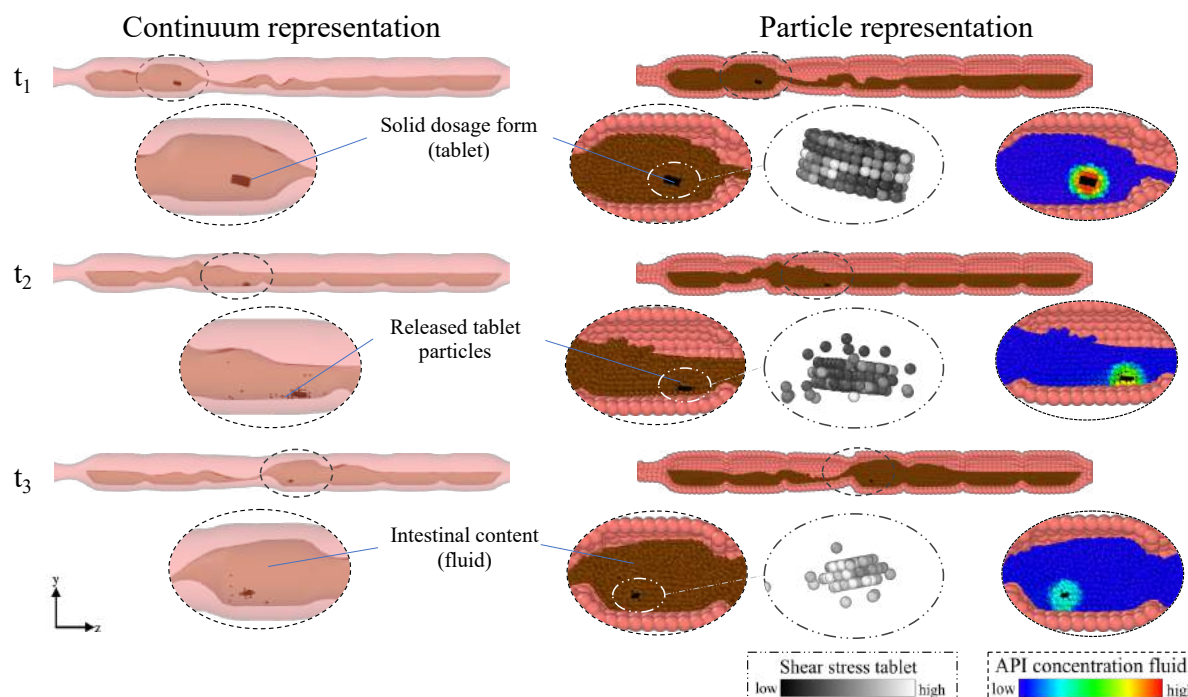


Figure 5.3 The model is represented in two different forms: 'Particle representation' and a more realistic 'Continuum representation'. This is an example of the dissolution process of a tablet in the colonic environment at three different time steps. Colonic contractions lead to the motion of the fluid and accordingly to the movement of the tablet which dissolves in the intestinal fluid. In the particle representation the shear stress acting on the tablet, and the API concentration in the surrounding of the tablet, i.e., in the fluid is shown.

The model is represented both in a 'continuum representation' and in a 'particle representation'. The API concentration in the fluid and the tablet are shown in the particle presentation. By diffusion and advection, the API decreases in the tablet and increases in the fluid. The shear stresses present contribute to the tablet breakage into pieces (i.e., disintegration).

Due to the different contractions caused by the motility pattern, the tablet is moved back and forth and gradually releases drug particles that dissolve further in the fluid. The mechanism of the disintegration of the tablet presented in this study can be compared to an extended-release (ER) tablet whose coating disintegrates in the upper gastrointestinal and small intestinal environment. When it enters the colon, the ER

tablet then behaves similar to an IR tablet and dissolves / disintegrates immediately in the colonic fluid.

Details on the simulation parameter are presented in Table 5.3. We are aware that under real-world conditions the tablet would not consist of 100% drug, but here the focus is on the different motility pattern and not on the tablet itself. It is also assumed that the tablet/drug is readily soluble and thus the drug release rate is equal to the dissolution rate.

5.3.3 Model Motility Patterns

The motility patterns used in this study are developed from the data produced by (Hoad et al., 2016, Marciani et al., 2014) and analysed in Stamatopoulos et al. (Stamatopoulos et al., 2020). Three different motility patterns at different conditions are considered: baseline (fasted state), stimulated with polyethylene glycol (PEG) electrolyte and stimulated with maltose. The motility patterns differ, for example, in the duration and direction of single contraction waves as well in the frequency of individual contractions. Besides those reported in (Stamatopoulos et al., 2020), two additional models are developed to study how much the colonic activity affects the dissolution of the modelled tablet. We use data from (Sarna, 2010) to establish a comparison pattern according to the 'Stimulant PEG' and the 'Stimulant Maltose' patterns, and data from (Dinning et al., 2014) to develop a cyclic propagating pressure wave (CPPW), which is the most frequently motor pattern identified in the colon (Dinning et al., 2014). The motility patterns consist of different actions: a single

contraction, antegrade waves and retrograde waves or a combination of these single actions.

To describe the colonic activity within a specific time interval $t_{iv,0}$ (e.g., predefined from the total number of available MRI images/analysed time) by a measurable value, Marciani et al. (Marciani et al., 2014) introduced the so-called Motility Index (MI). A high MI value means high colonic activity, a low MI value means, respectively, low activity. The unit of MI is 'segments \times s'.

$$MI = \sum_{k=1}^n (t_{iv} \cdot No_{seg})_k \quad , \quad \text{with } n = \frac{t_{iv,0}}{t_{iv}} \quad (5.13)$$

Here, t_{iv} is the considered time interval within the total interval $t_{iv,0}$ and No_{seg} is the number of segments showing activity during the time interval t_{iv} . For example, if a Motility Index should be determined for a period of 120 s and the analysed time interval is 20 s, n will be equal to 6. Is the colon divided into 4 equally sized segments and only 3 segments show activity in the first time interval, 2 in the second time interval, 4 in the third interval and no activity is recorded during the time intervals 4 - 6, the Motility Index is thus calculated as follows:

$$MI = (20 \cdot 3) + (20 \cdot 2) + (20 \cdot 4) = 140 \text{ segments} \times s$$

As mentioned above, the number of sections (*haustra*) varies from model to model, depending on the data available in (Stamatopoulos et al., 2020). Thus, a direct comparison only based on the determined MI is not possible. For this reason, we have

introduced an additional Specific Motility Index (*SMI*), which also takes the existing number of sections (*haustum*) into account and makes all models comparable.

$$SMI = \frac{\sum_{k=1}^n (t_{iv} \cdot No_{seg})_k}{No_{seg,total}} \quad , \quad \text{with } n = \frac{t_{iv,0}}{t_{iv}} \quad (5.14)$$

Here, $No_{seg,total}$ is the total number of sections (*haustra*) in the specific model. Thus, the result is a value describing the colonic activity per section (*haustum*).

The data represented in Stamatopoulos et al. (Stamatopoulos et al., 2020) are related to a period of two minutes. On this basis, we modelled the different motility patterns for the simulation. The differences between the individual motility patterns are presented in Figure 5.4 (a – e). The figure shows the different actions that occur, the duration of each action and the sections that are affected by the action.

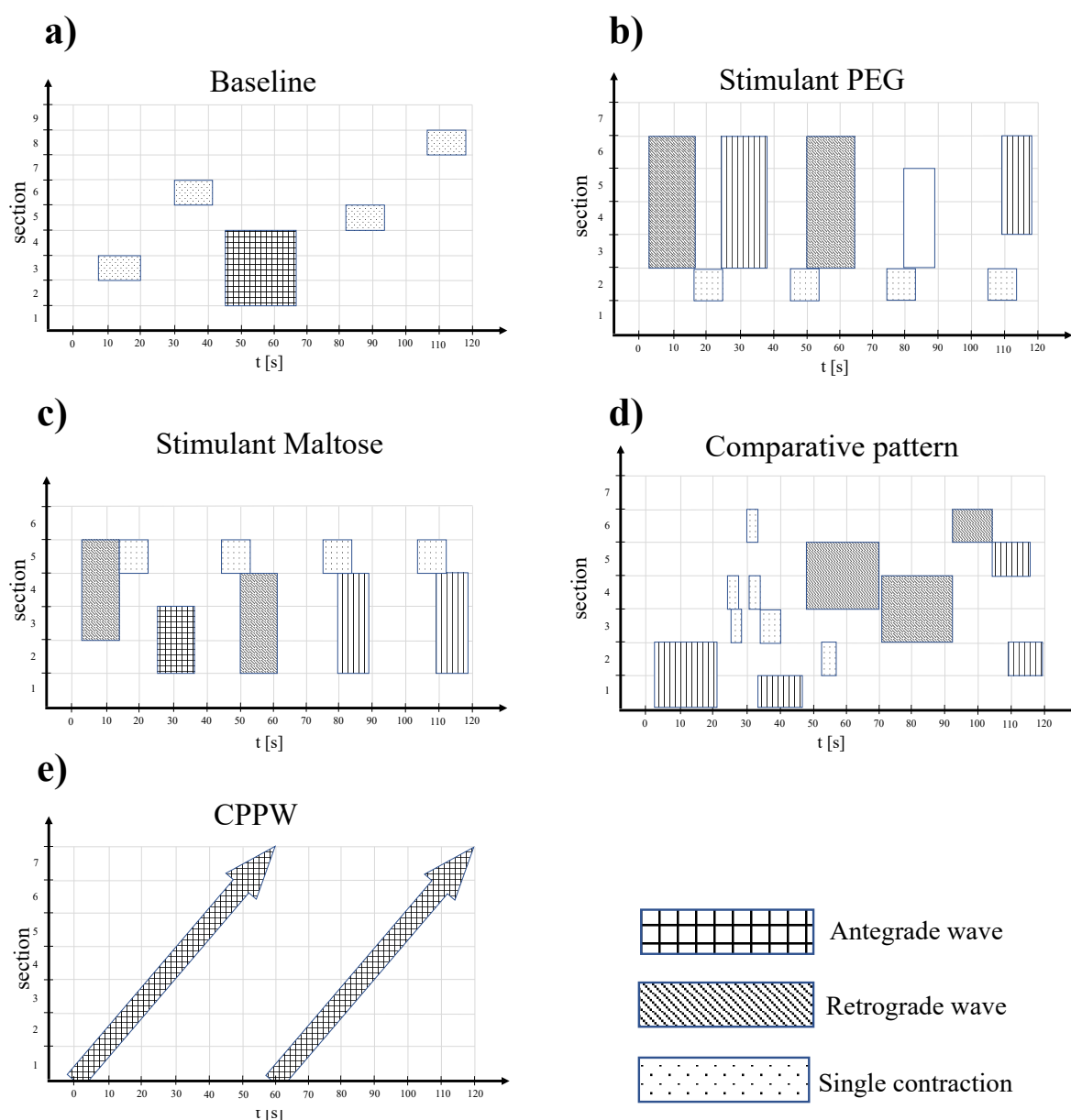


Figure 5.4 Illustration of the different motility pattern, where (a) is the Baseline, (b) the Stimulant PEG, (c) the Stimulant Maltose, (d) the Comparison pattern and (e) the CPPW motility pattern. Here, the x -axis represents the time and duration of the actions taking place and the y -axis the colon section (*hastrum*) addressed. The different actions are indicated by different hatches.

For the simulations, these two-minute datasets are repeated accordingly until the desired simulation time is reached (i.e., 5 repetitions for 10 min simulation time). Further details of the motility patterns are provided in Table 5.5.

Table 5.5. Model parameter motility patterns.

Parameters	Baseline	PEG	Maltose	Comparison	CPPW
No. of sections	9	7	6	7	7
Motility index [segment \times s]	140	460	380	300	280
Specific motility index [segment \times s \times s_{total}^{-1}]	16	66	63	43	40
Occlusion velocity 'wave' [cm/s]	0.1	2.3	2.3	0.8	0.1
Occlusion velocity 'single contraction' [cm/s]	0.1	0.1	0.1	0.25	-
Wave travel velocity [cm/s]	0.9	2.5	2.5	0.85	1.0
Occlusion degree OD [%]					
Single contraction 1	25	60	60	30	-
Single contraction 2	25	60	60	50	-
Single contraction 3	25	60	60	60	-
Single contraction 4	25	60	60	40	-
Single contraction 5	-	-	-	50	-
Single contraction 6	-	-	-	30	-
Antegrade wave 1	20	75	75	40	-
Antegrade wave 2	-	55	55	55	40
Antegrade wave 3	-	40	40	75	-
Antegrade wave 4	-	-	-	40	-
Retrograde wave 1	-	75	75	40	-
Retrograde wave 2	-	40	40	75	-
Retrograde wave 3	-	-	-	40	-

The occlusion degree OD , as shown in Figure 5.5 is defined by relating the initial cross-sectional area of the colon, A_R to the cross-sectional area of the colon after contraction, A_C (Equation (5.15)).

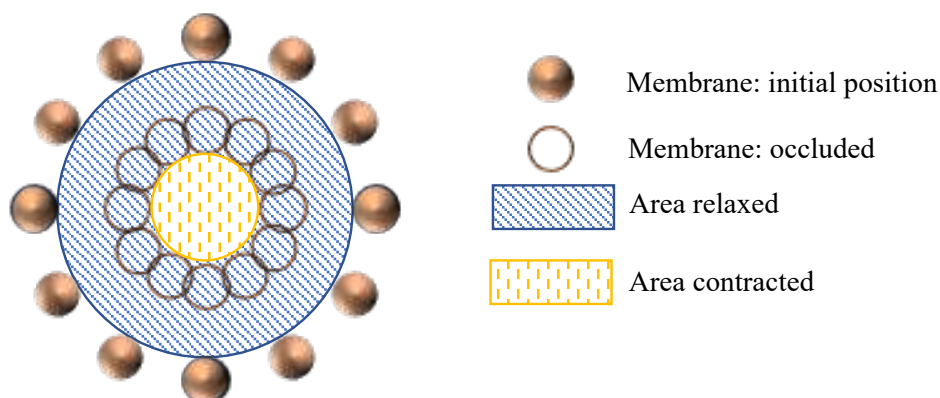


Figure 5.5 Representation of how the occlusion degree is defined.

$$OD [\%] = \left(1 - \frac{A_C}{A_R}\right) \cdot 100 \quad (5.15)$$

At the beginning of the simulation, the tablet is placed in the same initial position in all models (Figure 5.6). Here, the antegrade direction is from right to left.

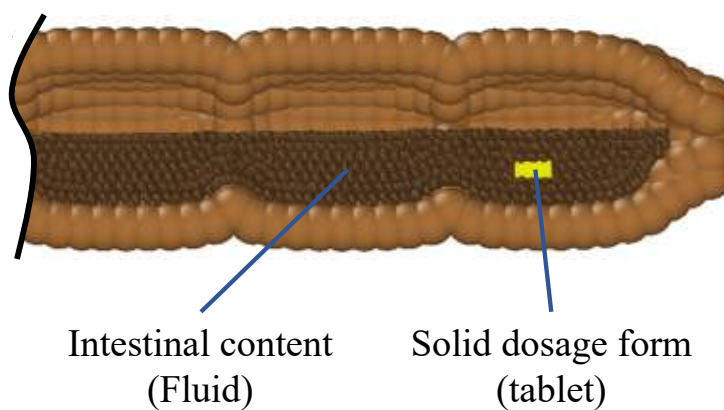


Figure 5.6 Representation of the initial position of the tablet, which is in all models identical.

5.3.4 Method of Analysis

While the previous section introduced several parameters for characterising the motility patterns (Table 5.5), this section discusses the parameters used to analyse the numerical results: a measure of the stress on the tablet and the cumulative drug release.

The action of the stresses on the tablet is a crucial factor affecting tablet disintegration. To condensate all the information of the stress tensor in one single parameter, we use the Frobenius norm:

$$\|\sigma\|_F = \sqrt{\sum_{i=1}^3 \sum_{j=1}^3 |\sigma_{ij}|^2} , \quad (5.16)$$

where the components σ_{ij} define the local stress on the x_i, x_j plane.

The cumulative drug release (*CDR*) of the tablet (Figure 5.7, Figure 5.8, Figure 5.9 and Figure 5.13) is calculated according to Equation (5.17)

$$CDR [-] = 1 - \frac{\sum c_{i,t}}{\sum c_0} , \quad (5.17)$$

where c_0 is the initial tablet particle concentration and $c_{i,t}$ is the actual concentration of each tablet particle i at time t .

The shear stress acting on the tablet (Figure 5.7, Figure 5.8, Figure 5.9 and Figure 5.13) is calculated according to Equation (5.18)

$$SST \text{ [Pa]} = \frac{\sum s_{i,t}}{No_{p,t}} , \quad (5.18)$$

where, $s_{i,t}$ is the shear stress acting on each tablet particle i and $No_{p,t}$ is the actual number of tablet particles at time t .

For the comparison of the different drug release profiles (Figure 5.7, Figure 5.8, Figure 5.9 and Figure 5.13) the two factor (f_1 and f_2) analysis is used (Moore and Flanner, 1996). Factor f_1 is the difference factor in percent, describing the difference (relative error) of two curves at a time point t . Factor f_2 is the similarity factor describing the similarity in the percent drug release between two drug release curves:

$$f_1 = \frac{\sum_{t=1}^{t=n} |R_t - T_t|}{\sum_{t=1}^{t=n} R_t} \times 100 , \quad (5.19)$$

$$f_2 = 50 \times \log \left[\frac{100}{\sqrt{1 + \frac{\sum_{t=1}^{t=n} (R_t - T_t)^2}{n}}} \right] , \quad (5.20)$$

where R_t is the drug release for reference formulation at time t , T_t is the drug release for comparison formulation at time t and n the number of time points. Values for f_1 close to zero (0–15) and f_2 greater than 50 (50–100) characterise the equivalence of the compared drug release profiles (Shah et al., 1997, Shah et al., 1998).

To access the disintegration degree or disintegration time in the case of the complete dissolution of the tablet, the following method is used: Throughout the simulation, the concentration of each tablet particle is tracked. As described in Chapter 5.3.2.2 and Chapter 5.3.2.4, each tablet particle is bonded to its neighbour particle until the

concentration of one of the neighbouring particles is fallen below a certain threshold concentration and the bond breaks. As soon as no particle with a higher concentration than the threshold concentration is present, then the tablet is completely disintegrated. In the case that the tablet has not completely disintegrated, the degree of disintegration is calculated at $t = 60$ min according to the following equation:

$$\phi[\%] = \left(1 - \frac{No_{T,th}}{No_{T,in}}\right) \cdot 100 \quad , \quad (5.21)$$

where $No_{T,th}$ is the number of tablet particles with a concentration higher than the threshold concentration and $No_{T,in}$ is the number of initial tablet particles.

The concentration of each tablet particle is tracked throughout the simulation. To assess the performance of each motility pattern on the API distribution along the colon (Figure 5.10, Figure 5.11, and Figure 5.12), we analyse and compare the concentration distribution only of the dissolved API at the corresponding time because only this part is available for absorption. The dimensionless concentration ζ in Figure 5.10, Figure 5.11, and Figure 5.12 is calculated according to the following equation:

$$\zeta[-] = \left(\frac{c_s}{\sum c_s}\right) \quad , \quad (5.22)$$

where s is the section number and c_s is the total drug concentration in section s .

The dimensionless time τ (Figure 5.13) is defined according to the following Equation (5.23)

$$\tau [-] = \frac{t}{t_0} , \quad (5.23)$$

where t_0 is the total simulated time and t is the actual time. For the high diffusion data in Figure 5.13, $t_0 = 60$ min and for the low diffusion data is $t_0 = 600$ min. The reason why we can use a reference time t_0 in the definition of τ is explained in Chapter 5.7.

5.3.5 Software

In this study, the simulations were performed using the University of Birmingham BlueBEAR HPC service (Birmingham), running the simulations on fifteen cores with 60 GB of memory. The open-source code LAMMPS (Ganzenmüller et al., 2011, Plimpton, 1995) is used for the numerical calculations, the open-source code OVITO (Stukowski, 2010) for the visualisation and MATLAB (Hinkle, 2020, MATLAB, 2022) for the postprocessing of the simulation data.

5.4 Results and Discussion

5.4.1 Comparison of Different Motility Patterns on the Drug Release/Disintegration on the Tablet at Different Fluid Viscosities

To assess the influence of the fluid viscosity on the drug release of a tablet in the colon environment, we performed all simulations at three different fluid viscosities: low viscosity ($\eta_L = 1$ mPa s), moderate viscosity ($\eta_L = 13$ mPa s) and high viscosity

($\eta_L = 98 \text{ mPa s}$). In all three cases, the dissolution process of the tablet, driven by pure diffusion, is represented by a so-called ‘Static’ model. In this model, the membrane does not move at all. Accordingly, no momentum is generated that moves the fluid. At low fluid viscosity conditions (Figure 5.7), after a certain time, all motility patterns cause the fluid to move in the colon.

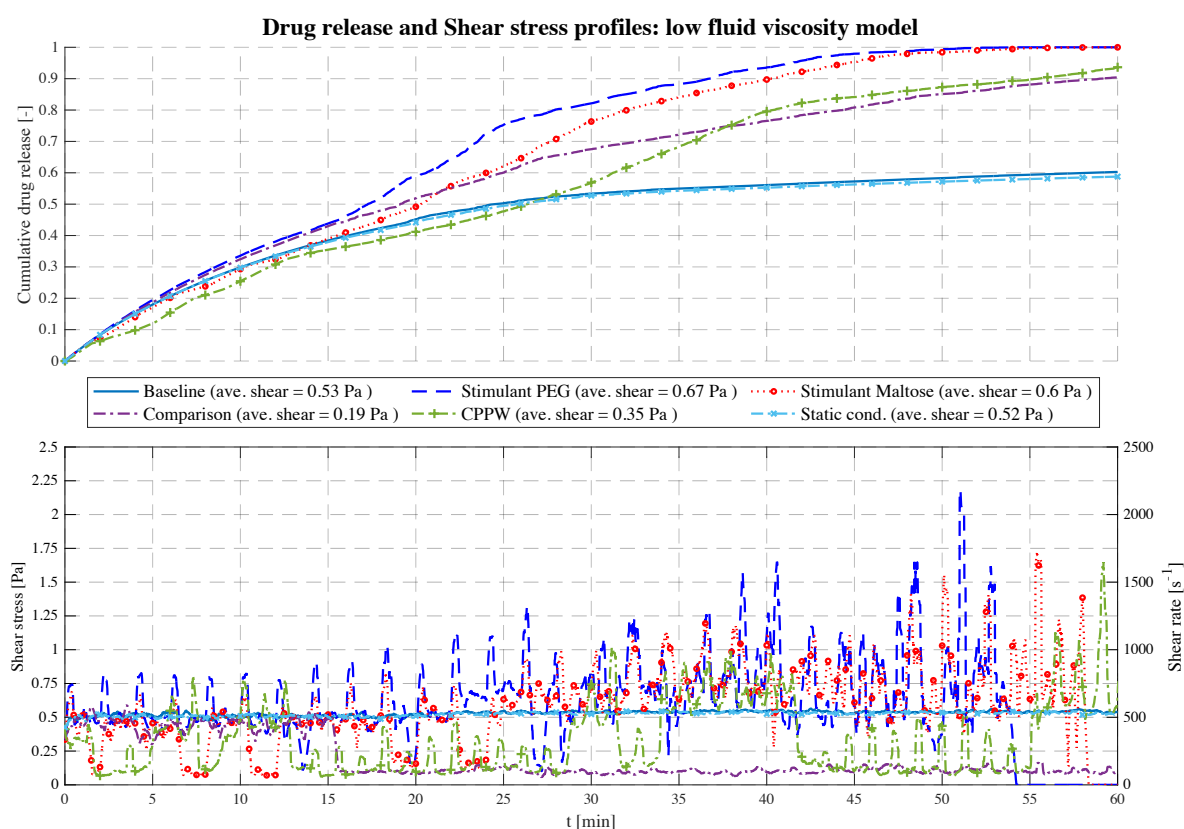


Figure 5.7 Comparison of the drug release profile of the different models at medium fluid viscosity conditions as well as the comparison of the shear stress/shear rate acting on the tablet.

Until $t = 18 \text{ min}$, in all models, the drug release of the tablet is driven almost by pure diffusion as the drug release profile has the same progression as the ‘Static’ model. The slope of the ‘CPPW’ model is not as steep as in the other models since the tablet is pushed to the surface and, thus, is not in complete contact with the fluid. From

$t = 18$ min on, the shear stress becomes a significant factor. In all models, the momentum caused by the different motility pattern is strong enough to set the fluid in motion. Even though the average shear stress does not differ significantly from model to model (see legend Figure 5.7), recurring shear stress peaks enhanced drug release. Additionally, small fluid motions, such as those that occur in the 'Baseline' model, lead to somewhat higher advection-induced mass transfer and thus to a higher release rate of the tablet compared to the 'Static' model. In a low viscous fluid environment, a complete dissolution of a tablet is only achieved, in the case of the 'Stimulant PEG', 'Stimulant Maltose' motility pattern. Figure 5.7 shows how the shear stress acting on the tablet increases with time as the wall motion transfers more and more momentum to the fluid. In the case of the 'Comparison' pattern, the tablet is pushed back and forth until $t = 15$ min, where the tablet is pushed to the end next to the initial position of the tablet, where the tablet remains until the end of the simulation. Here, the tablet does not receive significant momentum from the contractions, but some fluid still flows around it which leads to an increased advection-induced mass transfer and thus to a higher drug release. The sparse shear stress peaks in the 'CPPW' model are observed because only one wave is travelling from one end of the colon to the other, and always in one direction. Thus, at low fluid viscosity condition, the momentum induced by the wave reaches the tablet only occasionally.

When comparing the three different motility patterns found in (Hoad et al., 2016, Marciani et al., 2014, Stamatopoulos et al., 2020), at low fluid viscosity conditions, it can be seen from Figure 5.7 that the drug release profile of the 'Stimulant PEG' and 'Stimulant Maltose' model do not show significant differences (i.e., $f_1 = 12.0\%$, $f_2 = 57.7\%$). The drug release rate of the 'Stimulant PEG' model is somewhat higher

than the 'Stimulant Maltose' model where the drug is completely released from the tablet at $t = 54$ min and $t = 59$ min, respectively. The release rate in the 'Baseline' model is much smaller than in the other two models and does not deviate much from the 'Static' model (i.e., $f_1 = 1.6\%$, $f_2 = 93.9\%$).

At higher viscosities (Figure 5.8) the fluctuations of the shear stress decrease and the drug release profiles become similar (i.e., PEG - Maltose: $f_1 = 2.5\%$, $f_2 = 87.9\%$; PEG - CPPW: $f_1 = 6.2\%$, $f_2 = 68.5\%$; Maltose - CPPW: $f_1 = 6.8\%$, $f_2 = 69.5\%$; Static - Baseline: $f_1 = 1.3\%$, $f_2 = 97.8\%$).

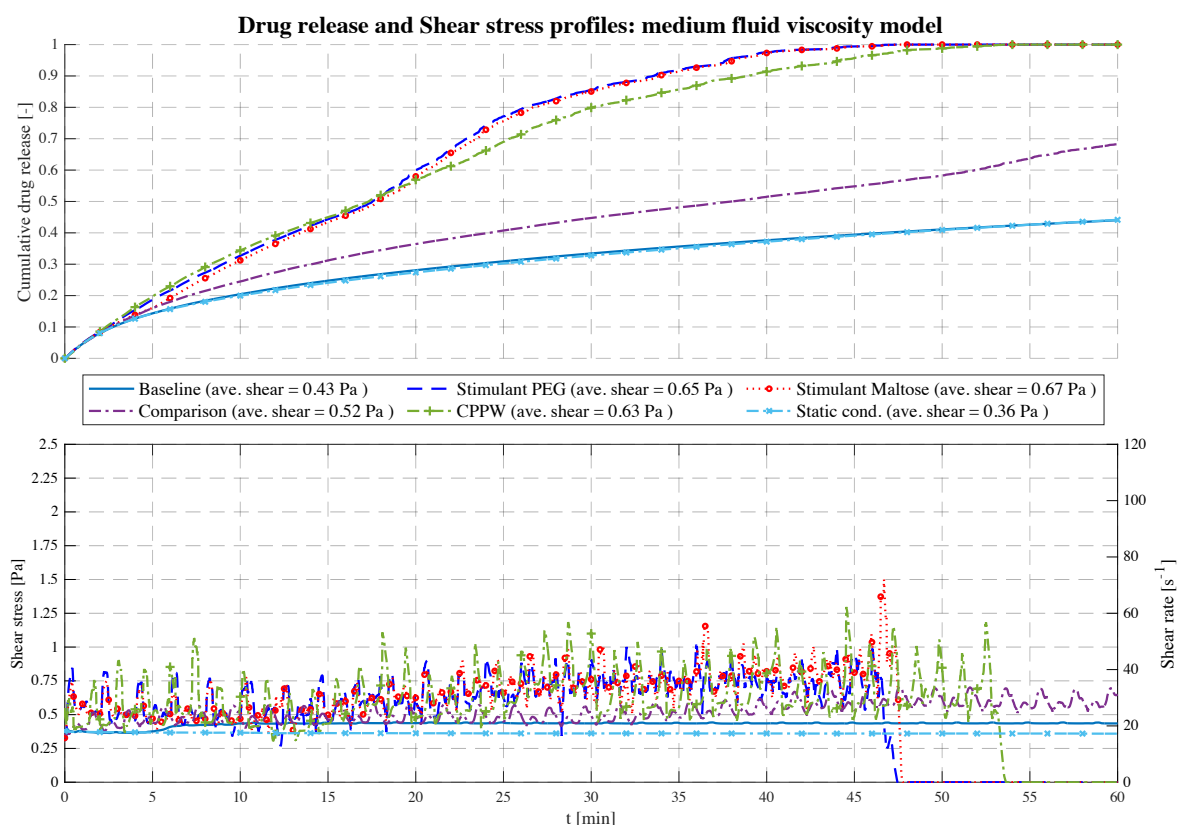


Figure 5.8 Comparison of the drug release profile of the different models at high fluid viscosity conditions as well as the comparison of the shear stress/shear rate acting on the tablet.

The most pronounced effect is in the 'Comparison' model where the drug release of the tablet decreases significantly compared to the low viscosity model. Only the momentum generated from the motility patterns of the models 'Stimulant PEG', 'Stimulant Maltose' and 'CPPW' are strong enough to agitate the fluid sufficiently with regard to an increased advection and thus accelerated drug release rate. In all three models, the increased drug release rate leads to complete disintegration of the tablet within the simulation time ($t = 54$ min). The most significant effect can be seen in the case of the 'CPPW'. At higher viscosity, the tablet is not pushed to the surface of the fluid and remains in the fluid for the majority of the time.

The comparison of the 'Stimulant PEG', 'Stimulant Maltose' and 'Baseline' cases at moderate fluid viscosities shows that the 'Stimulant PEG' and 'Stimulant Maltose' model has almost the same drug release profile. In both models, the drug of the tablet is completely released at $t = 48$ min. Since in the 'Baseline' model the impulse induced by the contraction is not sufficient to move the fluid, the drug release profile shows the same progression as the 'Static' model.

In the case of the highest fluid viscosity used in this study (Figure 5.9), the motility pattern of the 'CPPW' model is the only pattern capable of agitating the fluid at a high level, generating sufficient shear stress to promote the drug release process and lead to almost complete drug release of the tablet.

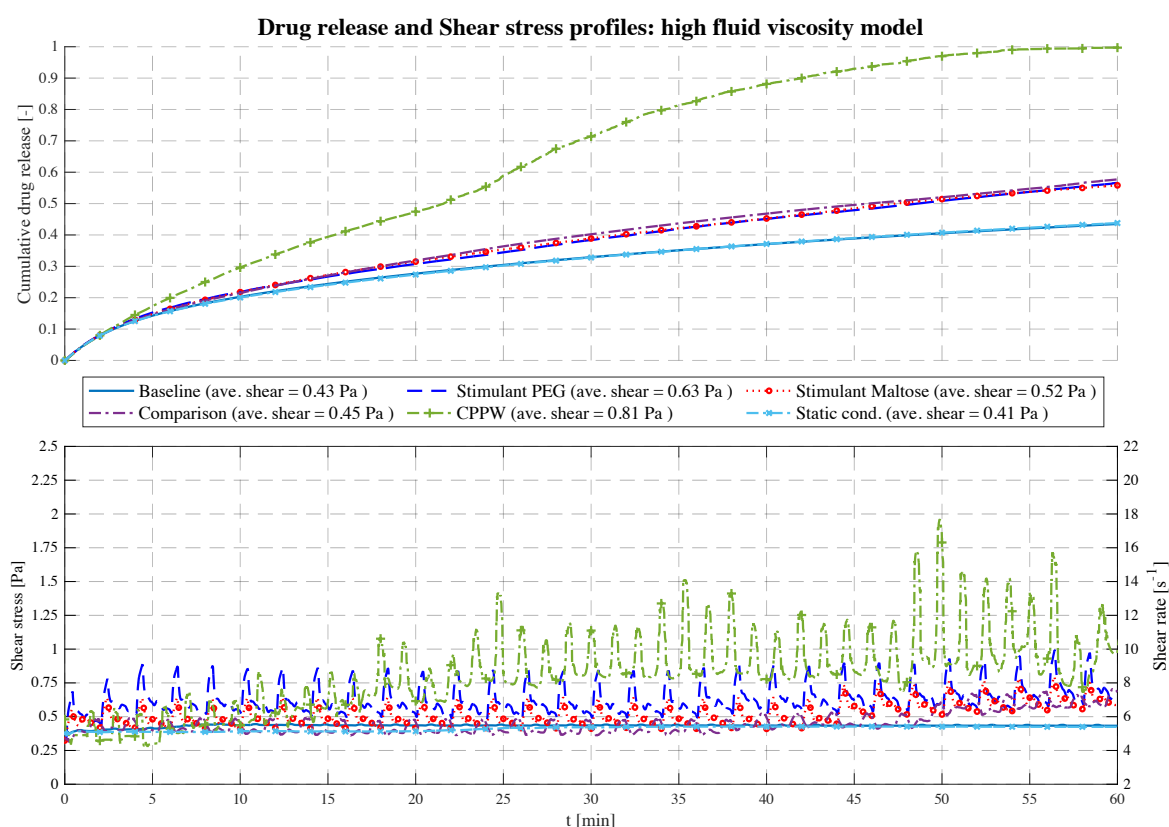


Figure 5.9 Comparison of the drug release profile of the different models at high fluid viscosity conditions as well as the comparison of the shear stress/shear rate acting on the tablet.

The contractions performed in the ‘Baseline’ model do not influence the drug release process. The impulse they generate is too weak to induce any influential fluid motion. At high viscosity conditions, the motility patterns in the ‘Stimulant PEG’, ‘Stimulant Maltose’ and ‘Comparison’ models result in almost the same drug release profile (i.e., Comparison - PEG: $f_1 = 3.1\%$, $f_2 = 89.1\%$; Comparison - Maltose: $f_1 = 2.0\%$, $f_2 = 95.1\%$; PEG - Maltose: $f_1 = 1.1\%$, $f_2 = 97.5\%$), even though they show partly different drug release profiles at lower viscosities.

The average shear stresses for each model and each viscosity are given in Figure 5.7, Figure 5.8 and Figure 5.9. Across all models and viscosities, we found 120 Pa for the maximum local shear stress acting on the surface of the tablet. These values correspond

very well with the shear stresses found in other studies, even though they focused on the stomach (Abrahamsson et al., 2005, Kindgen et al., 2015).

The shear rates acting on the tablet fluctuate sharply between 100 and 2170 s⁻¹ at low fluid viscosity, between 18 and 70 s⁻¹ at medium viscosity and between 5.5 and 18 s⁻¹ at high fluid viscosity. In the USP II, the shear rates are constant for a given location in the vessel and increase proportionally to the paddle speed (Salehi et al., 2020). The shear rates found in the USP II at fluid conditions comparable to the 'low viscosity model' are in the range of 5 s⁻¹ at 25 rpm and 250 s⁻¹ at 200 rpm paddle speed (Baxter et al., 2005, Hopgood et al., 2018, Kukura et al., 2004, Salehi et al., 2020). The linear shear rate profile of the USP II is not characteristic of the colonic environment, where the motility pattern evokes sharp shear rate spikes that significantly affect the dissolution/disintegration process. Especially at low fluid viscosity, the hydrodynamic parameters (i.e., shear rate and fluid velocity) enhance the dissolution/disintegration rate.

In addition to the dissolution profile, the degree of disintegration or the disintegration time for the complete disintegration of the solid dosage form (tablet) are also important parameters influencing the drug release rate. The corresponding results of all motility patterns/models and all fluid viscosities are summarised in Table 5.6.

Table 5.6. Disintegration degree or disintegration time of the solid dosage form (tablet) for all models/motility patterns at different fluid viscosities: % = degree of tablet disintegration φ at $t = 60$ min in %; min = time in minutes until complete tablet disintegration.

Model/Motility Pattern	Low Viscosity	Medium Viscosity	High Viscosity
Static	15%	0%	0%
Baseline	16%	0%	0%
PEG	54.3 min	45.6 min	16%
Maltose	58.4 min	46.1 min	13%
Comparison	81%	47%	33%
CPPW	93%	53.7 min	57.8 min

5.4.2 Comparison of the API Distribution along the Colon

Standard dissolution/drug release profiles, as commonly performed to access the properties of a solid dosage form, do not give any valuable information about the concentration gradient of the API along the colon. This information is important to determine the efficacy of the API in terms of drug absorption. To gain more insight into the concentration gradient along the colon, we divided the colon into six equal sections to see how the API concentration is distributed over time. Here, section one includes the initial position of the tablet and section six is at the end of the colon. The comparison and analysis of the concentration in each section and model are carried out at four different time points and the three different fluid viscosities: low viscosity, medium viscosity, and high velocity.

At low fluid viscosity (Figure 5.10) the models: 'Stimulant PEG', 'Stimulant Maltose', 'Comparison' and the 'CPPW' model can distribute the API completely along the whole colon at $t = 60$ min, but only the 'Stimulant PEG', 'Stimulant Maltose' and 'CPPW' models show a very uniform API distribution.

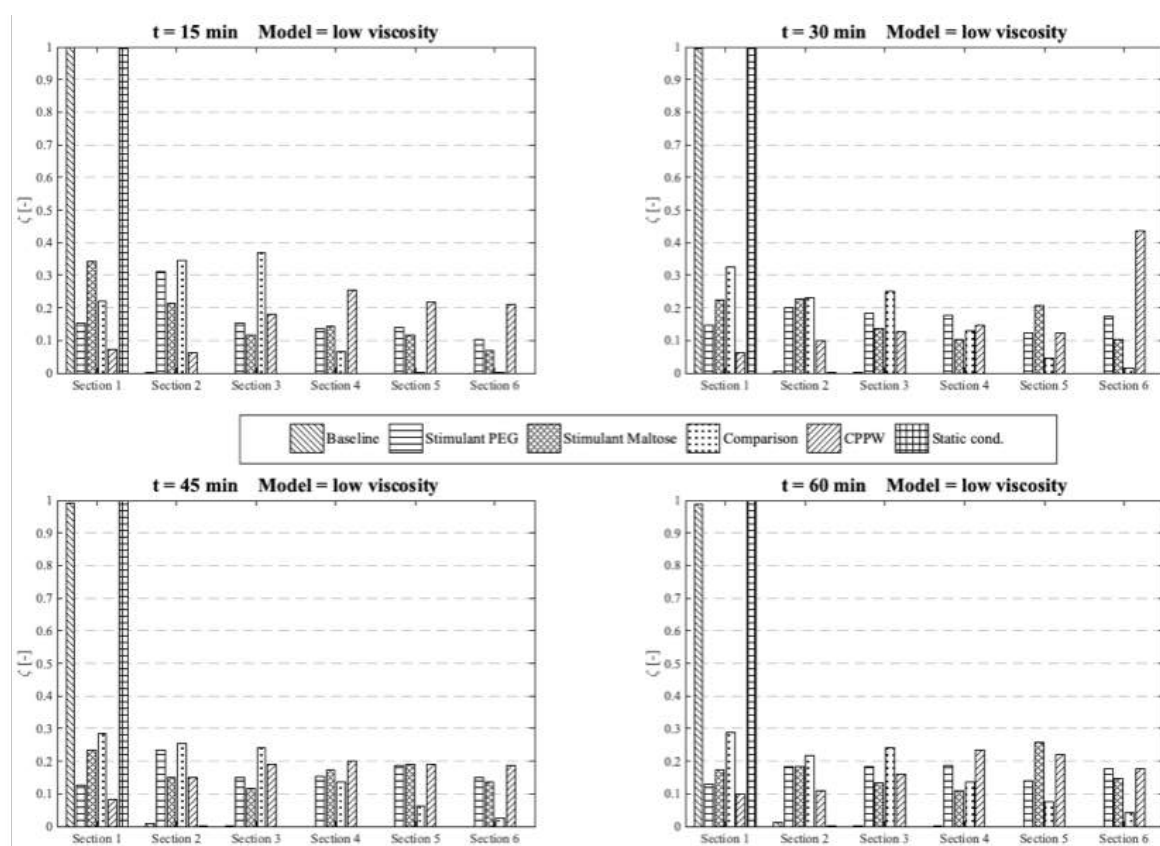


Figure 5.10 Comparison of the different models in respect to the distribution of the API along the colon at four different times at low fluid viscosity conditions.

These are also the models which achieved the highest drug release from the tablet (Figure 5.7). The 'Comparison' model is not as effective as the other three models in terms of API distribution, which means that in this model only a small part of the API reaches the last section at the end of the colon.

Since the wave in the 'CPPW' model only propagates in one direction (antegrade), the tablet is pushed to the end of the colon and dissolves there. Thus, the highest concentration in the course of the simulation (e.g., $t = 30$ min) is found at the end of the model. A backflow caused by the wave prevents the accumulation of the API at the end of the colon.

The 'Baseline' model is only able to transfer parts of the dissolved API into the sections one to four whereby the largest amount of dissolved API remains in the first segment.

At medium fluid viscosity conditions (Figure 5.11), at $t = 60$ min, only the ‘Stimulant PEG’, ‘Stimulant Maltose’ and ‘CPPW’ models distribute a notable portion of API along the entire colon.



Figure 5.11 Comparison of the different models in respect to the distribution of the API along the colon at four different times at medium fluid viscosity conditions.

In terms of uniform distribution of API across all segments, only the ‘Stimulant PEG’ and ‘Stimulant Maltose’ model show good results. As already seen at low viscosity conditions, in the ‘CPPW’ model the tablet is captured by the wave and pushed to the end of the colon where it dissolves. As the reflux is less pronounced at higher fluid viscosity conditions, at $t = 60$ min, the API accumulates in the last three sections of the colon. Nevertheless, the reflux generated in this model influences the mixing of the intestinal contents. By extending the simulation time, the reflux would very likely lead to an even API distribution along the colon. At the end of the simulation time, the

'Comparison' model is capable to distribute a notable amount of dissolved API across the first four segments, whereas the largest fraction remains in the first segment. The 'Baseline' model is not even capable to move a fraction of the dissolved API in the neighbouring segment.

In the case of high fluid viscosity conditions (Figure 5.12), only the motility pattern of the 'CPPW' model can distribute a significant amount of dissolved API across all segments.

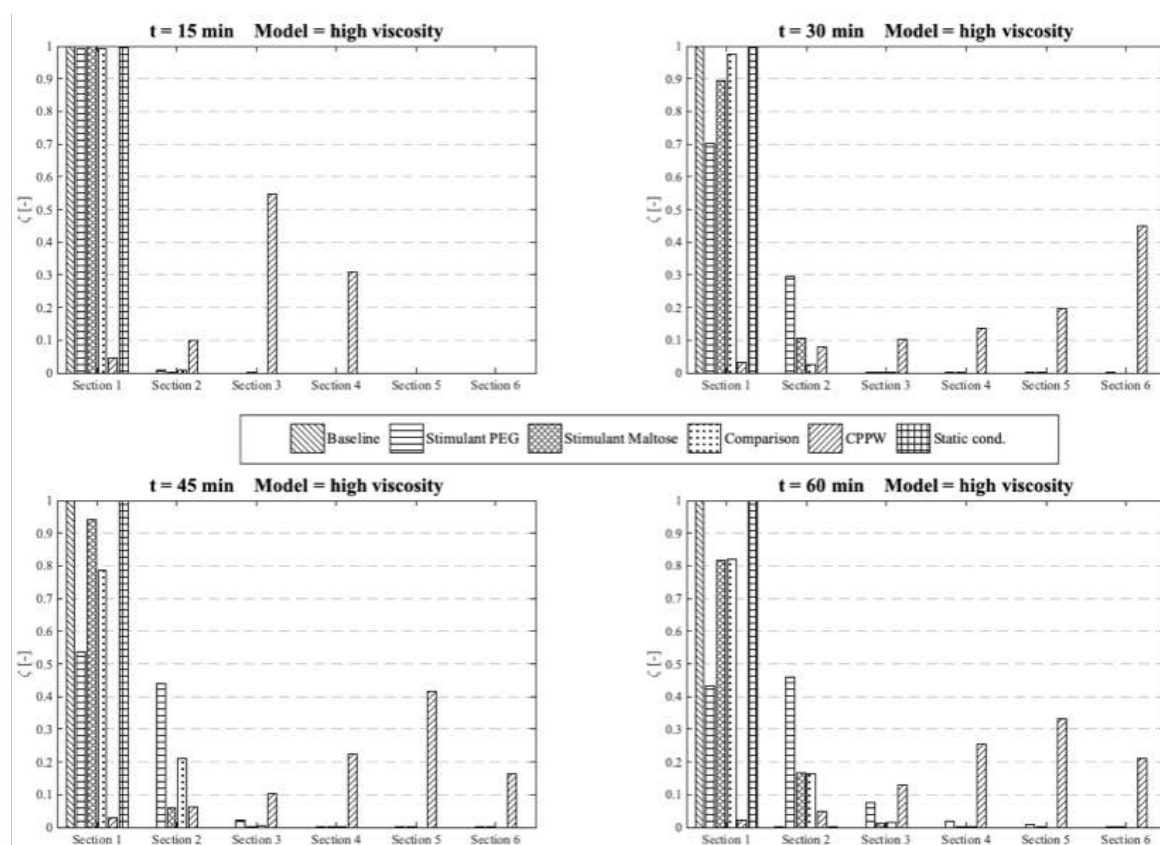


Figure 5.12 Comparison of the different models in respect to the distribution of the API along the colon at four different times at high fluid viscosity conditions.

As expected, the motility pattern of the 'Baseline' model does not distribute the dissolved API. The 'Comparison' model moves some dissolved API in segment two to four, but a notable amount is only found in segments one to three. The 'Stimulant

Maltose' model is comparable with the 'Comparison' model with the small difference that the 'Stimulant Maltose' model also distributes a very small amount of API into segments five and six. The relative amount of API in sections one to three is in both models almost the same. The 'Stimulant PEG' model can move a significant amount of dissolved API into the second segment and still a small but noteworthy amount into the third and fourth segment. The API amount in segment five and six is very small, but still, a very small amount reaches these segments.

The results show that the effectiveness of the motility pattern in terms of API distribution along the colon is highly dependent on the viscosity of the intestinal content. Contrary to the assumption that the motility pattern with the highest average shear stress automatically indicate the fastest drug release rate, the motility pattern that provokes frequent single shear stress peaks seem to be more effective in achieving a higher drug release rate. Another important parameter in terms of tablet drug release is the position of the tablet and the motility pattern itself. To achieve a faster tablet drug release compared to pure diffusion ('Static' model), the tablet must be in a region in which it can be caught by the motility pattern. When we compare the three different motility patterns found in (Hoad et al., 2016, Marciani et al., 2014, Stamatopoulos et al., 2020) in terms of their performance in drug release and drug distribution, the parameters described above play a crucial role. The motility pattern shows different performances in terms of tablet drug release and also in terms of the distribution of the dissolved drug. The motility pattern of the 'Baseline' model is extensively ineffective compared to the other two motility pattern found. The motility patterns of the 'Stimulant PEG' and 'Stimulant Maltose', on the other hand, show very similar performances in terms of tablet drug release. The motility pattern 'Stimulant PEG'

seems to be marginally more efficient in terms of drug distribution along the colon at higher viscosities.

The 'Baseline' motility pattern is the most predominant environment in a healthy human. As shown in the results, at higher fluid viscosities, the 'Baseline' motility pattern is not able to induce any influential fluid motion that would significantly affect the disintegration/drug release process. This biorelevant knowledge cannot be easily assessed with compendial disintegration/dissolution apparatuses which makes the *in silico* model valuable. From the results, it can deduce that care should be taken for the formulation design to mitigate prolong and/or partial disintegration/drug release.

5.4.3 Influence of the Diffusion Coefficient on the Drug Release from Tablet

As mentioned above, the required computational time is significantly higher when a lower diffusion coefficient is used, and complete drug release of the tablet is aimed for - at least for some motility patterns. Additionally, the tablet should dissolve in about one hour, which is not achievable with a low diffusion coefficient.

To estimate the impact of diffusion coefficients that differs by one order of magnitude on the drug release process in the models used in this study, we performed a dimensional analysis of the system and additionally ran simulations of each model for 10 days, regardless of how much time can be simulated in that period - this also varies from model to model. For this reason, the drug release profiles/results represented in Figure 5.13 may not show results for the entire time axis.

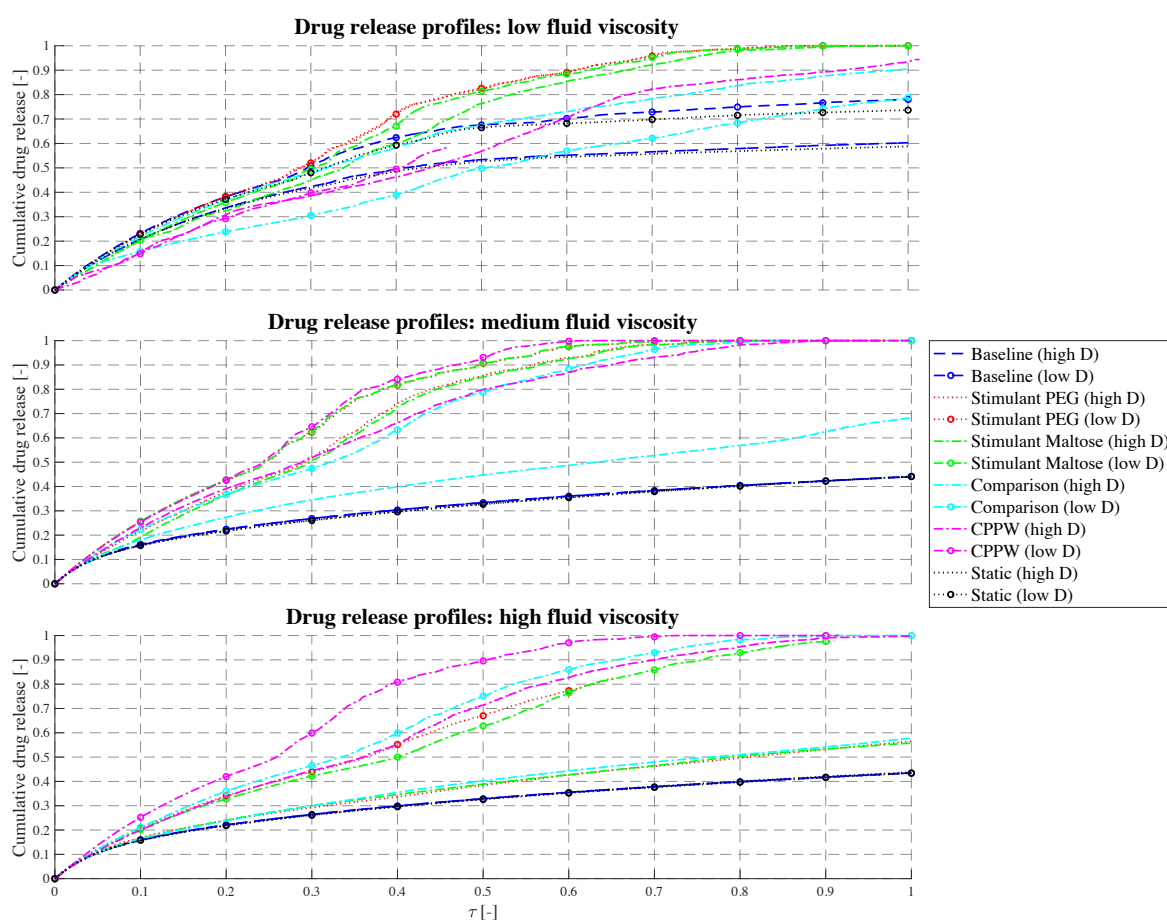


Figure 5.13 Comparison of the influence of different diffusion coefficients on the drug release profiles, where 'high D ' represents the drug release profile of the high diffusion coefficient and 'low D ' the drug release profile of the low diffusion coefficient simulation.

However, the target simulation time was 10 h (i.e., also one order of magnitude higher than in the case of high diffusion coefficient used). Results from the dimensional analysis confirm that it is possible to compare disintegration/dissolution profiles between different diffusion coefficients by proportionally rescaling time. Further detail of the analysis can be found in Chapter 5.7. From the dimensional analysis, it can be obtained that the differences of the curves shown in Figure 5.13 are resulting from the fluid dynamics in the colon as the diffusion coefficient and time are scaled proportionally.

The different models (motility pattern) and different diffusion coefficients are compared based on dimensionless time (Equation (5.22)).

In the simplest case, which is the 'Static' model, the drug release profiles coincide at medium and high fluid viscosities very well, which should be the case as the diffusion and time are proportional. In the case of low fluid viscosity, the drug release profiles are slightly different but show almost parallel curves. In this case, even if there is no fluid movement, the tablet can move very slightly, especially when it releases drug particles and the size of the tablet changes. These very small movements can result in a very small amount of advection in addition to diffusion and cause the difference in drug release profiles. As soon as a fluid motion occurs, introduced by the different motility pattern, the driving parameter in terms of drug release is very much dependent on the position of the tablet and on how the accelerated fluid can reach the tablet. At low fluid viscosity conditions, the tablet tends to be pushed to the surface of the fluid which slows down the drug release rate and consequently the dissolution rate. This phenomenon can especially be recognised in the 'Comparison' model, where a higher drug release can be achieved at higher diffusion coefficient conditions. In the case of a lower diffusion coefficient but longer simulation time, the worst case with regard to drug release has occurred. The tablet is pushed to the surface of the fluid and additionally into a region where the fluid circulation is quite low. Even the fact that significantly more fluid movement can be achieved in 10 h compared to 1 h, and thus the drug release rate should be higher with lower diffusion coefficients, is not given in this case. Here, diffusion is the driving parameter. The increased proportion of advection, due to prolonged fluid movement, in addition to pure diffusion is particularly well seen in the models with higher fluid viscosities. Here, in all cases, a higher or/and faster relative drug release could be achieved with lower diffusion and

longer simulation time compared to the case of the higher diffusion coefficient and shorter simulation time.

5.4.4 Strength and Limitations of the Model

The strengths of the model include that the anatomy, fluid volumes and motility patterns are informed by robust clinical data. The model presented within this paper is capable of simultaneously capturing data on drug dissolution and distribution within the ascending colon under a range of motility patterns and fluid viscosities. Generation of such data *in vivo* is complex due to the relative inaccessibility of the ascending colon plus the complexity in controlling either fluid viscosity or motility. However, it is recognised that validation of the model against clinical data would offer great benefits in demonstrating the utility of the model.

In the absence of clinical data that directly replicates observations in the model correlations have been sought from the most relevant literature to demonstrate the utility of the developed model. A comparison of 5-ASA pharmacokinetics in healthy adults; adults with CD and adults with UC showed that the time to reach the colon was faster with greater overall exposure for the diseased patients compared to the healthy controls (Norlander et al., 1990). This increased exposure is likely to be due to a combination of factors: an increase in permeability due to the inflamed mucosa or the reduction in viscosity of the colonic fluids in patients with CD or UC or the greater frequency of propagating contractions in the colon (Effinger et al., 2020a, Effinger et al., 2020b). The impact of reduced viscosity and greater frequency of contractions provides consistency with our model. The regional colonic distribution of material has

been shown to differ between healthy adults and those with UC where those with UC had a significantly lower percentage in the left side of the colon compared to controls (Hebden et al., 2000). The rapid transit observed in UC as a result of greater motility would explain these data, which is consistent with the findings from our model.

The rapid distribution of material within the ascending colon was demonstrated in a paper using scintigraphy to visualise mesalamine microspheres where complete distribution was observed within 30 min of entry to the ascending colon (Sinha et al., 2003) which is consistent with the low viscosity scenario presented within our model. Thorpe et al. (Thorpe et al., 2009), using a dynamic model of colonic concentrations that mimics published transit time data, reported that the distribution of 5-ASA within the colon was shown to change in response to a change in motility patterns with reduced motility resulting in higher concentrations of 5-ASA (Thorpe et al., 2009) which is also consistent with data from our model. This work considered a simple immediate release formulation as a first step in the development of the model. Future work will include evaluation of alternative formulations that target the colon, particularly formulations where clinical data is available so that the output can be compared to the existing clinical data.

5.5 Conclusions

This study describes the development of a computational model to describe the drug release from and the disintegration of a solid dosage form (tablet) and the distribution

of the API in the environment of the ascending colon. The model considers different motility patterns as well as different fluid viscosities.

The relationships between fluid viscosity, motility pattern, and consequently tablet drug release/disintegration and distribution along the ascending colon are investigated. For the targeted drug delivery predictions, conventional *in vitro* dissolution tests are commonly performed under standardised conditions and limited abilities to mimic the real colonic conditions. In particular, this applies to the different motility patterns that occur in the colonic environment (Long and Chen, 2009). Our results show how the combination of different motility patterns and fluid viscosities exerts different shear stresses on the tablet, resulting in different drug release rates and different drug distributions along the colon. Compared to the standard drug dissolution tests and apparatuses currently in use (Long and Chen, 2009), our model not only provides a more realistic environment but also an enhanced insight into the dissolution/drug release process itself, that to the best of our knowledge, represents the first step towards the ability to create spatiotemporal tablet drug release profiles. Since it can replicate almost any motility pattern, including propagating distance, propagating velocity, propagating direction or even single contractions and different occlusion degrees, the model allows to assess how different motility patterns affect the dissolution process of a solid dosage form. Additionally, of interest is the inter-individual variability, and this model can predict (to some extent) the variability for a given dosage form in a range of people. From the results, we can conclude that the movement of the fluid, caused by the different motility patterns, is one of the most important parameters in terms of drug release, besides diffusion, and the most important parameter when the tablet is exposed to the fluid flow. The model provides further insight into whether the motility pattern can transport the drug in the desired

concentration to the sites to be treated. The results obtained can be of great importance for both medical research and pharmaceutical applications, especially for the design and optimisation of a modified release dosage form.

5.6 Supplementary Materials

The following are available online at <https://www.mdpi.com/article/10.3390/pharmaceutics13060859/s1>, Video S1: Example 1, how the tablet moves back and forth in the colonic content (section from the simulation 'Stimulant PEG' at medium fluid viscosity), Video S2: Example 2, how the tablet moves back and forth in the colonic content (section from the simulation 'Stimulant Maltose' at medium fluid viscosity), Video S3: Section from the simulation 'CPPW' at low fluid viscosity, where the tablet is pushed to the surface of the fluid, Video S4: Section from the simulation 'CPPW' at medium fluid viscosity, where the tablet remains in the fluid.

5.7 Appendix A: Dimensional analysis of the system

According to the Buckingham π theorem, a physically meaningful equation involving n of physical variables can be rewritten in terms of a set of $p = n - k$ dimensionless parameters $\Pi_1, \Pi_2, \dots, \Pi_p$, where k is the number of physical dimensions involved.

In the case under investigation, ideally the results can be expressed as mathematical function f of the type

$$t = f(v, h, d, \mu, \rho, D, R, L) \quad , \quad (5.24)$$

where all the variables and their respective physical units are reported in Table 5.7 and shown in Figure 5.14. Since there are 9 variables and 3 units, the Equation (5.24) can be based on 6 dimensionless parameters be rewritten as:

$$\Pi_1 = \varphi(\Pi_2, \dots, \Pi_6) \quad , \quad (5.25)$$

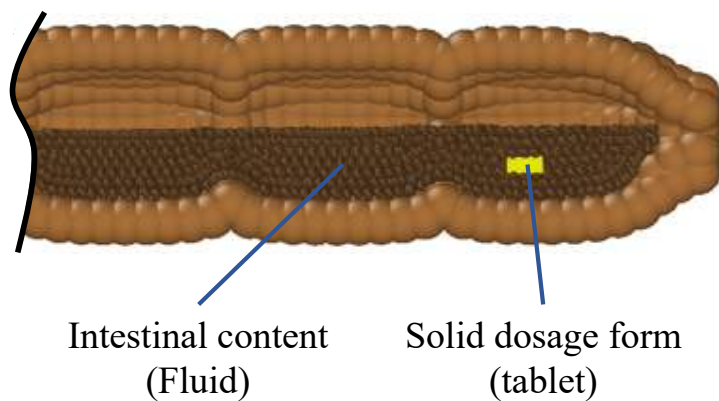


Figure 5.14 System parameter for the Dimensional Analysis.

Table 5.7. Variables for the Dimensional Analysis.

	Variable	Unit	Description
(1)	t	s	dissolution time
(2)	v	m s^{-1}	velocity of wave
(3)	h	m	thickness of tablet
(4)	d	m	diameter of tablet
(5)	μ	$\text{kg m}^{-1} \text{s}^{-1}$	dynamic viscosity
(6)	ρ	kg m^{-3}	density
(7)	D	$\text{m}^2 \text{s}^{-1}$	diffusion coefficient
(8)	R	m	radius of colon
(9)	L	m	length of colon

Table 5.8 shows a possible way to combine the nine dimensional variables into six dimensionless parameters. As it can be seen, with a fixed radius R , the dimensionless time Π_1 is proportional to the diffusivity, which justify the use of

$$t_0 \propto \frac{R^2}{D} \quad (5.26)$$

in Equation (5.23).

Table 5.8. Dimensionless variables for the Dimensional Analysis.

$\Pi_1 \propto \frac{t D}{R^2}$	$\Pi_2 \propto \frac{R}{L}$	$\Pi_3 \propto \frac{d}{h}$
$\Pi_4 \propto \frac{d}{L}$	$\Pi_5 \propto \frac{R v}{D}$	$\Pi_6 \propto \frac{\rho v R}{\mu}$

Chapter 6

Simulating the Hydrodynamic Conditions of the Human Ascending Colon: A Digital Twin of the Dynamic Colon Model

Published article:

Pharmaceutics 14 (2022)

6.1 Abstract

The performance of solid oral dosage forms targeting the colon is typically evaluated using standardised pharmacopeial dissolution apparatuses. However, these fail to replicate colonic hydrodynamics. This study develops a digital twin of the Dynamic Colon Model; a physiologically representative *in vitro* model of the human proximal colon. Magnetic resonance imaging of the Dynamic Colon Model verified that the digital twin robustly replicated flow patterns under different physiological conditions (media viscosity, volume, and peristaltic wave speed). During local contractile activity, antegrade flows of $0.06 - 0.78 \text{ cm s}^{-1}$ and backflows of $-2.16 - -0.21 \text{ cm s}^{-1}$ were measured. Mean wall shear rates were strongly time and viscosity dependent although peaks were measured between $3.05 - 10.12 \text{ s}^{-1}$ and $5.11 - 20.34 \text{ s}^{-1}$ in the Dynamic Colon Model and its digital twin respectively, comparable to previous estimates of the USP II with paddle speeds of 25 and 50 rpm. It is recommended that viscosity and shear rates are considered when designing future dissolution test methodologies for colon-targeted formulations. In the USP II, paddle speeds $>50 \text{ rpm}$ may not recreate physiologically relevant shear rates. These findings demonstrate how the combination of biorelevant *in vitro* and *in silico* models can provide new insights for dissolution testing beyond established pharmacopeial methods.

6.2 Introduction

In recent years, colon-targeted drug delivery has received increased attention due to regional conditions that present advantages for the delivery of certain types of pharmaceutical formulation compared to the small intestine (Sulaiman and Marciani,

2019, Watts and Illum, 1997). The hydrodynamics of the proximal colon are crucial for the design and optimisation of colon-targeted formulations, particularly in terms of disintegration, dissolution, and distribution of the dosage form. To gain a better understanding of the hydrodynamics and mixing conditions in the intestinal environment, *in vitro*, as well as *in silico*, studies have been carried out, focusing on both the colon (Alexiadis et al., 2017, Schütt et al., 2021, Schütt et al., 2020, Stamatopoulos et al., 2016b, Stamatopoulos et al., 2020) and the small intestine (Sinnott et al., 2012, Sinnott et al., 2017).

In Vitro dissolution apparatuses have historically been used for biopredictive testing. Although pharmacopeial dissolution apparatuses permit the control of media properties, the vessels bear little semblance to colonic geometry and use simplified mixing methods that fail to reproduce the hydrodynamic conditions of the human colon *in vivo* (Stamatopoulos et al., 2015, Wang et al., 2018). The Dynamic Colon Model (DCM), depicted in Figure 6.1, is a biorelevant *in vitro* model that replicates the architecture of the proximal colon and reproduces peristaltic/segmental activity (Stamatopoulos et al., 2016b, Stamatopoulos et al., 2020).

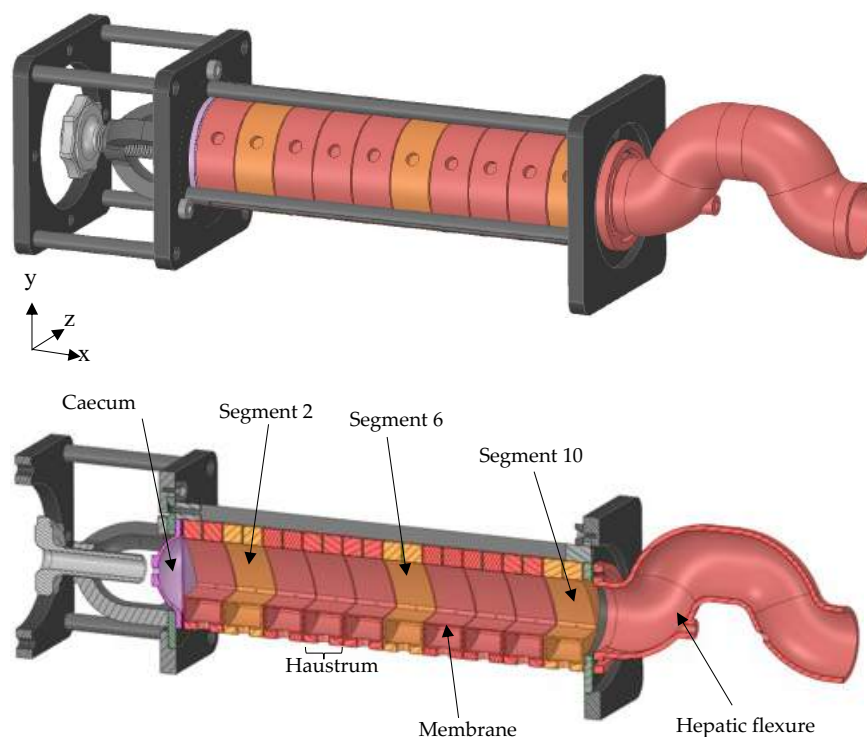


Figure 6.1 Schematic of the Dynamic Colon Model (DCM), Adapted from (O'Farrell et al., 2021). The DCM has a segmented appearance reflecting that of the human proximal colon: segment 1 is adjacent to the *caecum*, through to segment 10 adjacent to the *hepatic flexure*.

The design of the DCM was based on clinical data obtained from MRI images of the human (adult) proximal colon *in vivo*. The DCM is able to mimic the motor patterns of the colon, which mostly occur as propagating pressure waves (PPWs): one of the identified motor patterns in the colon (Dinning et al., 2014). The DCM is the most physiologically relevant *in vitro* colon model to date as it is the only model that replicates peristaltic motility in a lumen with the segmented architecture of the human colon (O'Farrell et al., 2021). A recent study has shown that when a PPW is applied to the DCM, the motion of the walls causes the contents of the lumen to flow in a way that closely reproduces the flow in the human proximal colon (O'Farrell et al., 2021, Wilson, 2010), verifying the hydrodynamics of the model.

In Vitro and *in silico* models that are based on *in vivo* data offer affordable alternatives to *in vivo* studies. Furthermore, *in vivo* studies are conducted, where possible, using

healthy volunteers, and this population does not represent the extremes of GI variability which are of interest in the design of a dosage form. The DCM can reproducibly replicate extreme GI motion. More advanced *in vitro* models that are physiologically representative offer the possibility of a deeper insight into *in vivo* conditions and therefore better understanding of the physical laws governing colonic space. This is especially important for pharmaceutical research and the development of new formulations of modified release solid oral dosage forms that reach the colon, as these data are necessary to predict release behaviour in the colonic environment.

Over the last few years, several *in silico* models of the human proximal colon have been developed (Alexiadis et al., 2021, Alexiadis et al., 2017, Schütt et al., 2020) based on a computational technique called Discrete Multiphysics (DMP) (Alexiadis, 2015a, Alexiadis, 2015b). Recently, this approach has been applied to the pharmaceutical field and used to model drug release from a solid dosage form under the influence of different *in vivo* motility patterns (Schütt et al., 2021). The major advantage of *in silico* models is that they are resource-saving compared to *in vitro* models and especially to *in vivo* experiments. Additionally, *in silico* models are highly versatile and provide additional insights that are difficult to acquire using common measurement techniques, often at resolutions that are equally unattainable. However, *in vitro* models are essential to make sure all relevant variables occurring in the real environment are accounted for, and to generate sufficient data to inform the development and the validation of their digital counterpart. Therefore, the quality and quantity of the data describing the colonic environment will always depend on the power of *in vitro* and *in silico* models. Together, myriad runs can be conducted, generating a high data output at low cost. This data is crucial for the pharmaceutical industry to create effective therapeutic delivery vehicles.

This study describes the development and validation of a digital twin (DT) of the DCM (DCMDT) using a particle modelling approach. The DCMDT is depicted in Figure 6.2.

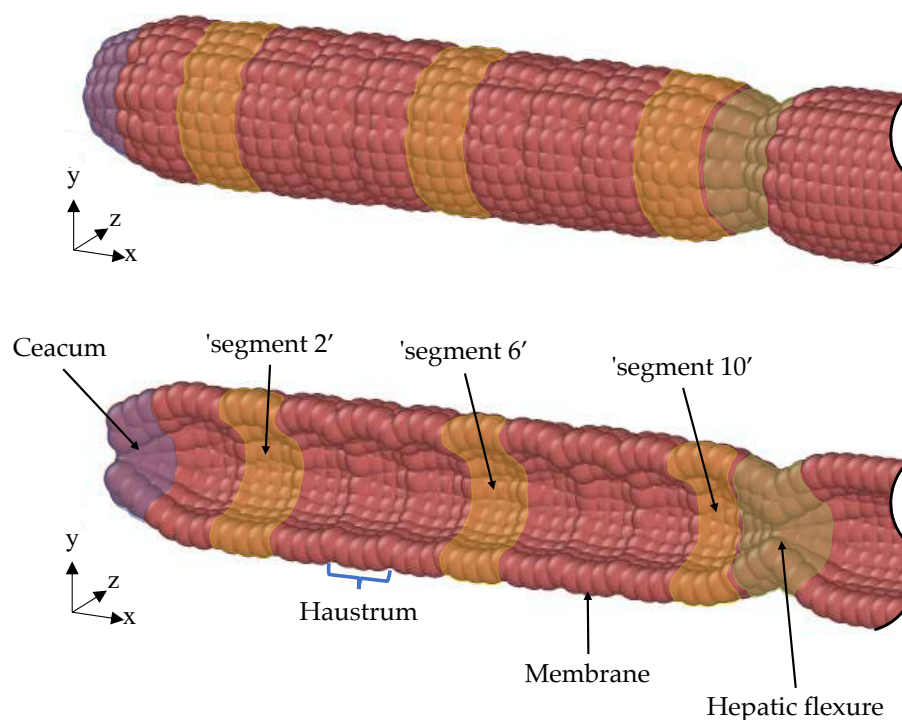


Figure 6.2 Schematic view (top) and a cross-sectional view (bottom) of the computational model (DCMDT). The DCMDT comprises 10 sections reflecting the DCM. Segment 1 is adjacent to the *caecum* and segment 10 is adjacent to the *hepatic flexure*. The *hepatic flexure* is modelled as a reduction to create a backpressure, guided by the *in vivo* situation.

The DCMDT is a digital informational construct of the physical DCM that exists in virtual space. It replicates the design and motility of the DCM and is similarly compatible with a range of fluids, which is achieved by modifying the physical properties of the computational fluid particles. Further details on the modelling methodology are given in Chapter 6.3.2.

The environmental conditions inside the lumen of the proximal colon are controlled by a range of factors, including but not limited to disease state, microbiota, prandial state, ingested food contents, and importantly, the inherent interindividual variation

(Vertzoni et al., 2019). The dynamic interplay of these influences can affect a wide range of parameters, which can ultimately be manipulated in the *in vitro* or/and *in silico* models. For example, media volume can change with prandial state and could affect the sink conditions of a formulation, resulting in accelerated or hampered release of the active pharmaceutical ingredient (API) which can influence bioavailability (Sinnott et al., 2017, Sulaiman and Marciani, 2019). Functional gastrointestinal disorders may affect the motility of the colonic walls; dampened motility may cause lower shear rates to be exerted on the surface of the dosage form, leading to incomplete release of the API. Contents of solid or liquid food ingested may affect the viscosity of the contents of the proximal colonic lumen (Vertzoni et al., 2019). A more viscous fluid demonstrates greater resistance to flow and may cause a different velocity profile in the lumen, affecting the transport and shear forces acting on a dosage form (Stamatopoulos et al., 2016b, Stamatopoulos et al., 2020).

The DCM and its DT permit the manipulation of these parameters individually, under fixed conditions, to scrutinise the effects. Thus, this study investigates how the interplay of media viscosity, media volume, and wall motility influence flows inside the DCM (Figure 6.1) and the DCMDT (Figure 6.2). This will facilitate assessment of the ability of the DCMDT to replicate the wall motion and the relationship this has with the flow of the contents. Flow analysis will cover the velocity and shear rate distributions at different locations along the models. Shear rates within the fluid determine the shear stresses exerted by the fluid on the surface of a dosage form in the colonic lumen, which governs the erosion of solid oral dosage forms inside the colon (Schütt et al., 2021). The ability of the DCMDT to extract shear rate data under a multitude of conditions with relative ease could establish it as a highly valuable tool to inform the design of formulations that are sensitive or insensitive to motion.

6.3 Methodology

6.3.1 Experimental work

Experimentally, a simulated antegrade PPW travelling from the *caecum* to the *hepatic flexure* was applied to the DCM and the velocity of the contents and the shear rate in the lower layer of fluid closest to the bottom wall were measured. The study investigated the effects of three factors: propagation speed of the contractile wall wave, media viscosity, and volume on the results as a full factorial design. *In vitro* measurements were made using phase contrast (PC) cine-MRI.

In the DCM, volume was varied from 150 to 200 mL, corresponding to filling levels of approximately 60% and 80% respectively. Viscosity was controlled by varying aqueous sodium carboxymethyl cellulose (NaCMC) concentration. The low viscosity fluid (LOVIS) consisted of 0.25% (w/v) NaCMC aqueous solution whilst the high viscosity fluid (HIVIS) was a 0.50% (w/v) NaCMC aqueous solution. Details of the fluids used are given in Chapter 6.3.2.2 'Fluid'. The motility pattern was varied by controlling the speed of the propagating wave along the DCM wall, varied between 0.4 and 0.8 cm s⁻¹. The occlusion degree was fixed at 60 ± 5% for each pattern.

6.3.1.1 MRI Protocol

Scanning was carried out using a 3T Philips Ingenia widebore scanner (Philips, Best, The Netherlands). Localiser scans were carried out prior to the tagging and PC scans for placement of these sequences across the DCM.

PC scans were conducted using a sequence adapted from a standard PC flow sequence that usually acquires multiple flow measurements in blood vessels throughout the cardiac cycle, described in detail in (Moser et al., 2000). In this work, a single fast field echo (FFE) image of 101×101 voxels was generated using flow-sensitive gradients. The scan was repeated for each parameter combination investigated. The parameters from the MRI scanner are shown in Table 6.1.

Table 6.1. MRI scanner parameters.

Parameter	Value
Scan duration [s]	60
TR [ms]	9.21
TE [ms]	7.60
FA [°]	10
FOV [mm ²]	177×200
Recon resolution [mm ²]	1.1×1.1
Slice thickness [mm]	8
SENSE	2.0
No. dynamics	30
Temporal Resolution [s]	2

Three different slice locations along the length of the DCM were used to investigate the spatial variation of the flow induced; at segment 2, close to the mimic *caecum*, segment 6, midpoint and segment 10, *hepatic flexure* (see Figure 6.1) sequentially with 10 s rest periods between scans. Following completion of all spatial locations for the default motility pattern, the protocol was repeated for the slower PPW. After completion of all scans, media volume and/or media type (LOVIS or HIVIS) were changed, and the protocol repeated. The flow was encoded only in the streamwise direction (x-axis). Maximum velocities were encoded at $\pm 3 \text{ cm s}^{-1}$ based on previous

work by O'Farrell et al. (O'Farrell et al., 2021). Positive and negative velocities represent flow along the x -axis towards the *hepatic flexure* and *caecum* (depicted in Figure 6.1) respectively.

To account for the background signal, initial velocity measurements were taken using PC cine-MRI prior to any induced motility (neutral wall position) when it was known the luminal contents were at rest. The mean velocity over the cross-sectional lumen flow area was close to zero at $4.32 \times 10^{-4} \text{ cm s}^{-1}$ with a standard deviation of $6.40 \times 10^{-3} \text{ cm s}^{-1}$. This standard deviation value was taken as the measurement error for a single voxel and hence accumulates in the error for PC cine-MRI mean velocity measurements.

6.3.2 Modelling Approach

The DCMDT employs Discrete Multiphysics (DMP), similar to Schütt et al. (Schütt et al., 2020). DMP is a meshless particle-based simulation technique where computational particles are used instead of a computational grid. DMP couples different particle-based modelling techniques, such as Smoothed Particle Hydrodynamics (SPH) Lattice Spring Model (LSM), and Discrete Element Method (DEM). The model in this study only accounts for SPH and LSM. SPH is used to model the fluid by calculating the viscous and pressure forces between the particles that represent the fluid. LSM is used to calculate the elastic forces between the particles that represent the solid walls of the DCM. The particle types and details of the model are highlighted in the cross section of the partially filled DCMDT in Figure 6.3. This partially filled state reflects the average situation where gas is also present in the colon.

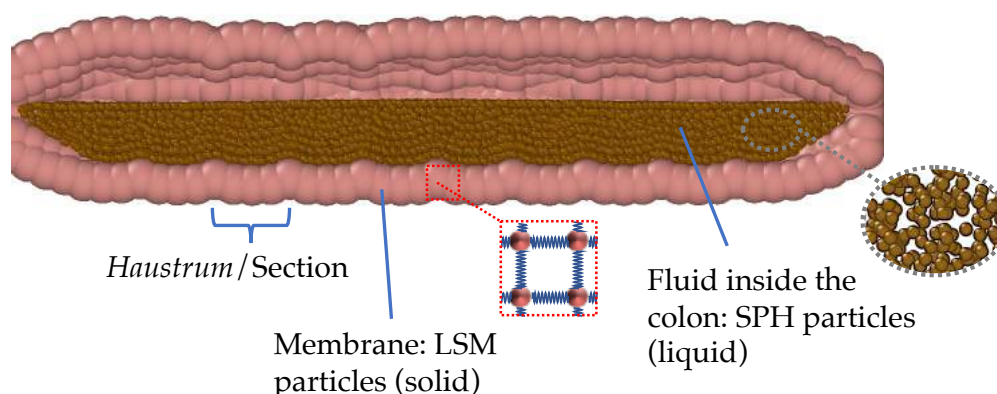


Figure 6.3 Particle representation of the model showing the colon *haustra*, the flexible membrane, and the fluid inside the colon.

Further details on the DT and the simulation parameters are given in Chapter 6.3.2.2. For a general overview on the DMP theory and how it can be applied to a variety of applications such as biological flows and/or fluid–structure interactions (Alexiadis et al., 2017, Ariane et al., 2017a, Ariane et al., 2018a, Ariane et al., 2017b, Baksamawi et al., 2021, Mohammed et al., 2020, Rahmat et al., 2019, Rahmat et al., 2020b, Schütt et al., 2020), solidification and dissolution (Alexiadis et al., 2018, Ariane et al., 2018b, Rahmat et al., 2020a), machine learning (Alexiadis, 2019b, Alexiadis, 2019a), and composite materials (Sanfilipo et al., 2021), the reader can refer to the available literature (e.g., DMP: (Alexiadis, 2015a, Alexiadis, 2015b), SPH: (Liu and Liu, 2003), LSM: (Kot et al., 2015, Lloyd et al., 2007, Pazdniakou and Adler, 2012)). For technical details and how it is applied to the large intestine, the reader is referred to Refs. (Alexiadis et al., 2021, Alexiadis et al., 2017, Schütt et al., 2020).

6.3.2.1 DCMDT Geometric Design

The DCMDT replicates the geometry and segmental appearance of the DCM, which is a biorelevant model of the human proximal colon (see Figure 6.1) (Stamatopoulos et al., 2016b, Stamatopoulos et al., 2020). It is composed of a cylindrical body with a total length of 0.622 m and an inner diameter of 4.0×10^{-2} m. Only 0.24 m of the total model represents the DCM whereas the remaining part serves as a 'drain tank' (Figure 6.4).

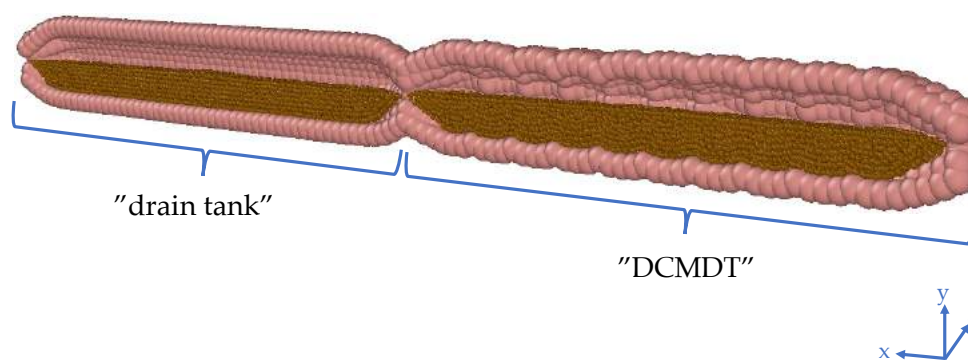


Figure 6.4 Cross section of the digital twin of the DCM and the 'drain tank'. The antegrade direction in this image is from the right to the left.

In the DCM, an antegrade PPW propels the fluid towards a rigid siphon that represents the *hepatic flexure* at the end of the DCM (see Figure 6.1); the sharp bend between the proximal and the transverse colon. Here, the fluid rises up the rigid siphon and falls back down when the PPW ends and the *haustra* return to the neutral position. The DCMDT is a closed system that mimics the presence of the *hepatic flexure* by separating the DCM-like compartment from the drain tank by constriction, enabling a small portion of fluid to escape the DCMDT lumen, if necessary, whilst still generating a back pressure when the wave reaches the end of the lumen.

The DCM consists of 10 individual segments of equal size. Each segment consists of three chambers, representing the sack-like *haustra* on the human colon, which are

controlled simultaneously to contract and relax the wall for each segment. In the DCMDT, the membrane is also divided into 10 segments of equal size. Each segment consists of 3 circular rings of 25 LSM 'wall' particles, one of which can be seen in Figure 6.5 (a).

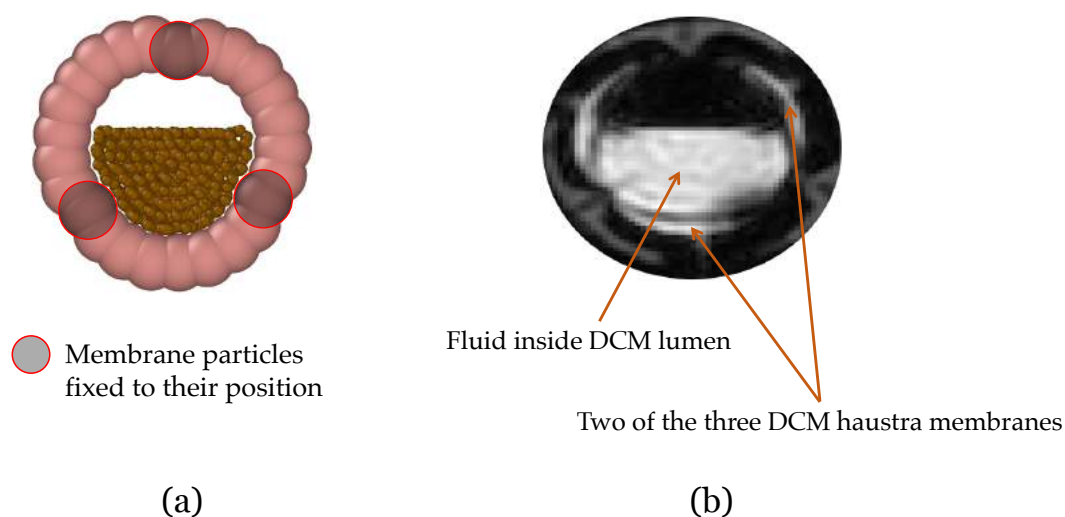


Figure 6.5 Shape of the segment during relaxing, where (a) is the computational model and (b) is a segment of the DCM.

To mimic the shape of the DCM segments during the relaxation and contraction phases, three particle rows along the DCMDT are fixed in position as highlighted in Figure 6.5 (a). This prevents them from moving during relaxation or contraction and consequently creates a similar three chamber system.

Membrane motion is segmental in that the rings inside each segment move together as one body through the radial axis, contracting and relaxing in response to the application of a positive or negative radial force and mimicking contraction and relaxation of the DCM membrane respectively. The radial motion of adjacent segments can be synchronised to replicate any DCM motility pattern in terms of contraction/relaxation pattern, luminal occlusion degree, and the speed that a contractile wave propagates along the colonic axis.

6.3.2.2 DCMDT and Computational Simulation Parameters

Membrane Design and Motility

The membrane is modelled similarly to (Schütt et al., 2020). The DCMDT membrane is represented by 975 LSM particles in total which are tethered to their initial position using a Hookean spring, so that the membrane particles return to their initial position after the activation by a radial force (i.e., contraction or relaxation). This also fixes the model in the domain during the simulation. Additionally, particles in close proximity are interconnected with an additional Hookean force. Analogously, the forces are calculated using Hooke's law:

$$F_{ij} = k(r_{ij} - r_0) \quad , \quad (6.1)$$

where F_{ij} represents the present spring force between particle i and j and k is the Hookean constant. The current distance between the particles i and j is represented by r_{ij} , while r_0 is the equilibrium distance between these particles. This creates a lattice structure that replicates the properties of an elastic solid (Kot et al., 2015). This approach has been used previously to model biological membranes (Mohammed et al., 2020, Mohammed et al., 2021). The Hookean coefficient used for the lattice is $k_{M,b}$, the coefficient used for the tethered springs is $k_{M,p}$. An additional viscous force

$$F_i = -k_{M,v}v_i \quad , \quad (6.2)$$

where v_i is the velocity of the particle, is added to the membrane particles to improve the stability of the simulation and simultaneously confer viscoelastic properties to the membrane as in (Sahputra et al., 2020).

Once the forces acting on each particle are calculated, the particles move according to the Newton equation of motion

$$m_i \frac{d\mathbf{r}_i}{dt} = \sum_j^N F_{ij} , \quad (6.3)$$

where \mathbf{r}_i is the position of particle i . The pattern of force application to the simulated wall follows that of the DCM, wherein the rate of relaxation from peak contraction to neutral position is slower than the rates of initial relaxation and contraction. This is intended to mimic the viscoelasticity of the intestinal wall *in vivo*. Further details of the simulated membrane are shown in Table 6.2.

Table 6.2. Model parameters of the membrane.

Parameter	Value
SPH	
Total number of membrane particles (one layer)	2500
Number of membrane particles (DCMDT)	975
Mass of each particle m	3.89×10^{-4} kg
LSM	
Hookean coefficient (bonds) $k_{M,b}$	0.1 J m^{-2}
Hookean coefficient (position) $k_{M,p}$	0.012 J m^{-2}
Viscous damping coefficient $k_{M,v}$	$1.0 \times 10^{-2} \text{ kg s}^{-1}$
Equilibrium distance r_0	$6.283 \times 10^{-3} \text{ m}$

Fluid

Two different fluid volumes of 150 and 200 mL (i.e., 60% and 80% respectively) were modelled with SPH particles. A resolution analysis to determine the number of SPH particles representing the fluid was carried out in (Schütt et al., 2020). The model also accounts for two different fluid viscosities, a LOVIS and a HIVIS fluid. The aqueous NaCMC solutions (see Chapter 6.3.1) used in the DCM lumen demonstrated a response to shear that follows the power law model ($R^2 = 0.999$). Therefore, the shear stress τ can be calculated according to Equation (6.4):

$$\tau = K\dot{\gamma}^n , \quad (6.4)$$

where K is the consistency index, $\dot{\gamma}$ the shear rate and n the power law exponent. The parameters describing the fluids used are provided in Table 6.3.

Table 6.3. Fluid rheological model parameter.

Fluid	K [Pa s ^{<i>n</i>}]	n [-]
Low viscosity fluid (LOVIS)	0.04	0.87
High viscosity fluid (HIVIS)	0.20	0.74

Figure 6.6 shows how the rheology of the simulated HIVIS, and LOVIS fluids compares to the power law model fitted to the experimental data.

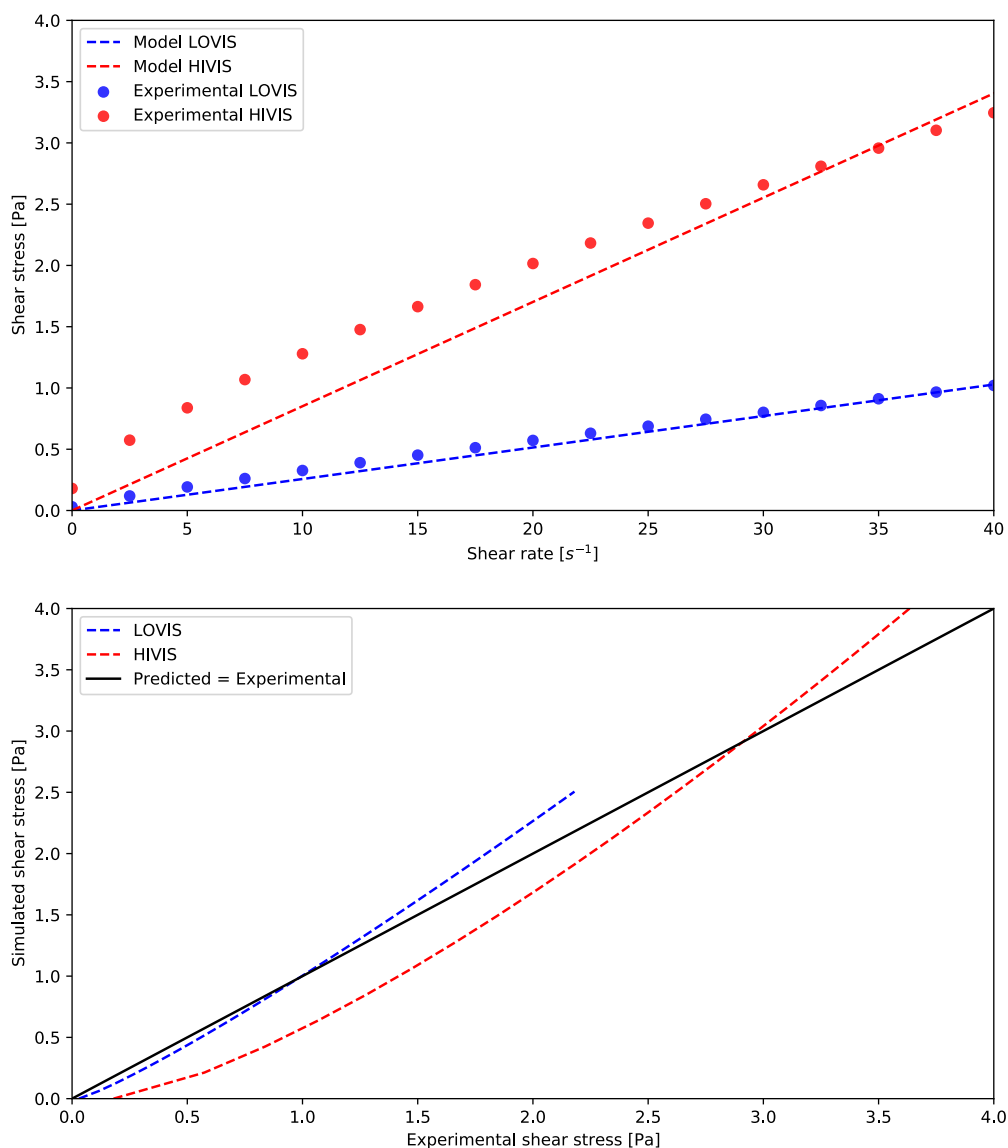


Figure 6.6 Rheological behaviour of LOVIS and HIVIS fluids in the DCM and the simulated counterparts *in silico*. Rheological measurements were made at 25 °C.

An approximately linear viscoelastic region was identified between 0 – 40 s^{-1} corresponding to a constant viscosity. Therefore, the fluid modelled in the DCMDT was assumed to be Newtonian for simplicity, with a viscosity equal to the gradient of the linear viscoelastic region; 26 mPa s ($R^2 = 0.9959$) for the model LOVIS and 85 mPa s ($R^2 = 0.9806$) for the model HIVIS fluid.

Fluid Structure and Global Boundary Conditions

In the SPH framework the continuum domain is discretised into a finite number of points which can be thought of as particles, which are characterised by their mass, velocity pressure, and density. The SPH equations of motion result from the discrete approximations of the Navier–Stokes equation. SPH is based on the mathematical identity:

$$f(\mathbf{r}) = \iiint f(\mathbf{r}')\delta(\mathbf{r} - \mathbf{r}')d\mathbf{r}' \quad , \quad (6.5)$$

where $f(\mathbf{r})$ is any scalar function defined over the volume V . The vector \mathbf{r} is position vector defined in the space V . $\delta(\mathbf{r})$ is the three-dimensional delta function and approximated in the SPH formulations by a smoothing kernel W and its characteristic width or smoothing length h :

$$\lim_{h \rightarrow 0} W(\mathbf{r}, h) = \delta(\mathbf{r}) \quad (6.6)$$

A variety of kernel functions can be found in literature. In this study, the so-called Lucy kernel function (Lucy, 1977) is used. By replacing the delta function by a kernel or smoothing function W , Equation (6.5) becomes

$$f(\mathbf{r}) \approx \iiint f(\mathbf{r}')W(\mathbf{r} - \mathbf{r}', h)d\mathbf{r}' \quad . \quad (6.7)$$

The discretisation over a series of particles of mass $m = \rho(\mathbf{r}')d\mathbf{r}'$, the identity equation results in

$$f(\mathbf{r}) \approx \sum_i \frac{m_i}{\rho_i} f(\mathbf{r}_i) W(\mathbf{r} - \mathbf{r}_i, h) , \quad (6.8)$$

here, m_i is the mass and ρ_i is the density of i th particle, where i ranges over all particles within the smoothing kernel W (i.e., $|\mathbf{r} - \mathbf{r}_i| < h$). Equation (6.8) represents the discrete approximation of a generic continuous field and can be used to approximate the Navier–Stokes equation

$$m_i \frac{dv_i}{dt} = \sum_j m_i m_j \left(\frac{P_i}{\rho_i^2} + \frac{P_j}{\rho_j^2} + \Pi_{i,j} \right) \nabla_j W_{i,j} + \mathbf{F}_i , \quad (6.9)$$

where v_i is the velocity of particle i , P is the pressure, $W_{i,j}$ is the concise form of $W(\mathbf{r}_j - \mathbf{r}_i, h)$, the term ∇_j is the gradient of the kernel with respect to the coordinate \mathbf{r}_j . \mathbf{F}_i accounts for a body force (e.g., gravity) and $\Pi_{i,j}$ denotes the viscous forces. For the tensor $\Pi_{i,j}$, there are different expressions available in the literature; here we use (Monaghan and Gingold, 1983)

$$\Pi_{ij} = -\alpha h \frac{c_0}{\rho_{ij}} \frac{v_{ij} r_{ij}}{\rho_{ij}^2 + b h^2} , \quad (6.10)$$

where α and b are dimensionless parameters to ensure the stability of the simulation. c_0 is the reference speed of sound at zero applied stress and v_{ij} represents the relative velocity and ρ_{ij} is the density of particle i and j , respectively. The constant b is used with $b \approx 0.01$. With the following relation, the artificial viscosity can be recognised as an effective kinematic viscosity ν . The value of α is chosen depending on the desired effective kinematic viscosity in the simulation, accordingly (Monaghan, 2005):

$$v = \frac{\alpha h c_0}{10} \quad (6.11)$$

To calculate the pressure forces between the fluid particles the Tait equation is used. This equation is also used to link the density ρ and the pressure P and correspondingly fulfil Equation (6.9):

$$P = \frac{c_0^2 \rho_0}{7} \left[\left(\frac{\rho}{\rho_0} \right)^7 - 1 \right]. \quad (6.12)$$

Here, ρ_0 the reference density at zero applied stress. Further details of the fluid properties are shown in Table 6.4.

Table 6.4. Model parameter of the fluid.

Parameter	Value
SPH	
Number of fluid particles (150 mL / 60% filling level)	11,507
Number of fluid particles (200 mL / 80% filling level)	18,076
Mass of each fluid particle $m_{F,low\ viscosity}$	1.324×10^{-5} kg
Mass of each fluid particle $m_{F,high\ viscosity}$	1.328×10^{-5} kg
Density (fluid) $\rho_{F,low\ viscosity}$	1017 kg m^{-3}
Density (fluid) $\rho_{F,high\ viscosity}$	1020 kg m^{-3}
Dynamic viscosity (fluid) $\eta_{F,low\ viscosity}$	26 mPa s
Dynamic viscosity (fluid) $\eta_{F,high\ viscosity}$	85 mPa s

To imitate the solid–fluid interactions (i.e., between the wall and the boundary layer of luminal fluid) a repulsive potential is used. This potential is used for the purpose of

avoiding overlap between solid and liquid particles. A soft potential of the following form is used:

$$E_{ij} = A \left[1 + \cos \left(\frac{\pi r_{ij}}{r_c} \right) \right] \quad \text{with} \quad r_{ij} < r_c, \quad (6.13)$$

where A is an energy constant, r_{ij} represents the distance between particle i and j and r_c is the cut-off distance. The no-slip boundary conditions between the solid and fluid particles are approximated by viscous forces similar to those of Equation (6.10), but applied to the interaction between the solid and the fluid particles.

Model parameters of the DCMDT used in the simulations are presented in Table 6.5:

Table 6.5. Fundamental model parameter.

Parameter	Value
SPH	
Artificial speed of sound c_0	0.1 m s^{-1}
Time-step Δt	$5 \times 10^{-4} \text{ s}$
Smoothing length, h	$4.71 \times 10^{-3} \text{ m}$
Momentum-Smoothing length, h_M	$9.42 \times 10^{-3} \text{ m}$

6.3.3 Software

The computational simulations in this study were performed using the University of Birmingham BlueBEAR HPC service (Birmingham), running the simulations on 10 cores with 40 GB of memory, resulting in a simulation time of about 10 min each. The open-source code LAMMPS (Ganzenmüller et al., 2011, Plimpton, 1995) is used

for the numerical calculations and the open-source code OVITO (Stukowski, 2010) for the visualisation of the results from the computational simulations. MATLAB (MATLAB, 2022) is used for the visualisation of the experimental data and the postprocessing of the DCMDT data as well as the experimental data.

6.3.4 Methods of Analysis

6.3.4.1 MRI Data Analysis

Using PC cine-MRI, the mean velocity of the DCM lumen contents was measured by taking the mean of all weighted-average velocities measured in voxels that constitute the through-plane lumen cross sectional flow area (denoted as 'MRI' in Figure 6.7, Figure 6.8, Figure 6.9, Figure 6.10, Figure 6.11, and Figure 6.12). Additionally, peak velocity was estimated by taking the mean of the five voxels in the centre of the lumen (denoted as 'MRI (peak)' in Figure 6.7, Figure 6.10, Figure 6.11, and Figure 6.12), to assess the impact of any stagnant regions of fluid close to the walls on through-plane mean velocity. Furthermore, peak velocities were also measured by taking the mean of the four highest value pixels within each region of interest (ROI). Due to the potential for high noise in individual pixel velocity measurements, MRI peak velocity estimates should be made using several pixels, rather than just one (O'Brien et al., 2008). The standard deviation of the mean velocity calculated using each ROI was considered to be the error associated with the MRI mean velocity measurement.

Since velocity was encoded only in the streamwise direction, x , as this is the principal direction of flow and it was assumed that the z and y components of velocity were of

negligible magnitude. $v_{\perp i}$ is the measured streamwise component of velocity of the fluid in pixel i . The measured value represents the weighted average of streamwise velocity inside the area entrapped within the pixel, which is dictated by the spatial resolution of the scanner. The flow rate through the pixel can therefore be determined by the following equation where q_i is flow rate through pixel i , and a_i is the area of pixel i .

$$q_i = v_{\perp i} a_i \quad (6.14)$$

The shear rate distribution can be mapped by evaluating the spatial gradient of the velocity distribution. Encoding velocity only in the streamwise direction simplifies the problem, eliminating the components of the shear rate tensor that involve measured velocity of the element of fluid inside pixel i in the z -direction, $v_{\perp z, i}$ and in the y -direction, $v_{\perp y, i}$. Additionally, the gradient of streamwise velocity with respect to the change in x -direction becomes unattainable as velocity values in only a single slice are obtained, therefore $\frac{\delta v_{\perp x, i}}{\delta x_i}$ also assumes a zero value. Equation (6.15) presents the simplification of the shear rate tensor acting on a pixel, where γ_i is the shear rate acting on pixel i and ∇v_i is the velocity vector across pixel i .

$$\gamma_i = (\nabla v_i)^T = \begin{matrix} \frac{\delta v_{\perp x, i}}{\delta x_i} & \frac{\delta v_{\perp y, i}}{\delta x_i} & \frac{\delta v_{\perp z, i}}{\delta x_i} & 0 & 0 & 0 \\ \frac{\delta v_{\perp x, i}}{\delta y_i} & \frac{\delta v_{\perp y, i}}{\delta y_i} & \frac{\delta v_{\perp z, i}}{\delta y_i} & \frac{\delta v_{\perp x, i}}{\delta y_i} & 0 & 0 \\ \frac{\delta v_{\perp x, i}}{\delta z_i} & \frac{\delta v_{\perp y, i}}{\delta z_i} & \frac{\delta v_{\perp z, i}}{\delta z_i} & \frac{\delta v_{\perp x, i}}{\delta z_i} & 0 & 0 \end{matrix} \quad (6.15)$$

To obtain values for the nonzero components of the shear rate tensor for each pixel, the velocity gradient was obtained using Equations (6.16) and (6.17). All voxels are of equal size and have a square face, where δy_i is equal to δz_i , so the spatial difference is denoted as L , the length of one voxel.

$$\gamma_{z,i} = \frac{v_{\perp z,i+1} - v_{\perp z,i-1}}{L} \quad (6.16)$$

$$\gamma_{y,i} = \frac{v_{\perp y,i+1} - v_{\perp y,i-1}}{L} \quad (6.17)$$

where $\gamma_{z,i}$ and $\gamma_{y,i}$ are the z and y components of streamwise shear rate across pixel i . To map the shear rate distribution, the nonzero components for each pixel in the ROI were computed using a convolution matrix that performed the operations in Equations (6.16) and (6.17) on each voxel.

The remaining shear rate components can then be resolved as in Equation (6.18) to give the overall shear rate acting over the voxel i by using the Frobenius norm.

$$\|\gamma_i\| = \sqrt{\left(\frac{\delta v_{xi}}{\delta z_i}\right)^2 + \left(\frac{\delta v_{xi}}{\delta y_i}\right)^2} \quad (6.18)$$

6.3.4.2 DCMDT Data Analysis

In the DCMDT, the shear rates were calculated from the stress tensor shown in Equation (6.19). The components σ define the local normal stress and τ the local shear

stress in the xy -plane, xz -plane, and yz -plane respectively. Because only the velocity component in the streamwise direction (x -direction) is available from the DCM data, the stress tensor can be simplified. The simplification reduces the stress tensor to the local stress on the yx -, and zx -plane, assuming zero values for all other elements. This facilitates comparison to the experimental data:

$$\tau = \begin{bmatrix} \sigma_x & \tau_{xy} & \tau_{xz} \\ \tau_{yx} & \sigma_y & \tau_{yz} \\ \tau_{zx} & \tau_{zy} & \sigma_z \end{bmatrix} = \begin{bmatrix} 0 & 0 & 0 \\ \tau_{yx} & 0 & 0 \\ \tau_{zx} & 0 & 0 \end{bmatrix} . \quad (6.19)$$

The remaining shear stress components were condensed into a single value using the Frobenius norm:

$$\|\tau\| = \sqrt{(\tau_{yx})^2 + (\tau_{zx})^2} . \quad (6.20)$$

For simplicity, a Newtonian fluid was used in the computational part. Thus, for the calculation of the shear rate $\dot{\gamma}$, the following relationship between shear stress, shear rate and fluid velocity was used:

$$\dot{\gamma} = \frac{\tau}{\eta} , \quad (6.21)$$

where τ is the shear stress and η the dynamic viscosity of the fluid.

6.3.4.3 *In Vitro* and *In Silico* Comparison Data Analysis

For each combination of parameters, the total sum of squares (*TSS*) between the different velocity data sets was calculated to evaluate the correlation of the experimental and computational data and the difference between the mean and peak measurements inside the DCM:

$$TSS_j = \sum_{i=1}^n (y_{j,i} - x_{j,i})^2 , \quad (6.22)$$

where $y_{j,i}$ and $x_{j,i}$ are the discrete datapoints of a data set j which should be compared (i.e., computational data and experimental data). The *TSS* is calculated for each colon section and data set j separately.

The main effects of three factors - wave speed, media viscosity and volume - on the response and mean shear rate at the bottom wall during local contractile activity were estimated and visualised using a main effects plot (see Figure 6.14). Main effects plots (also known as a design of experiment mean plot) are an efficient data visualisation technique that help to identify differences between mean values of experiment parameters and thus depict how individual luminal parameters may influence the shear rate.

6.4 Results and Discussion

6.4.1 Wall Motion

Figure 6.7, Figure 6.8, Figure 6.9, Figure 6.10, and Figure 6.11 show the mean displacement (denoted as 'Wall displ.')

of the mimic intestinal wall beside the consequential velocity profiles of the lumen contents in both the DCM and the DCMDT over the course of a PPW. In both models, the PPW starts at segment 1 (left-hand side), and propagates to segment 10, over the course of 60 s for the slower wave and 35 s for the faster wave. Positive and negative wall displacement represent contraction and relaxation respectively. Figure 6.7, Figure 6.8, Figure 6.9, Figure 6.10, and Figure 6.11 demonstrate that the motility pattern of the DCMDT generally corresponded very well with that of the DCM in segments 2, 6 and 10, following an almost identical course of relaxation to -20% occlusion, contraction to 60% occlusion and subsequently a slower relaxation back to the neutral position. This shows that the computational model is suitable to replicate the contractile nature of the DCM walls and can be synchronised to follow the same peristaltic PPW along the colonic axis.

6.4.2 Velocity Profile of the Contents

To verify, the DCMDT can mimic the DCM under a range of environmental conditions and the fluid velocity profiles were compared with those measured in the DCM in all combinations of PPW speed, media viscosity, and luminal fluid volume. In all cases, the DCMDT generated flows of the contents that followed the same pattern as the

contents of the DCM. Before a PPW began, the contents were stationary with no measurable velocity. Low fluctuations in velocity between approximately 0.25 and -0.25 cm s^{-1} occurred prior to local wall displacement. Initial relaxation of the walls and contraction of the immediately upstream segment caused positive flows, propelling the contents towards the mimic *hepatic flexure*. Subsequently, contraction of the walls reversed the fluid direction and drove fluid backwards towards the *caecum* at greater velocities. The fluid–structure interactions modelled in the DCMDT were therefore suitable to reproduce the complex series of antegrade propulsion and back mixing observed in the DCM (O’Farrell et al., 2021, Stamatopoulos et al., 2020). Both models show similarity to the *in vivo* situation as the velocity of the human ascending colonic contents is also not constant and exhibits periods of rhythmic back and forth motion (Stathopoulos et al., 2005).

Overall, the PPW generated mean fluid velocities in the DCMDT of similar magnitude to that of the DCM. The mean fluid velocities at lower fluid viscosity conditions were slightly noisier than at higher fluid viscosities (for example Figure 6.7 (a) versus Figure 6.7 (b)). The DCM produced mean (Figure 6.7, Figure 6.9, Figure 6.10, and Figure 6.11) and peak (Figure 6.8) velocities of slightly higher magnitude during the fluctuations above and below the datum outside of the period of local wall contraction. Where small deviations in wall displacement were observed, there was no significant effect on mean velocity of the contents in either the DCM or the DCMDT. More detailed flow phenomena were captured in the DCMDT than the DCM as the experimental data were comparatively low in temporal resolution compared to the DCMDT (2 s versus 0.25 s in this study, respectively) which highlights a clear advantage of using the digital twin. The mean fluid velocities using HIVIS were considerably less noisy than with

LOVIS due to enhanced dampening of residual oscillatory motion caused before and after the contractile wave passes.

Figure 6.7 shows the results obtained when the lumen was filled to 60% capacity and the slower PPW (0.4 cm s^{-1}) was applied.

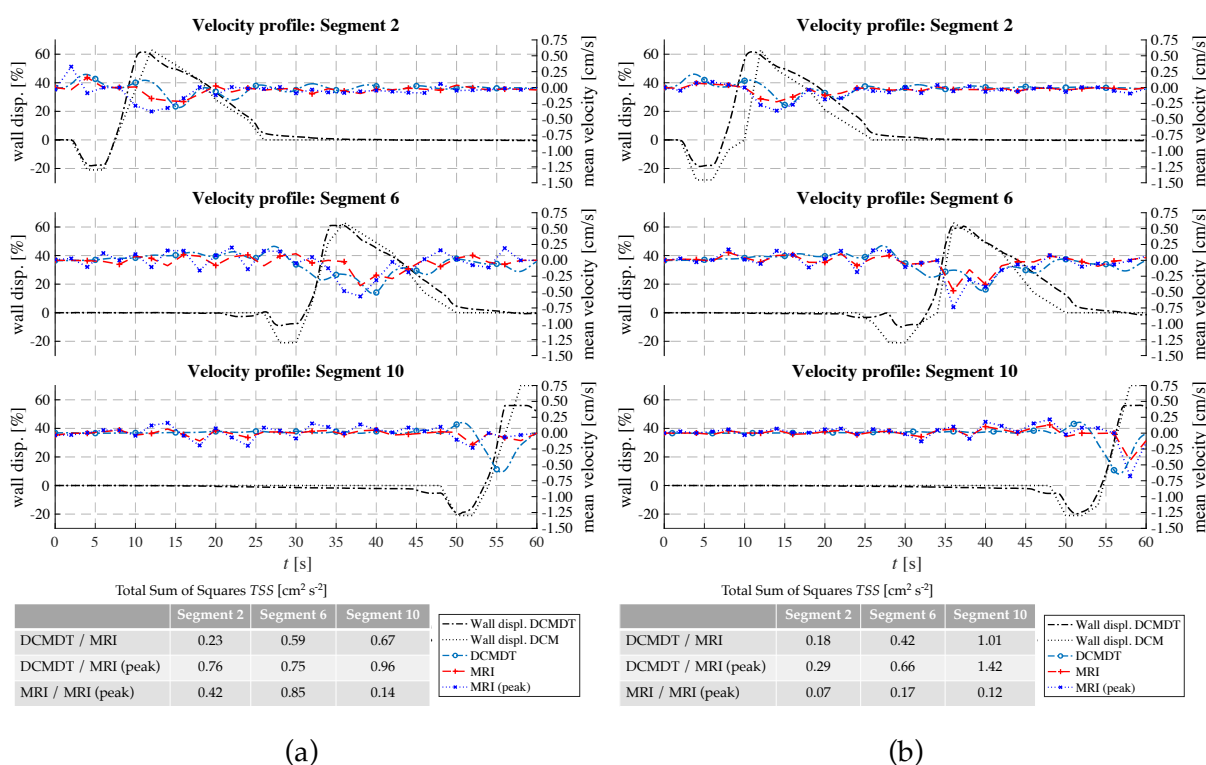


Figure 6.7 Comparison of the fluid velocities and wall displacement profiles of the DCM and the DCMDT with 60% fluid volume and slower propagating PPW. Parts (a) and (b) compare the mean fluid velocities with LOVIS and HIVIS respectively.

At the lower fill volume of 60%, the slow motility wave (Figure 6.7) generated particularly similar mean fluid velocities in segment 2, close to the *caecum* as demonstrated by the low *TSS* values of 0.23 and 0.18 for LOVIS and HIVIS fluids respectively. In segment 10, the LOVIS experimental data did not show the strong backflow phenomenon that typically occurred during the contraction phase, which, on the other hand, was evident in the DCMDT.

For the parameter combination shown in Figure 6.7 (a) (i.e., low fluid volume, low fluid viscosity and slow PPW), the peak fluid velocities that occurred in the experiment and the computation are presented in Figure 6.8.

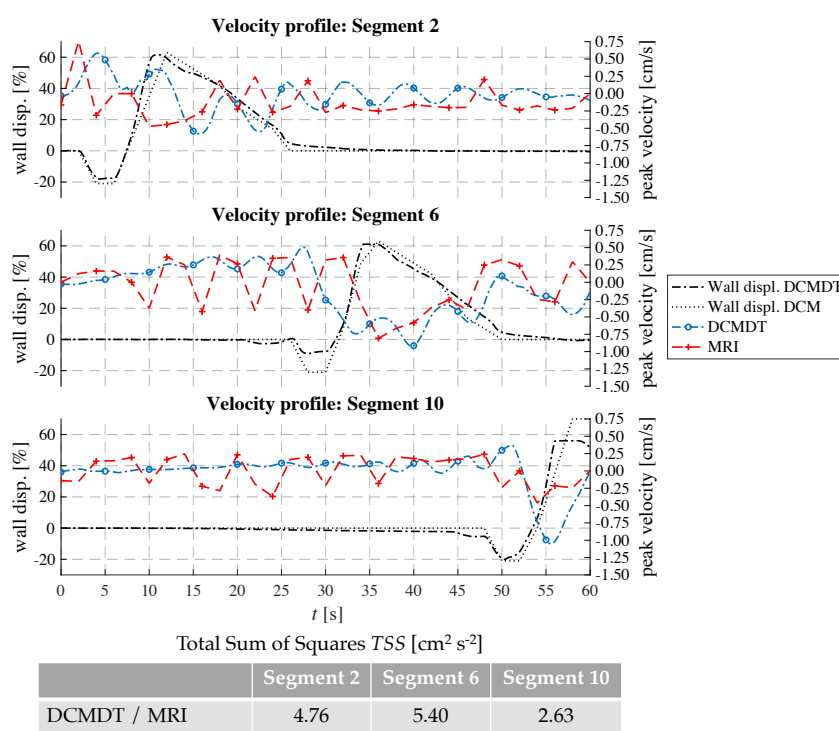


Figure 6.8 Comparison of the maximum fluid velocities and wall displacement profiles of the DCM and the DCMDT at low fluid volume, low fluid viscosity, and slow propagating PPW conditions are compared.

The peak velocities fluctuated in a wavelike pattern similar to the mean velocities. Despite the similarities between the DCM and the DCMDT upon visual analysis, TSS values were relatively high. This was due to the slight phase offset between the wavelike flow pattern of the DCM and the DCMDT which arose from marginally different initiation times. Next, the fill volume of the lumen was increased to 80% (Figure 6.9).

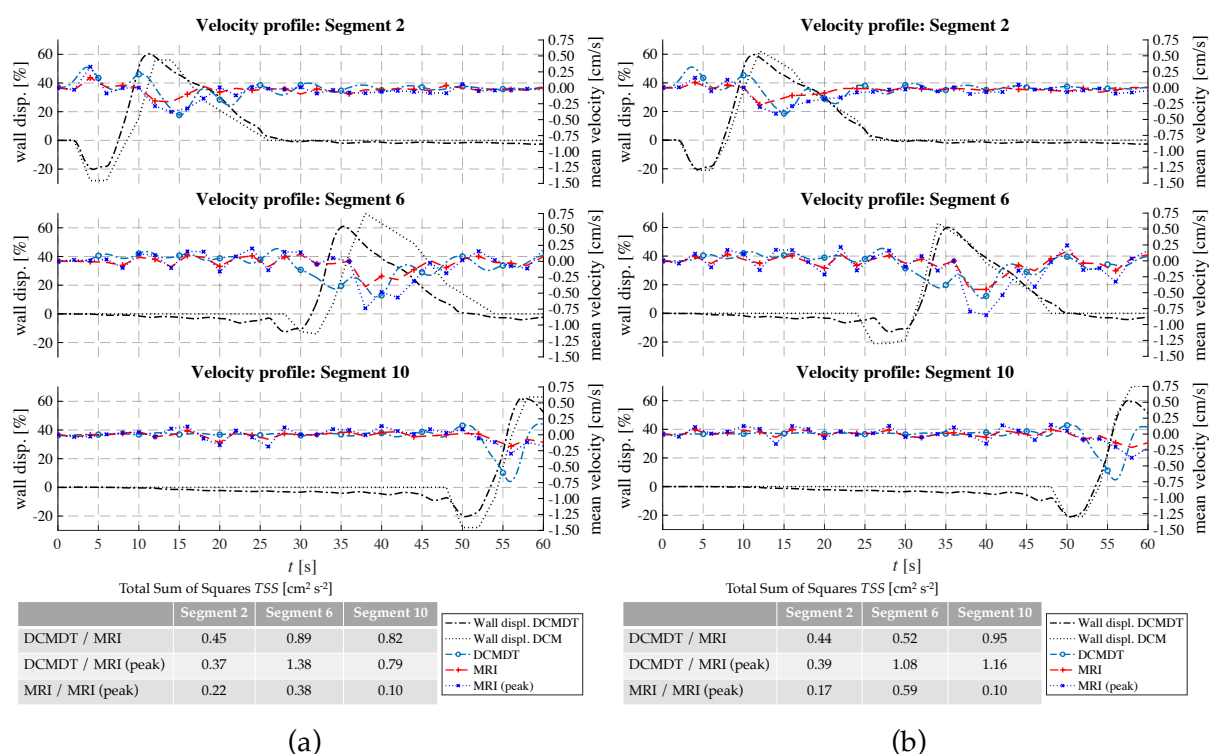


Figure 6.9 Comparison of the fluid velocities and wall displacement profiles of the DCM and the computational model at high fluid volume and slow propagating PPW. In (a) the mean fluid velocities at low fluid viscosity and in (b) the mean fluid velocities at high fluid viscosity are compared.

When volume was increased to 80%, TSS values were <1.4 with no significant deviations between the experimental and computational data. This shows that the simulation is robust at the elevated volume when the slower PPW is applied. At this stage, a limitation of the DCM and its DT is that the ‘neutral’ volume of the lumen is fixed, so when varying the fill volume of fluid inside the lumen below 100%, an air space is present at the top of the lumen. *In vivo*, the capacity of the ascending colon adapts according to the volume of its contents; the walls of the colon reduce their tone and encase the contents fully, leaving no air gap (unless gas is present as a product of microbial activity). However, the focus of this paper is to demonstrate that the digital twin can reproduce flows inside the DCM under different luminal conditions. Future *in silico* models of the human ascending colon could better represent the *in vivo*

situation by incorporating this morphological response to the volume of the contents to understand how this may affect the flow of the contents. The fluid volume was then reduced back to 60% and the faster PPW was applied (Figure 6.10). A faster PPW involved a faster occlusion rate which caused greater mean fluid velocities compared to the slower PPW seen in Figure 6.7.

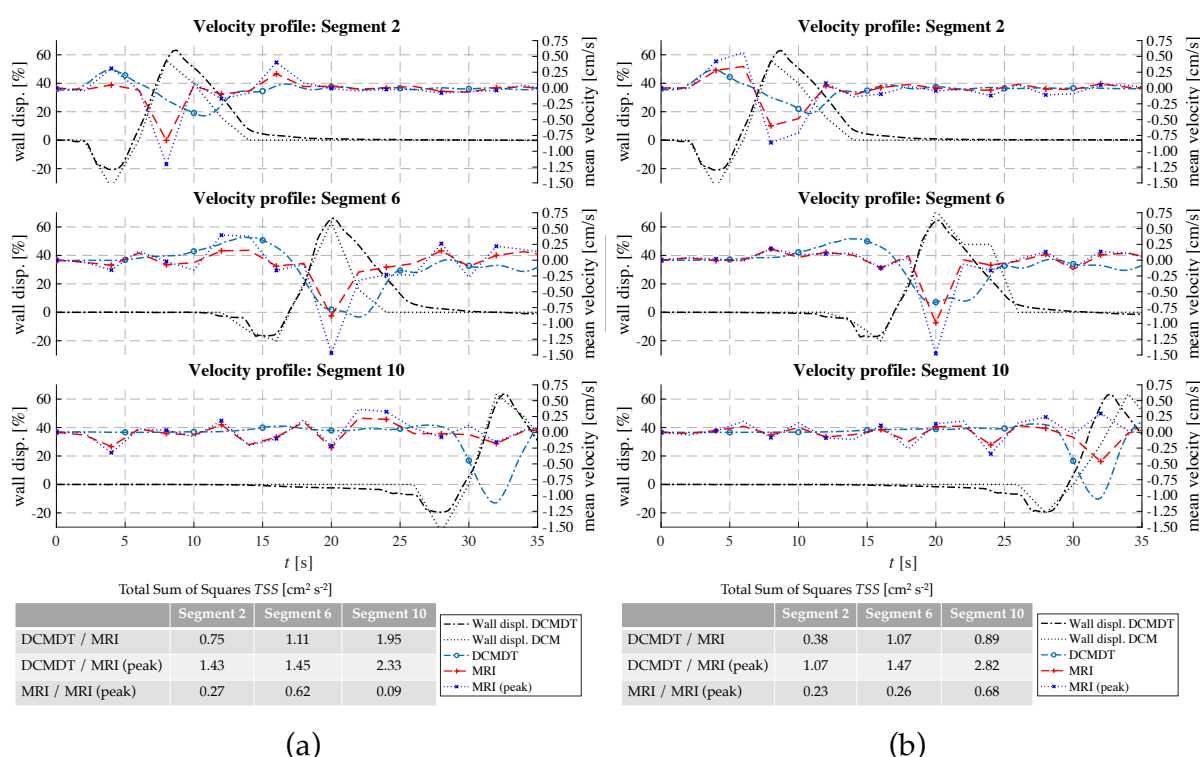


Figure 6.10 Comparison of the fluid velocities and wall displacement profiles of the DCM and the DCMDT at low fluid volume and fast propagating PPW. In (a) the mean fluid velocities at low fluid viscosity and in (b) the mean fluid velocities at high fluid viscosity are compared.

The experimental data shown in Figure 6.10 (a) segment 2 and segment 6 and Figure 6.10 (b) segment 2 exhibited a slightly higher mean fluid velocity ahead of the wall wave compared to the slower PPW. These elevated positive velocities were also accurately reproduced by the DCMDT in addition to the greater magnitude of

backflow velocity. Both models also showed a higher fluid velocity in segment 6 at high fluid viscosity Figure 6.10 (b).

Inside the DCM, media viscosity influenced the flow pattern, with a lower viscosity fluid causing more erratic wave-like behaviour. From the statistical analysis in Figure 6.10 (a), it can also be seen that the DCMDT data do not fully capture this fluid behaviour in the DCM. This could be attributed to shear rates at the extremes of, or outside of the linear viscoelastic region of the NaCMC solutions, causing the behaviour of the real fluid to deviate from that of the simulated fluid in the DCMDT. A small contribution may also result from small irregularities between the segments in the DCM that are not captured in the DCMDT.

In Figure 6.11, the faster PPW was maintained but fill volume was increased from 60% to 80%. In this case, there were no significant changes in mean velocity in the DCM that arose from increasing the fill volume from 60% to 80%. The DCMDT performed well to capture this as shown by a relatively low *TSS*.

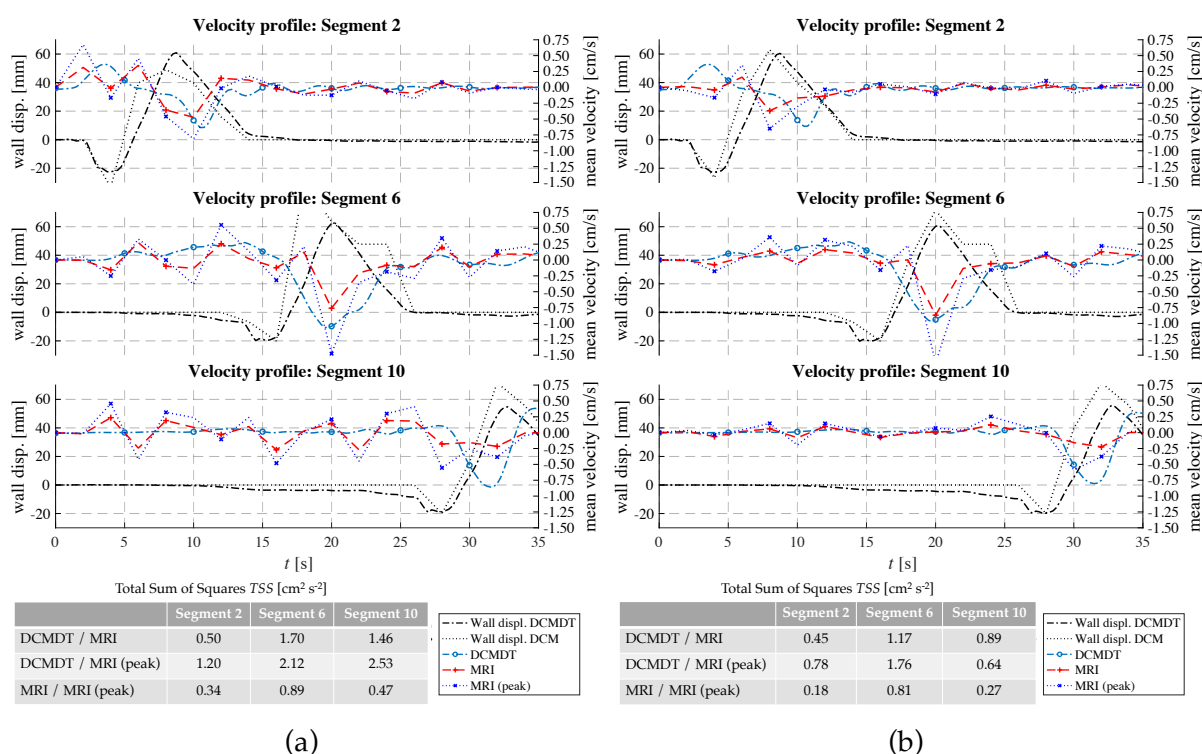


Figure 6.11 Comparison of the fluid velocities and wall displacement profiles of the DCM and the DCMDT at high fluid volume and fast propagating PPW. In (a) the mean fluid velocities at low fluid viscosity and in (b) the mean fluid velocities at high fluid viscosity are compared.

Generally, mean velocities were slightly higher in the DCM than in the DCMDT.

Comparison of Figure 6.12 parts (a) and (b) demonstrates the influence of propagating wave on the velocities achieved by the contents of the lumen, which follows intuition that a faster wave produces higher velocities in both the DCM and the DCMDT.

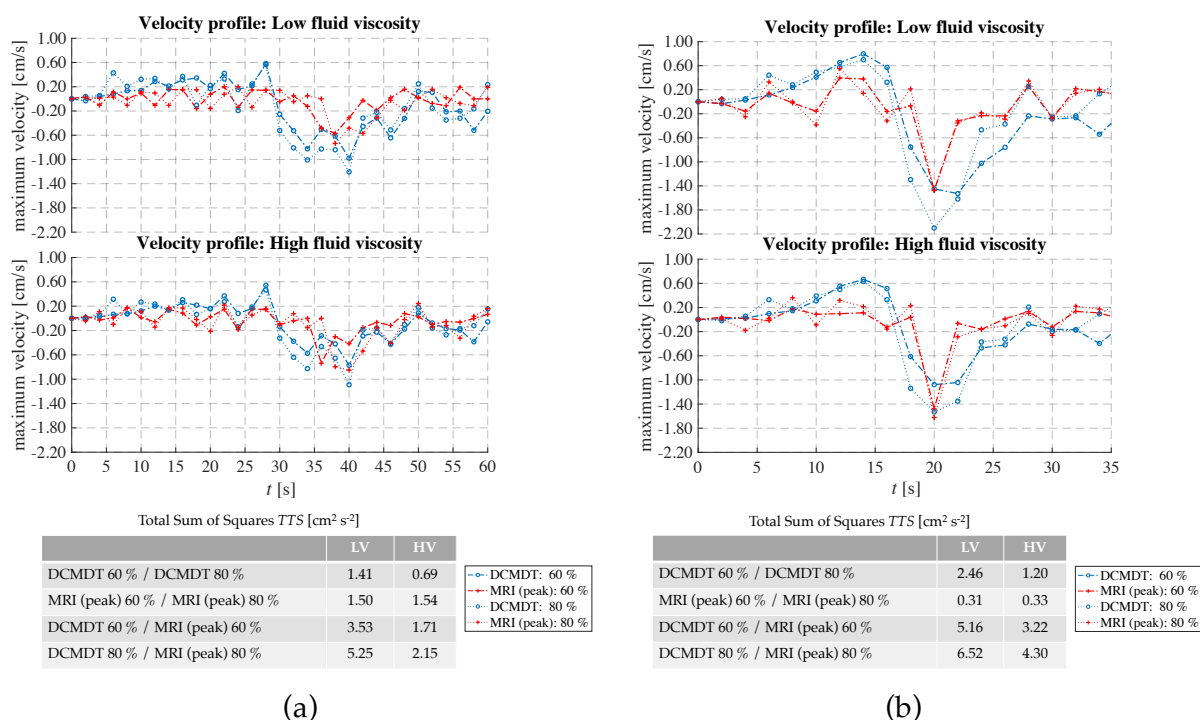


Figure 6.12 Comparison of the fluid velocities at different fluid volumes and different fluid viscosities of segment 6. (a) represents data for the slower propagating PPW and (b) for the faster propagating PPW (b). In the table for the Total Sum of Squares, the following abbreviations are used: LV-low viscosity, HV-high viscosity.

The antegrade velocities were less affected than the retrograde peak during local wall contraction. A lower fill volume increased the degree of retrograde velocity experienced in the DCM, and this was replicated in the DCMDT also. Increasing fluid viscosity in the DCMDT decreased average retrograde velocity during local wall contraction, however, there was no significant effect in the DCM.

6.4.2.1 Shear rates

Figure 6.13 presents the mean shear rate over time in the same cross section, and the maximum shear rate recorded for each of the same parameter combinations. In the

DCM, mean shear rate spiked during local contraction of the walls at approximately 6 s and 20 s for the fast wave in segments 2 and 6 respectively in Figure 6.13 A, B. Subsequently, shear rate dropped sharply, returning to low levels where small fluctuations between 0.01 s^{-1} and 3 s^{-1} were seen for the remainder of the motility wave. For the slow wave, local contractile activity occurred around 6 s and 40 s in segments 2 and 6 respectively, causing a lower, broader peak in average shear rate.

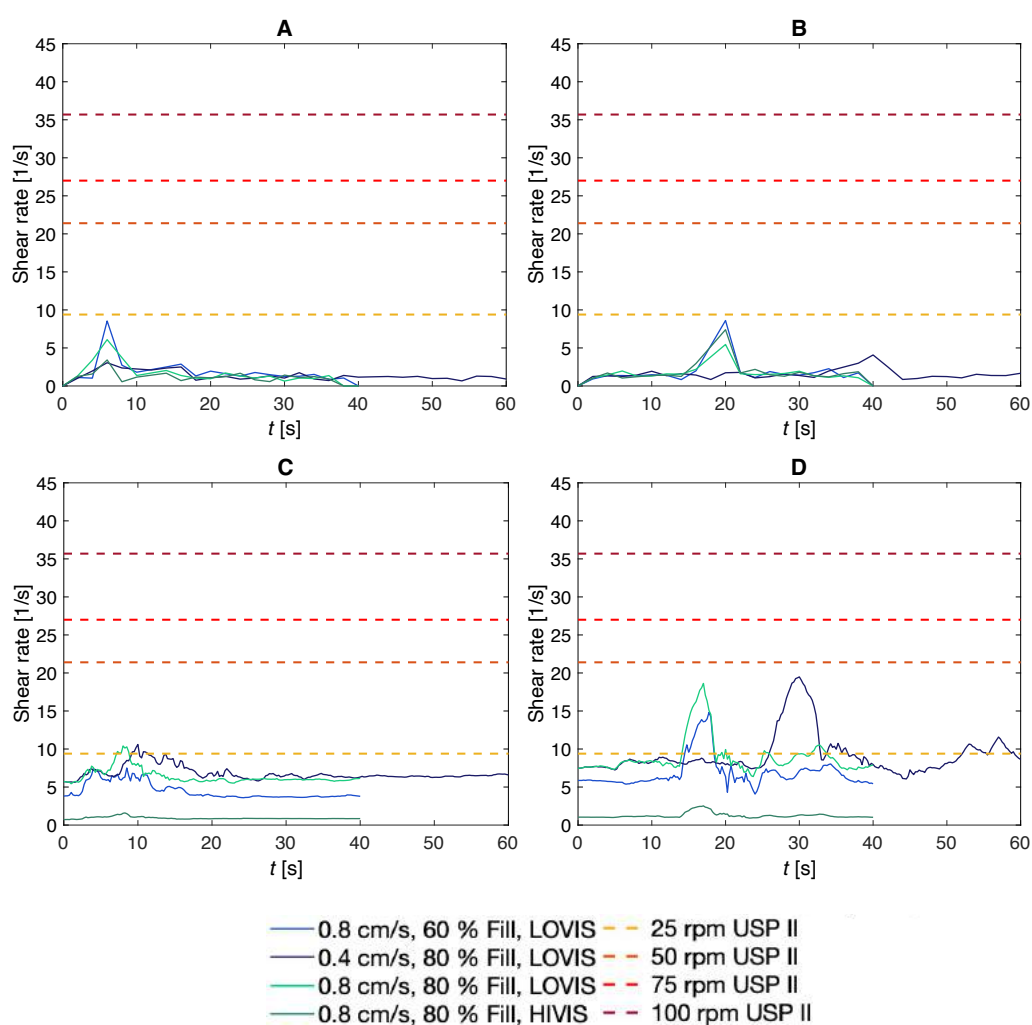


Figure 6.13 Average shear rates versus maximum shear rates for each parameter combination, where (A) represents DCM ‘segment 2’, (B) DCM ‘segment 6’, (C) DCMDT ‘segment 2’, and (D) DCMDT ‘segment 6’. USP II shear rate data was reproduced from (Hopgood et al., 2018). Here they use the CFD package Fluent version 17.2.0 (Fluent Incorporated, Canterra Resource Park, NH).

In the digital twin, a similar trend was observed in that there was a peak in average shear rate during a local wall contraction. However, instead of returning to low levels immediately, the average shear rate in segment 2 (Figure 6.13 C) followed the general trend of decreasing post-contraction but periodically peaking to progressively lower shear rates as the subsequent segments contract. This effect was most prominent with the slow wave at a low viscosity and the greater volume of 80%, which also gave rise to the highest mean wall shear rates in segment 6, peaking at 19.48 s^{-1} and in segment 2 at a height of 10.60 s^{-1} . In segment 6, shear rates were considerably higher than in segment 2, however, the periodic increases in shear rate following the highest peak arising from local contraction were irregular and less well defined. This suggests that a tablet located close to the *caecum* might experience more frequent peaks in shear rate and may erode faster, according to findings from a recent *in silico* study which suggested that is not the average shear rate that is important for tablet disintegration in the colon, but individual shear rate peaks that lead to accelerated tablet disintegration (Schütt et al., 2021). In both segments 2 and 6, shear rates were considerably lower when the lumen contained the higher viscosity fluid, HIVIS. Even though the DCMDT and DCM data show deviations in their course, the order of magnitude of the computational and the experimental data agree well.

The mean bottom wall shear rate in both the DCM and the digital twin were highly variable and time-dependent, in contrast to inside the USP II modelled by Hopgood and Barker (Hopgood et al., 2018). In the USP II model, tablet surface shear rates were approximately constant for a given paddle speed and increased linearly from 9 s^{-1} at 25 rpm to 36 s^{-1} at 100 rpm (Hopgood et al., 2018). At no combination of parameters covered in this study does the shear rate at the wall in the DCM or DCMDT reach that of the USP II at 50 rpm (21.4 s^{-1}) or higher. This finding suggests that a constant paddle

rotational speed greater than 50 rpm may bear low physiological relevance when studying the dissolution of colon-targeted dosage forms in the USP II. The spatiotemporal dependence of wall shear rate in the DCM is in line with observations in a CFD simulation of the TIM-Automated Gastric Compartment, which is a similar advanced biorelevant *in vitro* dissolution apparatus modelling the stomach (Hopgood et al., 2018).

Clearly, Figure 6.13 showed that mean wall shear rate in both models had some dependence on the speed of the propagating wave, media viscosity and media volume. The main effects plot in Figure 6.14 scrutinises this further, giving a clearer idea about the relative significance of these parameters on the mean wall shear rate.

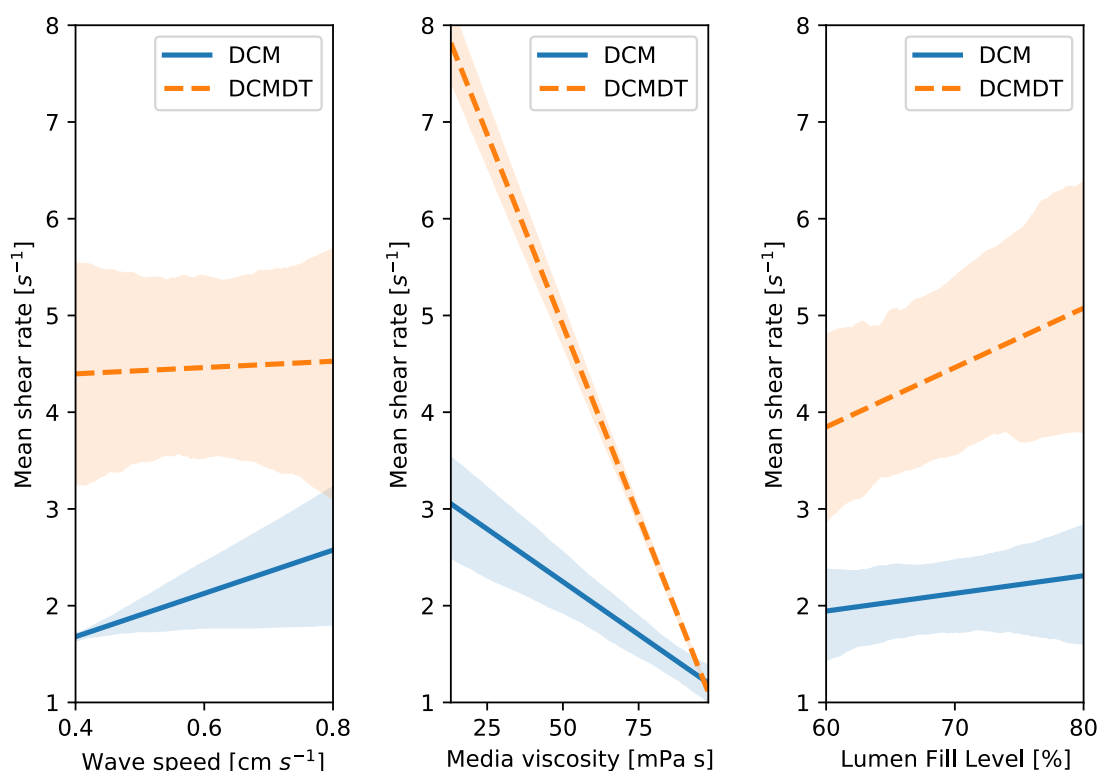


Figure 6.14 Main effects of wave speed, media viscosity and volume on mean shear rate at the bottom wall during local wall contraction at segment 6 in the DCM and the COM. $N = 4$ mean data points at each level (low and high). The shaded areas represent the confidence interval.

In all plots, the DCMDT is shown to represent the same type of effect as the DCM. Weak positive effects of wave speed and media volume and a strong positive effect of media viscosity on mean shear rate at the bottom wall during local wall contraction were evident. This shows that the DCMDT can model the influences of changes in wave speed, media viscosity, and volume on magnitude of luminal flow velocity. Effects were more pronounced in the DCMDT than the DCM.

Over the parametric range studied in this work, only the effect of media viscosity on mean shear rate was significant ($p < 0.05$) in both models. This demonstrates that media viscosity is a key parameter to consider when designing a biorelevant media for dissolution testing, since shear rate influences dissolution rate. Furthermore, this may mean that colonic disease states that alter media viscosity may divert the intended release profile towards a dose-dump-type scenario or the opposite, insufficient release and therefore administration of therapeutic molecules to the target site *in vivo*.

Although the main effects of wave speed and media volume on mean shear rates are insignificant at between $0.4 - 0.8 \text{ cm s}^{-1}$ and $60\% - 80\%$ fill level, the main effects plot suggests that these parameters may demonstrate some influence on shear rate over a broader range of levels. Considering wave speed, a recent study in the DCM showed that wave propagation speed increases the velocity of the contents due to the higher level of kinetic energy imparted to the luminal fluid (O'Farrell et al., 2021). Intuitively, this may cause steeper velocity gradients and therefore higher shear rates. Future work should therefore consider a wider range of wave propagation speeds. The range of speeds in this study ($0.4 - 0.8 \text{ cm s}^{-1}$) covers fed cyclic antegrade ($0.8 \pm 0.3 \text{ cm s}^{-1}$) and fed short single antegrade ($0.5 \pm 0.3 \text{ cm s}^{-1}$) (Dinning et al., 2014). However, long single waves have been reported to propagate at ($2.0 \pm 0.8 \text{ cm s}^{-1}$) (Dinning et al., 2014). Other factors are at play in a motility pattern other than propagation velocity, for example,

high amplitude propagating sequences (HAPSs, $0.4 \pm 0.1 \text{ cm s}^{-1}$ (Dinning et al., 2014), 0.71 (0.29 – 5.15, solid-state catheter, 0.76 (0.22 – 6.06, water perfused catheter (Liem et al., 2012)), $1.11 \pm 0.1 \text{ cm s}^{-1}$ (Bassotti and Gaburri, 1988)) which have a similar velocity, exhibit a higher pressure amplitude as a result of higher occlusion rate and/or degree, which is likely to influence shear rate. Also, it is unknown how a retrograde propagating contractile wave affects flow in the DCM or its digital twin. Increasing volume influences the pressure and gravitational forces associated with fluid inside the lumen during a contraction, which is likely to influence shear rates. Future hydrodynamic investigations could explore the effect of orientation of the DCM and DCMDT and the associated influence of gravity on shear rates.

As already mentioned, the size of the DCM segments is fixed so that the membrane does not adjust to the current amount of intestinal content. This feature is also difficult to visualise in practice. However, the DT might offer a feasible way to represent the *in vivo* environment in a more realistic way by implementing this feature to investigate how this effects shear rates, along with adding in the complexities of gravity by standing the model up so that the *hepatic flexure* is above the *caecum* - as is the case in normal life.

6.5 Conclusion

The alignment of advanced *in vitro* and *in silico* models of *in vivo* systems is a promising approach to begin addressing the gaps in knowledge that currently hamper the progression of drug delivery and disease therapy. This study describes the development of a digital twin of the Dynamic Colon Model, a biorelevant dissolution

apparatus representing the human proximal colon. The capabilities of the digital twin were verified using fluid velocity and shear rate data obtained through MRI imaging of the *in vitro* model. The DCMDT presents an addition to the available toolbox of *in silico* frameworks to model the fate of orally ingested dosage forms inside the gastrointestinal tract.

In the colon, hydrodynamic parameters such as shear rates are pivotal in the disintegration and dissolution of a solid dosage form, particularly erodible matrices. Both models permit modification of a range of physiologically relevant parameters that describe the colonic environment and influence the hydrodynamic conditions inside the respective mimic lumen. This study investigated the effects that the propagation speed of a contractile wall wave, media viscosity, and media volume have on the mean wall shear rate inside the Dynamic Colon Model. It was found that media viscosity had a significant negative effect on wall shear rate, whilst weak positive effects were seen by propagating wave speed and media volume, which are anticipated to be enhanced at more extreme levels. The digital twin was able to replicate these effects, meaning that it is robust over a range of physiologically relevant parameter combinations and may be useful to model particular disease states and the effect these may have on the delivery of colon-targeted dosage forms.

The findings in this paper indicate that viscosity is important to consider when designing a biorelevant media for dissolution testing of colon-targeted dosage forms. Additionally, constant paddle rotational speed greater than 50 rpm may bear low physiological relevance when studying the dissolution of colon-targeted dosage forms in the USP II dissolution apparatus. However, to consolidate the findings of this study, further work needs to be done that also considers the different motility conditions (i.e.,

wave speeds, direction of propagation and occlusion degrees) found in the colonic environment.

6.6 Acknowledgements

Acknowledgments go to the EPSRC Centre for Doctoral Training in Formulation Engineering (EP/L015153/1) and AstraZeneca AB R&D, Gothenburg for sponsoring the experimental research. We are grateful to the School of Medicine at the University of Nottingham for contributing to the MRI scanning costs as part of SS's postgraduate research study programme.

Chapter 7

Development of a Digital Twin of a Tablet that Mimics a Real Solid Dosage Form: Differences in the Dissolution Profile in Conventional mini-USP II and a Biorelevant Colon Model

Published article::

European Journal of Pharmaceutical Sciences 179 (2022)

7.1 Abstract

The performance of colon-targeted solid dosage forms is commonly assessed using standardised pharmacopeial dissolution apparatuses like the USP II or the miniaturised replica, the mini-USP II. However, these fail to replicate the hydrodynamics and shear stresses in the colonic environment, which is crucial for the tablet's drug release process. In this work, computer simulations are used to create a digital twin of a dissolution apparatus and to develop a method to create a digital twin of a tablet that behaves realistically. These models are used to investigate the drug release profiles and shear rates acting on a tablet at different paddle speeds in the mini-USP II and biorelevant colon models to understand how the mini-USP II can be operated to achieve more realistic (i.e., *in vivo*) hydrodynamic conditions.

The behaviour of the tablet and the motility patterns used in the simulations are derived from experimental and *in vivo* data, respectively, to obtain profound insights into the tablet's disintegration/drug release processes. We recommend an "on-off" operating mode in the mini-USP II to generate shear rate peaks, which would better reflect the *in vivo* conditions of the human colon instead of constant paddle speed.

7.1.1 Graphical abstract

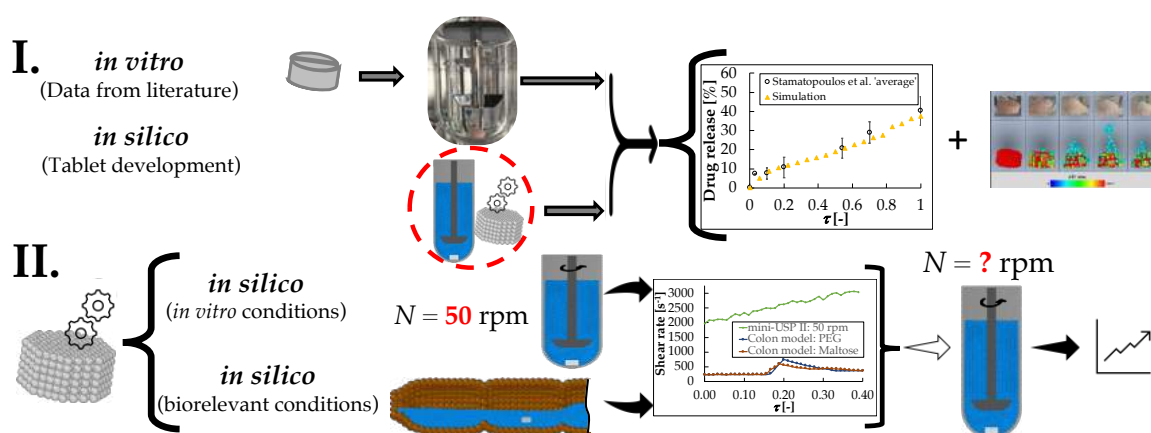


Figure 7.1 Graphical abstract

7.2 Introduction

The performance of a drug formulation is commonly accessed using United States Pharmacopeia (USP) dissolution apparatus. Besides drug performance analysis, this *in vitro* drug testing tool is also used in product development and quality control (Abrahamsson et al., 2005, Stamatopoulos et al., 2015). The USP dissolution apparatus are simplified *in vitro* models also used to replicate the complex *in vivo* conditions in the gastrointestinal tract that significantly control the disintegration/dissolution process of a solid dosage form (e.g., shear stresses evoked by wall motion) (Schütt et al., 2021). The USP II is the commonly most used USP dissolution apparatus for evaluating solid oral dosage forms (Stamatopoulos et al., 2015). The USP II is a container equipped with an agitator (paddle) and a fluid volume capacity of approximately one litre (Stamatopoulos et al., 2015). The most commonly used volumes are 500 and 900 mL. A miniaturised version of the USP II, the mini-USP II has

received more attention in recent years because this dissolution test device requires significantly less material mass than its larger counterpart (i.e., fluid volume of approximately 100 mL) (Klein and Shah, 2008, Stamatopoulos et al., 2015). This is of particular interest when biorelevant media or cost-intensive samples are used (Klein and Shah, 2008).

The dissolution profile of a solid dosage is of paramount importance in the development and optimisation of new formulations. Furthermore, the dissolution profile serves as a basis for physiologically based pharmacokinetic models (PBPK) to predict the absorption of drugs based on human physiology and their chemical properties (Stamatopoulos, 2022).

Investigations of the USP II showed that the shear rates in this dissolution apparatus depend on the paddle speed used (Hopgood et al., 2018). These results can also be transferred to the mini-USP II (Klein and Shah, 2008). However, Schütt et al. (Schütt et al., 2021) showed in a computational model of the proximal colon and a modelled tablet that the shear stresses acting on the tablet surface and thus influencing the tablet drug release process mainly depend on the colonic motility and the forces are dynamic.

In this study, we develop a method to model a digital twin of a tablet with the same disintegration/dissolution behaviour as a real tablet. Additionally, we create a digital twin of the mini-USP II dissolution apparatus and validate the hydrodynamic conditions with experimental and computational data from Stamatopoulos et al. (Stamatopoulos et al., 2015) and Wang et al. (Wang and Armenante, 2016). Then, we use experimental dissolution data of a tablet from Stamatopoulos et al. (Stamatopoulos et al., 2015) and model a tablet that behaves similarly in the modelled mini-USP II. Finally, this tablet is used in a biorelevant computational model of the proximal colon

replicating in vivo motility patterns to evaluate the difference in drug release profile in the simplified in vitro model and the more realistic colon model. The motility patterns used in the colon models (i.e., called 'PEG' and Maltose') are reproduced from Schütt et al. (Schütt et al., 2021).

7.3 Methodology

7.3.1 Modelling approach

This study uses a simulation technique called Discrete Multiphysics (DMP) (Alexiadis, 2015b, Alexiadis, 2014). DMP is a mesh-free technique that uses computational particles instead of computational grids and has been successfully used to model human organs: Ariane et al. (Ariane et al., 2017a, Ariane et al., 2018a, Ariane et al., 2018b, Ariane et al., 2017b), Baksamawi et al. (Baksamawi et al., 2021), Mohammed et al. (Mohammed et al., 2020, Mohammed et al., 2021), Alexiadis et al. (Alexiadis, 2015a, Alexiadis, 2015b, Alexiadis, 2019b, Alexiadis et al., 2017), and Schütt et al. (Schütt et al., 2022, Schütt et al., 2021, Schütt et al., 2020). It couples particle-based methods such as Smoothed Particle Hydrodynamics (SPH), Lattice Spring Model (LSM), and Discrete Element Method (DEM) and Peridynamics (Sanfilippo et al., 2021). In particular, the model in this study couples SPH and LSM. In the mini-USP II model and the colon models, SPH is used to model the fluid, while the colon models also account for LSM to model the colon's membrane. The reader can refer to Refs. (Alexiadis, 2015a, Alexiadis, 2015b), Ref. (Liu and Liu, 2003), and Refs. (Kot, 2021, Kot et al., 2015, Pazdniakou and Adler, 2012) for a general overview of the DMP, SPH and

LSM theory, respectively. The solid dosage form dissolution is modelled similarly to the methodology discussed in Schütt et al. (Schütt et al., 2021).

7.3.2 Mini-USP II

7.3.2.1 Geometry container and impeller

The mini-USP II dissolution apparatus (also called small volume dissolution apparatus) consists of a cylindrical container with a hemispherical bottom. The agitator, also called paddle, rotates at a specified speed and accelerates the fluid in the container. In this study, the rotational speed of the mini-USP II is 50 rpm as in Stamatopoulos et al. (Stamatopoulos et al., 2015). A schematic representation of the mini-USP II (100 mL capacity) and the computational model is given in Figure 7.2 a) and Figure 7.2 b), respectively.

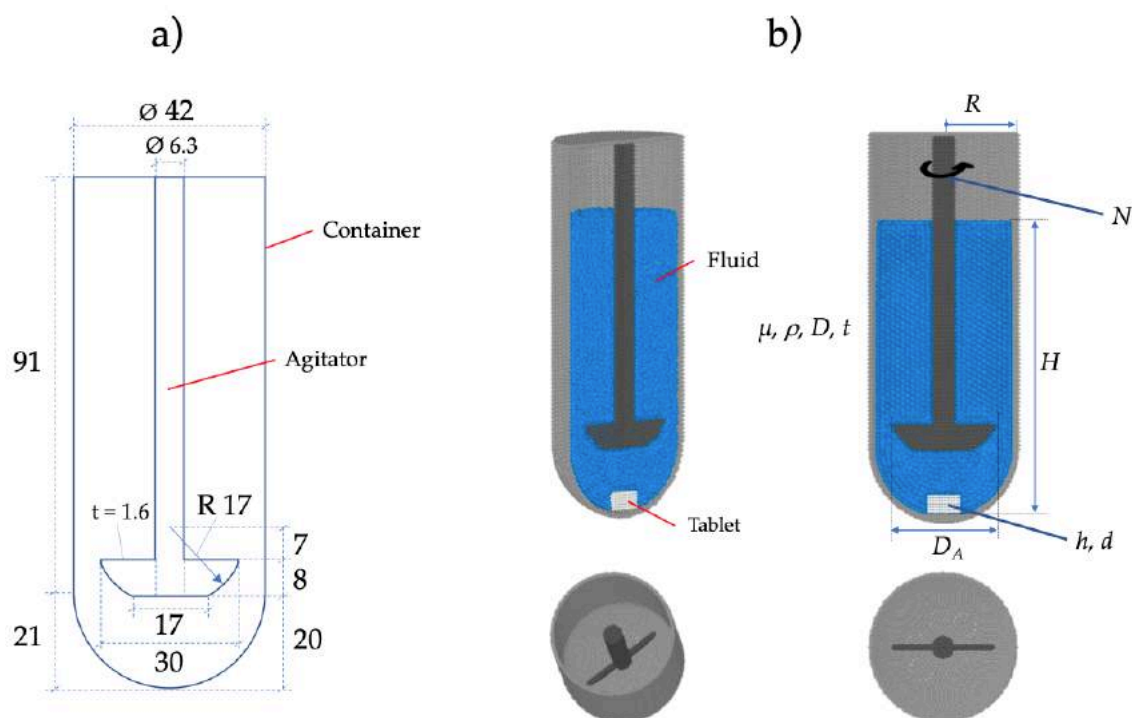


Figure 7.2 Schematic representation of the mini-USP II with the dimensions used in (Stamatopoulos et al., 2015) (a) and the computational model (b) including the variables for the dimensional analysis (Chapter 7.3.2.2).

The following model details refer only to the mini-USP II model, which replicates the experimental apparatus of Stamatopoulos et al. (Stamatopoulos et al., 2015). Data from literature (Wang and Armenante, 2016) are used for validation of the model velocity. For validation of the tablet drug release profile data from (Stamatopoulos et al., 2015) are used.

The dimensions of the mini-USP II dissolution apparatus used in (Stamatopoulos et al., 2015) and in (Wang and Armenante, 2016) differ slightly from each other. Therefore, to validate the velocity profile inside the container against experimental data from Wang et al. (Wang and Armenante, 2016), the dimensions of the model are adjusted (i.e., the paddle clearance, the container diameter, and the diameter of the agitator shaft, see Chapter 7.4.1) and the results are compared.

The mini-USP II model has a total height of 1.12×10^{-1} m, a diameter of 0.42×10^{-1} m and a paddle diameter of 0.30×10^{-1} m with a total capacity of 100 mL. Further details are given in Figure 7.2 a).

The container walls are built with 69,154 stationary SPH particles. The agitator or paddle is composed of 13,039 SPH particles building a rigid body that rotates at a constant speed of 50 rpm around its longitudinal axis. Further details of the mini-USP II model are given in Table 7.1.

Table 7.1. mini-USP II parameters

Parameter (mini-USP II)	Value
SPH	
Number of SPH particles (container)	69,154
Number of SPH particles (agitator)	13,039
Mass of each particle m_C	2.55×10^{-7} kg
Mass of each particle m_A	2.40×10^{-7} kg

7.3.2.2 Dimensionless analysis

From Buckingham's π -theorem, physically significant equations with n physical variables can be rephrased in terms of several $p = n - k$ dimensionless parameters $\Pi_1, \Pi_2, \dots, \Pi_p$, where k is the number of physical dimensions involved.

For the case analysed, the results can be expressed as a mathematical function f of the type

$$f(t, N, h, d, \mu, \rho, D, D_A, H, R) = 0 \quad , \quad (7.1)$$

where all the variables and their physical units are represented in Table 7.2. The listed variables are shown in Figure 7.2 b). With the ten variables listed in Table 7.2, and three units (kg, s, m), equation 7.1 can be rewritten based on seven dimensionless parameters:

$$\varphi(\Pi_1, \dots, \Pi_7) = 0 \quad , \quad (7.2)$$

Table 7.2. Variables for the dimensional analysis

	Variable	Unit	Description
(1)	t	s	Dissolution time
(2)	N	s^{-1}	Agitator rotational speed
(3)	h	m	Tablet thickness
(4)	d	m	Tablet diameter
(5)	μ	$kg\ m^{-1}\ s^{-1}$	Dynamic viscosity of the fluid
(6)	ρ	$kg\ m^{-3}$	Density of the fluid
(7)	D	$m^2\ s^{-1}$	Diffusion coefficient
(8)	D_A	m	Paddle diameter
(9)	H	m	Height of the fluid in container
(10)	R	m	Radius of the container

The ten dimensional variables are combined into seven dimensionless parameters. One possible way is shown in Table 7.3.

Table 7.3. Dimensionless variables for the dimensional analysis

$\Pi_1 = \frac{D t}{H^2}$	$\Pi_2 = \frac{H^2 N}{D}$	$\Pi_3 = \frac{h}{H}$	$\Pi_3 = \frac{d}{H}$
$\Pi_5 = \frac{D_A}{H}$	$\Pi_6 = \frac{R}{H}$	$\Pi_7 = \frac{\mu}{D \rho}$	

From the dimensionless Π_1 , we can see that the dimensionless time is inversely proportional to the diffusivity if the height of the fluid in the container is constant (i.e., fluid volume). This result will be used later on (see Chapter 7.3.5.2).

7.3.3 Colon model

7.3.3.1 Geometry, Membrane, Fluid, and Colonic motility

The models used in this study are similar to the ‘Stimulant PEG’ and ‘Stimulant Maltose’ represented in Schütt et al. (Schütt et al., 2021). Both are enlarged models of the human ascending colon (i.e., the length of the colon model is three times the length of the real ascending colon). The model has the form of a cylindrical body with a total length of 6.0×10^{-1} m and an inner diameter of 4.0×10^{-2} m. The membrane of the models is constricted at regular intervals, representing the colon *haustra*. The models are built with closed ends to ensure no fluid can exit the tube. The closed ends result in a back pressure when the fluid flow reaches the end of the tube. *In vivo* observations showed that most waves propagate only over a short distance in the proximal colon and usually terminate before the *hepatic flexure*, a sharp bend between the ascending

and the transverse colon, creating backflow/back pressure (Bampton et al., 2000, Dinning et al., 2008).

The membrane is composed of 2,500 LSM particles and modelled similarly to Schütt et al. (Schütt et al., 2020). These particles are tied to their initial position with a Hookean spring so that the membrane particles return to their initial position after activation (i.e., contraction or relaxation). This spring also ensures that the model is fixed in the domain during the simulation. The adjacent membrane particles are connected with an additional Hookean force to obtain an elastic membrane. The created lattice structure replicates, therefore, the properties of an elastic solid (Kot et al., 2015). The motility of the colon is achieved by applying a radial force to the particles representing the membrane in a specific pattern. Figure 7.3 shows a section of the colon model.

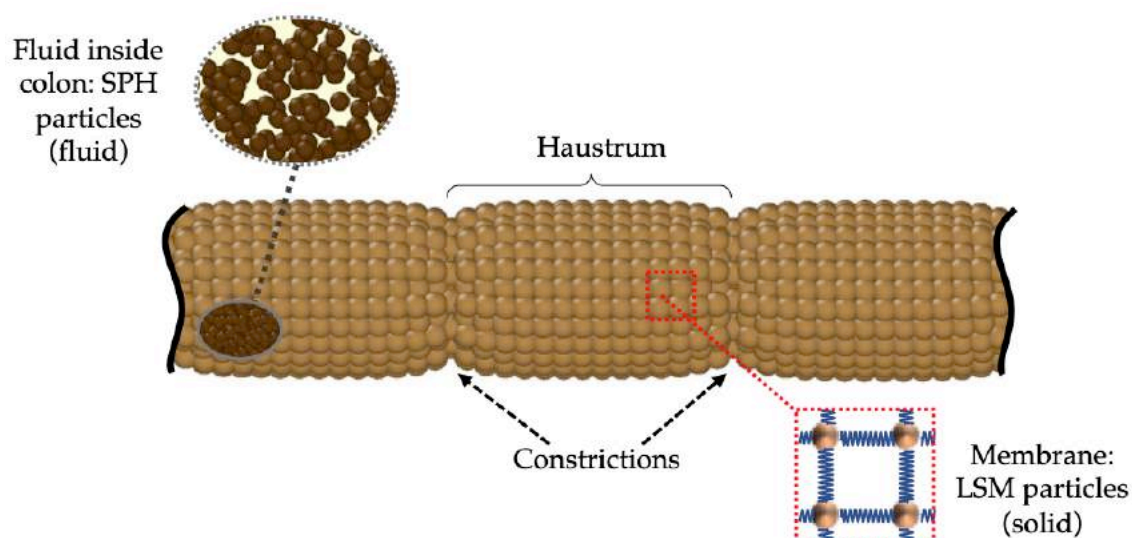


Figure 7.3 Representation of the colon model showing the construction of the membrane, the constrictions of the membrane building the haustrum, and the SPH particles representing the fluid inside the colon.

The Hookean forces are calculated using Hooke's law:

$$F_{ij} = k(r_{ij} - r_0) , \quad (7.3)$$

where F_{ij} is the resulting spring force between particle i and j . k is the Hookean constant, and r_{ij} represents the current distance between particles i and j . r_0 is the equilibrium distance between these particles. The Hookean coefficient used for the lattice of the membrane is $k_{M,b}$ and for the springs that return the particles to their initial position is $k_{M,p}$.

To improve the stability of the simulation and to give viscoelastic properties to the membrane (e.g., as in (Sahputra et al., 2020)), an additional viscous force of the following form is added to the membrane particles:

$$F_i = -k_{M,v}v_i \quad (7.4)$$

Here, v_i is the particle velocity, and $k_{M,v}$ is a viscous damping coefficient.

After calculating all the forces acting on each particle, the particles move according to Newton's equation of motion

$$m_i \frac{d\mathbf{r}_i}{dt} = \sum_j^N F_{ij} , \quad (7.5)$$

where \mathbf{r}_i is the position of particle i .

Further details of the simulated membrane are shown in Table 7.4.

Table 7.4. Colon membrane parameters

Parameter Membrane (Colon)	Value
SPH	
Number of SPH particles (1 layer)	2,500
Mass of each particle $m_{M,0}$	3.89×10^{-4} kg
LSM	
Hookean coefficient (bonds) $k_{M,b}$	0.2 J m^{-2}
Hookean coefficient (position anchor) $k_{M,p}$	0.012 J m^{-2}
Viscous damping coefficient $k_{M,v}$	$1.0 \times 10^{-2} \text{ kg s}^{-1}$
Equilibrium distance $r_{M,0}$	6.28×10^{-3} m

7.3.4 Fluid

The fluid volume in the mini-USP II is modelled with 131,422 SPH particles corresponding to a fluid volume of 100 mL as used in Stamatopoulos et al. (Stamatopoulos et al., 2015). The number of fluid particles used in the mini-USP II results from several simulations performed with different resolutions. By comparing the velocity fields obtained, the simulation with approximately 130,000 fluid particles proved to be the best compromise between accuracy and computational time.

The resolution obtained in the mini-USP II was accordingly also used in the colon models. Both models account for the same filling level of luminal content, modelled with approximal 64,000 SPH particles. The fluid level is taken from the study of Badley et al. (Badley et al., 1993), where they measure the fluid volume in the ascending colon using scintigraphy. The colonic fluid volume found in this study corresponds to a

filling level of about 40% in the ascending colon (Prasanth et al., 2012), which is accordingly used in the simulations.

In all models, the fluid is modelled as a Newtonian fluid; more complex rheology could be incorporated with the method developed in Duque-Daza and Alexiadis (Duque-Daza and Alexiadis, 2021).

Further details of the fluid used in the mini-USP II and colon model is given in Table 7.5.

Table 7.5. Fluid parameters

SPH Parameter Fluid	Value	Value
	mini-USP II	Colon
Number of SPH particles (fluid)	131,442	64,298
Mass of each particle m_{Fluid}	8.06×10^{-7} kg	4.72×10^{-6} kg
Density (fluid) ρ_{Fluid}	1000 kg m ⁻³	1000 kg m ⁻³
Dynamic viscosity (fluid) η_{Fluid}	1 mPa s	1 mPa s

7.3.4.1 Fluid structure interactions

In SPH, the equations of motion result from the discrete approximations of the Navier-Stokes equation on a number of points, which result from the discretisation of the continuum domain. These points can be considered as particles characterised by their mass, velocity, pressure, and density. SPH is based on the mathematical identity:

$$f(\mathbf{r}) = \iiint f(\mathbf{r}')\delta(\mathbf{r} - \mathbf{r}')d\mathbf{r}' , \quad (7.6)$$

where $f(\mathbf{r})$ is any scalar function defined over the volume V , with vector \mathbf{r} , a position vector in the space V . In the SPH formulations, the three-dimensional delta function $\delta(\mathbf{r})$ is approximated by a smoothing kernel W with its characteristic smoothing width or smoothing length h :

$$\lim_{h \rightarrow 0} W(\mathbf{r}, h) = \delta(\mathbf{r}) \quad (7.7)$$

Several kernel functions can be found in the literature. In this study, we use the simple Lucy kernel (Lucy, 1977). By replacing the delta function in equation 7.6 with a kernel or smoothing function W , the equation becomes

$$f(\mathbf{r}) \approx \iiint f(\mathbf{r}')W(\mathbf{r} - \mathbf{r}', h)d\mathbf{r}' . \quad (7.8)$$

By discretising the identity equation over a series of particles of mass $m = \rho(\mathbf{r}')d\mathbf{r}'$, the equation results in

$$f(\mathbf{r}) \approx \sum_i \frac{m_i}{\rho_i} f(\mathbf{r}_i)W(\mathbf{r} - \mathbf{r}_i, h) , \quad (7.9)$$

where m_i is the mass and ρ_i is the density of the i th particle. i ranges over all particles within the smoothing kernel W (i.e., $|\mathbf{r} - \mathbf{r}_i| < h$). The Navier-Stokes equation can be

approximated by equation 7.9 which represents a discrete approximation of a generic continuous field:

$$m_i \frac{dv_i}{dt} = \sum_j m_i m_j \left(\frac{P_i}{\rho_i^2} + \frac{P_j}{\rho_j^2} + \Pi_{i,j} \right) \nabla_j W_{i,j} + \mathbf{f}_i . \quad (7.10)$$

Here, v_i represents the velocity of particle i , P is the pressure, and $W_{i,j}$ is the concise form of $W(|\mathbf{r}_j - \mathbf{r}_i|, h)$. The term ∇_j is the gradient of the kernel with respect to the coordinate \mathbf{r}_j , and \mathbf{f}_i denotes a body force (e.g., gravity). $\Pi_{i,j}$ represents the viscous forces. In literature, various expressions are available for the tensor $\Pi_{i,j}$. Here we use the expression from (Morris et al., 1997).

$$\Pi_{i,j} = \frac{(\mu_i + \mu_j) v_{i,j}}{\rho_i \rho_j \mathbf{r}_{i,j}} , \quad (7.11)$$

where μ is the dynamic viscosity, and ρ is the density of particles i and j , respectively. $v_{i,j}$ is the relative velocity.

The Tait equation is used to calculate the pressure forces between the fluid particles and to link the density ρ and the pressure P in equation 7.10:

$$P = \frac{c_0^2 \rho_0}{7} \left[\left(\frac{\rho}{\rho_0} \right)^7 - 1 \right] , \quad (7.12)$$

where c_0 is the reference speed of sound and ρ_0 is the density at zero applied stress.

For the solid-fluid interactions (i.e., between the container and the fluid, the agitator and the fluid, the membrane and the fluid, and the tablet and the fluid), a repulsive potential in the form

$$E_{ij} = A \left[1 + \cos \left(\frac{\pi r_{ij}}{r_c} \right) \right] \quad \text{with} \quad r_{ij} < r_c \quad (7.13)$$

is used. Here, A is an energy constant, r_{ij} represents the distance between particles i and j . r_c is the cut-off distance. Viscous forces approximate the no-slip boundary conditions between the solid and fluid particles. These forces are similar to those of equation 7.11 but are applied to the interaction between solid and fluid particles.

Further details of the fundamental simulation parameters are given in Table 7.6.

Table 7.6. Fundamental model parameters

Parameter	Value mini-USP II	Value Colon
SPH		
Artificial speed of sound c_0	0.5 m s ⁻¹	0.1 m s ⁻¹
Time-step Δt	1.0×10^{-5} s	5.0×10^{-4} s
Momentum – Smoothing length (fluid) $h_{M,F}$	2.45×10^{-3} m	2.45×10^{-3} m
Momentum – Smoothing length (tablet) $h_{M,T}$	1.76×10^{-3} m	1.76×10^{-3} m
Momentum – Smoothing length (fluid / tablet) $h_{M,FT}$	1.80×10^{-3} m	1.80×10^{-3} m
Diffusion – Smoothing length (fluid / tablet) $h_{D,FT}$	1.39×10^{-3} m	1.39×10^{-3} m
Diffusion – Smoothing length (fluid) $h_{D,F}$	2.45×10^{-3} m	2.45×10^{-3} m
Diffusion – Smoothing length (tablet) $h_{D,T}$	1.14×10^{-3} m	1.14×10^{-3} m
Diffusion coefficient (tablet) D_T	1.0×10^{-30} m ² s ⁻¹ 8.0×10^{-6} m ² s ⁻¹	1.0×10^{-30} m ² s ⁻¹
Diffusion coefficient (fluid / tablet) D_{FT}	8.0×10^{-7} m ² s ⁻¹ 8.0×10^{-8} m ² s ⁻¹	8.0×10^{-8} m ² s ⁻¹
<i>(varies between simulation)</i>	8.0×10^{-9} m ² s ⁻¹ 8.0×10^{-10} m ² s ⁻¹	

7.3.5 Tablet

In our model, the tablet is modelled similarly to Schütt et al. (Schütt et al., 2021). The tablet is composed of 582 LSM particles and has a total weight of 566 mg, which

corresponds to the tablet in Stamatopoulos et al. (Stamatopoulos et al., 2015). The adjacent particles of the tablet are interconnected with linear and diagonal springs to archive a rigid structure according to equation 7.3. The Hookean coefficient used for the lattice of the tablet is $k_{T,b}$ and can be found in Table 7.7. The tablet is modelled accordingly to the tablet used in Stamatopoulos et al. (Stamatopoulos et al., 2015): a cylindrical body with a height of 5.0×10^{-3} m and a diameter of 1.0×10^{-2} m. A schematic 3D representation is shown in Figure 7.4. The magnification in the figure shows the linear and diagonal bonds of the neighbouring tablet particles.

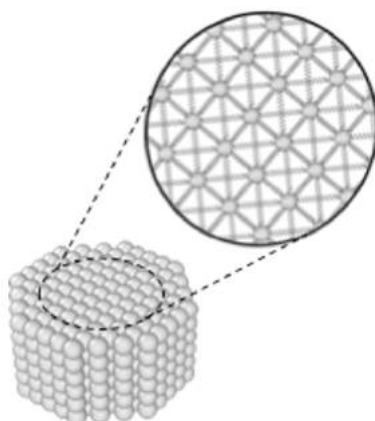


Figure 7.4 3D-representation of the tablet. Linear and diagonal springs connect the particles representing the tablet to obtain a solid structure.

7.3.5.1 Tablet disintegration

The dissolution/disintegration process of the tablet is modelled similarly to Schütt et al. (Schütt et al., 2021). Each of the 582 LSM particles representing the tablet is assigned a specific concentration representing the tablet's active pharmaceutical ingredient (API). The dissolution of the tablet is achieved by mass diffusion between the fluid and tablet particles and between the tablet particles themselves. In the SPH framework, the

diffusive mass balance for a multi-component system can be written in the following form (Alexiadis, 2015a):

$$\frac{dw_i}{dt} = - \sum_j \frac{m_i m_j (D_i + D_j)(C_i - C_j)}{\rho_i \rho_j r_{i,j}^2} r_{i,j} \cdot \nabla_j W_{i,j} . \quad (7.14)$$

Here, w_i is the mass of the fluid in the particle, and D_i is the diffusion coefficient. C_i is the concentration that belongs to each particle i . Equation 7.15 is used to close equation 7.14 with the following relation between m_i , C_i and ρ_i (Alexiadis, 2015a):

$$w_i = C_i \frac{m_i}{\rho_i} \quad (7.15)$$

The API used in the experimental tablet from Stamatopoulos et al. (Stamatopoulos et al., 2015) is Theophylline (THE), a highly water-soluble drug. The solubility of THE in water at 37°C is approximately 12.5 mg mL⁻¹ (Grassi et al., 2001). This means it is possible to dissolve the entire tablet in the fluid volume within these models. The diffusion coefficient of THE was determined in distilled water and estimated to be $8.21 \times 10^{-10} \text{ m}^2 \text{ s}^{-1}$ (Grassi et al., 2001).

The tablet is modelled as 100% drug and we assume that the drug is uniformly distributed within the real tablet. We are aware that the tablet used in Stamatopoulos et al. (Stamatopoulos et al., 2015) contains excipients (e.g., to control the drug release) and not only drug. However, this study focuses on the tablet's realistic dissolution/disintegration behaviour and not on the influence of different excipient compositions on the dissolution/disintegration behaviour. We indirectly accounted

for the influence of excipients on tablet dissolution/disintegration by using experimental tablet optimisation data and modifying the modelled tablet to behave like the experimental tablet as a whole (i.e., drug + excipients).

In the tablet model, all the neighbouring particles are interconnected with each other with bonds. If the concentration of at least one of two adjacent tablet particles falls below a predefined threshold X (e.g., $X = 0.90$ means 10% dissolved), the bond between these particles is removed weakening the solid structure of the tablet. A bond between two particles is also deleted if the distance between two bonded particles increases by 10% of their initial spacing (e.g., due to the influence of shear forces). If a computational tablet particle has no bond with any other tablet particles, the particle detaches completely from the tablet. In this way, the disintegration process of the tablet is simulated.

Finally, when the concentration of the active ingredient in the tablet is below its solubility concentration C_s (defined as 5%, i.e., 95% dissolved), the type of the tablet particle is changed from LSM to SPH: i.e., the particle stops behaving like a solid particle and behaves like a fluid particle.

In the models (i.e., mini-USP II and colon), the fluid and the tablet were discretised differently (i.e., different particle resolution). This results in a different initial particle distance between the fluid and the tablet particles. Thus, a different 'momentum' smoothing length is used between the fluid and tablet particles. The 'diffusion' smoothing length between the fluid and tablet particles is obtained from a weighted smoothing length based on the smoothing length of the fluid particles and the tablet particles. Further details of the general model parameter and specific model properties are given in Table 7.6 and Table 7.7, respectively.

Table 7.7. Tablet parameters

Parameter Tablet	Value
SPH	
Number of SPH tablet particles	582
Mass of each particle m_{Tablet}	9.73×10^{-7} kg
Density (Tablet) ρ_{Tablet}	1502 kg m ⁻³
LSM	
Hookean coefficient $k_{T,b}$	0.1 J m ⁻²
Equilibrium distance (linear bonds) $r_{TL,0}$	8.8×10^{-4} m
Equilibrium distance (diagonal bonds) $r_{TD,0}$	1.24×10^{-3} m

7.3.5.2 Development of the tablet and data analysis

The simulation of a disintegrating/dissolving tablet in a stirring tank with SPH is computational very intensive. In our case, to simulate approximately 2 minutes of real-time 144 cores with 576 GB memory, a wall time of 10 days is needed.

To overcome this problem, we notice that the time scale of the hydrodynamics T_H in the stirring tank and the time scale of the tablet dissolution process T_D are different (i.e., $T_H \sim 1$ s and $T_D \sim 1$ hour) and do not overlap ($T_D \gg T_H$). Since the tablet dissolution is considerably slower than the hydrodynamics, we can assume that, if we consider small time intervals of the order of T_H , the dissolution process does not affect the hydrodynamics. Furthermore, the results of the dimensional analysis (Chapter 7.3.2.2) confirms that it is possible to compare different diffusion coefficients D by rescaling time t , because t is inversely proportionally to the diffusion coefficient:

$$t \propto \frac{1}{D} , \quad (7.16)$$

By using equation 7.16, it is possible to compare the dissolution profiles of tablets with different diffusivities. For instance, the dissolution profile of a tablet with total dissolution time $t_0 = 10^4$ s and $D = 10^{-10}$ m² s⁻¹ has the same shape of the dissolution profile of a tablet with $t_0 = 1$ s and $D = 10^{-6}$ m² s⁻¹. That is, if we use dimensionless numbers, these two profiles overlap. In the following sections, we are going to use a dimensional time τ defined as

$$\tau[-] = \frac{t}{t_0} , \quad (7.17)$$

where t_0 is the total dissolution time and t is the actual time. For the simulation data $t_0 = 90$ s and for the experimental data of Stamatopoulos et al. (Stamatopoulos et al., 2015) $t_0 = 18000$ s.

Stamatopoulos et al. (Stamatopoulos et al., 2015) analysed the dissolution process in the mini-USP II across a time interval of approximately 8 hours, corresponding to a time scale of 10^4 seconds. The diffusion coefficient of the pure drug used in the experimental tablet is approximately 8.0×10^{-10} m² s⁻¹.

In order to find a tablet that behaves as similarly as possible to the experimental one, we built tablets with different thresholds X : 0.1, 0.35, 0.60, and 0.85 (see Chapter 7.3.5.1). This means that the bond between two tablet particles breaks when 90%, 65%, 40%, or 15%, respectively, of the API concentration of the bound particles, is dissolved

in the fluid. Simulations were carried out with the modelled tablets and with different diffusion coefficients of the API: $8.0 \times 10^{-6} \text{ m}^2 \text{ s}^{-1}$, $8.0 \times 10^{-7} \text{ m}^2 \text{ s}^{-1}$, $8.0 \times 10^{-8} \text{ m}^2 \text{ s}^{-1}$, $8.0 \times 10^{-9} \text{ m}^2 \text{ s}^{-1}$, and $8.0 \times 10^{-10} \text{ m}^2 \text{ s}^{-1}$.

Data analysis of the different tablets and diffusion coefficients D shows (Chapter 7.4.2) that the API mass flow ϕ^* for each tablet follows the following equation:

$$\phi^* = \epsilon D^\alpha, \quad (7.18)$$

where ϵ is a tablet specific constant and $\alpha = 0.61$ an exponential constant valid for all tablets.

To determine the model that best represents the behaviour of the experimental tablet from Stamatopoulos et al. (Stamatopoulos et al., 2015), the Péclet number Pe was used:

$$Pe = \frac{N d^2}{D}, \quad (7.19)$$

where N is the paddle speed, d the paddle diameter and D the diffusion coefficient.

The experimental dissolution data from Stamatopoulos et al. (Stamatopoulos et al., 2015) show a linear progression (see Chapter 7.4.2, Figure 7.11) and an average mass flow rate of the API from the tablet of approximately $8.29 \times 10^{-9} \text{ kg s}^{-1}$. The corresponding Pe number for these conditions is 9.15×10^5 . Due to the limited data available, only this single data point is used to select the computational tablet whose dissolution profile best matches the behaviour of the real tablet.

7.3.6 Software

The simulations in this study were performed using the University of Birmingham's BlueBEAR HPC service (Birmingham). For the numerical calculations, the open-source code LAMMPS (Ganzenmüller et al., 2011, Plimpton, 1995) is used. OVITO (Stukowski, 2010) is used for the visualisation and MATLAB (MATLAB, 2022) for the postprocessing of the simulation data.

7.4 Results and Discussion

7.4.1 Model validation – hydrodynamics

To validate our computational model of the mini-USP II in terms of hydrodynamics, we compared the obtained velocity profile with experimental and computational data from Wang et al. (Wang and Armenante, 2016). The experimental data were determined using Particle Image Velocimetry (PIV). The computational data were obtained by using ANSYS FLUENT 14.5.

Figure 7.5 a) represents the dimensions of the mini-USP II used by Wang et al. (Wang and Armenante, 2016), Figure 7.5 b) the experimental and computational results obtained from Wang et al. and Figure 7.5 c) the result from the DMP simulation. The DMP model shows good agreement with the results of Wang et al. (Wang and Armenante, 2016).

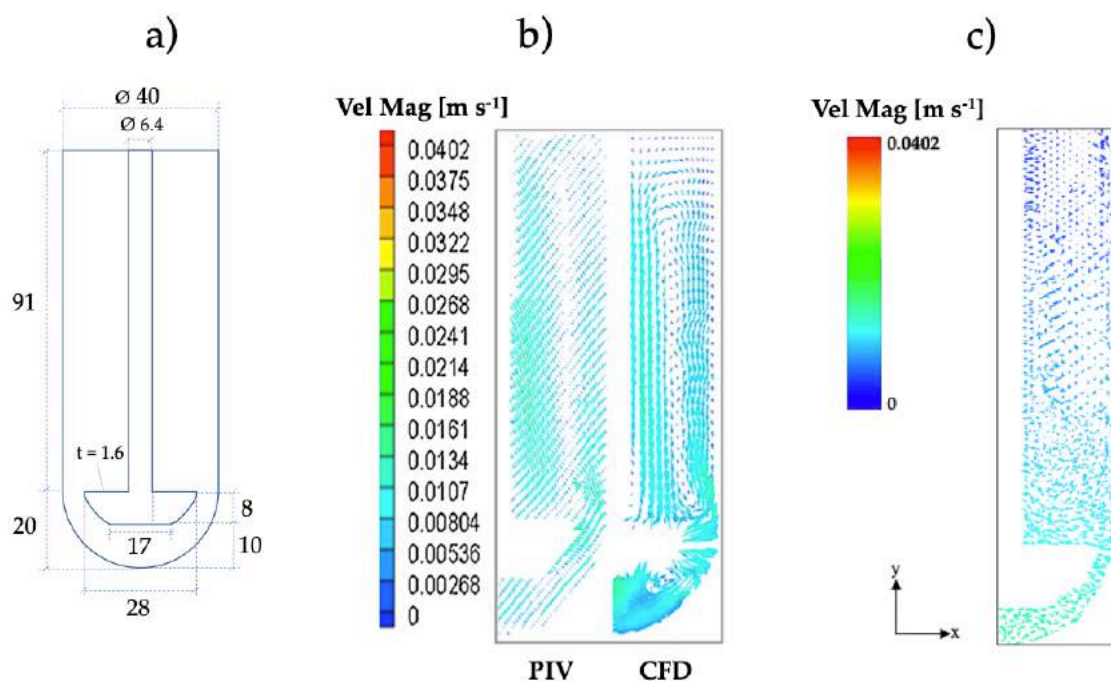


Figure 7.5 Validation of the computational mini-USP II model by comparison of the velocity profile from the simulation with experimental and simulated data from Wang et al. (Wang and Armenante, 2016). a) shows the dimensions of the mini-USP II used in both, the experimental and computational part, b) Experimental and computational data reproduced with permission from Wang et al., and c) the velocity profile obtained from the simulation.

7.4.2 Evaluation of the tablet disintegration/dissolution

As discussed in Chapter 7.3.5.2, four different tablets with different threshold values X (i.e., value for the bond/break specification) and different diffusion coefficients have been developed. In total, 20 different simulations were performed to investigate the tablet that best matches the performance of the experimental tablet from Stamatopoulos et al. (Stamatopoulos et al., 2015).

The results from the simulations for each X are represented in Figure 7.6.

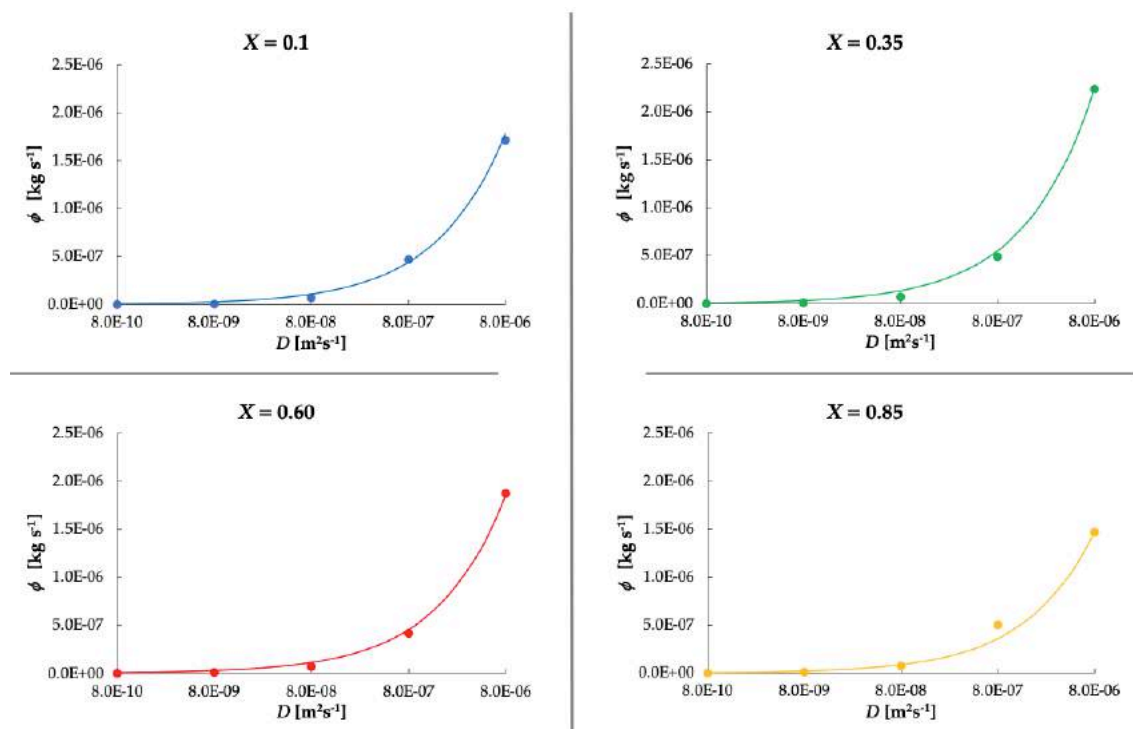


Figure 7.6 Mass flow rate ϕ of the API from the tablet obtained from the simulations in the mini-USP II for different X and for different diffusion coefficients D .

The data for the different threshold values X show that the Mass flow rate of the API from the tablet can be represented by equation 7.18. The exponential constant was determined to be $\alpha = 0.61$. The values for ϵ are shown in Table 7.8:

Table 7.8. Values for the constant ϵ

X	ϵ
0.1	2.3×10^{-3}
0.35	2.9×10^{-3}
0.60	2.4×10^{-3}
0.85	1.9×10^{-3}

Figure 7.7 a) shows the entire diagram of the simulations, where the mass flow rate ϕ^* (i.e., calculated using equation 7.18) of the different computational tablets is

represented over the Péclet number. The red star indicates the data point of the experimental tablet.

To be able to analyse the region of the experimental tablet (i.e., with the red star) more precisely, an enlarged section of this region is shown in Figure 7.7 b).

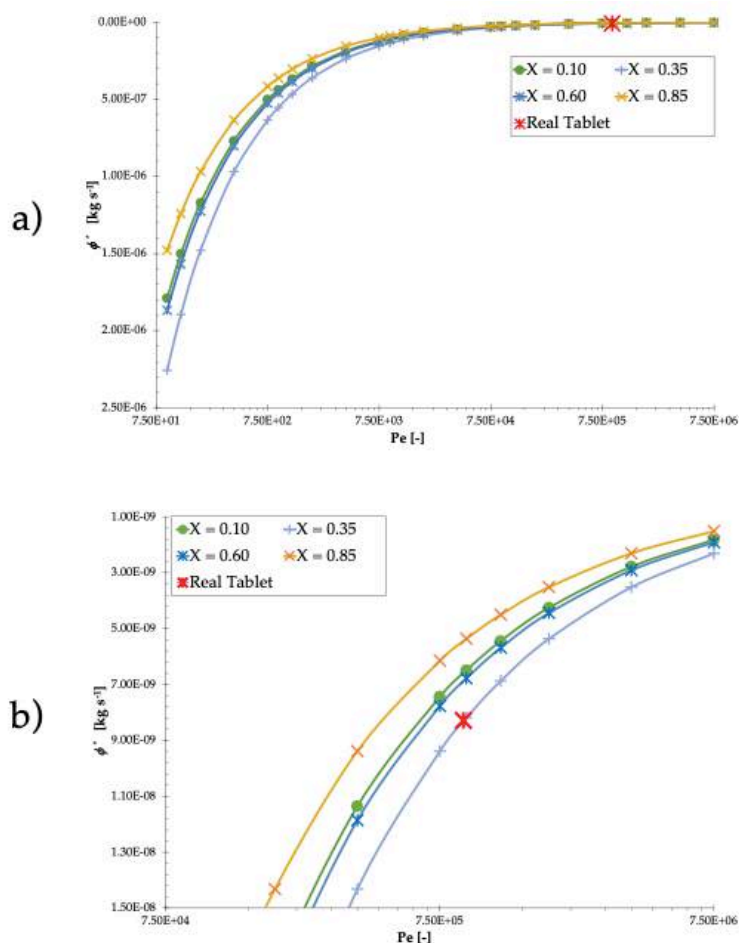


Figure 7.7 a) Representation of the results obtained from the simulations and a characteristic data point from the experimental tablet. b) Enlarged section from a) of the region of the experimental tablet.

From Figure 7.7 b) it can be observed that the modelled tablet with a bond/break threshold $X = 0.35$ best represents the behaviour of the experimental tablet.

To further verify the realistic disintegration behaviour of the modelled tablet, the disintegration course of the modelled tablet was compared with the disintegration course of a real tablet. Unfortunately, the tablet used in Stamatopoulos et al. (Stamatopoulos et al., 2015) is customized and therefore not available for direct comparison. Nevertheless, to be able to compare the disintegration process of the modelled tablet with a real tablet, we used a commercially available tablet. The reference tablet shown in Figure 7.8 (top) is an immediate-release (IR) tablet (i.e., Metoprolol tartrate, an oral administered tablet) from Aurobindo Pharm - Milpharm Ltd. Images of the disintegration/dissolution process of the tablet were taken at four different time points, each fifteen minutes apart. The conditions in the mini-USP II were similar to the model conditions: rotational speed of the paddle 50 rpm, water temperature 37°C.

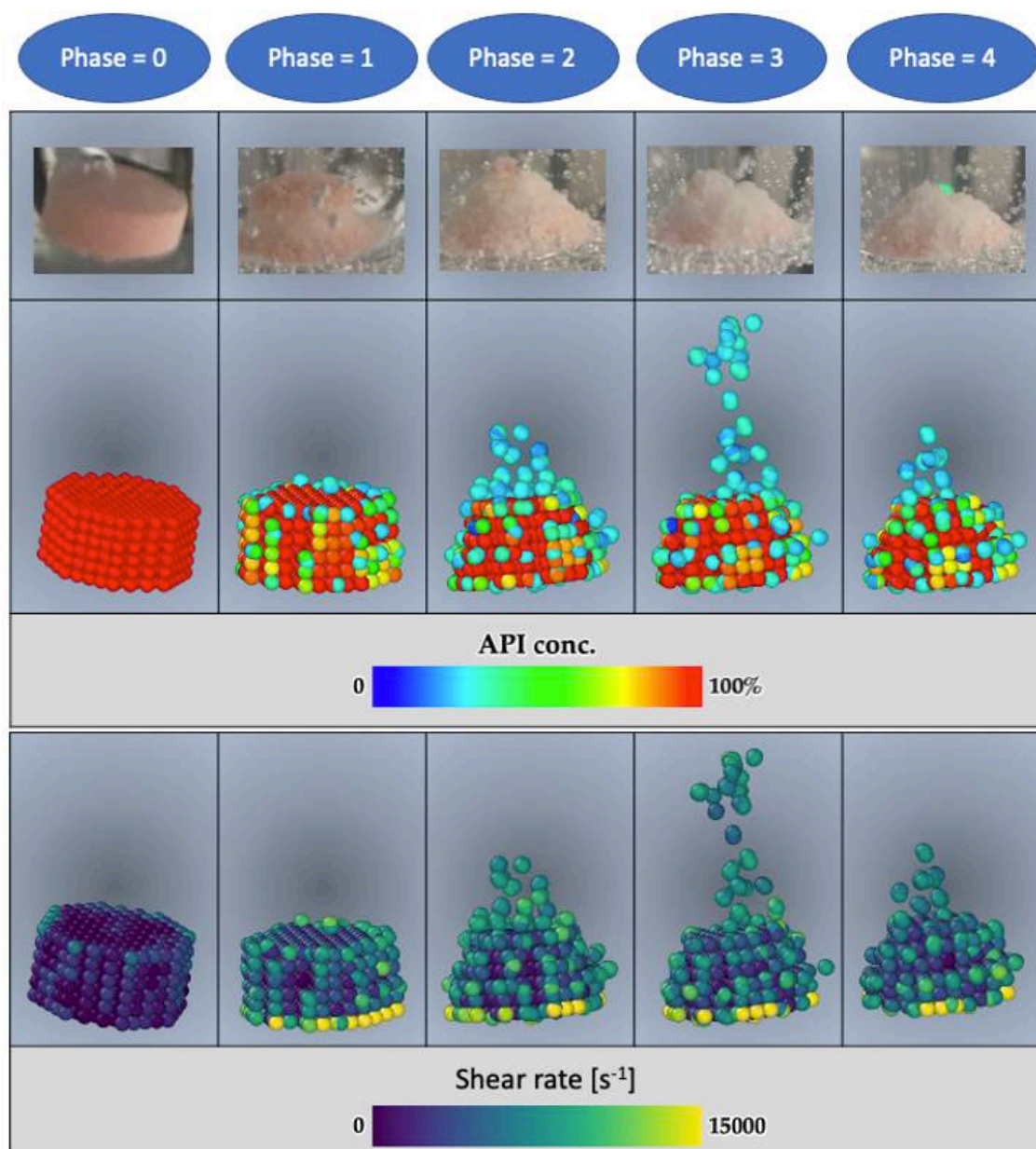


Figure 7.8 Comparison of the tablet disintegration/dissolution process of a real tablet (top) and the computational tablet (middle and bottom) at different phases of the tablet disintegration/dissolution process. The particles of the modelled tablet (middle) are coloured according to their API concentration, where red indicates 100% API and dark blue 0% API. At the bottom the particles of the modelled tablet are coloured according to the shear rate exposed, where purple indicates low, and yellow a high shear rate.

In Figure 7.8, the tablet is in its initial rigid state at t_0 and slowly disintegrates from the left to the right. The computational tablet shows a very similar behaviour to the real tablet. At Phase = 0, water diffuses into the tablet and some tablet particles detach from

the tablet. From Phase = 1 to Phase = 4, the tablet shape changes in both cases, the computational and the real tablet, from a cylindrical body to a cone and releases more and more particles.

The drug release process from the tablet and the disintegration/dissolution of the tablet occurs in four main steps as shown in Figure 7.9. As an example, we used the tablet that represents the real tablet and scaled the time and the diffusion coefficient according to equation 7.16. Thus, we use a diffusion coefficient of $D = 8.0 \times 10^{-6} \text{ m}^2 \text{ s}^{-1}$ for the simulation and the simulation is run for 120 s real time.

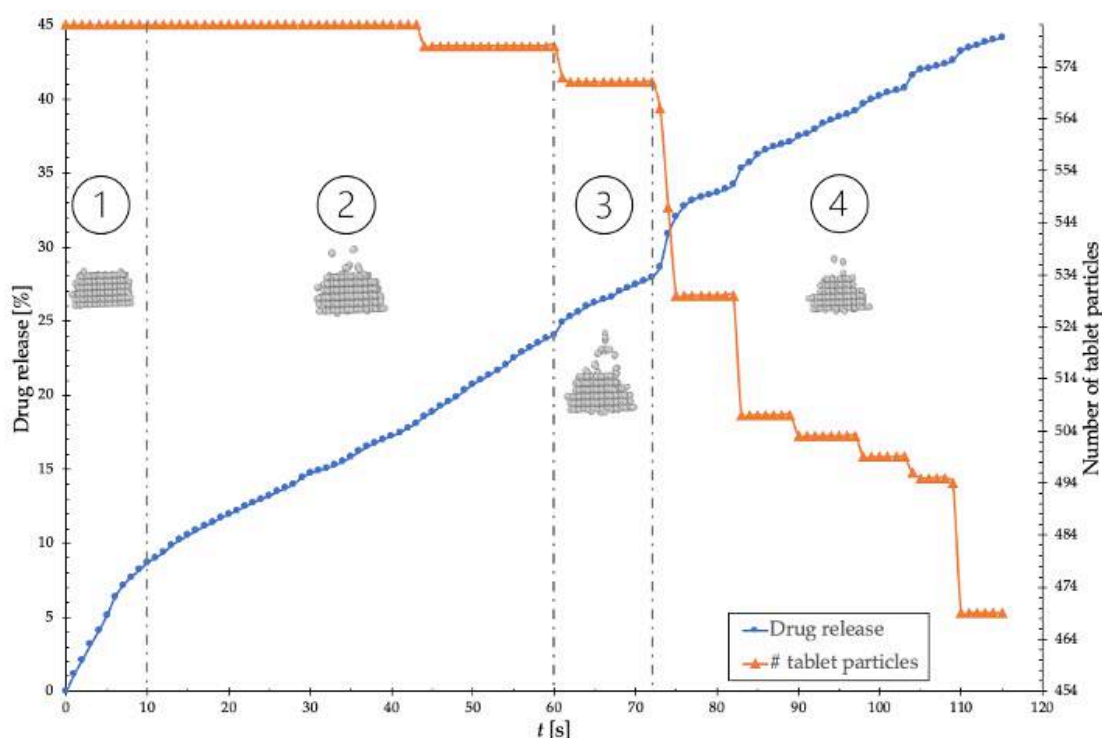


Figure 7.9 Drug release and tablet disintegration of the modelled tablet in the mini-USP II with $X = 0.35$ and $D = 8.0 \times 10^{-6} \text{ m}^2 \text{ s}^{-1}$. The blue line represents the drug release and the orange line the number of tablet particles not yet dissolved in the fluid.

In the first step, water diffuses into the tablet and the API into the fluid, resulting in an almost linear release of active ingredient. In the second step, the rigid structure of the tablet begins to weaken, and the first drug particles detach from the tablet into the fluid. In our case, a particle that detaches from the tablet but is not yet completely dissolved in the fluid is counted as a "tablet particle". The drug release profile is still linear, but with a lower slope. The outer layer absorbed water and thus its API content, creating an additional mass transfer resistance between the core of the tablet (rich in drug) and water. In the third step, more particles detach from the tablet. This temporarily leads to an increased release of the API, as a larger part of the tablet is exposed to the fluid. Finally, in the fourth step, the solid structure continues to weaken, resulting in fragments detaching from the tablet, and leading to an increased release of active ingredient.

One main parameter influencing the disintegration/dissolution of the tablet is the shear stress acting on the surface of the tablet (Schütt et al., 2021). Figure 7.10 represents the dissolution profile and the average shear rate acting on the tablet particles over time. The profile is taken from the same tablet used in Figure 7.9.

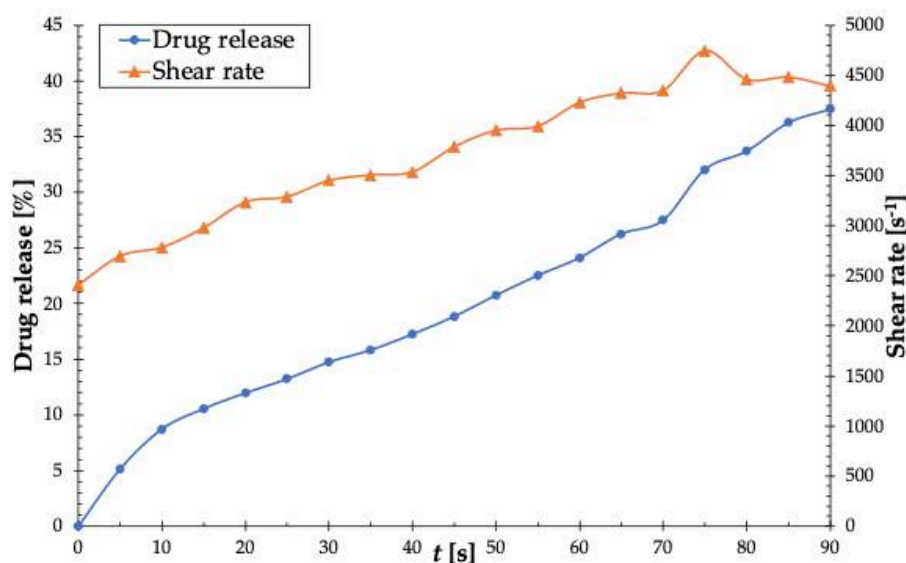


Figure 7.10 Drug release and tablet disintegration of the modelled tablet in the mini-USP II with $X = 0.35$ and $D = 8.0 \times 10^{-6} \text{ m}^2 \text{ s}^{-1}$. The blue line represents the drug release and the orange line the average shear stress acting on the tablet particles.

In the model, the paddle was ‘switched on’ and the tablet was ‘activated’ as soon as the hydrodynamics in the container were steady state. For this reason, the shear rate acting on the tablet is already at a higher value at $t = 0$. In the course of disintegration, the average shear rate also increases. This is because the structure of the rigid tablet becomes weaker and individual particles detach from the tablet, creating edges on the tablet on which the fluid can act more effectively.

The shear stresses and, consequently, shear rates acting on the tablet surface are in good agreement with the shear stresses found in Kindgen et al. (Kindgen et al., 2015), where they performed simulations of the hydrodynamics and stresses in the PhEur/USP Disintegration Tester with different fluids (i.e., Newtonian and non-Newtonian fluids and different fluid viscosities). These values also correspond very well with the shear stresses found in other studies, even though they focused on the stomach (Abrahamsson et al., 2005, Pal et al., 2003).

In Figure 7.11, the drug release data from the modelled tablet obtained in the mini-USP II model is compared to the experimental data from Stamatopoulos et al. (Stamatopoulos et al., 2015). This is done using the dimensionless time τ (equation 7.17). Stamatopoulos et al. (Stamatopoulos et al., 2015) received the drug release data using two different sampling points S_p in the mini-USP II container (i.e., 19 and 66 mm above the paddle). For comparison, we use an average of these measurements, indicated as Stamatopoulos et al. 'average' in Figure 7.11.

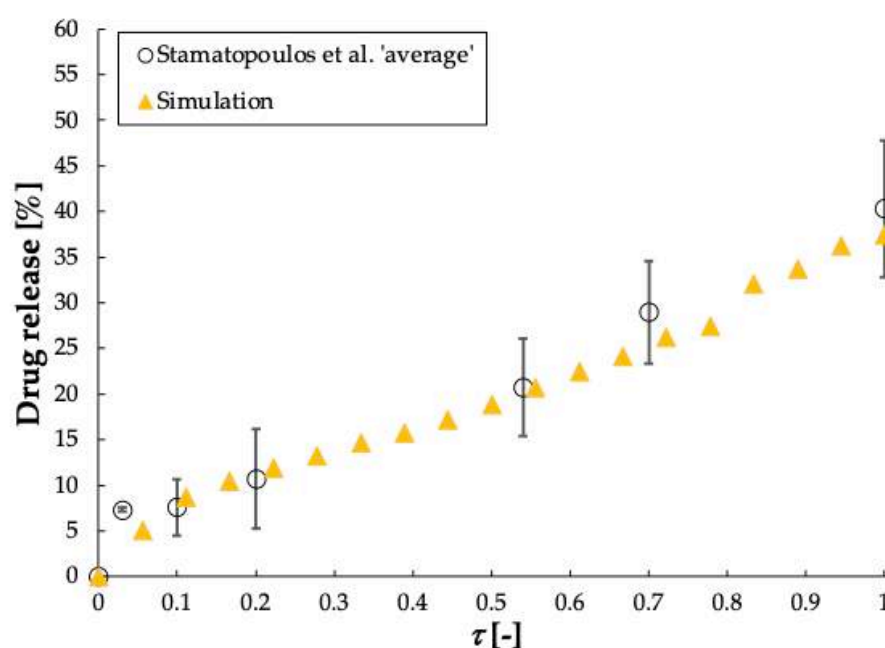


Figure 7.11 Drug release and tablet disintegration of the modelled tablet in the mini-USP II with $X = 0.35$ and $D = 8.0 \times 10^{-6} \text{ m}^2 \text{ s}^{-1}$ and the experimental data for a simple buffer reproduced from Stamatopoulos et al. (Stamatopoulos et al., 2015).

The standard deviation s in Figure 7.11 is calculated as follows:

$$s = \frac{|S_{p,1} - S_{p,2}|}{\sqrt{2}}, \quad (7.20)$$

7.4.3 Comparison of the drug release profile from the experimental tablet in the mini-USP II with the drug release profile of the modelled tablet in the colon model

To compare the dissolution profile of the conventional dissolution apparatus with the colon model, we run the simulation with the same tablet properties used in the mini-USP II model (i.e., $D = 8.0 \times 10^{-6} \text{ m}^2\text{s}^{-1}$, $X = 0.35$) in the colon model and determine drug release profile and shear stress acting on the tablet. Figure 7.12 shows the drug release profile in the colon models with two different in vivo motility patterns, 'PEG' and 'Maltose' (Schütt et al., 2021). The dimensionless time τ is calculated according to equation 7.14.

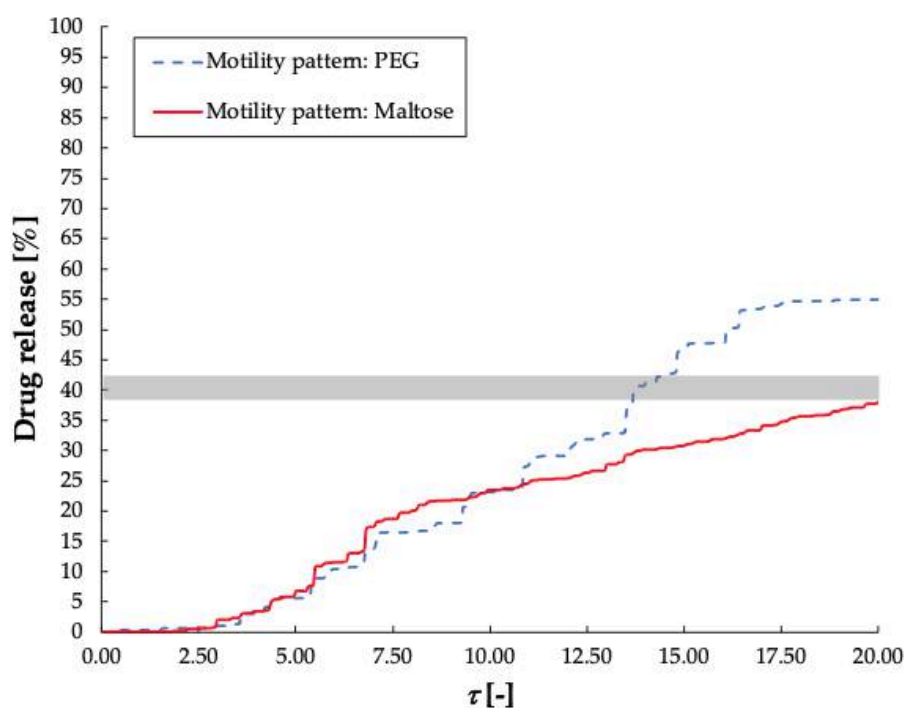


Figure 7.12 Drug release of the modelled tablet with $X = 0.35$ and $D = 8.0 \times 10^{-6} \text{ m}^2 \text{ s}^{-1}$ in the colon model using two different in vivo motility pattern from (Schütt et al., 2021).

The grey shaded area represents the drug release obtained in the mini-USP II in Figure 7.11 at $\tau = 1$. In the colon models, it takes approximately 13.5 times longer in the case of the PEG motility pattern and approximately 20 times longer in the case of the maltose motility pattern to achieve the same drug release as in the mini-USP II.

This can be explained by the shear rate acting on the tablet surface, represented in Figure 7.13. In the colon models, the shear stress is induced by the wall motion of the colon.

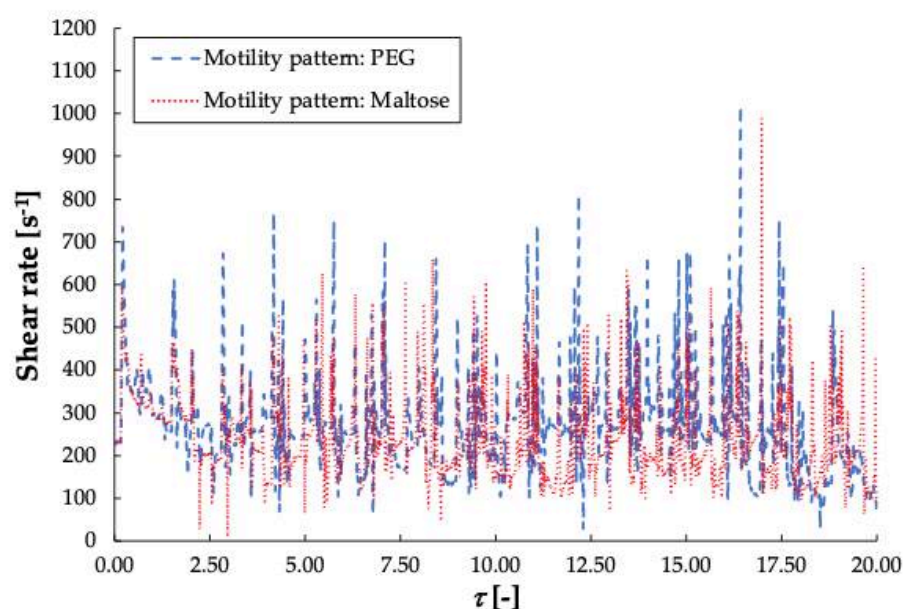


Figure 7.13 Shear rate acting on the modelled tablet during the drug release process represented in Figure 7.12 (colon model).

By comparing Figure 7.10 and Figure 7.13 (i.e., mini-USP II and colon model, respectively), it can be established that the shear rate acting on the tablet surface in the colon models is about one order of magnitude smaller than in the mini-USP II at 50 rpm. Also, the shear stress profile shows different progress in the mini-USP II compared to the colon model. In the mini-USP II, the shear rate acting on the tablet is

rather constant, whereas, in the colon model, it occurs in peaks, which accelerates the drug release process (Schütt et al., 2021).

To investigate whether a slower paddle speed in the mini-USP II results in a shear rate acting on the tablet that is of the same order of magnitude as in the colon model and thus more closely mimics in vivo conditions, we built several mini-USP II models with different paddle speeds. The paddle speed was set to 1, 5, 15, 25, 35 and 50 rpm accordingly. The properties of the tablet are the same as those used previously (i.e., $D = 8.0 \times 10^{-6} \text{ m}^2\text{s}^{-1}$, $X = 0.35$).

Figure 7.14 shows the influence of the paddle speed on the tablet's drug release profile in the min-USP II.

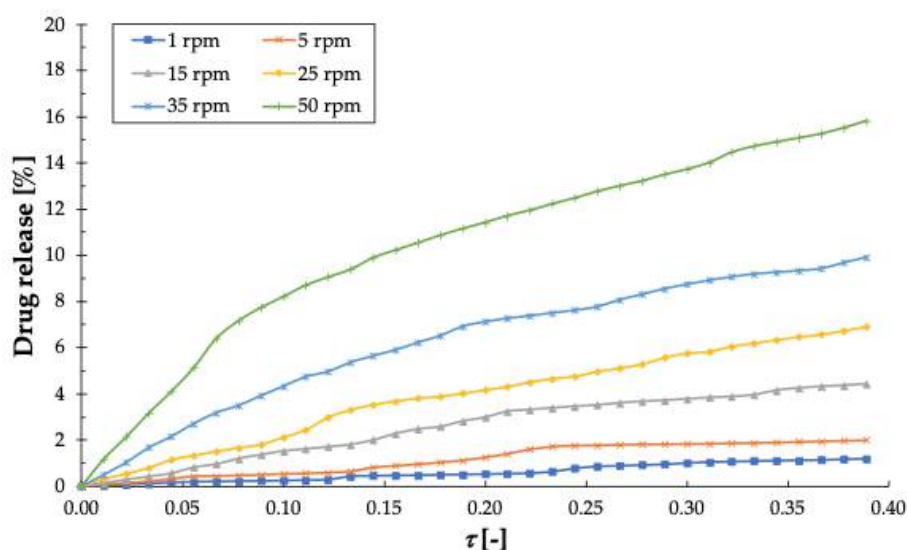


Figure 7.14 Drug release profile in the mini-USP II at different paddle speeds.

With an increased paddle speed and thus a higher fluid flow around the tablet, the drug release process is also accelerated.

Likewise, the shear rate acting in the tablet increases with an increase in paddle speed, which is represented in Figure 7.15.

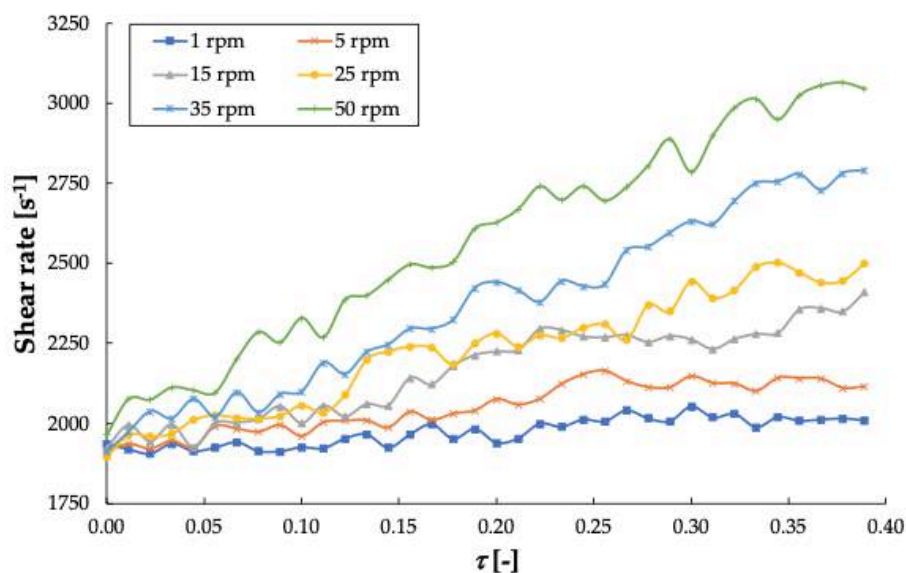


Figure 7.15 Shear rate acting on the modelled tablet during the drug release process in the mini-USP II shown in Figure 7.14.

According to Metzner et al. (Metzner et al., 1961), the average shear rate in the liquid is a function of the impeller speed and behaves proportionally. In this case, the shear rate experienced by the tablet is not proportional to the paddle speed. This can be attributed to the fact that different velocity profiles occur in the container and that the fluid flow around the tablet is not proportionally to the paddle speed. Even at low paddle speeds of 1 and 5 rpm, the average shear stress experienced by the tablet is about one order of magnitude larger than the ‘baseline’ shear stress acting on the tablet in the colon models (Figure 7.13). As mentioned previously, the tablet is ‘activated’ when the hydrodynamics in the container reaches steady-state conditions. Therefore, the shear stress is already at an increased value at $\tau = 0$. From the results in Figure 7.15, even a paddle speed of 1 rpm in the mini-USP II results in a slightly too high average

shear rate acting on the tablet compared to the colon models. However, by using an "on-off" operating mode in the mini-USP II, the conditions (i.e., the generation of shear rate peaks) would better reflect the in vivo conditions of the human colon instead of a constant paddle speed of 50 rpm normally used.

7.5 Conclusion

In this study, we reuse a computational model of ascending colon developed in Schütt et al. (Schütt et al., 2021) with in vivo motility patterns, a digital twin of the mini-USP II dissolution apparatus and a digital twin of a tablet that mimics a real tablet. The models are used to compare the disintegration/dissolution behaviour of a tablet in a standard dissolution apparatus and a biorelevant colon model. We show the extreme case where the fluid exerts higher shear rates on the tablet surface than a fluid with higher viscosity, as previously demonstrated in Schütt et al. (Schütt et al., 2021).

The shear rates acting on a tablet surface determined in the colon models are in the same order of magnitude as in Abrahamsson et al. (Abrahamsson et al., 2005), even though their study focuses on the stomach. This is probably due to elevated colon motility stimulated by PEG and maltose, resulting in increased shear rates that also occur in the fed stomach.

The results show that the average shear forces acting on a tablet are relatively low in the colon models and follow a different pattern than in the mini-USP II. A much lower paddle speed and a structured stirring profile could be used to replicate these conditions better. A different approach could be to lower the "baseline" shear rate acting on the tablet, increased clearance in the mini-USP II could be used. However,

whether the mini-USP II or even the USP II dissolution apparatus is the most appropriate apparatus to mimic in vivo conditions in the colon is worth considering. The current challenges and limitations of the approach to developing a computational tablet that mimics a real tablet are based on the available experimental data. Future work needs to incorporate more data from the real tablet, such as the release profile at different paddle speeds in the mini-USP II, to support further the accuracy of the method used. Nevertheless, the approach shows a first step towards modelling a real tablet.

7.6 Acknowledgements

We would like to thank Connor O'Farrell for conducting the tablet disintegration experiment in the mini-USP II dissolution apparatus and for providing the images.

Chapter 8

Conclusions and Future Work Suggestions

8.1 Conclusions

This thesis presents the development of biorelevant colon models using Discrete Multiphysics (DMP). DMP is a modelling approach that combines different particle-based simulation techniques. The simulation techniques used in this thesis are Smoothed Particle Hydrodynamics (SPH) for the fluid inside the models (i.e., intestinal content and solvent) and Lattice Spring Model (LSM) for the viscoelastic, deformable membrane of the colon and to model the disintegrating/dissolving tablet. The developed models were used to investigate the hydrodynamics, drug release of a solid dosage form, and the released Active Pharmaceutical Ingredient (API) distribution along the colon. The simulations were performed under different fluid conditions (i.e., fluid viscosities), different propagation speeds of a contractile wall wave, and various biorelevant motility patterns. By developing a computational counterpart to a validated, biorelevant dissolution apparatus, the Dynamic Colon Model (DCM), the modelling approach is validated with respect to hydrodynamic conditions.

Furthermore, the performance of a solid dosage form in a standardised dissolution apparatus (i.e., mini-USP II) and the biorelevant colon model were compared. Therefore, models of the mini-USP II and the colon were created, and a tablet was developed that behaves like a real tablet. For comparison, the drug release profiles as well as the shear rates acting on the tablet were analysed.

The results from the models show that the filling level (i.e., media volume) influences the shear stresses, the mixing efficiency, concentration distribution and hydrodynamic profiles inside the colonic environment. Also, in the extreme case of an undissolved, naturally buoyant tablet, the filling level impacts the transit time. A gaseous phase, on

the other hand, seems to be negligible. The motility in the colon is dependent on various parameters such as diet and disease. Analyses of shear rates under different motility patterns acting on a solid dosage form show that these are significantly dependent on the motility type. However, the results indicate that it is not high average shear stress that accelerates the decomposition/dissolution process, but individual shear stress peaks with high amplitude are decisive. The biorelevant colon models show a fluctuation of shear stress acting on the surface of the tablet for all motility patterns, which is entirely different from the USP II dissolution apparatus, where constant shear stress acts on the tablet. The shear stress magnitude acting on a solid dosage form significantly depends on the fluid viscosity. With an increase in fluid viscosity, lower shear stress was found. The fluid viscosity and the motility patterns significantly influence dissolved API distribution along the colon. To propel a high viscous fluid effectively and thus distribute the API evenly along the colon, a motility pattern is required that exerts a strong momentum on the fluid (e.g., a peristaltic wave or propagating waves with high occlusion degrees). Otherwise, the movement of the fluid is minimal.

The results of the DCM and DT, respectively, show that under the conditions investigated, the shear rates found are comparable to previous USP II estimates at paddle speeds of 25 and 50 rpm. Consequently, constant paddle speeds greater than 50 rpm may not correspond to physiologically relevant under these conditions. When investigating the dissolution of solid dosage forms in the USP II dissolution apparatus, attention must be paid to ensure that the biorelevant media used and the paddle speed replicate the physiological conditions in the colon.

In addition, the performance of a solid dosage form in a standardised dissolution apparatus (i.e., mini-USP II) and a biorelevant colon model were compared. Therefore,

models of the mini-USP II and the colon were created, and a tablet was developed that behaves like a real tablet. The drug release profiles, as well as the shear rates acting on the tablet, were analysed. These models gained profound insights into the tablet's disintegration/drug release process. Furthermore, the results show that even slow paddle speeds of 1 rpm in the mini-USP II lead to average shear rates acting on the tablet that are twice as high as the average shear rates experienced by the tablet in the biorelevant colon model. Another crucial point for the disintegration/dissolution process of the tablet is that the shear rate acting on the tablet has a different pattern in the mini-USP II and the colon model. Based on the results, whether the mini-USP II or even the USP II dissolution apparatus is the most suitable apparatus to mimic *in vivo* conditions in the colon should be considered.

The developed models have shown the potential of the computational approach to support *in vitro* and *in vivo* experiments and thus a promising tool for the pharmaceutical industry, especially in drug development and optimisation. Single parameters in these developed models (e.g., physiology, motility patterns, fluid viscosities, media volume, and tablet structure inclusive drug release mechanisms) can be manipulated individually to scrutinise the effects. Additionally, reduced drug solubility, as found in patients with Crohn's Disease and Ulcerative Colitis (Effinger et al., 2020a, Effinger et al., 2020b), can be realised in the models.

Although the models developed with Discrete Multiphysics can provide new insights into the colon's environment that are difficult or impossible to capture in *in vitro* or/and *in vivo* experiments, further research is still required, especially for the disintegration/dissolution of a solid dosage form. The limitations of this thesis arise

from the lack of clinical data that directly reflect the observations in the model for validation purposes. However, generating such data *in vivo* is complex due to the relative inaccessibility of the different parts of the colon, and it is a big challenge to control fluid viscosity or colon motility. Further limitations arise from the fluid properties used in this thesis. For simplicity, a Newtonian fluid is used in the simulations, although the intestinal content has a shear thinning behaviour. However, it is also shown that the differences are only more pronounced at high fluid viscosity and low shear rates.

General limitations of the work presented arise from the lack of experimental data in the literature verifying the dissolution profiles and drug distribution found in the computational colon.

8.2 Future work suggestions

In the previous work, a Newtonian fluid was used for simplification, which could be modelled as a real fluid (i.e., shear thinning) in future work. In addition, the dewatering process in the colon is not considered in the models. Water absorption leads to a solidification rate and can be added to the model. Furthermore, the tablets developed in this thesis are modelled in a simplified way, assuming, e.g., that tablets consist of 100% drug and partially disregarded the excipients that may influence the drug release process (Chapter 2.1.3). As also represented in Chapter 2.1.3, there are tablets in various forms and drug release mechanisms. Therefore, in future tablet models, these varieties can be considered. In Chapter 7.4, it is shown that the average shear rate acting on the tablet is about one order of magnitude larger in the mini-USP II

than in the colon models. Further investigations need to be carried out to show the effect of increasing the paddle clearance at the commonly used paddle speeds (i.e., 25 and 50 rpm) on the average shear rate experienced by the tablet.

As mentioned in Chapter 2.1.5, PBPK models so far do not consider shear forces acting on the tablet and consider the dissolution/disintegration process of the tablet as an immediate event. Furthermore, these models consider, for example, the colon as a single, well-mixed and homogenised container. In the future, the computational approaches presented in this thesis could be integrated into existing PBPK models to improve predictions, especially when transit times, shear forces and the distribution (i.e., mixing) of the Active Pharmaceutical Ingredient influence the performance of the solid dosage form.

Another area that has not been considered in the simulations so far is the absorption of the drug in the intestine.

Bibliography

- ABRAHAMSSON, B., PAL, A., SJOBERG, M., CARLSSON, M., LAURELL, E. & BRASSEUR, J. G. 2005. A novel in vitro and numerical analysis of shear-induced drug release from extended-release tablets in the fed stomach. *Pharmaceutical Research*, 22, 1215-1226.
- ADEPU, S. & RAMAKRISHNA, S. 2021. Controlled Drug Delivery Systems: Current Status and Future Directions. *Molecules*, 26.
- ALATAB, S., SEPANLOU, S. G., IKUTA, K., VAHEDI, H., BISIGNANO, C., SAFIRI, S., SADEGHI, A., NIXON, M. R., ABDOLI, A., ABOLHASSANI, H., ALIPOUR, V., ALMADI, M. A. H., ALMASI-HASHIANI, A., ANUSHIRAVANI, A., ARABLOO, J., ATIQUE, S., AWASTHI, A., BADAWI, A., BAIG, A. A. A., BHALA, N., BIJANI, A., BIONDI, A., BORZÌ, A. M., BURKE, K. E., CARVALHO, F., DARYANI, A., DUBEY, M., EFTEKHARI, A., FERNANDES, E., FERNANDES, J. C., FISCHER, F., HAJ-MIRZAIAN, A., HAJ-MIRZAIAN, A., HASANZADEH, A., HASHEMIAN, M., HAY, S. I., HOANG, C. L., HOUSEH, M., ILESANMI, O. S., JAFARI BALALAMI, N., JAMES, S. L., KENGNE, A. P., MALEKZADEH, M. M., MERAT, S., MERETOJA, T. J., MESTROVIC, T., MIRRAKHIMOV, E. M., MIRZAEI, H., MOHAMMAD, K. A., MOKDAD, A. H., MONASTA, L., NEGOI, I., NGUYEN, T. H., NGUYEN, C. T., POURSHAMS, A., POUSTCHI, H., RABIEE, M., RABIEE, N., RAMEZANZADEH, K., RAWAF, D. L., RAWAF, S., REZAEI, N., ROBINSON, S. R., RONFANI, L., SAXENA, S., SEPEHRIMANESH, M., SHAIKH, M. A., SHARAFI, Z., SHARIF, M., SIABANI, S., SIMA, A. R., SINGH, J. A., SOHEILI, A., SOTOUDEHMANESH, R., SULERIA, H. A. R., TEFAY, B. E., TRAN, B., TSOI, D., VACANTE, M., WONDMIENEH, A. B., ZARGHI, A., ZHANG, Z.-J., DIRAC, M., MALEKZADEH, R. & NAGHAVI, M. 2020. The global, regional, and national burden of inflammatory bowel disease in 195 countries and territories, 1990 - 2017: a systematic analysis for the Global Burden of Disease Study 2017. *The Lancet Gastroenterology & Hepatology*, 5, 17-30.
- ALBANO, A., LE GUILLOU, E., DANZÉ, A., MOULITSAS, I., SAHPUTRA, I. H., RAHMAT, A., DUQUE-DAZA, C. A., SHANG, X., CHING NG, K., ARIANE,

-
- M. & ALEXIADIS, A. 2021. How to Modify LAMMPS: From the Prospective of a Particle Method Researcher. *ChemEngineering*, 5, 30.
- ALDERBORN, G. & FRENNING, G. 2018. Chapter 30 - Tablets and compaction. In: AULTON, M. E. & TAYLOR, K. M. G. (eds.) *Aulton's Pharmaceutics (Fifth Edition)*. Elsevier.
- ALEXIADIS, A. 2014. A smoothed particle hydrodynamics and coarse-grained molecular dynamics hybrid technique for modelling elastic particles and breakable capsules under various flow conditions. *International Journal for Numerical Methods in Engineering*, 100, 713-719.
- ALEXIADIS, A. 2015a. The Discrete Multi-Hybrid System for the Simulation of Solid-Liquid Flows. *Plos One*, 10, e0124678.
- ALEXIADIS, A. 2015b. A new framework for modelling the dynamics and the breakage of capsules, vesicles and cells in fluid flow. *Procedia IUTAM*, 16, 80-88.
- ALEXIADIS, A. 2019a. Deep Multiphysics and Particle-Neuron Duality: A Computational Framework Coupling (Discrete) Multiphysics and Deep Learning. *Applied Sciences-Basel*, 9, 5369.
- ALEXIADIS, A. 2019b. Deep multiphysics: Coupling discrete multiphysics with machine learning to attain self-learning in-silico models replicating human physiology. *Artificial Intelligence in Medicine*, 98, 27-34.
- ALEXIADIS, A., GHRAYBEH, S. & QIAO, G. 2018. Natural convection and solidification of phase-change materials in circular pipes: A SPH approach. *Computational Materials Science*, 150, 475-483.
- ALEXIADIS, A., SIMMONS, M. J. H., STAMATOPOULOS, K., BATCHELOR, H. K. & MOULITSAS, I. 2021. The virtual physiological human gets nerves! How to account for the action of the nervous system in multiphysics simulations of human organs. *Journal of the Royal Society Interface*, 18, 20201024.
- ALEXIADIS, A., STAMATOPOULOS, K., WEN, W., BATCHELOR, H. K., BAKALIS, S., BARIGOU, M. & SIMMONS, M. J. H. 2017. Using discrete multi-physics for detailed exploration of hydrodynamics in an in vitro colon system. *Computers in Biology and Medicine*, 81, 188-198.
- ALVAREZ-FUENTES, J., FERNANDEZ-AREVALO, M., GONZALEZ-RODRIGUEZ, M. L., CIRRI, M. & MURA, P. 2004. Development of enteric-coated timed-release matrix tablets for colon targeting. *Journal of Drug Targeting*, 12, 607-612.
-

- AMICARELLI, A., KOCAK, B., SIBILLA, S. & GRABE, J. 2017. A 3D smoothed particle hydrodynamics model for erosional dam-break floods. *International Journal of Computational Fluid Dynamics*, 31, 413-434.
- AMIDON, S., BROWN, J. E. & DAVE, V. S. 2015. Colon-Targeted Oral Drug Delivery Systems: Design Trends and Approaches. *Aaps Pharmscitech*, 16, 731-741.
- ARIANE, M., ALEXIADIS, A. & BARIGOU, M. April 2016. Smoothed particle hydrodynamic modelling of an aortic valve with flexible leaflets. *ChemEngDay. Bath United Kingdom*.
- ARIANE, M., ALLOUCHE, M. H., BUSSONE, M., GIACOSA, F., BERNARD, F., BARIGOU, M. & ALEXIADIS, A. 2017a. Discrete multi-physics: A mesh-free model of blood flow in flexible biological valve including solid aggregate formation. *Plos One*, 12, e1002047.
- ARIANE, M., KASSINOS, S., VELAGA, S. & ALEXIADIS, A. 2018a. Discrete multi-physics simulations of diffusive and convective mass transfer in boundary layers containing motile cilia in lungs. *Computers in Biology and Medicine*, 95, 34-42.
- ARIANE, M., VIGOLO, D., BRILL, A., NASH, F. G. B., BARIGOU, M. & ALEXIADIS, A. 2018b. Using Discrete Multi-Physics for studying the dynamics of emboli in flexible venous valves. *Computers & Fluids*, 166, 57-63.
- ARIANE, M., WEN, W., VIGOLO, D., BRILL, A., NASH, F. G. B., BARIGOU, M. & ALEXIADIS, A. 2017b. Modelling and simulation of flow and agglomeration in deep veins valves using discrete multi physics. *Computers in Biology and Medicine*, 89, 96-103.
- ARKWRIGHT, J. W., BLENMAN, N. G., UNDERHILL, I. D., MAUNDER, S. A., SZCZESNIAK, M. M., DINNING, P. G. & COOK, I. J. 2009a. In-vivo demonstration of a high resolution optical fiber manometry catheter for diagnosis of gastrointestinal motility disorders. *Optics Express*, 17, 4500-4508.
- ARKWRIGHT, J. W., UNDERHILL, I. D., MAUNDER, S. A., BLENMAN, N., SZCZESNIAK, M. M., WIKLENDT, L., COOK, I. J., LUBOWSKI, D. Z. & DINNING, P. G. 2009b. Design of a high-sensor count fibre optic manometry catheter for in-vivo colonic diagnostics. *Optics Express*, 17, 22423-22431.
- ASKEVOLD, F. 1956. Investigations on the Influence of Diet on the Quantity and Composition of Intestinal Gas in Humans. *Scandinavian Journal of Clinical & Laboratory Investigation*, 8, 87-94.

- AWAD, A., TRENFIELD, S. J. & BASIT, A. W. 2021. Chapter 19 - Solid oral dosage forms. In: ADEJARE, A. (ed.) *Remington (Twenty-third Edition)*. Academic Press.
- BADLEY, A. D., CAMILLERI, M. & OCONNOR, M. K. 1993. Noninvasive Measurement of Human Ascending Colon Volume. *Nuclear Medicine Communications*, 14, 485-489.
- BAI, G. & ARMENANTE, P. M. 2008. Velocity Distribution and Shear Rate Variability Resulting from Changes in the Impeller Location in the USP Dissolution Testing Apparatus II. *Pharmaceutical Research*, 25, 320-336.
- BAI, G., ARMENANTE, P. M. & PLANK, R. V. 2007a. Experimental and computational determination of blend time in USP Dissolution Testing Apparatus II. *Journal of Pharmaceutical Sciences*, 96, 3072-3086.
- BAI, G., ARMENANTE, P. M., PLANK, R. V., GENTZLER, M., FORD, K. & HARMON, P. 2007b. Hydrodynamic Investigation of USP Dissolution Test Apparatus II. *Journal of Pharmaceutical Sciences*, 96, 2327-2349.
- BAI, G., WANG, Y. & ARMENANTE, P. M. 2011. Velocity profiles and shear strain rate variability in the USP Dissolution Testing Apparatus 2 at different impeller agitation speeds. *International Journal of Pharmaceutics*, 403, 1-14.
- BAKSAMAWI, H. A., ARIANE, M., BRILL, A., VIGOLO, D. & ALEXIADIS, A. 2021. Modelling Particle Agglomeration on through Elastic Valves under Flow. *ChemEngineering*, 5, 40.
- BAMPTON, P. A. & DINNING, P. G. 2013. High resolution colonic manometry--what have we learnt?--A review of the literature 2012. *Curr Gastroenterol Rep*, 15, 328.
- BAMPTON, P. A., DINNING, P. G., KENNEDY, M. L., LUBOWSKI, D. Z., DECARLE, D. & COOK, I. J. 2000. Spatial and temporal organization of pressure patterns throughout the unprepared colon during spontaneous defecation. *Am J Gastroenterol*, 95, 1027-35.
- BASSOTTI, G., ANTONELLI, E., VILLANACCI, V., SALEMME, M., COPPOLA, M. & ANNESE, V. 2014. Gastrointestinal motility disorders in inflammatory bowel diseases. *World Journal of Gastroenterology*, 20, 37-44.
- BASSOTTI, G. & GABURRI, M. 1988. Manometric investigation of high-amplitude propagated contractile activity of the human colon. *American Journal of Physiology-Gastrointestinal and Liver Physiology*, 255, G660-4.

-
- BAXTER, J. L., KUKURA, J. & MUZZIO, F. J. 2005. Hydrodynamics-induced variability in the USP apparatus II dissolution test. *International Journal of Pharmaceutics*, 292, 17-28.
- BHARUCHA, A. E. & CAMILLERI, M. 2019. Chapter 144 - Physiology of the Colon and Its Measurement. In: YEO, C. J. (ed.) *Shackelford's Surgery of the Alimentary Tract, 2 Volume Set (Eighth Edition)*. Philadelphia: Elsevier.
- BIRMINGHAM, U. *University of Birmingham's BlueBEAR HPC service* [Online]. Available: <http://www.birmingham.ac.uk/bear> [Accessed 01/09/2021 2021].
- BONAPACE, E. S., MAURER, A. H., DAVIDOFF, S., KREVSKY, B., FISHER, R. S. & PARKMAN, H. P. 2000. Whole gut transit scintigraphy in the clinical evaluation of patients with upper and lower gastrointestinal symptoms. *American Journal of Gastroenterology*, 95, 2838-2847.
- BRELY, L., BOSIA, F. & PUGNO, N. M. 2015. A Hierarchical Lattice Spring Model to Simulate the Mechanics of 2-D Materials-Based Composites. *Frontiers in Materials*, 2.
- BURISCH, J., JESS, T., MARTINATO, M. & LAKATOS, P. L. 2013. The burden of inflammatory bowel disease in Europe. *Journal of Crohns & Colitis*, 7, 322-337.
- CHEN, J. H., YU, Y. J., YANG, Z. X., YU, W. Z., CHEN, W. L., YU, H., KIM, M. J. M., HUANG, M., TAN, S. Y., LUO, H. S., CHEN, J. F., CHEN, J. D. Z. & HUIZINGA, J. D. 2017. Intraluminal pressure patterns in the human colon assessed by high-resolution manometry. *Scientific Reports*, 7.
- CHRISTENSEN, J. 1989. Chapter 24 - Handbook of Physiology, the Gastrointestinal System: Colonic Motility. *American Physiological Society*, 939-973.
- CHRISTENSEN, J. 1994. *Physiology of the Gastrointestinal Tract*, New York, Raven Press.
- CONNINGTON, K., KANG, Q. J., VISWANATHAN, H., ABDEL-FATTAH, A. & CHEN, S. Y. 2009. Peristaltic particle transport using the lattice Boltzmann method. *Physics of Fluids*, 21.
- CUMMINGS, J. H., POMARE, E. W., BRANCH, W. J., NAYLOR, C. P. & MACFARLANE, G. T. 1987. Short chain fatty acids in human large intestine, portal, hepatic and venous blood. *Gut*, 28, 1221-7.
- D'ARCY, D. M., CORRIGAN, O. I. & HEALY, A. M. 2006. Evaluation of hydrodynamics in the basket dissolution apparatus using computational fluid dynamics - Dissolution rate implications. *European Journal of Pharmaceutical Sciences*, 27, 259-267.
-

- D'ARCY, D. M., CORRIGAN, O. I. & HEALY, A. M. 2010. Hydrodynamic simulation (computational fluid dynamics) of asymmetrically positioned tablets in the paddle dissolution apparatus: impact on dissolution rate and variability. *Journal of Pharmacy and Pharmacology*, 57, 1243-1250.
- DIAKIDOU, A., VERTZONI, M., GOUMAS, K., SODERLIND, E., ABRAHAMSSON, B., DRESSMAN, J. & REPPAS, C. 2009. Characterization of the Contents of Ascending Colon to Which Drugs are Exposed After Oral Administration to Healthy Adults. *Pharmaceutical Research*, 26, 2141-2151.
- DIAZ TARTERA, H. O., WEBB, D. L., AL-SAFFAR, A. K., HALIM, M. A., LINDBERG, G., SANGFELT, P. & HELLSTRÖM, P. M. 2017. Validation of SmartPill® wireless motility capsule for gastrointestinal transit time: Intra-subject variability, software accuracy and comparison with video capsule endoscopy. *Neurogastroenterology & Motility*, 29, e13107.
- DINNING, P. G., BAMPTON, P. A., ANDRE, J., KENNEDY, M. L., LUBOWSKI, D. Z., KING, D. W. & COOK, I. J. 2004. Abnormal predefecatory colonic motor patterns define constipation in obstructed defecation. *Gastroenterology*, 127, 49-56.
- DINNING, P. G. & DI LORENZO, C. 2011. Colonic dysmotility in constipation. *Best Practice & Research Clinical Gastroenterology*, 25, 89-101.
- DINNING, P. G., SZCZESNIAK, M. M. & COOK, I. J. 2008. Proximal colonic propagating pressure waves sequences and their relationship with movements of content in the proximal human colon. *Neurogastroenterology and Motility*, 20, 512-520.
- DINNING, P. G., WIKLENDT, L., GIBBINS, I., PATTON, V., BAMPTON, P., LUBOWSKI, D. Z., COOK, I. J. & ARKWRIGHT, J. W. 2013a. Low-resolution colonic manometry leads to a gross misinterpretation of the frequency and polarity of propagating sequences: Initial results from fiber-optic high-resolution manometry studies. *Neurogastroenterology and Motility*, 25, E640-E649.
- DINNING, P. G., WIKLENDT, L., MASLEN, L., GIBBINS, I., PATTON, V., ARKWRIGHT, J. W., LUBOWSKI, D. Z., O'GRADY, G., BAMPTON, P. A., BROOKES, S. J. & COSTA, M. 2014. Quantification of in vivo colonic motor patterns in healthy humans before and after a meal revealed by high-resolution fiber-optic manometry. *Neurogastroenterology and Motility*, 26, 1443-1457.

-
- DINNING, P. G., WIKLENDT, L., PATTON, V. E., BAMPTON, P. A., COOK, I. J., GIBBINS, I., LUBOWSKI, D. Z. & ARKWRIGHT, J. W. 2013b. Spatial Aliasing of Colonic Manometry Data: What Have We Been Missing or Mislabeling? *Gastroenterology*, 144, S919-S919.
- DUQUE-DAZA, C. & ALEXIADIS, A. 2021. A Simplified Framework for Modelling Viscoelastic Fluids in Discrete Multiphysics. *Chemengineering*, 5.
- EDSMAN, K. & HÄGERSTRÖM, H. 2005. Pharmaceutical applications of mucoadhesion for the non-oral routes. *Journal of Pharmacy and Pharmacology*, 57, 3-22.
- EFFINGER, A., O'DRISCOLL, C. M., MCALLISTER, M. & FOTAKI, N. 2020a. Gastrointestinal diseases and their impact on drug solubility: Crohn's disease. *European Journal of Pharmaceutical Sciences*, 152.
- EFFINGER, A., O'DRISCOLL, C. M., MCALLISTER, M. & FOTAKI, N. 2020b. Gastrointestinal diseases and their impact on drug solubility: Ulcerative Colitis. *European Journal of Pharmaceutical Sciences*, 152.
- ELLIS, H. & MAHADEVAN, V. 2014. Anatomy of the caecum, appendix and colon. *Surgery (Oxford)*, 32, 155-158.
- FRENCH, D. L. & MAUGER, J. W. 1993. Evaluation of the Physicochemical Properties and Dissolution Characteristics of Mesalamine - Relevance to Controlled Intestinal Drug-Delivery. *Pharmaceutical Research*, 10, 1285-1290.
- FRENKEL, D. & SMIT, B. 2002. Chapter 4 - Molecular Dynamics Simulations. In: FRENKEL, D. & SMIT, B. (eds.) *Understanding Molecular Simulation (Second Edition)*. San Diego: Academic Press.
- FRIEND, D. R. 1991. Colon-Specific Drug Delivery. *Advanced Drug Delivery Reviews*, 7, 149-199.
- FRIEND, D. R. 2005. New oral delivery systems for treatment of inflammatory bowel disease. *Advanced Drug Delivery Reviews*, 57, 247-265.
- GANZENMÜLLER, G. C., STEINHAUSER, M. O. & VAN LIEDEKERKE, P. 2011. The Implementation of Smoothed Particle Hydrodynamics in LAMMPS. Retrieved from (lammms.sandia.gov/doc/PDF/SPH_LAMMPS_userguide.pdf), (last accessed 17.10.2019).
- GINGOLD, R. A. & MONAGHAN, J. J. 1977. Smoothed Particle Hydrodynamics - Theory and Application to Non-Spherical Stars. *Monthly Notices of the Royal Astronomical Society*, 181, 375-389.

-
- GOFFREDO, R., PECORA, A., MAIOLO, L., FERRONE, A., GUGLIEMELLI, E. & ACCOTO, D. 2016. A Swallowable Smart Pill for Local Drug Delivery. *Journal of Microelectromechanical Systems*, 25, 362-370.
- GRASSI, M., COLOMBO, I. & LAPASIN, R. 2001. Experimental determination of the theophylline diffusion coefficient in swollen sodium-alginate membranes. *Journal of Controlled Release*, 76, 93-105.
- HABASHY, R., KHODER, M., ISREB, A. & ALHNAN, M. A. 2022. A Novel Multilayer Natural Coating for Fed-State Gastric Protection. *Pharmaceutics*, 14, 283.
- HAMMER, J. & PHILLIPS, S. F. 1993. Fluid loading of the human colon: Effects on segmental transit and stool composition. *Gastroenterology*, 105, 988-998.
- HARI, B., BAKALIS, S. & FRYER, P. 2012. Computational Modelling and Simulation of the Human Duodenum. *COMSOL Conference*. Milan.
- HAYWOOD, A. & GLASS, B. D. 2011. Pharmaceutical excipients – where do we begin? *Australian Prescriber*, 34, 112-114.
- HEBDEN, J. M., BLACKSHAW, P. E., PERKINS, A. C., WILSON, C. G. & SPILLER, R. C. 2000. Limited exposure of the healthy distal colon to orally-dosed formulation is further exaggerated in active left-sided ulcerative colitis. *Alimentary Pharmacology & Therapeutics*, 14, 155-161.
- HINKLE, B. 2020. *MATLAB Central File Exchange: Hatched Fill Patterns*, Natick, MA, USA, The MathWorks Inc.
- HINTON, J. M., LENNARD-JONES, J. E. & YOUNG, A. C. 1969. A new method for studying gut transit times using radiopaque markers. *Gut*, 10, 842-847.
- HOAD, C. L., MENYS, A., GARSED, K., MARCIANI, L., HAMY, V., MURRAY, K., COSTIGAN, C., ATKINSON, D., MAJOR, G., SPILLER, R. C., TAYLOR, S. A. & GOWLAND, P. A. 2016. Colon wall motility: comparison of novel quantitative semi-automatic measurements using cine MRI. *Neurogastroenterology and Motility*, 28, 327-335.
- HOPGOOD, M., REYNOLDS, G. & BARKER, R. 2018. Using Computational Fluid Dynamics to Compare Shear Rate and Turbulence in the TIM-Automated Gastric Compartment With USP Apparatus II. *Journal of Pharmaceutical Sciences*, 107, 1911-1919.
- HUR, S. J., LIM, B. O., DECKER, E. A. & MCCLEMENTS, D. J. 2011. In vitro human digestion models for food applications. *Food Chemistry*, 125, 1-12.

-
- IACUCCI, M., DE SILVA, S. & GHOSH, S. 2010. Mesalazine in inflammatory bowel disease: a trendy topic once again? *Can J Gastroenterol*, 24, 127-33.
- JOHNS CREEK (GA): EBIX, I. c1997-2021. *A.D.A.M. Medical Encyclopedia* [Online]. A.D.A.M. Available: <https://medlineplus.gov/ency/imagepages/19218.htm> [Accessed 02/09/2021].
- KAPLAN, G. G. 2015. The global burden of IBD: from 2015 to 2025. *Nature Reviews Gastroenterology & Hepatology*, 12, 720-727.
- KHOCHTALI, H., BENBELGACEM, I., ZEMZEMI, F. & BENSALÉM, W. 2021. Comparison of Coupled Eulerian-Lagrangian and Coupled Smoothed Particle Hydrodynamics-Lagrangian in Fluid-Structure Interaction Applied to Metal Cutting. *Arabian Journal for Science and Engineering*.
- KIDO, A. & TOGASHI, K. 2016. Uterine anatomy and function on cine magnetic resonance imaging. *Reprod Med Biol*, 15, 191-199.
- KINDGEN, S., WACHTEL, H., ABRAHAMSSON, B. & LANGGUTH, P. 2015. Computational Fluid Dynamics Simulation of Hydrodynamics and Stresses in the PhEur/USP Disintegration Tester Under Fed and Fasted Fluid Characteristics. *Journal of Pharmaceutical Sciences*, 104, 2956-2968.
- KIRCHHOFF, S., NICOLAUS, M., SCHIRRA, J., REISER, M. F., GOKE, B. & LIENEMANN, A. 2011. Assessment of colon motility using simultaneous manometric and functional cine-MRI analysis: preliminary results. *Abdominal Imaging*, 36, 24-30.
- KLEIN, S. & SHAH, V. 2008. A Standardized Mini Paddle Apparatus as an Alternative to the Standard Paddle. *Aaps Pharmscitech*, 9, 1179-1184.
- KOHL, P., NOBLE, D., WINSLOW, R. L. & HUNTER, P. J. 2000. Computational modelling of biological systems: tools and visions. *Philosophical Transactions of the Royal Society a-Mathematical Physical and Engineering Sciences*, 358, 579-610.
- KOT, M. 2021. Mass Spring Models of Amorphous Solids. *Chemengineering*, 5.
- KOT, M., NAGAHASHI, H. & SZYMCZAK, P. 2015. Elastic moduli of simple mass spring models. *Visual Computer*, 31, 1339-1350.
- KUKURA, J., BAXTER, J. L. & MUZZIO, F. J. 2004. Shear distribution and variability in the USP Apparatus 2 under turbulent conditions. *International Journal of Pharmaceutics*, 279, 9-17.

-
- KUMAR, S. P., PRATHIBHA, D., PARTHIBARAJAN, R. & REICHAL, C. R. 2012. Novel Colon Specific Drug Delivery System: A Review. *International Journal of Pharmacy and Pharmaceutical Sciences*, 4, 22-29.
- KURBEL, S., KURBEL, B. & VCEV, A. 2006. Intestinal gases and flatulence: Possible causes of occurrence. *Medical Hypotheses*, 67, 235-239.
- LAMPRECHT, A., UBRICH, N., YAMAMOTO, H., SCHAFFER, U., TAKEUCHI, H., MAINCENT, P., KAWASHIMA, Y. & LEHR, C. M. 2001. Biodegradable nanoparticles for targeted drug delivery in treatment of inflammatory bowel disease. *Journal of Pharmacology and Experimental Therapeutics*, 299, 775-781.
- LEE, J. 2003. Drug nano- and microparticles processed into solid dosage forms: Physical properties. *Journal of Pharmaceutical Sciences*, 92, 2057-2068.
- LIEM, O., BURGERS, R. E., CONNOR, F. L., BENNINGA, M. A., REDDY, S. N., MOUSA, H. M. & DI LORENZO, C. 2012. Solid-state vs water-perfused catheters to measure colonic high-amplitude propagating contractions. *Neurogastroenterology & Motility*, 24, 345-e167.
- LIU, G. R. & LIU, M. B. 2003. *Smoothed Particle Hydrodynamics : a meshfree particle method*, Singapore, World Scientific.
- LLOYD, B. A., SZEKELY, G. & HARDERS, M. 2007. Identification of spring parameters for deformable object simulation. *Ieee Transactions on Visualization and Computer Graphics*, 13, 1081-1094.
- LONG, M. & CHEN, Y. 2009. *Developing Solid Oral Dosage Forms*, Cambridge, MA, USA, Academic Press: .
- LOVE, R. J., LENTLE, R. G., ASVARUJANON, P., HEMAR, Y. & STAFFORD, K. J. 2013. An Expanded Finite Element Model of the Intestinal Mixing of Digesta. *Food Digestion*, 4, 26-35.
- LUCY, L. B. 1977. A numerical approach to the testing of the fission hypothesis. *The Astronomical Journal*, 82, 1013-1024.
- MAQBOOL, S., PARKMAN, H. P. & FRIEDENBERG, F. K. 2009. Wireless Capsule Motility: Comparison of the SmartPill(A (R)) GI Monitoring System with Scintigraphy for Measuring Whole Gut Transit. *Digestive Diseases and Sciences*, 54, 2167-2174.
- MARCIANI, L., GARSED, K. C., HOAD, C. L., FIELDS, A., FORDHAM, I., PRITCHARD, S. E., PLACIDI, E., MURRAY, K., CHADDOCK, G., COSTIGAN, C., LAM, C., JALANKA-TUOVINEN, J., DE VOS, W. M., GOWLAND, P. A. &

-
- SPILLER, R. C. 2014. Stimulation of colonic motility by oral PEG electrolyte bowel preparation assessed by MRI: comparison of split vs single dose. *Neurogastroenterology and Motility*, 26, 1426-1436.
- MARKL, D. & ZEITLER, J. A. 2017. A Review of Disintegration Mechanisms and Measurement Techniques. *Pharmaceutical Research*, 34, 890-917.
- MATLAB 2022. *MATLAB 9.12.0.1927505 (R2022a)*, Natick, MA, USA, The MathWorks Inc.
- MCCANCE, K. L. & HUETHER, S. E. 2019. *Pathophysiology: The Biologic Basis for Disease in Adults and Children*, St. Louis, Missouri, ELSEVIER.
- METCALF, A. M., PHILLIPS, S. F., ZINSMEISTER, A. R., MACCARTY, R. L., BEART, R. W. & WOLFF, B. G. 1987. Simplified assessment of segmental colonic transit. *Gastroenterology*, 92, 40-47.
- METZNER, A. B., FEEHS, R. H., RAMOS, H. L., OTTO, R. E. & TUTHILL, J. D. 1961. Agitation of Viscous Newtonian and Non-Newtonian Fluids. *Aiche Journal*, 7, 3-9.
- MINEKUS, M. 2015. The TNO Gastro-Intestinal Model (TIM). In: VERHOECKX, K., COTTER, P., LOPEZ-EXPOSITO, I., KLEIVELAND, C., LEA, T., MACKIE, A., REQUENA, T., SWIATECKA, D. & WICHERS, H. (eds.) *The Impact of Food Bioactives on Health: in vitro and ex vivo models*. Cham (CH).
- MOHAMMED, A. M., ARIANE, M. & ALEXIADIS, A. 2020. Using Discrete Multiphysics Modelling to Assess the Effect of Calcification on Hemodynamic and Mechanical Deformation of Aortic Valve. *ChemEngineering*, 4, 48.
- MOHAMMED, A. M., ARIANE, M. & ALEXIADIS, A. 2021. Fluid-Structure Interaction in Coronary Stents: A Discrete Multiphysics Approach. *Chemengineering*, 5, 60.
- MOLODECKY, N. A., SOON, I. S., RABI, D. M., GHALI, W. A., FERRIS, M., CHERNOFF, G., BENCHIMOL, E. I., PANACCIONE, R., GHOSH, S., BARKEMA, H. W. & KAPLAN, G. G. 2012. Increasing Incidence and Prevalence of the Inflammatory Bowel Diseases With Time, Based on Systematic Review. *Gastroenterology*, 142, 46-54.
- MONAGHAN, J. J. 1992. Smoothed Particle Hydrodynamics. *Annual Review of Astronomy and Astrophysics*, 30, 543-574.
- MONAGHAN, J. J. 1994. Simulating Free Surface Flows with SPH. *Journal of Computational Physics*, 110, 399-406.
-

-
- MONAGHAN, J. J. 2005. Smoothed particle hydrodynamics. *Reports on Progress in Physics*, 68, 1703-1759.
- MONAGHAN, J. J. 2012. Smoothed Particle Hydrodynamics and Its Diverse Applications. *Annual Review of Fluid Mechanics, Vol 44*, 44, 323-346.
- MONAGHAN, J. J. & GINGOLD, R. A. 1983. Shock Simulation by the Particle Method SPH. *Journal of Computational Physics*, 52, 374-389.
- MOORE, J. W. & FLANNER, H. H. 1996. Mathematical Comparison of Curves with an Emphasis on in Vitro Dissolution Profiles. *Pharmaceutical Technology*, 20, 64-74.
- MORRIS, J. P., FOX, P. J. & ZHU, Y. 1997. Modeling low Reynolds number incompressible flows using SPH. *Journal of Computational Physics*, 136, 214-226.
- MOSER, K. W., KUTTER, E. C., GEORGIADIS, I. G., BUCKIUS, R. O., MORRIS, H. D. & TORCZYNSKI, J. R. 2000. Velocity measurements of flow through a step stenosis using Magnetic Resonance Imaging. *Experiments in Fluids*, 29, 438-447.
- MÜLLER, M., SCHIRM, S., TESCHNER, M., HEIDELBERGER, B. & GROSS, M. 2004. Interaction of fluids with deformable solids. *Computer Animation and Virtual Worlds*, 15, 159-171.
- MURRAY, K., HOAD, C. L., MUDIE, D. M., WRIGHT, J., HEISSAM, K., ABREHART, N., PRITCHARD, S. E., AL ATWAH, S., GOWLAND, P. A., GARNETT, M. C., AMIDON, G. E., SPILLER, R. C., AMIDON, G. L. & MARCIANI, L. 2017. Magnetic Resonance Imaging Quantification of Fasted State Colonic Liquid Pockets in Healthy Humans. *Molecular Pharmaceutics*, 14, 2629-2638.
- NOKHODCHI, A., RAJA, S., PATEL, P. & ASARE-ADDO, K. 2012. The role of oral controlled release matrix tablets in drug delivery systems. *Bioimpacts*, 2, 175-87.
- NORLANDER, B., GOTTHARD, R. & STROM, M. 1990. Pharmacokinetics of a 5-Aminosalicylic Acid Enteric-Coated Tablet in Patients with Crohns-Disease or Ulcerative-Colitis and in Healthy-Volunteers. *Alimentary Pharmacology & Therapeutics*, 4, 497-505.
- NOTGHI, A., KUMAR, D., PANAGAMUWA, B., TULLEY, N. J., HESSLEWOOD, S. R. & HARDING, L. K. 1993. Measurement of Colonic Transit-Time Using Radionuclide Imaging - Analysis by Condensed Images. *Nuclear Medicine Communications*, 14, 204-211.
- O'BRIEN, K. R., COWAN, B. R., JAIN, M., STEWART, R. A. H., KERR, A. J. & YOUNG, A. A. 2008. MRI phase contrast velocity and flow errors in turbulent stenotic jets. *Journal of Magnetic Resonance Imaging*, 28, 210-218.
-

-
- O'FARRELL, C., STAMATOPOULOS, K., SIMMONS, M. J. & BATCHELOR, H. 2021. In vitro models to evaluate ingestible devices: present status and current trends. *Advanced Drug Delivery Reviews*, 178, 113924.
- O'FARRELL, C., HOAD, C. L., STAMATOPOULOS, K., MARCIANI, L., SULAIMAN, S., SIMMONS, M. J. H. & BATCHELOR, H. K. 2021. Luminal Fluid Motion Inside an In Vitro Dissolution Model of the Human Ascending Colon Assessed Using Magnetic Resonance Imaging. *Pharmaceutics*, 13, 1545.
- PACHECO, D. P., BUTNARASU, C. S., VANGOSA, F. B., PASTORINO, L., VISAI, L., VISENTIN, S. & PETRINI, P. 2019. Disassembling the complexity of mucus barriers to develop a fast screening tool for early drug discovery. *Journal of Materials Chemistry B*, 7, 4940-4952.
- PAL, A., ABRAHAMSSON, B., SCHWIZER, W., HEBBARD, G. S. & BRASSEUR, J. G. 2003. Application of a virtual stomach to evaluate gastric mixing and breakdown of solid food. *Gastroenterology*, 124, A673-A674.
- PALMADA, N., CATER, J. E., CHENG, L. K. & SURESH, V. Modelling Flow and Mixing in the Proximal Small Intestine. 2020 42nd Annual International Conference of the IEEE Engineering in Medicine & Biology Society (EMBC), 20-24 July 2020 2020. 2496-2499.
- PALMADA, N., CATER, J. E., CHENG, L. K. & SURESH, V. 2022. Experimental and Computational Studies of Peristaltic Flow in a Duodenal Model. *Fluids*, 7, 40.
- PATEL, G. & MIRSA, A. 2011. *Challenges in Delivery of Therapeutic Genomics and Proteomics*, London, Elsevier.
- PAZDNIAKOU, A. & ADLER, P. M. 2012. Lattice Spring Models. *Transport in Porous Media*, 93, 243-262.
- PITHADIA, A. B. & JAIN, S. 2011. Treatment of inflammatory bowel disease (IBD). *Pharmacological Reports*, 63, 629-642.
- PLIMPTON, S. 1995. Fast Parallel Algorithms for Short-Range Molecular-Dynamics. *Journal of Computational Physics*, 117, 1-19.
- PRASANTH, V. V., JAYAPRAKAS, R. & MATHEW, S. T. 2012. Colon Specific Drug Delivery Systems: A Review on Various Pharmaceutical Approaches. *Journal of Applied Pharmaceutical Science*, 2, 163-169.
- PRITCHARD, S. E., MARCIANI, L., GARSEED, K. C., HOAD, C. L., THONGBORISUTE, W., ROBERTS, E., GOWLAND, P. A. & SPILLER, R. C. 2014. Fasting and postprandial volumes of the undisturbed colon: normal

- values and changes in diarrhea-predominant irritable bowel syndrome measured using serial MRI. *Neurogastroenterol Motil*, 26, 124-30.
- PUTTEWAR, T. Y., KSHIRSAGAR, M. D., CHANDEWAR, A. V. & CHIKHALE, R. V. 2010. Formulation and evaluation of orodispersible tablet of taste masked doxylamine succinate using ion exchange resin. *Journal of King Saud University - Science*, 22, 229-240.
- RAHMAT, A., BARIGOU, M. & ALEXIADIS, A. 2019. Deformation and rupture of compound cells under shear: A discrete multiphysics study. *Physics of Fluids*, 31, 051903.
- RAHMAT, A., BARIGOU, M. & ALEXIADIS, A. 2020a. Numerical simulation of dissolution of solid particles in fluid flow using the SPH method. *International Journal of Numerical Methods for Heat & Fluid Flow*, 30, 290-307.
- RAHMAT, A., WESTON, D., MADDEN, D., USHER, S., BARIGOU, M. & ALEXIADIS, A. 2020b. Modeling the agglomeration of settling particles in a dewatering process. *Physics of Fluids*, 32, 123314.
- RAMAKRISHNA, B. S. 2013. Role of the gut microbiota in human nutrition and metabolism. *Journal of Gastroenterology and Hepatology*, 28, 9-17.
- RUIZ-RIANCHO, I. N., ALEXIADIS, A., ZHANG, Z. B. & HERNANDEZ, A. G. 2021. A Discrete Multi-Physics Model to Simulate Fluid Structure Interaction and Breakage of Capsules Filled with Liquid under Coaxial Load. *Processes*, 9.
- SADAHIRO, S., OHMURA, T., YAMADA, Y., SAITO, T. & TAKI, Y. 1992. Analysis of Length and Surface-Area of Each Segment of the Large-Intestine According to Age, Sex and Physique. *Surgical and Radiologic Anatomy*, 14, 251-257.
- SAHPUTRA, I. H., ALEXIADIS, A. & ADAMS, M. J. 2020. A Coarse Grained Model for Viscoelastic Solids in Discrete Multiphysics Simulations. *Chemengineering*, 4, 30.
- SALEHI, N., AL-GOUSOUS, J., MUDIE, D. M., AMIDON, G. L., ZIFF, R. M. & AMIDON, G. E. 2020. Hierarchical Mass Transfer Analysis of Drug Particle Dissolution, Highlighting the Hydrodynamics, pH, Particle Size, and Buffer Effects for the Dissolution of Ionizable and Nonionizable Drugs in a Compendial Dissolution Vessel. *Molecular Pharmaceutics*, 17, 3870-3884.
- SANFILIPO, D., BAHMAN, G., ALEXIADIS, A. & HERNANDEZ GARCIA, A. 2021. Combined Peridynamics and Discrete Multiphysics to Study the Effects of Air

-
- Voids and Freeze-Thaw on the Mechanical Properties of Asphalt. *Materials*, 14, 1579.
- SARNA, S. K. 2010. *Colonic Motility: From Bench Side to Bedside*, Williston, VT, USA, Morgan & Claypool Publishers:.
- SCHILLER, C., FRÖHLICH, C. P., GIESSMANN, T., SIEGMUND, W., MÖNNIKES, H., HOSTEN, N. & WEITSCHIES, W. 2005. Intestinal fluid volumes and transit of dosage forms as assessed by magnetic resonance imaging. *Alimentary Pharmacology & Therapeutics*, 22, 971-979.
- SCHÜTT, M., O'FARRELL, C., STAMATOPOULOS, K., HOAD, C. L., MARCIANI, L., SULAIMAN, S., SIMMONS, M. J. H., BATCHELOR, H. K. & ALEXIADIS, A. 2022. Simulating the Hydrodynamic Conditions of the Human Ascending Colon: A Digital Twin of the Dynamic Colon Model. *Pharmaceutics*, 14, 184.
- SCHÜTT, M., STAMATOPOULOS, K., BATCHELOR, H. K., SIMMONS, M. J. H. & ALEXIADIS, A. 2021. Modelling and Simulation of the Drug Release from a Solid Dosage Form in the Human Ascending Colon: The Influence of Different Motility Patterns and Fluid Viscosities. *Pharmaceutics*, 13, 859.
- SCHÜTT, M., STAMATOPOULOS, K., SIMMONS, M. J. H., BATCHELOR, H. K. & ALEXIADIS, A. 2020. Modelling and simulation of the hydrodynamics and mixing profiles in the human proximal colon using Discrete Multiphysics. *Computers in Biology and Medicine*, 121, 103819.
- SHAH, V. P., LESKO, L. J., FAN, J., FLEISCHER, N., HANDERSON, J., MALINOWSKI, H., MAKARY, M., DUDERKIRK, L., ROY, S., SATHE, P., SINGH, G. J. P., TILLMAN, L., TSONG, Y. & WILLIAMS, R. L. 1997. FDA Guidance for Industry Dissolution Testing of immediate Release Solid Oral Dosage Forms. *Dissolution Technologies*, 15-22.
- SHAH, V. P., TSONG, Y., SATHE, P. & LIU, J. P. 1998. In vitro dissolution profile comparison--statistics and analysis of the similarity factor, f₂. *Pharm Res*, 15, 889-96.
- SINHA, A., BALL, D. J., CONNOR, A., NIGHTINGALE, J. & WILDING, I. 2003. Intestinal Performance of Two Mesalamine Formulations in Patients with Active Ulcerative Colitis as Assessed by Gamma Scintigraphy. *Pract. Gastroenterol.*, 27, 56-69.
- SINNOTT, M. D., CLEARY, P. W., ARKWRIGHT, J. W. & DINNING, P. G. 2012. Investigating the relationships between peristaltic contraction and fluid
-

-
- transport in the human colon using Smoothed Particle Hydrodynamics. *Computers in Biology and Medicine*, 42, 492-503.
- SINNOTT, M. D., CLEARY, P. W., DINNING, P. G., ARKWRIGHT, J. W. & COSTA, M. 2015. Interpreting manometric signals for propulsion in the gut. *Computational Particle Mechanics*, 2, 273-282.
- SINNOTT, M. D., CLEARY, P. W. & HARRISON, S. M. 2017. Peristaltic transport of a particulate suspension in the small intestine. *Applied Mathematical Modelling*, 44, 143-159.
- SIRI, S., ZHAO, Y., MAIER, F., PIERCE, D. M. & FENG, B. 2020. The Macro- and Micro-Mechanics of the Colon and Rectum I: Experimental Evidence. *Bioengineering*, 7, 130.
- SNOECK, V., GODDEERIS, B. & COX, E. 2005. The role of enterocytes in the intestinal barrier function and antigen uptake. *Microbes and Infection*, 7, 997-1004.
- SÖDERLIND, E. & DRESSMAN, J. B. 2010. *Oral Drug Absorption - Prediction and Assessment*, New York, CRC Press.
- STAMATOPOULOS, K. 2022. Integrating Biopharmaceutics to Predict Oral Absorption Using PBPK Modelling. *Biopharmaceutics*. John Wiley & Sons Ltd.
- STAMATOPOULOS, K., ALBERINI, F., BATCHELOR, H. & SIMMONS, M. J. H. 2016a. Use of PLIF to assess the mixing performance of small volume USP 2 apparatus in shear thinning media. *Chemical Engineering Science*, 145, 1-9.
- STAMATOPOULOS, K., BATCHELOR, H. K., ALBERINI, F., RAMSAY, J. & SIMMONS, M. J. H. 2015. Understanding the impact of media viscosity on dissolution of a highly water soluble drug within a USP 2 mini vessel dissolution apparatus using an optical planar induced fluorescence (PLIF) method. *International Journal of Pharmaceutics*, 495, 362-373.
- STAMATOPOULOS, K., BATCHELOR, H. K. & SIMMONS, M. J. H. 2016b. Dissolution profile of theophylline modified release tablets, using a biorelevant Dynamic Colon Model (DCM). *European Journal of Pharmaceutics and Biopharmaceutics*, 108, 9-17.
- STAMATOPOULOS, K., KARANDIKAR, S., GOLDSTEIN, M., O'FARRELL, C., MARCIANI, L., SULAIMAN, S., HOAD, C. L., SIMMONS, M. J. H. & BATCHELOR, H. K. 2020. Dynamic Colon Model (DCM): A Cine-MRI Informed Biorelevant In Vitro Model of the Human Proximal Large Intestine Characterized by Positron Imaging Techniques. *Pharmaceutics*, 12, 659.
-

-
- STAMATOPOULOS, K., O'FARRELL, C., SIMMONS, M. J. H. & BATCHELOR, H. 2021. In vivo models to evaluate ingestible devices: Present status and current trends. *Advanced Drug Delivery Reviews*, 177, 113915.
- STATHOPOULOS, E., SCHLAGETER, V., MEYRAT, B., DE RIBAUPIERRE, Y. & KUCERA, P. 2005. Magnetic pill tracking: a novel non-invasive tool for investigation of human digestive motility. *Neurogastroenterology and Motility*, 17, 148-154.
- STRUGALA, V., ALLEN, A., DETTMAR, P. W. & PEARSON, J. P. 2003. Colonic mucin: methods of measuring mucus thickness. *Proceedings of the Nutrition Society*, 62, 237-243.
- STUKOWSKI, A. 2010. Visualization and analysis of atomistic simulation data with OVITO-the Open Visualization Tool. *Modelling and Simulation in Materials Science and Engineering*, 18, 015012.
- SULAIMAN, S. & MARCIANI, L. 2019. MRI of the Colon in the Pharmaceutical Field: The Future before us. *Pharmaceutics*, 11, 146.
- TAHERALI, F., VARUM, F. J. O. & BASIT, A. W. 2018. A slippery slope: On the origin, role and physiology of mucus. *Advanced Drug Delivery Reviews*, 124, 16-33.
- TENJARLA, S. 2015. Dissolution of Commercially Available Mesalamine Formulations at Various pH Levels. *Drugs R D*, 15, 211-5.
- TERUEL, A. H., GONZALEZ-ALVAREZ, I., BERMEJO, M., MERINO, V., MARCOS, M. D., SANCENON, F., GONZALEZ-ALVAREZ, M. & MARTINEZ-MANEZ, R. 2020. New Insights of Oral Colonic Drug Delivery Systems for Inflammatory Bowel Disease Therapy. *International Journal of Molecular Sciences*, 21, 6502.
- THOMPSON, A. P., AKTULGA, H. M., BERGER, R., BOLINTINEANU, D. S., BROWN, W. M., CROZIER, P. S., IN 'T VELD, P. J., KOHLMAYER, A., MOORE, S. G., NGUYEN, T. D., SHAN, R., STEVENS, M. J., TRANCHIDA, J., TROTT, C. & PLIMPTON, S. J. 2022. LAMMPS - a flexible simulation tool for particle-based materials modeling at the atomic, meso, and continuum scales. *Computer Physics Communications*, 271, 108171.
- THORPE, M. P., EHRENPREIS, E. D., PUTT, K. S. & HANNON, B. 2009. A dynamic model of colonic concentrations of delayed-release 5-aminosalicylic acid (Asacol). *Alimentary Pharmacology & Therapeutics*, 29, 1193-1201.

-
- TRUSOV, P. V., ZAITSEVA, N. V. & KAMALTDINOV, M. R. 2016. A Multiphase Flow in the Antroduodenal Portion of the Gastrointestinal Tract: A Mathematical Model. *Computational and Mathematical Methods in Medicine*, 2016.
- VAN DEN MOOTER, G. 2006. Colon drug delivery. *Expert Opin Drug Deliv*, 3, 111-25.
- VENEMA, K. 2015. The TNO In Vitro Model of the Colon (TIM-2). In: VERHOECKX, K., COTTER, P., LOPEZ-EXPOSITO, I., KLEIVELAND, C., LEA, T., MACKIE, A., REQUENA, T., SWIATECKA, D. & WICHERS, H. (eds.) *The Impact of Food Bioactives on Health: in vitro and ex vivo models*. Cham (CH).
- VERMA, R. K., KRISHNA, D. M. & GARG, S. 2002. Formulation aspects in the development of osmotically controlled oral drug delivery systems. *Journal of Controlled Release*, 79, 7-27.
- VERTZONI, M., AUGUSTIJNS, P., GRIMM, M., KOZIOLEK, M., LEMMENS, G., PARROTT, N., PENTAFRAGKA, C., REPPAS, C., RUBBENS, J., VAN DEN ABEELE, J., VANUYTSEL, T., WEITSCHIES, W. & WILSON, C. G. 2019. Impact of regional differences along the gastrointestinal tract of healthy adults on oral drug absorption: An UNGAP review. *European Journal of Pharmaceutical Sciences*, 134, 153-175.
- VIOLEAU, D. & ISSA, R. 2007. Numerical modelling of complex turbulent free-surface flows with the SPH method: an overview. *International Journal for Numerical Methods in Fluids*, 53, 277-304.
- VON DER OHE, M. R. & CAMILLERI, M. 1992. Measurement of Small-Bowel and Colonic Transit - Indications and Methods. *Mayo Clinic Proceedings*, 67, 1169-1179.
- VON DER OHE, M. R., HANSON, R. B. & CAMILLERI, M. 1994. Comparison of Simultaneous Recordings of Human Colonic Contractions by Manometry and a Barostat. *Neurogastroenterology and Motility*, 6, 213-222.
- VRIESMAN, M. H., DE JONGE, C. S., KUIZENGA-WESSEL, S., ADLER, B., MENYS, A., NEDERVEEN, A. J., STOKER, J., BENNINGA, M. A. & DI LORENZO, C. 2021. Simultaneous assessment of colon motility in children with functional constipation by cine-MRI and colonic manometry: a feasibility study. *European Radiology Experimental*, 5.
- WANG, B. & ARMENANTE, P. M. 2016. Experimental and computational determination of the hydrodynamics of mini vessel dissolution testing systems. *International Journal of Pharmaceutics*, 510, 336-349.
-

- WANG, B., BREDAEL, G. & ARMENANTE, P. M. 2018. Computational hydrodynamic comparison of a mini vessel and a USP 2 dissolution testing system to predict the dynamic operating conditions for similarity of dissolution performance. *International Journal of Pharmaceutics*, 539, 112-130.
- WATTS, P. J. & ILLUM, L. 1997. Colonic drug delivery. *Drug Development and Industrial Pharmacy*, 23, 893-913.
- WILSON, C. G. 2010. The transit of dosage forms through the colon. *International Journal of Pharmaceutics*, 395, 17-25.
- YANG, L. B., CHU, J. S. & FIX, J. A. 2002. Colon-specific drug delivery: new approaches and in vitro/in vivo evaluation. *International Journal of Pharmaceutics*, 235, 1-15.
- YE, B. & VAN LANGENBERG, D. R. 2015. Mesalazine preparations for the treatment of ulcerative colitis: Are all created equal? *World J Gastrointest Pharmacol Ther*, 6, 137-44.
- ZHA, J., ZOU, S., HAO, J., LIU, X., DELAPLACE, G., JEANTET, R., DUPONT, D., WU, P., CHEN, X. D. & XIAO, J. 2021. The role of circular folds in mixing intensification in the small intestine: A numerical study. *Chemical Engineering Science*, 229, 116079.
- ZHAO, G.-F., FANG, J. & ZHAO, J. 2011. A 3D distinct lattice spring model for elasticity and dynamic failure. *International Journal for Numerical and Analytical Methods in Geomechanics*, 35, 859-885.
- ZULEGER, S., FASSIHI, R. & LIPPOLD, B. C. 2002. Polymer particle erosion controlling drug release. II. Swelling investigations to clarify the release mechanism. *International Journal of Pharmaceutics*, 247, 23-37.